

TRANSCUTANEOUS AURICULAR VAGUS NERVE
STIMULATION FOR VISUALLY INDUCED MOTION SICKNESS

A THESIS SUBMITTED TO
THE UNIVERSITY OF KENT
IN THE SUBJECT OF COMPUTER SCIENCE
FOR THE DEGREE
OF DOCTOR OF PHILOSOPHY

By
Emmanuel Molefi
September 2024

Abstract

Transcutaneous auricular vagus nerve stimulation (taVNS), a non-invasive form of electrical brain stimulation, has shown potent therapeutic potential for a myriad of diseases and disorders. How taVNS influences the neural and physiological response of motion sickness – a complex syndrome marked by progressive, multidimensional symptoms – remains unknown. To examine this, I developed a nauseogenic visual stimulus for nausea induction coalesced with taVNS (200 μ s, 20 Hz) administration during continuous electroencephalogram (EEG) and electrocardiogram (ECG) data acquisition from healthy human participants in crossover randomized sham-controlled studies.

To assess taVNS-induced effects on brain dynamics in response to motion-induced nausea, cortical neuronal generators were estimated from the obtained EEG using exact low-resolution brain electromagnetic tomography (eLORETA). Because taVNS has been shown to modulate the autonomic nervous system (ANS) toward parasympathetic predominance, and that motion-induced nausea is known to perturb ANS function, I performed analysis of ECG-derived heart rate variability (HRV) to quantify autonomic effects of taVNS for motion-induced nausea. Moreover, I obtained the symmetric projection attractor reconstruction (SPAR) transforms of ECG signals to parse taVNS-mediated effects on ECG morphology and variability. Subsequently, I trained machine learning algorithms on ECG SPAR transforms to classify differential response to motion-induced nausea, in addition to taVNS response detection.

taVNS increased activity in the insula and middle frontal gyrus compared to baseline. Following taVNS, brain regions including the supramarginal, parahippocampal,

middle frontal, and precentral gyri demonstrated a differential increase in neuronal activity. My HRV analyses revealed that taVNS restored autonomic balance to healthy levels during concurrent exposure to nauseogenic stimulation. Morphological and variability measures obtained from ECG-derived attractors showed differential effects of taVNS compared to sham. I also show that machine learning models can determine taVNS response from ECG SPAR-based features.

To summarise, these findings provide new insights into taVNS-induced neural and autonomic changes, in addition to suggesting that small doses of electricity delivered at the tragus of the left ear may play an important role in motion sickness management.

Acknowledgements

First and foremost, I would like to thank my PhD supervisor, Dr Palaniappan Ramaswamy, for his mentorship and continued support over the last three years; without his tutelage, I would have not been able to navigate this PhD journey.

I will forever be grateful for the support, guidance, and advice from Professor Ian McLoughlin of Singapore Institute of Technology; I am exceedingly fortunate to have had the opportunity to be encouraged and challenged by him. I am hugely indebted to Dr Anna Jordanous for her marked and continued support. I would also like to give special thanks to my panel, Dr Rogério de Lemos, Professor Alex Freitas, and Dr Ioanna Giorgi, for their valuable feedback and advice. I am grateful to Professor Francisco Sepulveda of University of Essex and Dr Giovanni Luca Masala, for taking the time to examine my thesis, and for their useful, constructive, and insightful comments.

Thank you so much to Dr Marek Grześ, Dr Yang He, Dr Matteo Migliavacca, George Ramzi, Dan Bard, and many others, who have made my journey here memorable. I also thank my office mates, Yanxi Wei, Aidin Kazempour, Zhao Liu, Ben Alison, Simon Provost, Meryem Bagriacik, Aruna Duraisingam, Pierre Mondon, Joshua Sylvester, and Andrew Swinn, for all the great interactions and moments spent together. Thank you to the CEMS PGR Team, Sonnary Dearden and Sandrine O'Neill, for their continued support and help. Further, this research would not have been possible without the important study participants who volunteered in my taVNS studies; thank you for your support and help. To my brother, Bakang Dithapelo Molefi, thank you for your support, encouragement, and believing in me.

I am beyond grateful for the funding and support from the University of Kent School of Computing EPSRC PhD studentship (EP/T518141/1).

Contents

Abstract	ii
Acknowledgements	iv
Contents	v
List of Tables	ix
List of Figures	xii
List of Codes	xix
List of Abbreviations	xx
1 Introduction	1
1.1 Overview	1
1.2 Aims and Objectives	4
1.3 Contributions	5
1.4 Research Outputs	6
1.5 Thesis Structure	7
2 Literature Review	11
2.1 Introduction	11
2.2 Electroencephalography	12
2.3 Electrocardiography	14
2.4 Transcutaneous Auricular Vagus Nerve Stimulation	17

2.4.1	Neural Effects of taVNS	17
2.4.2	Autonomic Effects of taVNS	22
2.5	Visually Induced Motion Sickness	27
2.5.1	Neural Effects of Motion Sickness	30
2.5.2	Autonomic Effects of Motion Sickness	34
2.6	Electrical Stimulation for Motion Sickness	37
2.7	Summary	47
3	Materials and Methods	48
3.1	Introduction	48
3.2	Participants	49
3.3	Experimental Protocol	50
3.4	EEG and ECG Data Acquisition	51
3.5	Behavioral Data Acquisition	52
3.5.1	Motion Sickness Susceptibility Questionnaire (MSSQ)	52
3.5.2	Motion Sickness Assessment Questionnaire (MSAQ)	54
3.5.3	Simulator Sickness Questionnaire (SSQ)	57
3.6	Nauseogenic Stimulation	58
3.7	Electrical Stimulation	60
3.8	Summary	62
4	Effects of taVNS on the Human Brain in Visually Induced Motion Sickness	63
4.1	Introduction	63
4.2	Methods	65
4.2.1	EEG Data Processing	65
4.2.2	Spectral and Time-Frequency Decomposition	66
4.2.3	Exact LORETA (eLORETA)	66
4.2.4	Statistical Analysis	67
4.3	Results	68
4.3.1	EEG Spectral Responses to taVNS during Motion-Induced Nausea	68

4.3.2	EEG Source Localization Reveals Differential Response to taVNS for Motion-Induced Nausea	70
4.4	Discussion	77
4.5	Conclusion	85
5	Autonomic Effects of taVNS on Visually Evoked Motion Sickness in Hu- mans	87
5.1	Introduction	87
5.2	Methods	89
5.2.1	ECG Data Processing	89
5.2.2	Heart Rate Variability (HRV)	90
5.2.3	Symmetric Projection Attractor Reconstruction (SPAR)	102
5.2.4	Statistical Analysis	105
5.3	Results	107
5.3.1	HRV Responses to Motion-Induced Nausea	107
5.3.2	Effects of taVNS on HRV for Motion-Induced Nausea	112
5.3.3	Differential Effects of taVNS for Motion Sickness on ECG SPAR Transforms	113
5.4	Discussion	114
5.5	Conclusion	118
6	Using Supervised Learning to Predict Motion-Induced Nausea, and Effects of taVNS	119
6.1	Introduction	119
6.2	Experiment 1: Transfer Learning of Motion-Induced Nausea ECG SPAR Transforms	121
6.2.1	Methods	121
6.2.2	Results	129
6.3	Experiment 2: Detection of taVNS Response Using ECG SPAR-Based Features	131
6.3.1	Methods	131

6.3.2 Results	134
6.4 Discussion	136
6.5 Conclusion	139
7 General Discussion	141
7.1 Overview	141
7.2 Sham Condition in taVNS Studies	142
7.3 taVNS Dosage for Motion-Induced Nausea	143
7.4 Interpreting Differential eLORETA	145
7.5 HRV as a Biomarker for taVNS	147
7.6 Implications of Sex Differences	148
7.7 Influence of Sample Size	149
8 Conclusions and Future Directions	151
8.1 Conclusions	151
8.2 Future Directions	153
Bibliography	155
A Ethics Approvals	197
B Nauseogenic Visual Stimulus	202

List of Tables

1	Brain effects of taVNS in healthy human participants.	20
2	Autonomic effects of taVNS in healthy human participants.	24
3	Brain effects of motion sickness in healthy human participants.	32
4	Autonomic effects of motion sickness in healthy human participants. . .	36
5	Electrical stimulation countermeasures for motion sickness.	40
6	Motion sickness susceptibility questionnaire short-form (MSSQ-Short) (modified from Golding, 2006).	55
7	Motion sickness assessment questionnaire (MSAQ) (modified from Gianaros et al., 2001).	56
8	Simulator sickness questionnaire (SSQ) instrument with example ratings (red ovals) (modified from Kennedy et al., 1993).	58
9	Simulator sickness questionnaire (SSQ) weights for subscales and example rating (modified from Kennedy et al., 1993).	59
10	Electrical Stimulation Current.	62
11	A summary of the MSAQ results. Data are mean \pm SEM. Reproduced from Molefi, McLoughlin and Palaniappan (2023b).	69
12	Spearman Correlation between brain activity and MSAQ. Reproduced from Molefi, McLoughlin and Palaniappan (2023b).	69

13	Summary of motion sickness assessment questionnaire (MSAQ), and simulator sickness questionnaire (SSQ) total and subscale scores across participants, respectively; in participants receiving transcutaneous auricular vagus nerve stimulation (taVNS) compared with sham. Data are shown as mean \pm SEM. Reproduced from Molefi, McLoughlin and Palaniappan (2025).	73
14	HRV time-domain measures.	93
15	HRV frequency-domain measures.	96
16	HRV nonlinear measures.	97
17	A summary of the results. Data are mean \pm SEM. Adapted from Molefi, McLoughlin and Palaniappan (2023c).	110
18	Dataset description for Experiment 1: Transfer Learning of Motion-Induced Nausea ECG SPAR Transforms; these data are attractor images computed from 10 s ECG signals obtained from 12 participants during states of “baseline” and “nausea” (see Figure 28 for how an attractor image is computed from an ECG time series).	122
19	Pretrained neural networks results for binary classifications at four attractor embedding dimensions, presented as accuracy % (top), majority vote % (bottom). Reproduced from Molefi and Palaniappan (2024). . . .	129
20	Dataset description for Experiment 2: Detection of taVNS Response Using ECG SPAR-Based Features; these data are attractor images computed from 10 s ECG signals obtained from 29 participants during sham and taVNS conditions (see Figure 28 for how an attractor image is computed from an ECG time series).	132
21	All the hyperparameters examined for each of the classification models used for detection of taVNS response.	135

22 The AUC values of ten models for binary classification of taVNS therapy response derived using LOPOCV with nested 5-fold, 10-fold, and leave-one-participant-out cross-validation. AUC, area under the receiver operating characteristic (ROC) curve; taVNS, transcutaneous auricular vagus nerve stimulation; LOPOCV, leave-one-participant-out cross-validation; SVM, support vector machine. Reproduced from Molefi, McLoughlin and Palaniappan (2024). 136

List of Figures

1	Electrical system of the heart. From Johns Hopkins Medicine (2019).	15
2	An electrocardiogram (ECG) excerpt for an example participant – with annotations of different ECG waves.	16
3	The Vagus Nerve. From Prescott and Liberles (2022).	18
4	Experimental overview illustrations. (a) For active taVNS, the electrode was clipped to the tragus of the left ear. (b) And clipped to the left ear-lobe for sham stimulation. (c) The schematic of the randomized, sham-controlled, crossover design timeline. (d) For a typical lab visit, participants completed a pre and post motion sickness assessment questionnaire (MSAQ) and simulator sickness questionnaire (SSQ); additionally, participants underwent a baseline period, followed by nauseogenic visual stimulation concurrent with electrical stimulation (taVNS or sham), then a recovery period, while electroencephalogram (EEG) and electrocardiogram (ECG) acquisition was performed.	49
5	A BioSemi ActiveTwo system opened from the top and being upgraded to use 64 channels.	52
6	The EM6300A TENS (www.tensmachineuk.com) vagus nerve stimulation device; CE 2460.	61
7	EEG theta power comparisons for sham and taVNS conditions for all participants at the right frontal, right parietal and occipital cortices. Reproduced from Molefi, McLoughlin and Palaniappan (2023b).	70

8	Time-frequency difference between sham and taVNS conditions across regions of interest for all participants. Black contours denote significant temporal clusters after a two-sided non-parametric permutation test with cluster-correction. Reproduced from Molefi, McLoughlin and Palaniappan (2023b).	71
9	(a) Box plot showing MSSQ-Short raw scores of MSA and MSB for all participants. Solid lines indicate mean; dashed lines indicate median. (b) Spearman correlation between MSA and MSB where each data point represents a participant (Spearman $\rho = 0.35$). MSSQ, motion sickness susceptibility questionnaire; MSA, below 12 years of age MSSQ scores; MSB, over the last 10 years MSSQ scores. Reproduced from Molefi, McLoughlin and Palaniappan (2025).	72
10	eLORETA of taVNS versus Baseline contrast. (a) Differential estimated source activity (delta) at the right insula (BA 13, peak $MNI_{x,y,z} = 35 -20 15$, $t = 5.96$). (b) Changes in source activity (theta) observed at the left middle frontal gyrus (BA 46, peak $MNI_{x,y,z} = -45 35 20$, $t = 5.47$). Slice views of source locations from left to right are axial, coronal, and sagittal images; viewed from top, back, and right. In all of the images, the left side of the brain is shown on the left. BA, Brodmann area. Reproduced from Molefi, McLoughlin and Palaniappan (2025).	74

- 11 eLORETA of active Post-taVNS versus Baseline contrast. **(a)** Following taVNS, increased estimated source activity was observed at the supra-marginal gyrus (BA 40, peak $MNI_{x,y,z} = -40 -50 35$, $t = 4.53$) for delta, **(b)** the middle frontal gyrus (BA 6, peak $MNI_{x,y,z} = 40 0 45$, $t = 3.84$) for theta, **(c)** the parahippocampal gyrus (BA 35, peak $MNI_{x,y,z} = 20 -25 -15$, $t = 4.62$) for alpha, **(d)** and the precentral gyrus (BA 6, peak $MNI_{x,y,z} = -55 -5 50$, $t = 3.98$) for gamma. Slice views of source locations from left to right are axial, coronal, and sagittal images; viewed from top, back, and right. In all of the images, the left side of the brain is shown on the left. taVNS, transcutaneous auricular vagus nerve stimulation; BA, Brodmann area. Reproduced from Molefi, McLoughlin and Palaniappan (2025). 75
- 12 eLORETA of Sham versus Baseline, and Post-Sham versus Baseline contrasts. **(a)** Changes in estimated source activity (delta) between Sham (i.e., during stimulation period) and Baseline were identified in the right insula (BA 13, peak $MNI_{x,y,z} = 35 -20 20$, $t = 7.83$). **(b)** Estimated source activity (alpha) differences between Post-Sham and Baseline were identified at the right middle frontal gyrus (BA 9, peak $MNI_{x,y,z} = 45 30 40$, $t = 5.70$). Slice views of source locations from left to right are axial, coronal, and sagittal images; viewed from top, back, and right. In all of the images, the left side of the brain is shown on the left. BA, Brodmann area. Reproduced from Molefi, McLoughlin and Palaniappan (2025). 77
- 13 Exact low-resolution brain electromagnetic tomography (eLORETA) of active Sham versus Baseline contrast. Differential source activity of beta oscillation was observed at the anterior cingulate (BA 24, limbic lobe, $MNI_{x,y,z} = 5 35 10$, $t = 3.34$). Slice views of source locations from left to right are axial, coronal, and sagittal images; viewed from top, back, and right. BA, Brodmann area. Reproduced from Molefi, McLoughlin and Palaniappan (2025). 78

14	eLORETA of active taVNS versus Sham contrast. Differential source activity of theta oscillation was observed at the left middle occipital gyrus (BA 19, peak $MNI_{x,y,z} = -50 -60 -10$, $t = 3.97$). Slice views of source locations from left to right are axial, coronal, and sagittal images; viewed from top, back, and right. In all of the images, the left side of the brain is shown on the left. taVNS, transcutaneous auricular vagus nerve stimulation; BA, Brodmann area. Reproduced from Molefi, McLoughlin and Palaniappan (2025).	79
15	(a) Scatter plots show that the change in activation of the left middle occipital gyrus (L.MOG) between sham and taVNS stimulation was positively associated with MSA responses (Pearson $r = 0.43$), (b) and correlated with the change in SSQ total scores (Spearman $\rho = 0.35$). MSSQ, motion sickness susceptibility questionnaire; MSA, below 12 years of age MSSQ scores; SSQ, simulator sickness questionnaire. Reproduced from Molefi, McLoughlin and Palaniappan (2025).	79
16	Pan–Tompkins QRS algorithm procedures. (a) A 10 s ECG signal for one example participant. (b) Output of bandpass filter. (c) Output of differentiator. (d) Output of squaring procedure. (e) Output from performing moving-window integration.	91
17	Using <code>p1omb</code> to estimate and plot the PSD of the nonuniformly sampled signal. (a) A 10 s ECG signal for one example participant. (b) RR interval for a 120 s ECG segment. (c) Output of <code>p1omb</code> function. (d) Output of <code>pwelch</code> function.	95
18	Poincaré plot for the normal-to-normal interval (NN_{n+1}) versus the subsequent interval (NN_n).	98

19	Generation of a two-dimensional (2D) attractor from an electrocardiogram (ECG) signal. (a) A 10 s ECG signal for one example participant. (b) A three-dimensional (3D) reconstructed attractor for $N = 3$ embedding using Takens' delay coordinates. (c) A 3D reconstructed attractor projected onto a plane (v, w) perpendicular to the vector $[1, 1, 1]$. (d) A 2D attractor overlaid with a density (i.e., heatmap). Reproduced from Molefi, McLoughlin and Palaniappan (2024).	104
20	Electrocardiogram (ECG)-derived symmetric projection attractor reconstruction (SPAR) images in response to sham and taVNS. (sham) The (N, k) attractors generated from a 10 s ECG signal of one example participant for $N = 3, 4, 5, 6$ embeddings from sham condition, (taVNS) and taVNS condition. Reproduced from Molefi, McLoughlin and Palaniappan (2024).	105
21	Example attractors for embedding dimensions $N = 4$, derived from electrocardiogram (ECG) signals of a participant at sham and taVNS conditions (left) , and respective attractor measures including the radial density distribution (r density), θ density distribution (θ density), and attractor outline r from the obtained attractors (right)	106
22	Time-varying power representations of heart rate variability (HRV) using the smoothed pseudo Wigner-Ville distribution (SPWVD) for an example participant. (a) Time-frequency power during sham (baseline subtracted) condition (b) and tES (baseline subtracted) condition. (c) Shows the time-frequency power difference between (Sham vs Baseline) and (tES vs Baseline). A statistical pixel-based permutation test using a pixel-level significance threshold of $p < 0.05$ revealed 1 cluster around 270-290 s (two-tailed non-parametric permutation tests). The significant cluster (region) is outlined by a black contour in (c) . Reproduced from Molefi, McLoughlin and Palaniappan (2023a).	108

23	Time-varying power representations of heart rate variability (HRV) using the smoothed pseudo Wigner-Ville distribution (SPWVD) at the sample level. (a) Time-frequency power representation showing the power differences in tES and sham condition (after baseline subtraction within each condition). (b) Statistical z-map of the time-frequency power representation at the sample level, based on a cluster-level significance threshold $p < 0.05$ (two-tailed non-parametric permutation tests). Significant clusters (regions) are indicated by black contours on the statistical z-map. Reproduced from Molefi, McLoughlin and Palaniappan (2023a).	109
24	Poincaré plots illustrations for Baseline and Nausea states for two example participants. Reproduced and rearranged from Molefi, McLoughlin and Palaniappan (2023c).	111
25	Nonlinear HRV comparisons for Baseline and Nausea states for all participants ($n = 14$) (a) Sample entropy (SampEn), (b) Fuzzy entropy (FuzzyEn), (c) Largest Lyapunov exponent (LLE). Adapted from a poster for Molefi, McLoughlin and Palaniappan (2023c).	112
26	Time- and frequency-domain HRV comparisons for sham and taVNS conditions for all participants ($n = 32$) (a) Root mean square of successive differences of NN intervals (RMSSD), (b) Percentage of successive NN intervals that differ by > 20 ms (pNN20), (c) Percentage of successive NN intervals that differ by > 50 ms (pNN50), (d) high frequency HRV power (HF).	113
27	Attractor features show marked reductions by taVNS versus sham stimulation. (a-d) Violin plots showing attractor measures as percentage change from baseline across all participants for $N = 3, 4, 5, 6$ embeddings during sham and taVNS administration. (e-h) And following sham and taVNS administration. Solid lines indicate mean; dashed lines indicate median. n.s., not significant. Reproduced from Molefi, McLoughlin and Palaniappan (2024).	115

28	<p>Generation of a two-dimensional (2D) attractor from an electrocardiogram (ECG) signal. (a) A 10 s ECG signal for one example participant. (b) A three-dimensional (3D) reconstructed attractor for $N = 3$ embedding using Takens' delay coordinates. (c) A 3D reconstructed attractor projected onto a plane (v, w) perpendicular to the vector $[1, 1, 1]$. (d) A 2D attractor overlaid with a density (i.e., heatmap). Reproduced from Molefi, McLoughlin and Palaniappan (2024).</p>	123
29	<p>Example attractors for embedding dimensions $N = 3, 4, 5, 6$, generated from electrocardiogram (ECG) signals of a participant at baseline (i.e., rest) and during nausea states. Modified from Molefi and Palaniappan (2024).</p>	126
30	<p>Deep transfer learning of ECG-derived attractor image data from ECG signals recorded at Baseline and Nausea states. Adapted from a poster for Molefi and Palaniappan (2024).</p>	127
31	<p>(a-f) ROC curves of all explored pretrained deep neural networks and embedding dimensions showing the true positive rate (TPR), or sensitivity, versus the false positive rate (FPR), or 1-specificity, for the "nausea" class. Reproduced from Molefi and Palaniappan (2024).</p>	130
32	<p>Electrocardiogram (ECG)-derived symmetric projection attractor reconstruction (SPAR) images in response to sham and taVNS. (sham) The (N, k) attractors generated from a 10 s ECG signal of one example participant for $N = 3, 4, 5, 6$ embeddings from sham condition, (taVNS) and taVNS condition. Reproduced from Molefi, McLoughlin and Palaniappan (2024).</p>	133

List of Codes

5.1	Mean subtraction and cubic spline interpolation for HRV spectral power decomposition via FFT- or wavelet-based PSD estimates.	94
5.2	Computing the smoothed pseudo Wigner-Ville distribution (SPWVD). . .	102
5.3	MATLAB code to compute average cycle length (ACL) via the Fourier transform.	103
6.1	Performing SVD on mean-subtracted attractor image data.	124
6.2	Attractor image category (baseline vs. nausea) classification using bag of features.	124
6.3	A Slurm script to request the required GPU resources.	128
B.1	Nauseogenic visual stimulus.	202

List of Abbreviations

ANS	Autonomic nervous system
AUC	Area under the ROC curve
BA	Brodmann area
BOLD	Blood oxygen level dependent
CNN	Convolutional neural network
CNS	Central nervous system
CV	Cross-validation
DL	Deep learning
dIPFC	Dorsolateral prefrontal cortex
ECG	Electrocardiogram
EEG	Electroencephalogram
eLORETA	Exact low-resolution brain electrical tomography
FFT	Fast Fourier transform
fMRI	Functional magnetic resonance imaging
FuzzyEn	Fuzzy entropy
HF	High frequency

HRV	Heart rate variability
ICA	Independent component analysis
LC	Locus coeruleus
LF	Low frequency
LLE	Largest Lyapunov exponent
LOPOCV	Leave-one-participant-out cross-validation
LORETA	Low resolution brain electrical tomography
MFG	Middle frontal gyrus
ML	Machine learning
MNI	Montreal Neurological Institute
MOG	Middle occipital gyrus
MSAQ	Motion sickness assessment questionnaire
NTS	Nucleus tractus solitarius
PCG	Precentral gyrus
PHG	Parahippocampal gyrus
PSD	Power spectral density
RMSSD	Root mean square of successive differences
ROC	Receiver-operating characteristic curve
RPCA	Robust principal component analysis
SampEn	Sample entropy
SDNN	Standard deviation of NN intervals
SEM	Standard error of the mean

SGDM	Stochastic gradient descent with momentum
sLORETA	Standardized low-resolution brain electrical tomography
SMG	Supramarginal gyrus
SnPM	Statistical non-Parametric Mapping
SPAR	Symmetric projection attractor reconstruction
SPWVD	Smoothed pseudo Wigner-Ville distribution
SSQ	Simulator sickness questionnaire
SVD	Singular value decomposition
taVNS	Transcutaneous auricular vagus nerve stimulation
tcVNS	Transcutaneous cervical vagus nerve stimulation
tDCS	Transcranial direct current stimulation
TEA	Transcutaneous electrical acustimulation
TENS	Transcutaneous electrical nerve stimulation
tVNS	Transcutaneous vagus nerve stimulation
VNS	Vagus nerve stimulation

Chapter 1

Introduction

1.1 Overview

Our brains maintain a neural library of expected motions and movements learned from visual, vestibular, and proprioceptive inputs during normal or experienced conditions. Under most circumstances, these brain expectations are congruent with actual visual-vestibular sensory inputs, but when they disagree – for example, during travel by air, land, or sea, when our bodies detect motion that our eyes cannot perceive – it often results in conflicts; a phenomenon known as sensory conflict or neural mismatch ([Reason and Brand, 1975](#); [Reason, 1978](#); [Oman, 1990, 1991](#)). This sensory conflict is the most widely accepted theory about the cause of motion sickness – a complex syndrome that has plagued humans for over two millennia.

Previous research has long recognized the important role of the vestibular system in the development of motion sickness ([Irwin, 1881](#); [James, 1883](#); [Money, 1970](#); [Money, Lackner and Cheung, 1996](#)), including how individuals with complete bilateral loss of labyrinthine (vestibular apparatus) function are virtually immune to motion-induced malaise ([Kennedy et al., 1968](#); [Money, 1990](#); [Cheung, Howard and Money, 1991](#); [Money, Lackner and Cheung, 1996](#); [Johnson, Sunahara and Landolt, 1999](#); [Dai, Raphan and Cohen, 2007](#)). With the exception of an intact vestibular apparatus, everyone can be made motion sick provided there is sufficient exposure to a provocative stimulus. While it has long remained unclear why some individuals are better able to

tolerate sensory conflict, we do know that other individuals are notoriously prone to motion sickness – especially those who experience migraine headaches ([Marcus, Furman and Balaban, 2005](#)), and those with history of traumatic brain injury ([Classen and Owens, 2010](#)).

Nausea is the hallmark of motion sickness. In fact, the term “nausea” – derived from the Greek for ship (*naus*) – was synonymous with seasickness in ancient days of sea travel. An elevated sensation of nausea can hasten vomiting – or repeated bouts of vomiting in severely susceptible individuals, and in severe motion sickness cases observed in parabolic flight experiments ([Graybiel and Lackner, 1987](#)). Because motion sickness is polysymptomatic, nausea and vomiting are most commonly accompanied by a conglomeration of significant features such as cold sweating, dizziness, and drowsiness, among others ([Lackner, 2014](#)) – which detrimentally influence task performance and cognitive function ([Gresty et al., 2008](#); [Gresty and Golding, 2009](#); [Matsangas, McCauley and Becker, 2014](#)). Moreover, the incidence of motion sickness could be exacerbated by automated vehicles ([Diels and Bos, 2016](#)) and in virtual reality settings ([Saredakis et al., 2020](#)).

Despite the ubiquity of motion sickness, managing it effectively without undesirable side effects has remained elusive. In fact, habituation (or adaptation) remains the most effective non-pharmacological strategy – but requires long-term compliance – to alleviate symptoms without medication ([Keshavarz and Golding, 2022](#)). Meanwhile, the efficacy of mainstay pharmaceutical agents is not without unacceptable side effects. For example, antiemetic compounds such as antihistamines (e.g., dimenhydrinate), antimuscarinics (e.g., scopolamine), and sympathomimetics (e.g., amphetamine) are accompanied by drowsiness, blurred vision, and depression of the central nervous system (CNS) ([Lackner, 2014](#); [Golding and Gresty, 2015](#)), including negative effects on psychomotor performance ([Schmäl, 2013](#)). Thus, this underscores the need for new, innovative methods of intervention with the least side effects, to navigate the burden of this debilitating malady.

In recent years, research has revealed important insights into the profound autonomic changes that underlie motion-induced nausea onset and evolution ([Kim et al.,](#)

2011; Farmer et al., 2015); in particular, the notion that a reduction in parasympathetic nervous system tone that is observed in nausea-sensitive individuals could be a key target for new therapeutics (Farmer et al., 2014b). We have long known that the vagus nerve – a paired cranial nerve consisting of sensory and motor neurons – is a primary component of the parasympathetic nervous system. Importantly, it means that we could therapeutically harness its role to reorient the ANS in motion sickness-induced nausea. Advances in neural engineering in the field of bioelectronic medicine have provided safe non-invasive neuromodulation tools that can alter brain and autonomic function, as well as other processes. One such tool is transcutaneous auricular vagus nerve stimulation (taVNS), a non-invasive form of electrical brain stimulation, with the auricular branch of the vagus nerve serving as a sensory conduit between the outer ear regions – most commonly the cymba concha and tragus – and the brainstem (Peuker and Filler, 2002; Ellrich, 2019; Butt et al., 2020; Kreisberg et al., 2021). Prior studies performed in healthy individuals have demonstrated that taVNS application can shift ANS activity toward parasympathetic predominance (Clancy et al., 2014; Geng et al., 2022; Forte et al., 2022).

Moreover, neuroimaging studies have provided evidence for taVNS-induced brain effects in numerous brain regions (Kraus et al., 2007; Dimitrov and Gatev, 2015; Badran et al., 2018); in particular, brain regions such as the insula, precuneus, and cuneus, that have also been implicated with visually induced motion sickness (Kovács, Raabe and Greenlee, 2008; Napadow et al., 2013; Farmer et al., 2015). In light of these findings, this thesis hopes to provide novel insights into the brain and autonomic responses to taVNS, and accompanying behavioural changes during motion sickness-induced nausea, from a therapeutic perspective.

1.2 Aims and Objectives

The primary aim of this research is a novel investigation into the effects of taVNS on brain activity and autonomic function in healthy human volunteers undergoing nauseogenic visual stimulation that induces motion sickness. Specifically, the research assesses whether taVNS-induced brain and autonomic effects are indicative of a reduction in motion sickness severity, as determined by well-established and long-validated motion sickness questionnaires. While numerous studies have investigated taVNS effects on a plethora of diseases and disorders, until now, none have examined the therapeutic potential of this non-invasive vagal nerve stimulation in visually induced motion sickness. Prompted by recent findings that provide an increasingly better understanding of both motion sickness and taVNS, my hypothesis is that active taVNS administration can demonstrate beneficial brain, autonomic, and behavioural effects than sham stimulation. To achieve these aims, the formulated objectives were to:

- Develop a motion sickness model to induce nausea, and thereby study motion sickness expression in the laboratory.
- Examine the physiological – as measured by electrocardiography (ECG) – and behavioural responses to motion-induced nausea during and after taVNS administration.
- Examine the neural – as measured by electroencephalography (EEG) – and behavioural responses to motion-induced nausea during and after taVNS administration.
- Identify quantitative ECG and EEG markers for visually induced motion sickness, to complement or be utilised as surrogates to existing measures.
- Explore with machine learning and deep learning tools to analyse physiological responses to motion-induced nausea, and/or taVNS administration.

1.3 Contributions

Owing to the complexity of motion-induced nausea, a interdisciplinary approach appears essential to understanding and managing symptoms. Hence the thesis draws on the disciplines of computer science, neuroscience, and mathematics to propose a novel non-invasive electrical stimulation of the auricular branch of the vagus nerve – taVNS – for motion sickness management. In addition to the novelty herein, the thesis contributes a visually nauseating stimuli [[Nauseogenic Stimulation](#); [Molefi, McLoughlin and Palaniappan \(2023a\)](#)] – a convenient model of inducing motion sickness in the laboratory that may aid in standardised paradigms of taVNS and motion sickness.

In Chapter 4 [Effects of taVNS on the Human Brain in Visually Induced Motion Sickness](#), the thesis provides a significant contribution suggesting, for the first time, that taVNS may have potential to alleviate motion sickness symptoms through neural activity analysis ([Molefi, McLoughlin and Palaniappan, 2023b](#)). By performing EEG-based source localization analysis, this chapter shares another important contribution, demonstrating that taVNS has differential effects on source localized neuronal activity in comparison to sham, and that these taVNS-induced neuronal effects are linked with reductions in malaise symptoms ([Molefi, McLoughlin and Palaniappan, 2025](#)).

The thesis shares a further contribution in Chapter 5 [Autonomic Effects of taVNS on Visually Evoked Motion Sickness in Humans](#), proposing a set of metrics that measure physiologic complexity and chaos and highlights how these newly proposed indices may have important implications for evaluating new therapeutics for motion sickness, in addition to providing a deeper understanding of this complex syndrome ([Molefi, McLoughlin and Palaniappan, 2023c](#)). Additionally, this chapter uses heart rate variability (HRV) analysis to provide first insights into the potential of auricular electrical stimulation in attenuating motion sickness severity ([Molefi, McLoughlin and Palaniappan, 2023a](#)). Moreover, a recent novel SPAR analysis to examine taVNS effects on ECG morphology and variability serves as an additional contribution to this chapter ([Molefi, McLoughlin and Palaniappan, 2024](#)).

Chapter 6 [Using Supervised Learning to Predict Motion-Induced Nausea, and Effects of taVNS](#) offers an important finding showing that pretrained deep neural networks can be fine-tuned to read ECG-derived attractor images of healthy human volunteers at rest and during motion-induced nausea with implications for evaluating new therapeutics for motion sickness and related conditions ([Molefi and Palaniappan, 2024](#)).

Together, the scientific contribution herein sheds light on taVNS-induced neuromodulatory effects to offset motion-induced nausea, validated through neuroimaging (EEG) and physiologic (ECG) data, and accompanying behavioural data. The findings of this thesis may have translational potential to combat other nausea-related conditions, e.g., chemotherapy-induced nausea. Given the prevalence of motion sickness now and in future due to the proliferation of autonomous and semi-autonomous vehicles, as well as virtual reality (VR) technology, this thesis presents very timely research through the lens of computational neuromodulation, to potentially guide development of taVNS protocols for optimised and effective motion sickness management.

1.4 Research Outputs

Journal Articles

- **Molefi, E.**, McLoughlin, I., and Palaniappan, R. (2024). Symmetric projection attractor reconstruction: Transcutaneous auricular vagus nerve stimulation for visually induced motion sickness. *Autonomic Neuroscience*, Under Review.
- **Molefi, E.**, McLoughlin, I., and Palaniappan, R. (2025). Transcutaneous Auricular Vagus Nerve Stimulation for Visually Induced Motion Sickness: An eLORETA Study. *Brain Topography*, 38(1), 11. <https://doi.org/10.1007/s10548-024-01088-6>
- **Molefi, E.**, McLoughlin, I., and Palaniappan, R. (2023). On the potential of transauricular electrical stimulation to reduce visually induced motion sickness. *Scientific Reports*, 13(1), 3272. <https://doi.org/10.1038/s41598-023-29765-9>

Conference Proceedings

- **Molefi, E.**, and Palaniappan, R. (2024). Deep Transfer Learning for Visually Induced Motion Sickness Detection Using Symmetric Projection Attractor Reconstruction of the Electrocardiogram. In *2024 Computing in Cardiology (CinC)*, Vol. 51, 8-11 September 2024, Karlsruhe, Germany. <https://doi.org/10.22489/CinC.2024.212>
- **Molefi, E.**, McLoughlin, I., and Palaniappan, R. (2023). Heart Rate Variability Responses to Visually Induced Motion Sickness. In *2023 45th Annual International Conference of the IEEE Engineering in Medicine & Biology Society (EMBC)*, 24-27 July 2023, Sydney, Australia. <https://doi.org/10.1109/EMBC40787.2023.10340636>
- **Molefi, E.**, McLoughlin, I., and Palaniappan, R. (2023). Transcutaneous Auricular Vagus Nerve Stimulation towards Visually Induced Motion Sickness Reduction: A Pilot Study. In *2023 45th Annual International Conference of the IEEE Engineering in Medicine & Biology Society (EMBC)*, 24-27 July 2023, Sydney, Australia. <https://doi.org/10.1109/EMBC40787.2023.10340374>

1.5 Thesis Structure

This thesis has been structured into 8 chapters; prior to reading chapters 4 [Effects of taVNS on the Human Brain in Visually Induced Motion Sickness](#), 5 [Autonomic Effects of taVNS on Visually Evoked Motion Sickness in Humans](#), and 6 [Using Supervised Learning to Predict Motion-Induced Nausea, and Effects of taVNS](#), the reader may find it useful to consider going over the [Materials and Methods](#) chapter first – for context.

1 Introduction

Motion sickness is an enigma that has plagued humans for millennia. This chapter provides an overview of this complex and multifactorial syndrome, and considers physiological and neuroimaging evidence that might aid application and evaluation of the proposed non-pharmacological strategy – non-invasive stimulation of the auricular

branch of the vagus nerve. It identifies that literature on non-invasively stimulating the vagus nerve for managing motion sickness is lacking, highlighting the importance and potential of the proposed research.

2 Literature Review

Here, the EEG and ECG modalities – techniques that enable non-invasive monitoring of brain and heart activity, respectively – are described. Subsequently, this review discusses our current understanding of taVNS mechanism, including the neuroanatomy of the vagus nerve (cranial nerve X), and the application of the above-mentioned monitoring modalities in taVNS literature. Similarly, our current knowledge of motion sickness physiology is covered, including a survey of the literature examining motion-induced nausea via EEG and ECG. A summary of evidence suggesting that motion sickness symptoms may be alleviated using non-invasive electrical stimulation is provided; notably, highlighting the novel application of taVNS for motion sickness management herein.

3 Materials and Methods

This chapter describes the characteristics of human volunteers who took part in this research, including experimental design, materials for biomedical signal acquisition, behavioural instruments for measuring motion sickness severity, the development of a nauseogenic visual stimulus, and taVNS administration protocol used for this research.

4 Effects of taVNS on the Human Brain in Visually Induced Motion Sickness

Motion sickness changes brain cortical activity. In this chapter, brain activity data obtained via EEG during an experimental platform designed to induce motion sickness coalesced with taVNS administration are analysed using spectral decomposition, time-frequency decomposition, and exact low-resolution brain electromagnetic tomography (eLORETA). eLORETA – a technique that computes images of electric neuronal activity from EEG recordings – is employed for estimating cortical neuronal generators of

taVNS administration. Differences in sham- and taVNS-induced neural activity during exposure to motion sickness are presented, and findings comprehensively discussed.

5 Autonomic Effects of taVNS on Visually Evoked Motion Sickness in Humans

It has long been known that motion sickness disrupts autonomic nervous system function. This chapter employs a set of analytical methods both to propose new metrics for assessing this autonomic dysfunction in motion-induced nausea, as well as to examine the effects of taVNS administration simultaneous with motion sickness provocation. Notably, measures of physiologic complexity and chaos are proposed for motion sickness monitoring; and for the first time, symmetric projection attractor reconstruction (SPAR) transforms are used to examine the differential effects of taVNS in motion sickness. The findings and their implications are discussed at depth.

6 Using Supervised Learning to Predict Motion-Induced Nausea, and Effects of taVNS

The ECG-based SPAR analysis performed in Chapter 5 [Autonomic Effects of taVNS on Visually Evoked Motion Sickness in Humans](#) generates attractor images that encapsulate useful information which may be indicative of malaise state, or taVNS-induced response. This chapter explores the use of machine learning and deep learning tools to analyse the characteristics of these attractor images to determine the effects of nauseogenic visual stimulation, including detection of stimulation type, sham versus active taVNS. Finally, the presented results are discussed.

7 General Discussion

Here, a more in-depth discussion of limitations in the studies conducted, including how such limitations affect the findings and conclusions is provided. Specifically, topics such as sham condition in taVNS studies, taVNS dosage for motion-induced nausea, and heart rate variability (HRV) as a biomarker for taVNS are comprehensively discussed. Furthermore, this chapter examines the limitations, validation, and interpretation of

eLORETA; and considers the implications of sex differences and sample size on the main findings herein.

8 Conclusions and Future Directions

This chapter summarises the findings presented in the thesis, and how the scientific contributions herein could yield important future impact for navigating nausea-related conditions, stress, and mental health, etc. Importantly, it considers future directions for taVNS therapy in motion sickness management, including opportunities for the optimisation, personalisation, and commercialisation of taVNS for motion sickness.

Chapter 2

Literature Review

2.1 Introduction

Though the burden of motion sickness can be alleviated via pharmacologic agents, their undesirable side effects, including the foreseeable incidence of malaise that could be exacerbated by virtual reality, and automated vehicles and flights, highlight the need for new strategies of managing it effectively with the least side effects. In this review, I provide an overview background and description of electroencephalography (EEG) and electrocardiography (ECG) data modalities; and discuss EEG and ECG evidence for the effects of both transcutaneous auricular vagus nerve stimulation (taVNS) and visually induced motion sickness on brain and autonomic function, respectively. Additionally, I consider evidence from functional magnetic resonance imaging (fMRI) studies from both taVNS and motion sickness literature.

Finally, I summarise the literature that sought to ameliorate symptoms of motion sickness via non-invasive electrical stimulation. On the basis of current evidence, I find that taVNS is yet to be examined as a potential neurostimulation tool in motion sickness management; in particular, when aiming to evaluate its effects on the development of malaise at the level of behaviour, physiology, and underlying brain activity dynamics.

2.2 Electroencephalography

Our brains are constantly generating electrical signals. Ubiquitous across the cerebral cortex are pyramidal neurons (Spruston, 2008) – also commonly found in various brain regions, including in subcortical structures such as the hippocampus and the amygdala – whose primary function is to perform synaptic integration, like any other type of neuron. That is, to respond to synaptic inputs via generation of action potentials that excite postsynaptic targets. Their numerical dominance, including the fact that they are ‘projection neurons’ – however – makes them important. Postsynaptic activity of ensembles of these neurons generates local field potentials (LFPs); these LFPs are the main source of potentials that can be detected at the scalp surface (i.e., from outside the head). In fact, these are considered the building blocks of electroencephalography (EEG) (da Silva, 2013).

EEG is a safe and non-invasive method for monitoring the brain’s electric fields, and was discovered in humans by *Hans Berger*, a German psychiatrist, in 1924 (Berger, 1929; Haas, 2003) – marking one hundred years of EEG at the time of writing this. It is important to note that prior to the discovery of EEG in humans by *Hans Berger*, EEG had long been demonstrated in animals by *Richard Caton* (Caton, 1875; Haas, 2003) and *Adolf Beck* (Beck, 1890; Coenen and Zayachkivska, 2013; Pietrzak, Grzybowski and Kaczmarczyk, 2014). EEG uses electrodes placed on the scalp to record summed up postsynaptic potentials of large, synchronous neuronal populations with high temporal precision but coarse spatial resolution. Features of the electrical activity recorded by EEG – commonly called brain waves – are complex, and the signal detected by each electrode include dynamics from various brain regions. Moreover, it is important to note that the signal measured at the scalp level is attenuated and transformed by volume conduction via intracranial media such as the cerebral spinal fluid, dura matter, and skull (Biasiucci, Franceschiello and Murray, 2019). While the above points highlight our partial and incomplete understanding of the content of scalp-recorded EEG (Cohen, 2017), it is indisputable that EEG plays an important role in the characterization of electrophysiological dynamics of brain (dys)function. In particular, since its inception,

it has led to marked advances in the characterization, detection, and management of epilepsy.

Normally, to interpret patterns in the EEG signal, many studies perform spectral decomposition of the data into delta (δ ; ~ 0.2 - 3.5 Hz), theta (θ ; ~ 4 - 7.5 Hz), alpha (α ; ~ 8 - 13 Hz), beta (β ; ~ 14 - 30 Hz), gamma (γ ; ~ 30 - 90 Hz), and high-frequency oscillations (HFO; > 90 Hz) (Biasiucci, Franceschiello and Murray, 2019). These classical frequency bands have been shown to be in overlap with clusters of frequency components obtained via statistical factor analysis of EEG spectral properties (da Silva, 2011). It should be noted that, in interpreting these frequency bands, there is no direct mapping of neural oscillations of a frequency band of interest with a specific brain process; rather, evidence indicates, for example, that complex amplitude-phase relationships across frequencies exist. Moreover, it is reasonable to assume that there are other features intrinsic to the EEG signal, such as non-sinusoidal and arrhythmic patterns rather than just a mixture of sinusoids, when computing EEG spectra. Nonetheless, spectral characteristics of the EEG provide unique insights in examining both evoked (time- and phase-locked) and induced (not time- or phase-locked) brain dynamics – and an effective means to distinguish between them. However, it should not be overlooked that EEG is equally important in its raw form (i.e., time domain), especially when evaluating and interpreting features such as burst suppression, sleep, and epileptiform patterns.

EEG has a diverse spectrum of applications, ranging from brain-computer interfaces (BCIs) to sleep, anxiety, and brain disorder diagnosis, treatment outcome prediction, to practical ways that allow combination with other brain imaging methods – for instance, functional near-infrared spectroscopy (fNIRS) and functional magnetic resonance imaging (fMRI) – and non-invasive brain stimulation – for example, transcranial alternating current stimulation (tACS) and transcranial magnetic stimulation (TMS). Here, I leverage EEG to gain insight into the neural effects of non-invasive stimulation of the vagus nerve in human participants undergoing nauseogenic visual stimulation.

2.3 Electrocardiography

A hallmark feature of the human heart is its ability to generate its own electricity, via specialised cardiomyocytes that network to form the intrinsic cardiac conduction system; reliably maintaining blood circulation around the body in a precisely coordinated and regulated process. Anatomically, and on the most basic level, the heart comprise four distinct pumping chambers, two superior atria and two inferior ventricles. Each chamber has a corresponding valve; the atrioventricular valves – mitral (bicuspid) and tricuspid valves – provide a one-way path for the atria to pump blood into the ventricles, and the semilunar valves – aortic and pulmonary semilunar valves – similarly offer a single pathway for the ventricles to propel blood to the rest of the body. To function best, a cluster of neurons in the sinoatrial (SA) node (the heart's natural pacemaker) generate an electrical impulse at regular intervals – often 60 to 100 times per minute – for a heartbeat. Dynamics between the sympathetic and parasympathetic of the autonomic nervous system, a branch of the peripheral nervous system, regulate the frequency of these electrical impulses. The SA node, or sinus node, reside in the upper portion of the right atrium (Figure 1). Under normal circumstances, the electrical stimulus triggered by the SA node is conducted via the internodal pathways, initiating atrial contraction while propagating toward the atrioventricular (AV) node – the heart's "gatekeeper", which reside between the atria (Figure 1) – where it gets delayed for a short period of time while the atria empty blood into the ventricles. From the AV node, the electrical signal travels through the atrioventricular bundle (i.e., His bundle), the Purkinje fibers, and the ventricular myocardium – this happens very quickly – causing the ventricles to contract, and thus producing a heartbeat. Then the next cardiac cycle begins.

An electrocardiogram (ECG or EKG) is a non-invasive procedure performed to record the electrical activity of the heart over time. The ECG was invented by a Dutch physician named *Willem Einthoven* in 1901 as a string galvanometer; the 600-pound instrument translated the electrical activity in the heart into "electrocardiogram" (a term he coined) waves that are recorded on graph paper, conveying the heart rate and

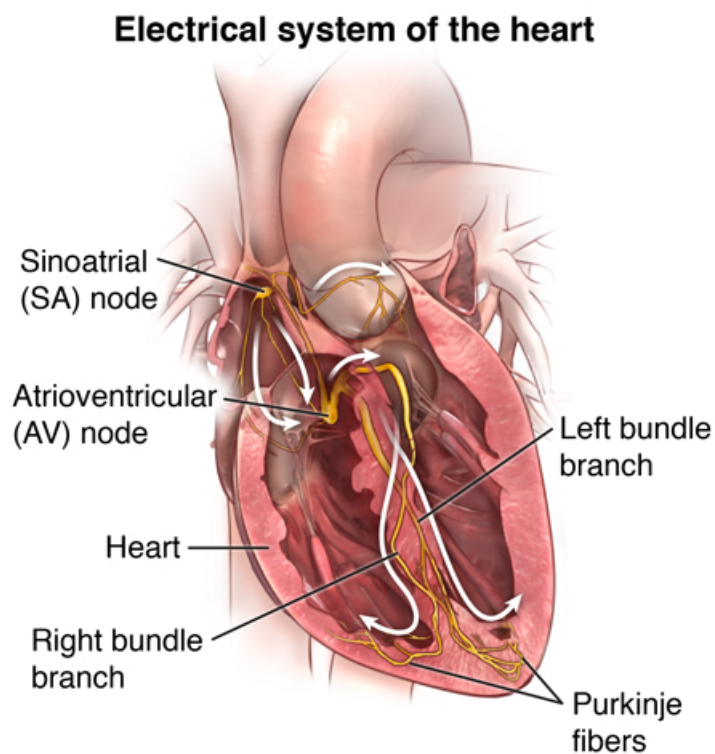


Figure 1: Electrical system of the heart. From [Johns Hopkins Medicine \(2019\)](#).

heart rhythm ([Einthoven, 1901](#)). Einthoven received the Nobel Prize in Physiology or Medicine in 1924 for his discovery of the mechanism of ECG. It is important to remark however that prior to the discovery made by Einthoven, the early pioneering work of *Augustus Waller* had demonstrated that electrical currents generated by the human heart could be recorded using a mercury capillary electrometer ([Waller, 1887](#)).

Importantly, it should be noted that an ECG does not measure the actual electric current that propagates through the cardiac conduction system; rather, it measures the ventricular and atrial myocardial depolarization (activation) and repolarization. That is, an ECG device or machine transforms the signals detected and transmitted by the electrodes – commonly placed on an individual’s wrists, ankles and chest – into patterns or waves that represent the function of the cardiac conduction system. [Figure 2](#) is an illustration of the various waves that can be observed on an ECG. The *P wave* represents

atrial depolarization; the *QRS complex* (a conglomeration of *Q*, *R*, and *S* waves) indicates ventricular depolarization; and the *T wave* represents ventricular repolarization. Of note, the *QRS complex* additionally reflects masked atrial repolarization. These ECG waves have important clinical implications, and their appearance can give vital clues about abnormal heart rhythms, i.e., arrhythmias.

It has long been observed that the heartbeat varies over time (Billman, 2011). The discovery of the ECG provided a proxy by which physiological variation in time between heartbeats, called heart rate variability (HRV), could be assessed with millisecond temporal precision. But it was not until the 1996 standardisation document by the [Task Force of the European Society of Cardiology and the North American Society of Pacing and Electrophysiology \(1996\)](#) – a widely referenced document – that HRV analyses received increased research interest. While the HRV signal can be obtained via various methods, for example, derived from photoplethysmography (PPG) (e.g., [Lu et al., 2008, 2009](#)) or arterial blood pressure (ABP) (e.g., [McKinley et al., 2003](#)) waveforms, the ECG signal is well-recognized as the gold standard for HRV estimation. To construct an HRV signal, the time interval between the R waves in the QRS complex of the ECG is most commonly used. Herein I utilise the ECG – including ECG-derived HRV – to evaluate the effects of taVNS on autonomic function in tandem with nauseogenic stimulation.

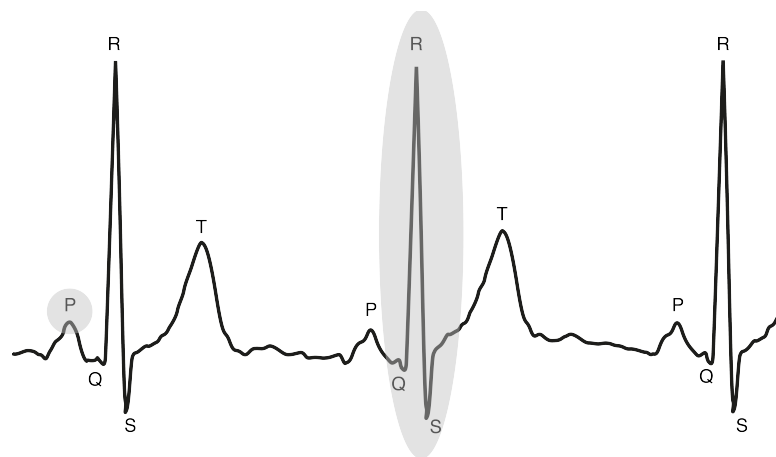


Figure 2: An electrocardiogram (ECG) excerpt for an example participant – with annotations of different ECG waves.

2.4 Transcutaneous Auricular Vagus Nerve Stimulation

While the idea that therapeutic solutions could be derived from stimulating the vagus nerve date back to the 1880s, when American neurologist *James L. Corning* coalesced transcutaneous electrical stimulation of efferent vagal nerve fibers with a “carotid fork” – an instrument Corning developed for bilateral carotid artery compression – it was not until a century later that this method was adopted based on evidence from animal models suggesting potential antiepileptic effects ([Zabara, 1985, 1992](#)).

The vagus nerve (cranial nerve X; [Figure 3](#)) is a paired neural structure that helps maintain homeostasis; and among the longest nerves in the human body. It plays a critical role in parasympathetic nervous function. Essentially, the vagus nerve has crucial involvement on functions such as the autonomic, cardiovascular, respiratory, gastrointestinal, immune and endocrine systems ([Yuan and Silberstein, 2016a](#)). A comprehensive review of the physiology of the vagus nerve has been provided ([Yuan and Silberstein, 2016a,b,c](#)).

Depending on the stimulation method, researchers distinguish between cervically implanted VNS (VNS or iVNS), transcutaneous cervical VNS (tcVNS), transcutaneous auricular VNS (taVNS), and percutaneous auricular VNS (paVNS). taVNS targets nerve endings of the auricular branch of the vagus nerve, which provides a neural pathway for afferent signaling to brainstem nuclei, such as the nucleus tractus solitarius (NTS). Both taVNS and tcVNS are delivered transcutaneously, so these modalities are often jointly referred to as tVNS ([Farmer et al., 2021](#)). Despite limited data on the differential biological effects of taVNS against tcVNS, I restrict my scope to the neural and autonomic effects induced by taVNS in the ensuing summary of the literature.

2.4.1 Neural Effects of taVNS

Electrical stimulation of the vagus nerve has been found to influence brainstem neuronal response. Modern research has revealed that the same brain effects can be achieved via non-invasive modalities including taVNS and tcVNS. However, neural mechanisms mediating the effects of taVNS and tcVNS are not well understood. Here,

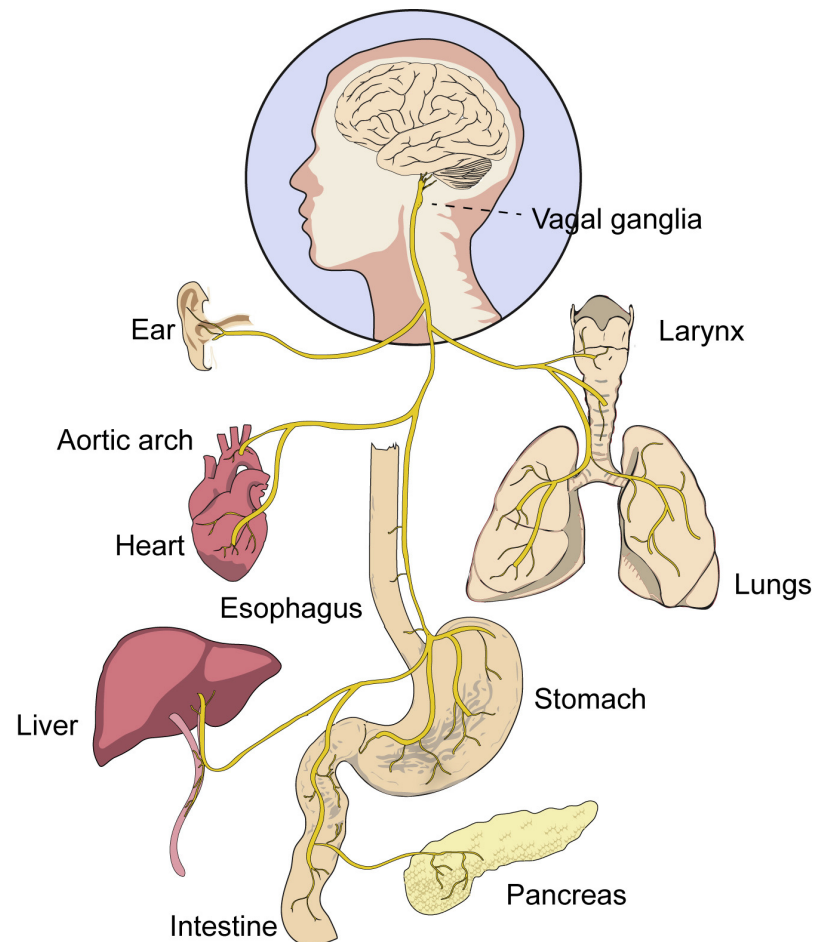


Figure 3: The Vagus Nerve. From [Prescott and Liberles \(2022\)](#).

I summarise both EEG and fMRI findings on the modulatory effects of non-invasive vagal nerve stimulation, restricting my scope to taVNS ([Table 1](#)).

Early fMRI analyses by [Kraus et al. \(2007\)](#) revealed that taVNS (delivered at 20 μ s, 8 Hz) evoked neuronal activation in brain regions including the insula, precentral gyrus, thalamus, right accumbens and led to a differential deactivations in regions, such as parahippocampal gyrus, hippocampus, amygdala, middle temporal gyrus, and superior temporal gyrus when outer ear canal was contrasted with the earlobe. Using a different set of parameters (250 μ s, 25 Hz), [Dietrich et al. \(2008\)](#) implicated similar brain activation in the thalamus and insula by stimulating the inner tragus. Additionally, the authors identified brain activation at the left locus coeruleus (LC) and left prefrontal cortex, including deactivations at the right nucleus accumbens, right cerebellum ([Dietrich](#)

et al., 2008). Several years past, Kraus et al. (2013) investigated with the same taVNS dosage (20 μ s, 8 Hz), but slightly different stimulation duty cycle of (30 s on, 60 s off). Tragus stimulation revealed brain activation at the parahippocampal gyrus, posterior cingulate cortex, and right thalamus. When comparing tragus and posterior ear canal to earlobe, the authors observed differential activation in insula (Kraus et al., 2013).

Studies targeting the cymba conchae have demonstrated brain activation at brain structures including the left NTS, nucleus accumbens, and LC (Frangos, Ellrich and Komisaruk, 2015), and caudate, cerebellum, and hypothalamus (Yakunina, Kim and Nam, 2017); these different results may be attributed to the different parameters the studies applied. Indeed, Frangos, Ellrich and Komisaruk (2015) observed a deactivation in the hypothalamus while (Yakunina, Kim and Nam, 2017) noted an increase in the same region. Comparing tragus stimulation with earlobe, Badran et al. (2018) observed brain activation in brain regions including the caudate, left middle frontal gyrus, and bilateral anterior cingulate cortex while using the same taVNS parameters (500 μ s, 25 Hz) as Yakunina, Kim and Nam (2017); interestingly, the authors did not observe NTS activation similar to Yakunina, Kim and Nam (2017); possibly due the different duty cycle applied by both studies, and the different samples sizes.

In comparison to fMRI, EEG provides high temporal resolution of brain dynamics modulated by vagal stimulation; however, findings from EEG studies have been lacking, and current ones provide mixed evidence. For example, Ricci et al. (2020) reported increased EEG delta spectral power when comparing post-taVNS to pre-stimulation baseline. taVNS was demonstrated to attenuate occipital alpha oscillations when administered at the cymba conchae (Sharon, Fahoum and Nir, 2021). A more likely explanation for these contrasting results is methodological differences.

Together, while these findings are interesting and have potential to further understanding of mechanisms by which taVNS influences brainstem neuronal response, other studies had low sample sizes (e.g., Dietrich et al., 2008; Ricci et al., 2020); thus, warranting caution when interpreting findings therein. Nonetheless, evidence from these studies (Table 1) taken together suggests that neuronal response may aid assess taVNS response.

Table 1: Brain effects of taVNS in healthy human participants.

Study	Site	N	Stimulation parameters	Findings
Kraus et al. (2007)	Outer ear canal (vs. earlobe)	6	30 s on, 120 s off; 20 μ s, 8 Hz	taVNS increased BOLD in insula, precentral gyrus, thalamus, right accumbens; and decreased BOLD in parahippocampal gyrus, hippocampus, amygdala, middle temporal gyrus, superior temporal gyrus
Dietrich et al. (2008)	Inner tragus	4	50 s on, 100 s off; 250 μ s, 25 Hz	taVNS increased BOLD in left LC, thalamus (left > right), left prefrontal cortex, left insula; and decreased BOLD in right nucleus accumbens, right cerebellum
Kraus et al. (2013)	Tragus vs. posterior ear canal (vs. earlobe)	8	30 s on, 60 s off; 20 μ s, 8 Hz	taVNS (tragus) revealed increased BOLD in parahippocampal gyrus, posterior cingulate cortex, right thalamus (pulvinar); Tragus and posterior ear canal compared to earlobe showed increased BOLD in insula

(Continued)

Study	Site	N	Stimulation parameters	Findings
Frangos et al. (2015)	Cymba conchae (left; vs. earlobe)	12	7 min on, 11 min off; 250 μ s, 25 Hz	taVNS showed increased BOLD in left NTS, bilateral spinal trigeminal nucleus, dorsal raphe, LC, right parabrachial area, amygdala, nucleus accumbens, bilateral paracentral lobule; and decreased BOLD in hippocampus, hypothalamus
Yakunina et al. (2017)	Tragus, conchae (vs. earlobe)	37	6 min on, 90 s off; 500 μ s, 25 Hz	taVNS (cymba conchae and tragus) compared to sham revealed increased BOLD in NTS, LC, caudate, cerebellum, hypothalamus, thalamus, putamen
Badran et al. (2018)	Tragus (left; vs. earlobe)	17	60 s on, 60 s off; 500 μ s, 25 Hz	taVNS vs. sham revealed increased BOLD in caudate, right caudate, bilateral midcingulate, bilateral cerebellum, bilateral anterior cingulate cortex, left middle frontal gyrus, left superior frontal gyrus
Ricci et al. (2020)	External acoustic meatus (left; vs. earlobe)	8	30 s on, 5 min off; 0.5 ms, 30 Hz	taVNS increased EEG delta (1-4 Hz) power compared to pre-stimulation baseline
Sharon et al. (2021)	Cymba conchae (left; vs. earlobe)	24	3.4 s on; 200-300 μ s, 25 Hz	taVNS attenuated occipital alpha (8-13 Hz) compared to sham

2.4.2 Autonomic Effects of taVNS

In Section [Electrocardiography](#), I underscored that ECG-derived HRV can be used to extract measures that describe the state of the autonomic nervous system. From those measures, some of them have been proposed to be reliable indicators of cardiac vagal activity. These include the (1) root mean square of successive RR interval differences (RMSSD); (2) percentage of consecutive RR intervals differing by $> x$ ms (pNN x , %); (3) respiratory sinus arrhythmia (RSA); and (4) high frequency (HF) spectral component of HRV ([Laborde, Mosley and Thayer, 2017](#)). Here, I examine evidence of the administration of taVNS in modulating autonomic function as indexed by these aforementioned measures; however, I also describe evidence of the involvement of nonlinear HRV measures ([Table 2](#)).

The effects of non-invasive vagal nerve stimulation have been investigated in several studies. However, similar to the observation made in the [Neural Effects of taVNS](#) section, studies here have also provided mixed evidence. In their pivotal study, [Clancy et al. \(2014\)](#) demonstrated that tragus stimulation led to a differential reduction in LF/HF, and observed no effect on either LF or HF; suggesting that taVNS reduces sympathetic neural activity. Of note, the LF/HF is not among those considered to assess cardiac vagal activity, and thus should be interpreted with caution. One important observation about this study is that it was not clear which tragus was stimulated (left or right). A later study by [Antonino et al. \(2017\)](#) revealed that stimulating the left tragus significantly reduced the LF/HF; this finding was observed when comparing taVNS to baseline – the authors made no comparisons between taVNS and sham (left earlobe). While both these studies suggested there is a taVNS effect on the LF/HF measure, the findings of [Bretherton et al. \(2019\)](#) contrasted this, and instead showed that taVNS induced a differential increase in RMSSD and pNN50 – which represent cardiac vagal activity – including LF, SD1, and SD2 when taVNS was compared to pre-stimulation baseline. Improvements in HRV with tragus stimulation observed in a study that measured RSA ([Lamb et al., 2017](#)).

Although the cymba conchae is thought to be innervated by a greater proportion of the auricular branch of the vagus nerve ([Butt et al., 2020](#)), studies investigating with this

anatomical location have mostly reported no taVNS effect on the RMSSD (De Couck et al., 2017; Borges, Laborde and Raab, 2019; Burger et al., 2019a,b; Vosseler et al., 2020), HF (De Couck et al., 2017; Gancheva et al., 2018), or LF/HF (De Couck et al., 2017; Gancheva et al., 2018). Cymba conchae stimulation on the right ear was demonstrated to produce marked changes in the SDNN (De Couck et al., 2017). In a recent parametric study, Machetanz et al. (2021) implicated strong effects were the cymba conchae and fossa triangularis, and to a lesser extent the inner tragus. Importantly, it should be noted that there are potential limitations in these studies, which comprise differential methodology, small sample sizes, and incomplete reporting of stimulation parameters, including missing sham control.

Table 2: Autonomic effects of taVNS in healthy human participants.

Study	Site	N	Stimulation parameters	Autonomic parameters	Findings
Clancy et al. (2014)	Tragus	48	Continuous; 10-50 mA, 200 μ s, 30 Hz	LF, HF, LF/HF	Significant decrease in LF/HF; no effect on LF or HF
De Couck et al. (2017)	Cymba conchae (bilateral)	30	30 s on, 30 s off; mean 0.7 mA, 200 μ s, 25 Hz	RMSSD, SDNN, HF, LF/HF	taVNS (right-sided) increased SDNN compared to baseline, but no effect on RMSSD, HF, LF/HF; No differences observed for taVNS (right-sided) vs. sham (left cymba concha with null stimulation) or taVNS(left-sided)
Lamb et al. (2017)	Tragus (left)	22	Mean 5.6 (3-11.3) mA, 20 Hz	RSA	taVNS increased RSA compared to sham (tragus with null stimulation)

(Continued)

Study	Site	N	Stimulation parameters	Autonomic parameters	Findings
Antonino et al. (2017)	Tragus (left)	13	Continuous; 10-50 mA, 200 μ s, 30 Hz	LF, HF, LF/HF	taVNS decreased HR and LF/HF compared to baseline, this was not observed during sham; taVNS and sham (left earlobe) not compared
Gancheva et al. (2018)	Cymba conchae (left)	14	Continuous; 0.6-1.4 mA, 250 μ s, 25 Hz	LF, HF, LF/HF	No taVNS effect on HRV compared to sham (left earlobe)
Bretherton et al. (2019)	Tragus	Exp 1: 51; Exp 2: 26	2-4 mA, 200 μ s, 30 Hz	LF, HF, LF/HF, RR interval, SDNN, RMSSD, pNN50, SD1, SD2	Exp 1: taVNS increased RMSSD, pNN50, LF, SD1, and SD2 compared pre-stimulation baseline. No taVNS effect on other measures. Exp 2: taVNS increased SDNN, RR mean, LF, and SD2. No taVNS effect on other measures.
Borges et al. (2019)	Cymba conchae (left)	60	30 s on, 30 s off; 0.5 mA, 250 μ s, 25 Hz	RMSSD	No taVNS effect on HRV compared to sham (left earlobe)

(Continued)

Study	Site	N	Stimulation parameters	Autonomic parameters	Findings
Burger et al. (2019a)	Cymba conchae (left)	58	30 s on, 30 s off; 0.5 mA, 250 μ s, 25 Hz	RMSSD	No taVNS effect on HRV compared to sham (left earlobe)
Burger et al. (2019b)	Cymba conchae (left)	97	30 s on, 30 s off; 0.5 mA, 250 μ s, 25 Hz	RMSSD	No taVNS effect on HRV compared to sham (left earlobe)
Vosseler et al. (2020)	Cymba conchae (left)	15	30 s on, 30 s off; 25 Hz; taVNS: 2.5 mA \pm SD 0.9; sham: 3.2 mA \pm SD 1.5	RMSSD, LF, HF, LF/HF	No taVNS effect on HRV compared to sham (left earlobe)
Machetanz et al. (2021)	6 targets including cymba conchae (bilateral) and tragus (inner and outer; bilateral)	13	30 bursts; 1 Hz periodicity, 25 Hz stimulation	RR mean, SDNN, RMSSD, pNN50, SD1, SD2, rrHRV relative	taVNS effect on improved HRV with 2 mA, 100 μ s

2.5 Visually Induced Motion Sickness

Although motion sickness is common, it is also a complex syndrome; with a multitude of symptoms that can have negative consequences for susceptible individuals even at mild levels – for instance, reducing cognitive multitasking performance ([Matsangas, McCauley and Becker, 2014](#)). But it has long remained unclear as to what its underlying physiological causes are. In a review that describes some of the factors that contribute to motion sickness besides nausea and vomiting, [Lackner \(2014\)](#) additionally discussed the three major hypotheses that have been debated among researchers over the past several decades; the evolutionary, ecological, and sensory conflict theories.

The evolutionary theory posits that our vestibular (balance) system may have been designed to detect ingested toxins, therefore motion sickness arises because there is a neurotoxin that has been ingested that we need to be protected from and thus vomiting is initiated ([Money, 1990](#); [Treisman, 1977](#)); whereas, the ecological theory – which is based on postural instability – states that we become sick because we are in a new situation/environment wherein we do not yet possess or have learned effective coping strategies to maintain postural stability ([Riccio and Stoffregen, 1991](#)). To date, the sensory conflict theory is the most influential; it posits that because of ambiguous sensory information from our eyes and the vestibular, motion sickness is onset ([Reason, 1969, 1970, 1978](#); [Reason and Brand, 1975](#); [Oman, 1990](#); [Bles et al., 1998](#); [Bos, Bles and Groen, 2008](#)). This latter theory is the one considered for the explanation of motion sickness herein.

Importantly, it is worth highlighting that, of the manifold theories proposed to explain the enigma of motion sickness, what remains consistent is that the vestibular apparatus – which resides in a structure referred to as the labyrinth in the inner ear ([Yates and Miller, 2019](#)) – is noted as a crucial component for malaise to arise. Early evidence demonstrated that stimuli that would normally trigger motion sickness has no effect in individuals with bilateral vestibular dysfunction ([Reason, 1978](#); [Cheung, Howard and](#)

[Money, 1991](#); [Maruta, 2024](#)). It must also be mentioned that although the visual system is associated with effective motion sickness generation alongside the vestibular system, visual signals are not necessarily essential for induction of motion sickness, as indicated by previous work demonstrating that blind individuals are susceptible to motion-induced malaise ([Graybiel, 1970](#)).

Because balance is a function of multiple inputs ([Angelaki and Cullen, 2008](#)), the neurobiology of motion sickness is complex and remains less well understood. However, recent evidence for the existence of “sensory conflict” neurons and their putative role in motion sickness ([Oman and Cullen, 2014](#)), has provided marked progress in parsing the neurobiological underpinnings of this elusive malady. Furthermore, previous research has pointed to a key role for the NTS, lateral tegmental field (LTF), and parabrachial nucleus (PBN) brainstem areas, in the integration of signals contributing to nausea and vomiting via mapping of neuronal activity during emetic responses ([Yates et al., 2014](#); [Lackner, 2019](#)). In a recent mouse model study, [Machuca-Márquez et al. \(2023\)](#) provide further support for the role of the vestibular system in the development of motion sickness, and extend on this notion by describing the vestibular pathways eliciting motion-induced nausea responses; in addition to identifying a central role for cholecystinin (CCK)-expressing vestibular neurons in motion-induced malaise. While motion sickness remains a complex syndrome, these previous studies have provided greater insight into the neural substrates of motion-induced nausea.

As briefly mentioned in the [Overview](#) section of [Chapter 1](#), motion sickness is characterised primarily by nausea and vomiting; other symptoms include – but are not limited to – sweating, dizziness, drowsiness, headache, eyestrain, and elevated levels of plasma vasopressin ([Golding and Gresty, 2015](#)). We have long known that some of these objective signs of motion-induced malaise are autonomically mediated ([Money, Lackner and Cheung, 1996](#); [Himi et al., 2004](#)). Examining the evidence in support of this notion in their systematic review and meta-analysis study, [Farmer et al. \(2014b\)](#) demonstrated that a marked decrease in parasympathetic nervous system tone – as computed from measures of cardiac function – is observed in individuals susceptible

to visually induced motion sickness; furthermore, the study also suggested that baseline autonomic characteristics are not useful measures for predicting who is likely to develop motion-induced nausea. Behaviourally, while severe motion sickness can easily be identified in individuals through signs such as emesis, a study by [Matsangas and McCauley \(2014\)](#) introduced evidence to suggest that yawning may have an important role as a behavioural marker of mild motion-induced malaise, including sopite syndrome.

Markers for motion sickness susceptibility are influenced by various factors, such as age, sex, and genetics. Previous studies have found that children particularly in the age range of 6-12 years, including females have a high propensity to develop motion sickness ([Klosterhalfen et al., 2005](#); [Bos et al., 2007](#); [Paillard et al., 2013](#)); for children, susceptibility exhibits a differential increase and a peak at around 9 years ([Henriques et al., 2014](#)). While females are known to be markedly susceptible to malaise than males, it has been suggested that this effect is small compared to that of age ([Golding and Gresty, 2015](#)). Genetic influences on motion sickness susceptibility have been supported by both early and recent studies ([Abe, Oda and Hatta, 1984](#); [Reavley et al., 2006](#); [Hromatka et al., 2015](#)). Furthermore, individuals who experience migraine headaches ([Marcus, Furman and Balaban, 2005](#)), and those with history of traumatic brain injury ([Classen and Owens, 2010](#)) are known to be particularly prone to this malady.

Research from neuroimaging studies has now demonstrated that ambiguity in sensory information, particularly arising from visual stimulation, triggers prominent areas of the brain, for example the limbic system (known for regulating autonomic and endocrine function) ([Napadow et al., 2013](#); [Lackner, 2019](#)) and the insula (also involved in autonomic regulation) ([Sclocco et al., 2016](#)). In addition, a motion video was shown to elicit autonomic changes leading to increased sympathetic and reduced parasympathetic activities of the ANS ([Farmer et al., 2015](#)). Here, I examine the evidence for these motion sickness-induced nausea neural and autonomic perturbations.

2.5.1 Neural Effects of Motion Sickness

At the time of writing, conducting a PubMed search using the terms (“motion sickness” AND “EEG”) without any restrictions, produces a graph that suggests that the past decade has seen an increasing interest in the mechanisms by which motion sickness influences the brain. We have long known that motion sickness changes brain cortical activity. Here, I examine evidence for the effects of motion-induced nausea on the human brain. I focus on research employing non-invasive neuroimaging techniques including EEG, fMRI, and fNIRS (Table 3); for EEG studies, I restrict our scope to at least 32-channel neural recordings.

Because of its high temporal resolution, in addition to the observation that most studies utilise simulators, or VR tools (Table 3), EEG is often the preferred modality for examining neural changes induced by motion sickness. Mounting evidence shows that motion sickness perturbs these slow oscillations of the brain (i.e., delta, theta, alpha). Previous studies using various stimuli for nausea induction, such as a VR driving simulator (Chen et al., 2009; Huang, Jung and Makeig, 2009; Chen et al., 2010; Chuang et al., 2016; Huang et al., 2021), 3D movie (Naqvi et al., 2015), and 3D VR video (Kim et al., 2019), reported differential brain activity in these frequency bands, with very mixed results. For example, while Naqvi et al. (2015) observed a reduction in EEG theta spectral power, other studies found an increase (Huang, Jung and Makeig, 2009; Chen et al., 2010); although it is worth noting that these changes were observed at different regions of the brain (Table 3). Moreover, although studies using a VR driving simulator have consistently demonstrated increased EEG spectral power in the occipital, parietal, and somatosensory (left and right motor) brain areas, Huang, Jung and Makeig (2009) observed that EEG alpha spectral power exhibits distinct suppression or augmentation over time in motion sickness. This may also explain why findings have been mixed; that is, depending on which parts of the EEG signal may reveal different results, perhaps because malaise might not be severe at those timepoints.

EEG beta spectral power increase has also been observed (Lin et al., 2007; Naqvi et al., 2015); and in one study (Chuang et al., 2016), increased gamma oscillations were observed in motor, parietal, and occipital brain areas. Collectively, these EEG

findings implicate motion-induced nausea to different neural responses across various EEG frequency bands. Analyses of fNIRS data in one study (Zhang et al., 2020) also revealed disrupted brain dynamics in regions including frontal, parietal, and occipital cortices in straight and curved simulated driving conditions; increased frontal and occipital activity was noted in both driving conditions (Zhang et al., 2020).

Considering fMRI data, in their pivotal study, Napadow et al. (2013) implicated motion sickness with increasing phasic activity preceding nausea in amygdala, putamen, and dorsal pons/locus ceruleus, including increasing sustained response following increased nausea in a broader network encompassing insular, anterior cingulate, orbitofrontal, somatosensory and prefrontal cortices. Furthermore, the authors noted a strong link between sustained anterior insula activation to strong nausea and mid-cingulate activation (Napadow et al., 2013). However, an important limitation to highlight regarding this previous study is that only females were recruited for participation, and thus, hampering its findings to be generalised. In fact, this limitation may have contributed to the contrasting findings observed by Farmer et al. (2015) in their much larger study, who implicated motion-induced nausea with inferior frontal gyrus including a negative correlation with the cerebellar tonsil, declive, lingual gyrus, culmen, cuneus and posterior cingulate cortex. Another possible explanation for the differences in both these studies could be attributed differences in methodology as Farmer et al. (2015) points out.

In addition to the aforementioned fMRI studies, recent fMRI data were provided by Ruffle et al. (2019); implicating motion-induced nausea with a functional brain network including thalamus, anterior, middle and posterior cingulate cortices, caudate nucleus and nucleus accumbens, while also observing previously identified brain regions such as amygdala and putamen. sLORETA analyses performed by Kim et al. (2019) revealed previously observed brain regions comprising the cuneus and posterior cingulate cortex. Overall, functional brain studies, including the EEG-based based using sLORETA provide evidence for effects of motion-induced nausea on regions of the brain responsive when there are elevated levels of autonomic arousal.

Table 3: Brain effects of motion sickness in healthy human participants.

Study	Modality	Stimulus	N	Findings
Lin et al. (2007)	EEG	VR driving simulator	9	EEG power increase in 8-10 Hz and 18-20 Hz in parietal and motor areas
Chen et al. (2009)	EEG	VR driving simulator	19	EEG power alpha increase or decrease in parietal and somatosensory (left and right motor) areas
Huang et al. (2009)	EEG	VR driving simulator	11	EEG power increase in delta, theta, alpha in occipital, posterior parietal, and middle temporal cortex. Strong increases observed in alpha in occipital and parietal areas
Chen et al. (2010)	EEG	VR driving simulator	19	EEG power decrease in alpha in parietal and motor areas. Occipital delta, and theta power increase. Broadband power increase in occipital midline
Napadow et al. (2013)	fMRI	Nauseogenic stimulation (black and white stripes)	28	Increasing phasic activity preceding nausea in amygdala, putamen, and dorsal pons/locus ceruleus. Increasing sustained response following nausea in broader network including insular, anterior cingulate, orbitofrontal, somatosensory, and prefrontal cortices. Sustained anterior insula activation to strong nausea revealed a strong link with midcingulate activation
Naqvi et al. (2015)	EEG	3D movie	46	EEG power decrease in theta (frontal), beta (temporal) with 3D movie
Farmer et al. (2015)	fMRI	Motion video	28	Left anterior cingulate cortex; Positive correlation between nausea VAS scores and left inferior and middle occipital gyri activation; Negative correlation between nausea VAS scores and right cerebellar tonsil, declive, culmen, lingual gyrus, and cuneus
Chuang et al. (2016)	EEG	VR driving simulator	19	Spectrally fixed and temporally independent modulators revealed increased alpha and gamma in motor, parietal, and occipital areas

(Continued)

Study	Modality	Stimulus	N	Findings
Ruffle et al. (2019)	fMRI	Motion video	28	Increased nausea scores positively linked with morphological variation of the left amygdala, right caudate, and bilateral putamen; Functional brain network implicating the thalamus, anterior, middle, and posterior cingulate cortices, caudate nucleus and nucleus accumbens
Kim et al. (2019)	EEG	3D VR video	30	Increases in SSQ measures; Increased alpha1 (8-10 Hz) in cuneus (sLORETA) and alpha2 (10-12 Hz) in cuneus and posterior cingulate cortex (sLORETA); Negative correlation between change in SSQ scores and change in posterior cingulate gyrus activation
Zhang et al. (2020)	fNIRS	VR driving simulator	52	Straight driving condition: increase (occipital, frontal), decrease (posterior frontal cortex, postcentral gyri, anterior frontal cortex, lower parietal cortex); Curved driving condition: increase (occipital, frontal), decrease (posterior prefrontal cortex, posterior frontal cortex, postcentral gyri)
Huang et al. (2021)	EEG	VR driving simulator	18	Passengers exhibited independent modulator power increase in alpha (8-12 Hz) in parietal, occipital midline, and left and right motor areas; Drivers showed relatively smaller increases in alpha (8-12 Hz) power

2.5.2 Autonomic Effects of Motion Sickness

We have long known that motion sickness changes ANS response, but the mechanisms remain unclear. An early exhaustive review by [Money \(1970\)](#) noted inconsistencies both in the methods and the results reported by studies seeking to understand the importance of ANS in motion sickness. Although since then the landscape of techniques used to study motion sickness has improved, the evidence of autonomic changes implicated with motion sickness is mixed. In a relatively recent review, [Farmer et al. \(2014b\)](#) concluded that while baseline parasympathetic nervous system parameters are not reliable for predicting the probability of motion sickness, a decrease in parasympathetic tone was a key characteristic in sensitive individuals.

A myriad of studies have examined the autonomic changes induced by the subjective sensation of motion sickness. Here, while keeping the theme of examining evidence for motion sickness influence on parameters similar to those in the [Autonomic Effects of taVNS](#) section above; I also survey autonomic parameters reported for visually induced motion sickness that may not be presented above for our overall understanding of this complex syndrome ([Table 4](#)).

Because chemotherapy-induced nausea has long been linked with a differential reduction in cardiac parasympathetic activity, [Gianaros et al. \(2003\)](#) tested the hypothesis that motion-induced nausea would relate with a time-related decrease in cardiac parasympathetic activity. The authors exposed a cohort of 59 participants to a rotating drum for nausea induction and measured RSA to estimate parasympathetic activity. A marked reduction in RSA related with greater motion sickness severity was observed, suggesting that parasympathetic withdrawal may be an important correlate of motion-induced nausea ([Gianaros et al., 2003](#)). However, the findings of [Himi et al. \(2004\)](#) were not consistent with that observation. This difference in reported findings could have been due to different stimuli for nausea induction, including different modalities used to assess autonomic nervous function – in [Himi et al. \(2004\)](#), HRV was used to estimate parasympathetic activity. [Himi et al. \(2004\)](#) also concluded that motion-induced nausea had no effect on LF/HF.

While the work of [Himi et al. \(2004\)](#) and [Naqvi et al. \(2013\)](#) demonstrated that

motion-induced nausea does not alter parasympathetic activity, sympathetic activity, or their ratio (i.e., LF/HF), several other studies noted motion sickness-induced nausea perturbations on autonomic function. Through stimuli such as rotating images (Yokota et al., 2005), driving simulation (Zużewicz et al., 2011; Lin et al., 2011, 2013), and 3D movie (Wibirama, Nugroho and Hamamoto, 2018), including visual stripes (LaCount et al., 2009; Kim et al., 2011), a significant reduction in cardiac parasympathetic activity (HF or normalised HF), and marked increases in sympathetic activity (LF or normalised LF), and LF/HF were shown.

Evaluating autonomic function using cardiac vagal tone (CVT) (Farmer et al., 2014a), a real time index of brainstem parasympathetic nervous system efferent activity, and cardiac sympathetic index (CSI) (Toichi et al., 1997), an index of cardiac sympathetic activity, Farmer et al. (2015) found that 98 healthy participants presented with a 10 min motion video showed an increase in CSI, and concomitant significant reduction in CVT. Taken together, the findings from these previous studies suggest that motion-induced nausea elicits a differential reduction in parasympathetic tone.

Table 4: Autonomic effects of motion sickness in healthy human participants.

Study	Stimulus	N	Autonomic parameters	Findings
Gianaros et al. (2003)	Optokinetic drum	59	RSA	Motion sickness severity linked with RSA reduction
Himi et al. (2004)	Movie of oscillating pictures	17	LF, HF, LF/HF	No motion-induced nausea effect on LF/HF
Yokota et al. (2005)	Rotating image	15	LF, HF, LF/HF	Severe malaise linked to increased LF, and LF/HF; and decreased HF
LaCount et al. (2009)	Nauseogenic stimulation (black and white stripes)	10	HRV, SCL	“No nausea”-to-“mild” revealed increased HF power; Right before “strong” nausea, transient HF increase observed
Zużewicz et al. (2011)	Driving simulation	24	LF, HF, LF/HF	Severe malaise found to increase LF, and LF/HF; and decrease HF
Kim et al. (2011)	Nauseogenic stimulation (black and white stripes)	12	HR, HF	Motion-induced nausea revealed increased HR and decreased HF
Lin et al. (2011)	VR driving simulator	5	LF, HF, LF/HF	Increasing motion sickness levels found to increase LF, and LF/HF; and decrease HF
Lin et al. (2013)	VR driving simulator	20	Normalized LF and HF power, LF/HF	Severe malaise linked to increased normalised LF, and LF/HF; and decreased normalized HF
Naqvi et al. (2013)	3D movie	39	LF, HF, LF/HF	No motion-induced nausea effect on LF/HF
Farmer et al. (2015)	Motion video	98	CSI, CVT	Motion-induced nausea increased CSI and decreased CVT
Wibirama et al. (2018)	3D movie	40	LF, HF, LF/HF	Malaise exposure increased LF/HF

2.6 Electrical Stimulation for Motion Sickness

Although no studies have examined the physiological and neural changes induced by transcutaneous electrical stimulation of the vagus nerve, and whether these changes are associated with improvements in motion sickness symptoms until now, several findings in the literature support the hypothesis that non-invasive electrical stimulation may provide therapeutic benefits for motion sickness sufferers. [Table 5](#) provides a summary of physiological and subjective effects of non-invasive electrical stimulation modalities described for motion sickness management.

Galvanic vestibular stimulation (GVS) ([Dlugaiczky, Gensberger and Straka, 2019](#)), a technique whereby a small electric current is applied to the inner ear, was one of the earliest tools to be investigated for relieving motion sickness symptoms. When applied at 2.5 mA pulses for 20 minutes, GVS was demonstrated to improve the symptoms of motion sickness as measured by the SSQ instrument in participants engaged in a helicopter flight simulation ([Cevette et al., 2012](#)). Confirming this finding but using a different stimulus to induce motion sickness, [Sra, Jain and Maes \(2019\)](#) showed in a repeated measures study that participants immersed in a virtual rollercoaster experienced less malaise symptoms – evaluated using the SSQ – during GVS compared to when GVS was not applied. Despite using a VR immersion stimulus similarly to the study by [Sra, Jain and Maes \(2019\)](#), and even double the sample size (total, $n = 40$), [Weech, Wall and Barnett-Cowan \(2020\)](#) did not observe any differences in the SSQ measures between GVS and sham conditions. However, the authors additionally used the FMS instrument, which revealed significant symptom improvements during GVS exposure compared to sham in a post hoc analyses. This mixed findings may be attributable to differences in stimulation parameters, duration of GVS stimulation, and study design.

Using a modified version of GVS, termed galvanic cutaneous stimulation (GCS), whereby similar electrodes to GVS are applied, but positioned approximately 3–4 cm below the mastoid process, on the cutaneous skin over the sternocleidomastoid muscle ([Reed-Jones et al., 2008](#)), two previous studies showed that participants engaged in

a driving simulation for nausea induction showed improved SSQ total symptoms when comparing GCS to no stimulation (Gálvez-García, Hay and Gabaude, 2015), and when comparing to a baseline condition (Gálvez-García et al., 2020). In (Gálvez-García et al., 2020), the authors further suggested combining GCS with auditory stimulation (AS) to ameliorate motion sickness.

In a within-participants crossover study of 15 healthy young men, Chu et al. (2012) investigated the effects of transcutaneous electrical nerve stimulation (TENS) – a well-established therapeutic tool for pain management (Vance et al., 2014) – on motion sickness induced by a Coriolis rotary chair. Motion sickness severity was evaluated objectively using HR, HRV, and skin temperature, and subjectively using the MSSQ and motion sickness symptom ratings (MSSR) instruments; including assessing for cognitive function, salivary and cortisol concentrations, in addition to blood pressure. The authors observed that in addition to participants exhibiting improvement in cognitive function with TENS (100 Hz; intensity range = 1-10, 20 min) administration, participants also showed increased parasympathetic activity accompanied by decreased sympathetic activity – indicating parasympathetic predominance – and reduced motion sickness symptoms with TENS intervention; which was administered at the midline posterior nuchal region and right *Zusanli* acupoint.

In a subsequent study, Chu et al. (2013) investigated the effects of TENS on simulator sickness – a syndrome akin to motion sickness (Dużmańska, Strojny and Strojny, 2018) – induced by a flight simulator. The authors administered 30 min of electrical stimulation (100 Hz; intensity range = 1-10) compared to null stimulation, and evaluated objective measures including HR, and HRV, and recorded subjective responses of motion sickness severity using the MSSQ and SSQ instruments. Substantiating their previous findings in Chu et al. (2012), the authors demonstrated improvements in cognitive impairment, including observing a shift toward parasympathetic predominance as evaluated by the LF/HF, with higher and lower levels of parasympathetic and sympathetic activity TENS, respectively. However, while Chu et al. (2013) observed improvements in total scores of the SSQ, they did not find differences in the subscale measures (nausea, oculomotor, and disorientation) of the same instrument. This is in

contrast to previous findings applying GVS ([Cevette et al., 2012](#); [Sra, Jain and Maes, 2019](#)), suggesting that TENS may be inducing therapeutic subjective effects in a different manner compared to GVS. [Chu et al. \(2013\)](#) also found that the MSSQ was a poor predictor of motion sickness symptom severity; this was also observed to be the case by a study characterising changes in functional brain networks and neuroanatomy underpinning nausea severity ([Ruffle et al., 2019](#)).

In addition to GVS, GCS, and TENS, a further electrical stimulation modality that has been investigated for motion sickness is transcranial direct current stimulation (tDCS) – a common non-invasive brain stimulation technique that applies weak electrical currents for cortical excitability modification ([Nitsche et al., 2008](#)). To examine whether suppression of vestibular activity using tDCS may alleviate motion sickness, [Arshad et al. \(2015\)](#) stimulated healthy individuals undergoing off-axis rotation for nausea induction using 1.5 mA tDCS pulses over the left parietal cortex for 15 min prior a second bout of nausea induction. The authors observed that cathodal tDCS prolonged time to develop moderate nausea and that participants showed rapid symptom relief. However, these findings have been challenged by recent studies suggesting that no differences in the time to recovery prolongation of symptom onset exist in healthy individuals receiving tDCS administration of similar stimulation parameters ([Takeuchi et al., 2018](#); [Li et al., 2020](#)). The work from [Takeuchi et al. \(2018\)](#) did demonstrate, however, that there were improvements in the disorientation subscale measure of the SSQ instrument – this instrument was not administered in the study by [Arshad et al. \(2015\)](#).

In a more recent study ([Zhao et al., 2022](#)), the newly developed transcutaneous electrical acustimulation (TEA) – which applies electrical stimulation to acupoints via surface electrodes ([Chen, Yin and Wei, 2017](#)) – was employed to investigate its therapeutic potential for motion sickness. [Zhao et al. \(2022\)](#) observed prolonged tolerable time during motion sickness provocation using a rotary chair, in addition to noting lowered motion sickness symptom scores, and significantly enhanced vagal activity as measured by HRV, when comparing TEA with sham-TEA (whereby same electrical stimulation parameters were applied but at a different location).

Table 5: Electrical stimulation countermeasures for motion sickness.

Study	Modality	Design	N	Stimulus	Stimulation parameters	Explored variables	Findings
Cevette et al. (2012)	GVS	Between	21 (6 F)	Flight simulation	2.5-mA GVS pulse for 20 m	SSQ	GVS-induced vestibular sensations improved gastrointestinal, central, and peripheral symptom scores compared to a control group
Chu et al. (2012)	TENS	Within	15 (0 F)	Rotary chair	100 Hz TENS pulse for 20 m	MSSQ, MSSR, BP, HR, HRV, Skin temperature, sAA, Cortisol, d2 test	TENS significantly lowered MSSR, LF power, and LF/HF ratio measures; and increased HF power. Cognitive impairment improved with TENS

(Continued)

Study	Modality	Design	N	Stimulus	Stimulation parameters	Explored variables	Findings
Chu et al. (2013)	TENS	Within	15 (0 F)	Flight simulation	100 Hz TENS pulse for 30 m	MSSQ, SSQ, HR, HRV, sAA, Cortisol	TENS improved SSQ total scores but not nausea, oculomotor, and disorientation subscale scores. MSSQ was a poor predictor of SS symptom severity. TENS lowered HR, LF power, and LF/HF ratio measures; increased HF power. Cognitive impairment improved with TENS
Arshad et al. (2015)	tDCS	Mixed	20	Rotary chair	1.5 mA with a ramp-up and fade-out latency of 10 s	MSSQ, OVAR duration, Onset of symptom, Time to recovery	tDCS (cathodal) increased time to moderate nausea and improved time to recovery

(Continued)

Study	Modality	Design	N	Stimulus	Stimulation parameters	Explored variables	Findings
Gálvez-García et al. (2015)	GCS	Within	15	Driving simulation	Individually adapted stimulus intensity (0.6-1.25 mA)	SSQ	SSQ total scores revealed significant effect for the experiment condition, GCS curve and intermittent conditions showed improved scores compared to no stimulation condition. GCS curve and intermittent conditions were not different

(Continued)

Study	Modality	Design	N	Stimulus	Stimulation parameters	Explored variables	Findings
Takeuchi et al. (2018)	tDCS	Within	20	VR immersion (rollercoaster)	tDCS: 1.5 mA for 15 m; sham: 1.5 mA for 30	SSQ, HR, Length of COP	No effect of stimulation condition or stimulation order for VR immersion duration. tDCS (anodal) improved SSQ disorientation subscale scores compared to sham and cathodal tDCS
Sra et al. (2019)	GVS	Within	20 (12 F)	VR immersion (rollercoaster)		SSQ	GVS improved SSQ total, and nausea, oculomotor, and disorientation subscale scores compared to no GVS

(Continued)

Study	Modality	Design	N	Stimulus	Stimulation parameters	Explored variables	Findings
Gálvez-García et al. (2020)	GCS	Within	48	Driving simulation	Monophasic sinusoidal: 20 Hz, 10 ms phase duration and 40 ms inter-phase duration; 0.5-1.3 mA (direct current)	SSQ	SSQ total scores revealed a significant main effect for experimental condition. GCS, AS, and GCS-AS improved SSQ total scores. GCS and AS were not different; GCS-AS was different from AS and GCS

(Continued)

Study	Modality	Design	N	Stimulus	Stimulation parameters	Explored variables	Findings
Weech et al. (2020)	GVS	Mixed	40 (23 F)	VR immersion	GVS: $\pm 1750 \mu\text{A}$ for 15 s (5 s fade in, 10 s exposure); sham: 0 μA for 15 s (5 s fade in, 10 s exposure)	FMS, SSQ	Post-hoc analysis revealed first FMS repetition with GVS compared to sham for intense VR content; FMS repetition 10 scores were improved during GVS exposure compared to sham in post-hoc tests. No difference between GCS and sham in all SSQ measures. SSQ measures and FMS (final repetition) relations found at various VR immersion levels

(Continued)

Study	Modality	Design	N	Stimulus	Stimulation parameters	Explored variables	Findings
Li et al. (2020)	tDCS	Mixed	20	VR immersion (rollercoaster)	tDCS: constant current of 1.5 mA for 15 m (30 s ramp up and 30 s ramp down); sham: stimulator turned off after 30 s ramp up and ramp down period	Onset of symptom, Time to recovery	Cathodal tDCS did not delay onset of moderate symptoms nor improve time to recovery compared to anodal tDCS
Zhao et al. (2022)	TEA	Within	50	Rotary chair	TEA: 0.2 s on-time and 0.3 s off-time, 0.5 ms pulse width at 100 Hz, 2-10 mA; sham: same parameters to TEA applied at a sham-acupoint (15 to 20 cm away from PC6)	HRV, AVP, NE	TEA improved total tolerable time of MS exposure, normal gastric slow waves (%), and vagal activity compared to sham. Levels of AVP and NE were lowered by TEA compared to sham.

2.7 Summary

This review has compiled evidence for the neuromodulatory effects of taVNS on the human brain and autonomic function. While the brain data on taVNS from healthy individuals accumulated until today suggests that the modulatory role of this tool may be examined in this manner, autonomic data is currently showing inconsistencies – at least in human models. I noted that (among other differences) differential study methodology, small sample sizes, and missing sham, are likely the explanation for these inconsistencies. Here I also examined evidence for the influence of motion-induced nausea on the brain, including the autonomic nervous system. I noted the effects of malaise on slow oscillations of the brain, which may represent therapeutic target. Moreover, I found that evaluation of autonomic function using HRV dynamics yielded findings that suggest malaise produces a differential reduction in cardiac parasympathetic activity. Because there is evidence for taVNS effects on cardiac vagal activity – albeit mixed – and the observation that heretofore taVNS has not been investigated for motion sickness – a research gap identified in this review – I aim to harness this brain stimulation tool to ask for its effects on motion-induced malaise.

Chapter 3

Materials and Methods

3.1 Introduction

I conducted two randomized controlled crossover studies in neurotypical human volunteers ([Figure 4](#)). Both studies were conducted at the BioSensing Lab, School of Computing, and were approved by the Central Research Ethics Advisory Group (ref: CREAG015-12-2021) of the University of Kent. All experimental protocols were conducted in accordance with the tenets of the Declaration of Helsinki for human research. All participants provided written informed consent, and were eligible to withdraw their participation without reprisal. Participants received a small honorarium for their participation via an Amazon gift voucher. Hereinafter, the two studies are denoted as Study 1 and Study 2, respectively; and the data collected during each respective study are denoted Dataset 1 and Dataset 2. Parts of this chapter are reproduced, with edits, from [Molefi, McLoughlin and Palaniappan \(2023a, 2025\)](#).

The rationale for using a within-subjects study design is that this design is less affected by inter-individual variability, and achieves adequate statistical power with a relatively smaller sample size in comparison with between-subjects study designs. Moreover, this choice was guided by the review conducted in [Section Electrical Stimulation for Motion Sickness](#) which revealed that within-subjects studies are more common when investigating the effects of non-invasive electrical stimulation in motion-induced nausea.

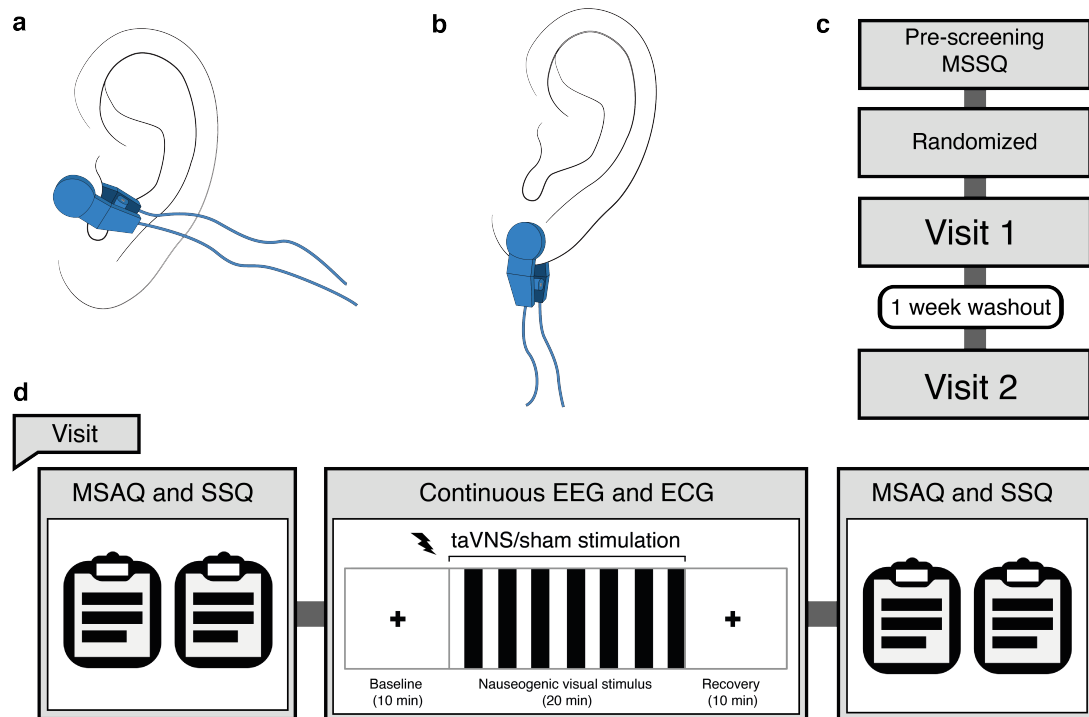


Figure 4: Experimental overview illustrations. (a) For active taVNS, the electrode was clipped to the tragus of the left ear. (b) And clipped to the left earlobe for sham stimulation. (c) The schematic of the randomized, sham-controlled, crossover design timeline. (d) For a typical lab visit, participants completed a pre and post motion sickness assessment questionnaire (MSAQ) and simulator sickness questionnaire (SSQ); additionally, participants underwent a baseline period, followed by nauseogenic visual stimulation concurrent with electrical stimulation (taVNS or sham), then a recovery period, while electroencephalogram (EEG) and electrocardiogram (ECG) acquisition was performed.

3.2 Participants

For both studies, all participants had normal or corrected-to-normal vision, were 18 years or older, healthy (i.e., no medical history of stroke, epilepsy or any neurological disorders), were not taking any medication, were not using a pacemaker, had no metal plates in their body, could sit alert during the length of the experiments, and had English knowledge to read and understand the information provided. In Study 1, 16 healthy volunteers were recruited, but one participant was excluded due to loss of follow-up. Thus $n = 15$ subjects were retained (mean age \pm SD = 28.2 ± 7.0 years, age range

= 21-49 years, 12 females). In Study 2, I recruited a total of 45 healthy participants following written informed consent, of whom $n = 42$ were retained (mean age \pm SD = 23.7 ± 6.7 years, age range = 18-49 years, 31 females) for further analysis after one participant was excluded due to not enough data, and two due to loss of follow-up.

3.3 Experimental Protocol

In both studies, I used a randomized, sham-controlled, crossover experimental design. Participants were required to attend two electrical stimulation sessions of sham and taVNS via two lab visits that were scheduled apart by at least 1 week, to allow for washout of any stimulation effects. The sequence of sham and taVNS administration was randomized and not disclosed to subjects. For each experimental session, participants were exposed to a contiguous visual stimulus, which comprised a baseline period of 10 min crosshair fixation, followed by nauseogenic visual stimulation (see [Nauseogenic Stimulation](#)) concurrent with electrical stimulation (see [Electrical Stimulation](#)) for a maximum of 20 min, and finally, a recovery period presented similar to baseline ([Figure 4d](#)). During nauseogenic visual stimulation, participants continuously rated the perceived intensity of their nausea sensation, uncued, by pressing on a keypad where (0 = “no nausea”; 1 = “mild”; 2 = “moderate”; and 3 = “strong”). The keypad also allowed participants to stop presentation of the nauseogenic visual stimulus when on the verge of vomiting – triggering automatic launch of the recovery period. None of the participants vomited during or after exposure to nauseogenic visual stimulation; however, one participant retched during nausea induction, and was one of the participants absent at a follow-up session. Electrical stimulation was delivered at the left tragus during active taVNS lab visits ([Figure 4a](#)), and at the left earlobe during sham lab visits ([Figure 4b](#)). For safety reasons and smooth running of the experiment, the experimenter was present in the lab but kept out of view. EEG and ECG acquisition was performed continuously between baseline onset and recovery offset, during which participants were required to minimize body movements and conversation, and to focus on stimuli presentation. To measure motion sickness, participants completed a pre- and

post-treatment motion sickness assessment questionnaire (MSAQ) ([Gianaros et al., 2001](#)) and simulator sickness questionnaire (SSQ) ([Kennedy et al., 1993](#)) (see Section [Behavioral Data Acquisition](#) for details). Overall, the duration of each experiment was in the range 60-90 min.

3.4 EEG and ECG Data Acquisition

I performed 64-channel EEG and modified Lead II ECG data acquisition using the BioSemi ActiveTwo system (BioSemi B, V., Amsterdam, Netherlands). During project setup, the BioSemi system, which initially could only record 32-channel EEG, was upgraded to provide 64-channel EEG acquisition. [Figure 5](#) shows the BioSemi system opened from the top during a 64-channel upgrade. Among other reasons, 64-channel recordings would allow for a deeper understanding of how motion sickness affects the human brain, including how effects induced by taVNS that may underlie the dampening of motion sickness symptoms are represented in the brain. Moreover, high-density EEG would allow for analysis such as EEG-based brain source localization to be performed on the recorded data [see [Exact LORETA \(eLORETA\)](#)]. As a side note, to maintain the electrodes, I performed regular cleaning after each experimental recording. Moreover, electrodes were routinely tested for defects via a process known as “The Bucket Test” (https://www.biosemi.com/faq/check_electrodes.htm).

The electrophysiological signals were recorded continuously for the duration of each experiment, and digitized at a sampling frequency of 256 Hz (2048 Hz with a decimation factor of 1/8) using LabVIEW (National Instruments, USA) software running on a MacBook Pro with 2.3 GHz Dual-Core Intel Core i5 and 8 GB of RAM. Electrode (Ag/AgCl pin-type) signal transduction was optimised by applying Signage[®] (Parker Laboratories Inc., Fairfield, NJ) conductive gel, and electrode offset was within ± 10 μ V. EEG electrode locations conformed to the extended international 10/20 system. Data acquisition was referenced to the common mode sense (CMS) and grounded to the driven right leg (DRL) electrodes. The recorded data were persisted as .bdf files for offline processing. The details for this offline processing are described elsewhere (i.e.,

the respective Methods of chapters [Effects of taVNS on the Human Brain in Visually Induced Motion Sickness](#), [Autonomic Effects of taVNS on Visually Evoked Motion Sickness in Humans](#), and [Using Supervised Learning to Predict Motion-Induced Nausea, and Effects of taVNS](#)).

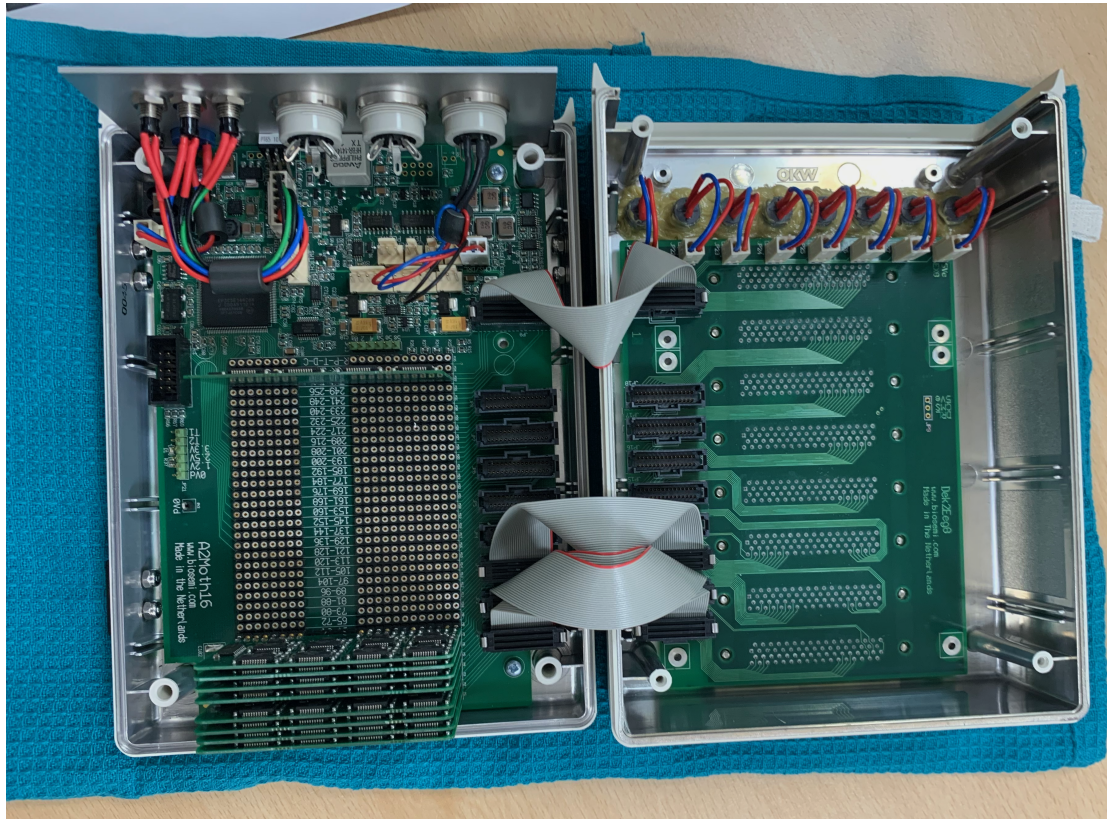


Figure 5: A BioSemi ActiveTwo system opened from the top and being upgraded to use 64 channels.

3.5 Behavioral Data Acquisition

3.5.1 Motion Sickness Susceptibility Questionnaire (MSSQ)

In Study 2, I prescreened all participants with the previously validated motion sickness susceptibility questionnaire short-form (MSSQ-Short) ([Golding, 2006](#)) – a condensed version of the early MSSQ ([Golding, 1998](#)) – to determine their propensity to motion sickness. I included participants reporting a percentile score > 60 (corresponding to

an MSSQ raw score of 14.36), based on prior autonomic and neuroimaging studies investigating motion sickness-induced nausea (e.g., [LaCount et al., 2011](#); [Sclocco et al., 2016](#); [Toschi et al., 2017](#)). Previous research has demonstrated that participants reporting MSSQ scores > 60 experienced moderate nausea in response to nauseogenic visual stimulation more reliably and rapidly compared to participants who scored below this inflection point ([Golding, 1998](#)). The MSSQ-Short prompts participants to recall experiences of nausea or vomiting at childhood (below 12 years of age; MSA), and over the last decade (MSB) following various transport or entertainment modalities. Data were scored using guidance from [Golding \(2006\)](#). [Table 6](#) shows the MSSQ-Short form with an example (ticks) where recalled experiences were indicated. To perform scoring, the number of ticks in the 't' column ([Table 6](#)) are totalled for both MSA (Child) and MSB (Adult). In addition, the totals of the sickness scores for each mode of transportation – from 'cars' to 'big dippers' – computed using the 0-3 score keys for each respective column for both MSA and MSB ([Table 6](#)). These computations are illustrated using formulae below [Golding \(2006\)](#).

$$\begin{aligned}
 \text{MSA} &= \frac{(\text{total sickness score child}) \times 9}{9 - (\text{number of types not experienced as a child})} \\
 &= \frac{(2 + 9) \times 9}{9 - (3)} \\
 &= 16.5
 \end{aligned} \tag{1}$$

$$\begin{aligned}
 \text{MSB} &= \frac{(\text{total sickness score adult}) \times 9}{9 - (\text{number of types not experienced as a adult})} \\
 &= \frac{(2 + 6 + 6) \times 9}{9 - (0)} \\
 &= 14
 \end{aligned} \tag{2}$$

$$\begin{aligned}
 \text{MSSQ raw score} &= \text{MSA} + \text{MSB} \\
 &= 16.5 + 14 \\
 &= 30.5
 \end{aligned} \tag{3}$$

Percentile conversions were performed using a close approximation provided by the fitted polynomial

$$\text{MSSQ percentile score} = ax + bx^2 + cx^3 + dx^4 \quad (4)$$

where 'x' is the MSSQ-Short raw score obtained using [Equation \(3\)](#), with a = 5.1160923, b = -0.055169904, c = -0.00067784495, and d = 0.000010714752 ([Golding, 2006](#)).

3.5.2 Motion Sickness Assessment Questionnaire (MSAQ)

To quantify the experience of motion sickness, participants completed the validated motion sickness assessment questionnaire (MSAQ) ([Gianaros et al., 2001](#)) – a tool that additionally measures motion sickness as a multidimensional construct with gastrointestinal, central, peripheral and sopite-related clusters. The MSAQ instrument is composed of 16 motion sickness symptoms with a Likert-type scale (1-9 = “not at all” to “severely”). Data were scored according to instructions outlined in [Gianaros et al. \(2001\)](#). [Table 7](#) shows the MSAQ form with example (ratings) provided next to each symptom. To compute the MSAQ total and subscale scores, ratings provided in [Table 7](#) are subjected to formulae given below using the legend (G, gastrointestinal; C, central; P, peripheral; S, sopite).

$$\begin{aligned} \text{MSAQ}_{score} &= \frac{\sum_{i=1}^{16} Q_i}{144} \times 100 \\ &= \frac{62}{144} \times 100 \\ &= 43.06 \end{aligned} \quad (5)$$

$$\begin{aligned} G_{score} &= \frac{\sum_{i=1}^4 Q_i}{36} \times 100 \\ &= \frac{19}{36} \times 100 \\ &= 52.78 \end{aligned} \quad (6)$$

Table 6: Motion sickness susceptibility questionnaire short-form (MSSQ-Short) (modified from [Golding, 2006](#)).

This questionnaire is designed to find out how susceptible to motion sickness you are, and what sorts of motion are most effective in causing that sickness. Sickness here means feeling queasy or nauseated or actually vomiting.

Your CHILDHOOD Experience Only (before 12 years of age), for each of the following types of transport or entertainment please indicate:

1. **As a CHILD (before age 12)**, how often you **Felt Sick or Nauseated** (tick boxes):

	Not Applicable - Never Travelled	Never Felt Sick	Rarely Felt Sick	Sometimes Felt Sick	Frequently Felt Sick
Cars				✓	
Buses or Coaches					✓
Trains	✓				
Aircraft		✓			
Small Boats	✓				
Ships, e.g. Channel Ferries	✓				
Swings in playgrounds		✓			
Roundabouts in playgrounds					✓
Big Dippers, Funfair Rides					✓
	t (3)	0 (2)	1 (0)	2 (1)	3 (3)

Your Experience over the LAST 10 YEARS (approximately), for each of the following types of transport or entertainment please indicate:

2. **Over the LAST 10 YEARS**, how often you **Felt Sick or Nauseated** (tick boxes):

	Not Applicable - Never Travelled	Never Felt Sick	Rarely Felt Sick	Sometimes Felt Sick	Frequently Felt Sick
Cars				✓	
Buses or Coaches					✓
Trains			✓		
Aircraft		✓			
Small Boats				✓	
Ships, e.g. Channel Ferries				✓	
Swings in playgrounds		✓			
Roundabouts in playgrounds			✓		
Big Dippers, Funfair Rides					✓
	t (0)	0 (2)	1 (2)	2 (3)	3 (2)

$$\begin{aligned}
 C_{score} &= \frac{\sum_{i=1}^5 Q_i}{45} \times 100 \\
 &= \frac{16}{45} \times 100 \\
 &= 35.56
 \end{aligned} \tag{7}$$

$$\begin{aligned}
 P_{score} &= \frac{\sum_{i=1}^3 Q_i}{27} \times 100 \\
 &= \frac{3}{27} \times 100 \\
 &= 11.11
 \end{aligned} \tag{8}$$

$$\begin{aligned}
 S_{score} &= \frac{\sum_{i=1}^4 Q_i}{36} \times 100 \\
 &= \frac{24}{36} \times 100 \\
 &= 66.67
 \end{aligned} \tag{9}$$

Table 7: Motion sickness assessment questionnaire (MSAQ) (modified from [Gianaros et al., 2001](#)).

<i>Not at all</i>					<i>Severely</i>				
1	2	3	4	5	6	7	8	9	
1. I felt sick to my stomach. (G) 5					9. I felt disoriented. (C) 6				
2. I felt faint-like. (C) 2					10. I felt tired/fatigued. (S) 8				
3. I felt annoyed/irritated. (S) 1					11. I felt nauseated. (G) 5				
4. I felt sweaty. (P) 1					12. I felt hot/warm. (P) 1				
5. I felt queasy. (G) 5					13. I felt dizzy. (C) 3				
6. I felt lightheaded. (C) 2					14. I felt like I was spinning. (C) 3				
7. I felt drowsy. (S) 9					15. I felt as if I may vomit. (G) 4				
8. I felt clammy/cold sweat. (P) 1					16. I felt uneasy. (S) 6				

3.5.3 Simulator Sickness Questionnaire (SSQ)

I additionally measured motion sickness severity using the long-validated simulator sickness questionnaire (SSQ) (Kennedy et al., 1993). While this instrument was initially developed to target simulator sickness specifically, it is now widely being used for all variants of motion sickness. The SSQ quantifies motion sickness as a whole, and also clusters symptoms into nausea, oculomotor and disorientation components. It includes 16 symptoms that are each rated on a four-point Likert scale ranging from 0 (“none”) to 3 (“severe”) in intensity. To illustrate how the total and subscale scores of the SSQ are computed, an example self-reported symptoms (red ovals) are shown in Table 8. The scoring procedures for the example ratings are illustrated in Table 9 based on guidance from Kennedy et al. (1993). From weighted totals obtained in Table 9, the total score, and (N, nausea; O, oculomotor; and D, disorientation) subscale scores are calculated using the following formulae

$$\begin{aligned}
 O_{score} &= O_{total} \times 7.58 \\
 &= 11 \times 7.58 \\
 &= 83.38
 \end{aligned}
 \tag{10}$$

$$\begin{aligned}
 D_{score} &= D_{total} \times 13.92 \\
 &= 6 \times 13.92 \\
 &= 83.52
 \end{aligned}
 \tag{11}$$

$$\begin{aligned}
 N_{score} &= N_{total} \times 9.54 \\
 &= 7 \times 9.54 \\
 &= 66.78
 \end{aligned}
 \tag{12}$$

$$\begin{aligned}
 SSQ_{score} &= (O_{total} + D_{total} + N_{total}) \times 3.74 \\
 &= (83.38 + 83.52 + 66.78) \times 3.74 \\
 &= 873.96
 \end{aligned}
 \tag{13}$$

Table 8: Simulator sickness questionnaire (SSQ) instrument with example ratings (red ovals) (modified from [Kennedy et al., 1993](#)).

SSQ Symptom		Rating		
1. General discomfort	None	Slight	Moderate	Severe
2. Fatigue	None	Slight	Moderate	Severe
3. Headache	None	Slight	Moderate	Severe
4. Eyestrain	None	Slight	Moderate	Severe
5. Difficulty focusing	None	Slight	Moderate	Severe
6. Salivation increasing	None	Slight	Moderate	Severe
7. Sweating	None	Slight	Moderate	Severe
8. Nausea	None	Slight	Moderate	Severe
9. Difficulty concentrating	None	Slight	Moderate	Severe
10. Fullness of the Head	None	Slight	Moderate	Severe
11. Blurred vision	None	Slight	Moderate	Severe
12. Dizziness with eyes open	None	Slight	Moderate	Severe
13. Dizziness with eyes closed	None	Slight	Moderate	Severe
14. Vertigo	None	Slight	Moderate	Severe
15. Stomach awareness	None	Slight	Moderate	Severe
16. Burping	None	Slight	Moderate	Severe

3.6 Nauseogenic Stimulation

Rotating optokinetic drums have long been used to induce motion sickness/nausea experimentally ([Stern et al., 1985](#); [Bos and Bles, 2004](#); [Levine, Stern and Koch, 2014](#)). Here, to induce nausea, I developed a nauseogenic visual stimulus that simulates the visual input provided by that of a rotating optokinetic drum. The nauseogenic stimulus was a horizontal translation of black and white vertical stripes with a circular shift

Table 9: Simulator sickness questionnaire (SSQ) weights for subscales and example rating (modified from Kennedy et al., 1993).

SSQ Symptom	Example Rating	Weight		
		<i>N</i>	<i>O</i>	<i>D</i>
General discomfort	Slight = 1	1 (1)	1 (1)	
Fatigue	Moderate = 2		1 (2)	
Headache	Moderate = 2		1 (2)	
Eyestrain	Slight = 1		1 (1)	
Difficulty focusing	Moderate = 2		1 (2)	1 (2)
Salivation increasing	Slight = 1	1 (1)		
Sweating	None = 0	1 (0)		
Nausea	Moderate = 2	1 (2)		
Difficulty concentrating	Moderate = 2	1 (2)	1 (2)	
Fullness of the Head	Slight = 1			1 (1)
Blurred vision	Slight = 1		1 (1)	1 (1)
Dizziness with eyes open	Slight = 1			1 (1)
Dizziness with eyes closed	None = 0			1 (0)
Vertigo	Slight = 1			1 (1)
Stomach awareness	Slight = 1	1 (1)		
Burping	None = 0	1 (0)		
Total score		a = 7	b = 11	c = 6

of 62.5% created with custom code in MATLAB R2021b (The MathWorks, Inc., Natick, MA, USA) using the Psychophysics Toolbox Version 3 extensions (Psychtoolbox-3.0.19; <http://www.psychtoolbox.org>) (Brainard, 1997; Pelli, 1997; Kleiner, Brainard and Pelli, 2007) running on a Dell Latitude 5420 PC with a 3.00GHz 11th Gen Intel(R) Core(TM) i7-1185G7 processor and 16 GB RAM operating on Windows 11 Pro (Microsoft UK, Reading, UK). I presented the stimulus on a 47-inch LG LCD Widescreen (47LW450U, LG Electronics UK, UK) at a refresh rate of 60 Hz. For an unimpeded view, the nauseogenic stimulus was presented at a distance covering the participant's full visual field. This translation of alternating black and white stripes is a well-known model of eliciting illusory self-motion (vection) and nausea (Koch, 1999; Kennedy, Drexler and Kennedy, 2010). Previous cardiac modulation and neuroimaging studies investigating motion sickness have used an fMRI-compatible variant of the nauseogenic stimulus to induce nausea (LaCount et al., 2009; Kim et al., 2011; LaCount et al., 2011; Napadow et al., 2013; Sclocco et al., 2016; Toschi et al., 2017). The nauseogenic visual

stimulus herein has previously been applied to induce nausea (e.g., [Molefi, McLoughlin and Palaniappan, 2023a](#)). Altogether, the complete and contiguous stimulus was made up of crosshair fixation at baseline period, nauseogenic visual stimulation, and a final crosshair fixation at recovery period ([Figure 4](#)). To encourage replicability and standardisation, I have provided the MATLAB source code of the nauseogenic visual stimulus herein ([Code B.1](#)).

3.7 Electrical Stimulation

I used the EM6300A TENS (Med-Fit UK Ltd, Stockport, UK) device ([Figure 6](#)) to administer taVNS. The EM6300A is a battery operated dual-channel device that generates asymmetrical biphasic square-wave electrical impulses with an adjustable amplitude 0-100 mA peak into 500 ohm load on each channel; and is CE marked (CE 2460)¹. During project setup, the generated waveform produced via various parameters (frequency and pulse width) was visualized using a RIGOL DS1074 oscilloscope (RIGOL Technologies Inc., China). In both studies, current-controlled electric pulses of 200 μ s generated at a rate of 20 Hz were delivered continuously for at most 20 min; taVNS was administered at the tragus of the left ear ([Figure 4a](#)), and sham administered at the left earlobe ([Figure 4b](#)). In addition to adhering to the manufacturers recommendations on using the EM6300A device, prior work of comparable protocols were reviewed and explored to adopt the other standard stimulation parameters (i.e., pulse width and frequency) of those studies (e.g., [Beh and Friedman, 2019](#); [Tran et al., 2019](#); [Cao et al., 2021](#)). In Study 1, the delivered stimulation current during taVNS was 1 mA; and for sham, 0 mA (i.e., no stimulation). In Study 2, the stimulation current was tailored to each participant via a staircase procedure from 0 mA in 1 mA increments. Data analysis was conducted separately for EEG and ECG; [Table 10](#) shows the average stimulation amplitude for the analysed data during sham and taVNS conditions, including an indication that this electric current was comparable in both conditions for the performed analyses. Crucially, observed comparable electric current suggests that

¹Conforming with European legal health, safety, and environmental protection standards.

my stimulation protocol, wherein taVNS was delivered at the tragus (left ear) and sham at the left earlobe, provides adequate blinding to taVNS administration. The earlobe is one of the most commonly used sites for sham stimulation because of the view that it is not innervated by the auricular branch of the vagus nerve (Peucker and Filler, 2002; Bermejo et al., 2017; Yakunina, Kim and Nam, 2017). My rationale for targeting the left ear was based on the fact that most previous studies had investigated with it (Farmer et al., 2021). All participants were taVNS-naïve. For all experiments, participants reported perception of the stimulation current without painful sensation, and stimulation parameters were tested before starting each experiment. I used the countdown timer feature on the EM6300A device to sync the delivered electrical stimulation with the nauseogenic visual stimulation. Because participants could interrupt presentation of the nauseogenic visual stimulus due to development of severe nausea, the experimenter was available to manually switch off the electrical stimulator. While studies that administer non-invasive vagal stimulation – especially those using the (NEMOS, tVNS Technologies GmbH) device – typically deliver electrical impulses in an on-and-off pattern (Farmer et al., 2021), my review on electrical stimulation for motion sickness in Section [Electrical Stimulation for Motion Sickness](#) revealed that continuous stimulation is most common in the research literature of that field.



Figure 6: The EM6300A TENS (www.tensmachineuk.com) vagus nerve stimulation device; CE 2460.

Table 10: Electrical Stimulation Current.

Study	Sample	sham	taVNS	p-value
Molefi et al. (2025)	42	5.45 ± 3.26	5.36 ± 2.66	0.8476 ¹
Molefi et al. (2024)	29	5.55 ± 3.41	6.03 ± 2.40	0.4440 ²

¹ Paired-sample *t*-test.

² Wilcoxon signed rank test.

3.8 Summary

This chapter has outlined methods for performing taVNS (200 μ s, 20 Hz) administration in randomized sham-controlled crossover studies of healthy human volunteers exposed to a nauseogenic visual stimulus, including concurrent EEG and ECG data acquisition, and motion sickness severity assessment via validated questionnaires with exemplified subjective data scoring. Notably, the nauseogenic visual stimulus described here may aid future motion sickness research studies to induce nausea in a reliable and easy manner.

Chapter 4

Effects of taVNS on the Human Brain in Visually Induced Motion Sickness

4.1 Introduction

In recent years, the non-pharmacological approach to motion sickness management has entailed a variety of non-invasive electrical stimulation techniques. For example, transcutaneous electrical nerve stimulation (TENS), transcranial direct current stimulation (tDCS), and transcutaneous electrical acustimulation (TEA), have shown potential efficacy for alleviating symptoms of motion sickness ([Chu et al., 2012](#); [Arshad et al., 2015](#); [Zhao et al., 2022](#)). Despite these striking examples of therapeutic neuromodulation for motion-induced malaise, these studies – and others alike (e.g., [Chu et al., 2013](#); [Li et al., 2020](#)) – were limited by lack of incorporating neuroimaging modalities for evaluation of brain dynamic changes accompanying subjective motion sickness symptoms.

Furthermore, although recent research has demonstrated beneficial effects of non-invasive vagus nerve stimulation for migraine ([Tassorelli et al., 2018](#); [Beh and Friedman, 2019](#)) – a condition that has been suggested to have a relationship with motion sickness ([Cuomo-Granston and Drummond, 2010](#)) – this therapeutic neuromodulation

has not been applied in motion sickness. Thus, whether non-invasively stimulating the vagus nerve influences motion-induced nausea central neural system response, is unknown.

In visually induced motion sickness, incongruent information from the visual and vestibular systems promotes nausea and, with intense nauseogenic stimulation, vomiting (Shupak and Gordon, 2006; Kennedy, Drexler and Kennedy, 2010; Schmääl, 2013). Previous research has shown that at the cerebral level, the development and severity of motion-induced nausea is characterised by electroencephalogram (EEG) power spectral perturbations in the slow oscillations – i.e., delta, theta, and alpha – of the frontal, parietal and occipital lobes (Naqvi et al., 2015; Liu et al., 2020; Yeo, Kwon and Park, 2022; Andrievskaia et al., 2023). Studies using functional magnetic resonance imaging (fMRI) have observed disrupted brain neural dynamics in regions including the cortex, brainstem, and cerebellum (Napadow et al., 2013; Farmer et al., 2015).

An important gap in the management of motion-induced nausea derives from the lack of harnessing the neurophysiological changes observed during malaise for therapy. Thus, given the positive results from the studies on migraine, and accumulating evidence suggesting that transcutaneous modalities of vagus nerve stimulation (VNS) – that is, transcutaneous auricular VNS (taVNS) and transcutaneous cervical VNS (tcVNS) (Kaniusas et al., 2019; Farmer et al., 2021) – can modify human neuronal activity (Kraus et al., 2013; Frangos, Ellrich and Komisaruk, 2015); including the interesting observation that these neuromodulation modalities (in particular, taVNS), modulate neural processes perturbed by motion-induced malaise, suggests a potential new therapeutic avenue for motion sickness.

It is important to note that while I specifically worked with taVNS in my studies, throughout this chapter and the next (i.e., [Autonomic Effects of taVNS on Visually Evoked Motion Sickness in Humans](#) chapter), I will coalesce interpretation and discussion of taVNS and tcVNS results as it has been suggested previously that these modalities may have similar biological effects (Farmer et al., 2021). Moreover, a recent study utilising a rodent model to investigate clinically relevant taVNS parameters demonstrated that invasive cervical vagus nerve stimulation (cVNS – or simply VNS

as termed herein) and taVNS showed produced similar overall brainstem activation but different responses on individual neurons, albeit via distinct neural pathways (Owens et al., 2024). In the same vein, I will seldom but extrapolate findings from studies performed in animal models to findings herein.

Here, I utilised 64-channel EEG recordings to examine the acute effects of taVNS on spectral and time-frequency decompositions during nauseogenic stimulation; including cortical source localisation with low-resolution brain electromagnetic tomography (LORETA). Furthermore, I studied whether potential differences in brain response would relate to subjective measures of motion-induced nausea severity. Of note, parts of this chapter have been modified from Molefi, McLoughlin and Palaniappan (2023b, 2025).

4.2 Methods

4.2.1 EEG Data Processing

EEG signal processing was performed in MATLAB R2023b using custom scripts, incorporating EEGLAB functions (v2023.0; <https://sccn.ucsd.edu/eeglab>) (Delorme and Makeig, 2004). The raw EEG signals were first notch filtered to remove electrical stimulation-evoked artifact of 20 Hz; and performed high-pass (1 Hz) and low-pass (30 Hz) zero-phase response Butterworth IIR filtering; cutoff frequencies in accordance with EEG processing from previous findings. Channels with noisy activity according to (spectrum = 3 S.D., probability = 3 S.D., and kurtosis = 5 S.D.) threshold measures were removed. To identify and remove eye-blink and muscle artifact components, I performed independent component analysis (ICA) and applied a threshold probability of 80% via ICLabel (v1.3) (Pion-Tonachini, Kreutz-Delgado and Makeig, 2019). The obtained neuronal sources following ICA were then back-projected to the EEG time series; and spherical interpolation applied. To identify and attenuate major signal outliers and non-brain artifacts, I performed robust principal component analysis (RPCA) (Wright et al., 2009; Candès et al., 2011). To minimise the effect of volume conductivity, surface Laplacian (Perrin et al., 1989) was performed. The artifact-free EEG

time series were used to extract 5 min windows at “baseline” (prior to nauseogenic stimulus onset), “stimulation” (prior to nauseogenic stimulus cessation), and “recovery” (following nauseogenic stimulus cessation). Finally, the obtained 5 min windows (“baseline”; “stimulation”; “recovery”) were epoched into 8 s segments to obtain smooth power spectral density (PSD) estimate, respectively.

4.2.2 Spectral and Time-Frequency Decomposition

The EEG signal spectral power decomposition was computed using a multitaper spectral analysis (Babadi and Brown, 2014). First, I obtained the back-projected EEG time series from above (EEG Data Processing), and performed common average referencing (CAR) using Equation (14); that is, subtracting the grand average of the voltage signals of the 64 channels from each EEG time series. Next, I performed spectral decomposition of the data into delta (δ ; 1-4 Hz), theta (θ ; 4-8 Hz), alpha (α ; 8-12 Hz), beta (β ; 12-26 Hz), gamma (γ ; 26-30 Hz). Power normalization was performed using a decibel (dB) transformation as presented in Equation (15); where “stimulus” denotes condition types (i.e., taVNS vs. sham), and “baseline” denotes epochs prior to stimulus onset.

$$V_i^{CAR} = V_i^{ER} - \frac{1}{n} \sum_{j=1}^n V_j^{ER} \quad (14)$$

$$dBpower = 10 * \log_{10} \left(\frac{Power_{stimulus}}{Power_{baseline}} \right) \quad (15)$$

4.2.3 Exact LORETA (eLORETA)

For EEG brain source localization, I performed the exact low-resolution brain electromagnetic tomography (eLORETA), using the LORETA-KEY software package (v20221229; <https://www.uzh.ch/keyinst/loreta>) (Pascual-Marqui, 2002, 2007; Pascual-Marqui et al., 2011) on the de-noised epoched EEG data from above (see EEG Data Processing).

eLORETA – a 3D distributed linear, regularized, weighted minimum-norm inverse solution with exact, zero error localization – is a widely used mathematical tool that estimates neural activity of 6239 voxels (voxel size = 5 mm³) of the cortical gray matter using a realistic head model with the MNI152 (Montreal Neurological Institute 152) template (Mazziotta et al., 2001; Fuchs et al., 2002). Previous studies performing other non-invasive brain stimulation techniques – for example, repetitive transcranial magnetic stimulation (rTMS) (Meijs et al., 2024) and transcranial alternating current stimulation (tACS) (Fiene et al., 2020) – have utilized the eLORETA method. Herein I computed cross-spectra and corresponding frequency domain generators for each participant for five EEG frequency bands: delta (1-4 Hz), theta (4-8 Hz), alpha (8-12 Hz), beta (12-26 Hz), and gamma (26-30 Hz). That is, for each cross-spectrum file, a corresponding .slor file (image of cortical neuronal oscillators) was obtained; statistical analyses were performed on these computed neuronal generators. Note that cross-spectra from the aforementioned EEG frequency bands indicate to us which EEG oscillations (i.e., frequency bands) demonstrate differential neural activity. Consequently, if there are significantly different oscillations, then eLORETA provides an exact localization of neuronal sources responsible for the difference.

4.2.4 Statistical Analysis

All statistics were computed using MATLAB (R2022b, R2023a, R2024a, and R2024b). Data are presented as mean \pm standard error of the mean (SEM). Paired-sample tests were used to compare brain activity (Student's *t*-test) and MSAQ scores (Wilcoxon signed rank test). Effect sizes were computed using Cohen's *d* (unbiased estimate) and Cliff's Delta for brain activity and MSAQ scores respectively. Descriptors for Cohen's *d* are ($d < 0.2 \rightarrow$ 'negligible'; $d < 0.5 \rightarrow$ 'small'; $d < 0.8 \rightarrow$ 'medium'; $d \geq 0.8 \rightarrow$ 'large') (Cohen, 2013); and those for Cliff's Delta are ($|\delta| < 0.147 \rightarrow$ 'negligible'; $|\delta| < 0.33 \rightarrow$ 'small'; $|\delta| < 0.474 \rightarrow$ 'medium', $|\delta| \geq 0.474 \rightarrow$ 'large') (Romano et al., 2006). Non-parametric cluster-based permutation tests (Maris and Oostenveld, 2007) were used for time-frequency matrices between conditions. 1000 random permutations were performed to generate a null-hypothesis *t*-value distribution at ($p < 0.05$) where at each

iteration extracting the maximum cluster mean of the t -values. Then cluster-correction was applied by discarding any clusters in the real tmap that had voxels lower than 95% of null-distribution. [Figure 8](#) shows brain voxels that are significant. Spearman correlation was used for computing the relationship between brain activity and MSAQ scores. All statistical tests were two-tailed at ($p < 0.05$).

To perform statistical analysis for EEG brain source localization, I used the LORETA-KEY software package. The output neuronal generators from above [see [Exact LORETA \(eLORETA\)](#)] were subjected to a Statistical non-Parametric Mapping (SnPM) ([Nichols and Holmes, 2002](#)) method for correction of multiple comparisons; performing 5000 randomizations with significance threshold of $p < 0.05$, to estimate the empirical probability distribution for the maximum t -statistic, under the null hypothesis. Because of the non-parametric nature of this method, its validity does not require Gaussianity assumptions ([Nichols and Holmes, 2002](#)). I utilized this procedure to test for effects on neural activity using paired t -statistic contrasts on log-transformed data, at the sample level. Computed source localization statistical maps were visualized with MRICroGL (v1.2.20220720; <https://www.nitrc.org/projects/mricrogl>) ([Rorden and Brett, 2000](#)). The functional neuroimages herein – for example, [Figure 10](#) – display t -values such that $p < 0.05$. For statistical analyses performed in MATLAB R2023b, voxel intensity values at peak MNI coordinates were extracted using scripts incorporating functions from Statistical Parametric Mapping 12 (SPM12; Wellcome Centre for Human Neuroimaging, London, UK; <https://www.fil.ion.ucl.ac.uk/spm>).

4.3 Results

4.3.1 EEG Spectral Responses to taVNS during Motion-Induced Nausea

Comparisons between taVNS and sham revealed a significant differential reduction of theta spectral power by taVNS at right frontal ($t_{(14)} = 2.32$, $p = 0.0360$, $d = 0.7$), right parietal ($t_{(14)} = 2.37$, $p = 0.0328$, $d = 0.5$) and occipital ($t_{(14)} = 2.22$, $p = 0.0434$, $d = 0.7$) brain cortical regions ([Figure 7](#)). A finding consistent with previous studies performed both in humans ([Lewine et al., 2019](#)) and canines ([Castillo et al., 2022](#)),

Table 11: A summary of the MSAQ results. Data are mean \pm SEM. Reproduced from Molefi, McLoughlin and Palaniappan (2023b).

MSAQ metrics	sham	taVNS	<i>p</i> -value	Cliff's δ
Total	18.0 \pm 2.6	8.3 \pm 1.9	7.1e-06	0.30
Gastrointestinal	17.4 \pm 6.5	10.2 \pm 5.8	0.3125	0.20
Central	18.2 \pm 4.1	8.3 \pm 3.3	0.0032	0.26
Peripheral	15.3 \pm 3.1	7.1 \pm 2.5	0.0012	0.24
Sopite	17.9 \pm 3.0	8.3 \pm 2.1	1.1e-04	0.28

Table 12: Spearman Correlation between brain activity and MSAQ. Reproduced from Molefi, McLoughlin and Palaniappan (2023b).

	Right frontal cortex	Right parietal cortex	Occipital cortex
Total	0.07	0.13	0.34
Gastrointestinal	0.06	0.22	0.06
Central	-0.22	-0.01	0.23
Peripheral	0.28	0.41	0.52*
Sopite	-0.22	-0.14	0.20

* Statistically significant correlations ($p < 0.05$).

wherein tcVNS was applied. Additionally, I observed significant taVNS-induced subjective effects in MSAQ central, peripheral, and sopite-related dimensions of malaise scores, including MSAQ total scores (Table 11); however, I found no significant effect in the MSAQ gastrointestinal dimension scores (Table 11).

I then analysed whether the observed brain changes were related with motion-induced nausea symptom reduction. There was a significant correlation between change in occipital-theta spectral power and improvements in Peripheral dimension symptom scores (Spearman $\rho = 0.52$, $p = 0.0462$), indicating that MSAQ peripheral subjective effects are reflective of and linked to taVNS-induced occipital-theta brain dynamics (Table 12). As presented in Table 12, I observed a moderate but non-significant correlation between right parietal cortical activity with MSAQ Peripheral scores.

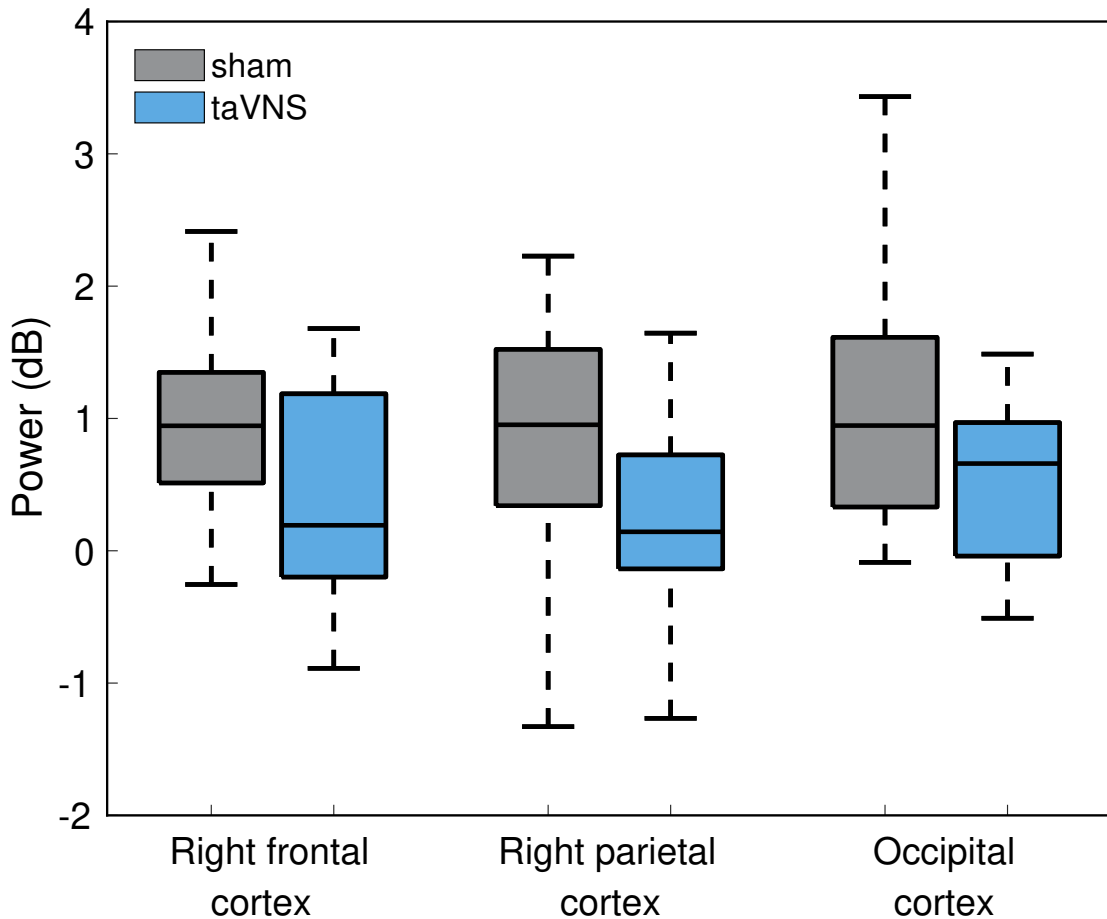


Figure 7: EEG theta power comparisons for sham and taVNS conditions for all participants at the right frontal, right parietal and occipital cortices. Reproduced from [Molefi, McLoughlin and Palaniappan \(2023b\)](#).

4.3.2 EEG Source Localization Reveals Differential Response to taVNS for Motion-Induced Nausea

Participant cohort ($n = 42$) average MSSQ scores were 26.54 (S.D. = 7.82, range = 15.75 – 48.00). In order to ascertain greater malaise susceptibility in adolescence for participant cohort herein, I performed a comparison between the MSA and MSB but found no difference ($p = 0.2394$, Wilcoxon signed rank test), with the distributions of the scores presented as box plots with mean and median depicted ([Figure 9a](#)). These MSSQ subscale scores (MSA, 13.36 ± 4.99 ; MSB, 13.18 ± 4.68) were higher than the mean \pm S.D. of normative data (MSA, 7.75 ± 5.94 ; MSB, 5.11 ± 4.84) ([Golding, 2006](#)).

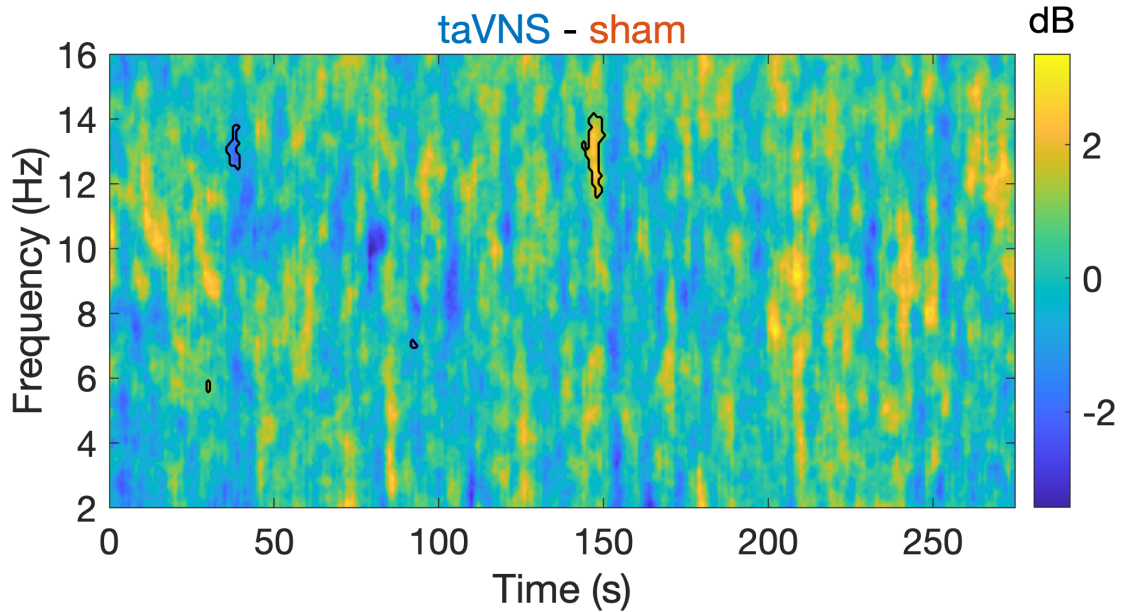


Figure 8: Time-frequency difference between sham and taVNS conditions across regions of interest for all participants. Black contours denote significant temporal clusters after a two-sided non-parametric permutation test with cluster-correction. Reproduced from [Molefi, McLoughlin and Palaniappan \(2023b\)](#).

Consistent with previous reports, however, there was an association between the MSA and MSB scores (Spearman $\rho = 0.35$, $p = 0.0251$; [Figure 9b](#)). None of the participants vomited during or after exposure to nauseogenic visual stimulation; however, one participant retched during nausea induction, and was one of the participants absent at a follow-up session. There were no significant differences between electrical current delivered at taVNS and that at sham ($p = 0.8476$, paired-sample t -test).

A summary of the MSAQ and SSQ scores is presented in [Table 13](#). There were no differences in the MSAQ subjective responses between sham and taVNS ([Table 13](#)). The two-way repeated measures ANOVA revealed a significant effect of stimulation ($F_{1,41} = 32.02$, $p = 1.32 \times 10^{-6}$), time ($F_{1,41} = 63.37$, $p = 7.52 \times 10^{-10}$), and an interaction ($F_{1,41} = 4.58$, $p = 0.0382$) for the SSQ total scores. Further, taVNS significantly reduced the SSQ nausea factor scores (two-way repeated measures ANOVA; effect of stimulation, $F_{1,41} = 21.47$, $p = 3.61 \times 10^{-5}$, effect of time, $F_{1,41} = 41.34$, $p = 1.06 \times 10^{-7}$, and stimulation \times time interaction, $F_{1,41} = 5.78$, $p = 0.0208$). Notably, no significant effect of order (*sham* \rightarrow *taVNS* vs. *taVNS* \rightarrow *sham*) was observed for

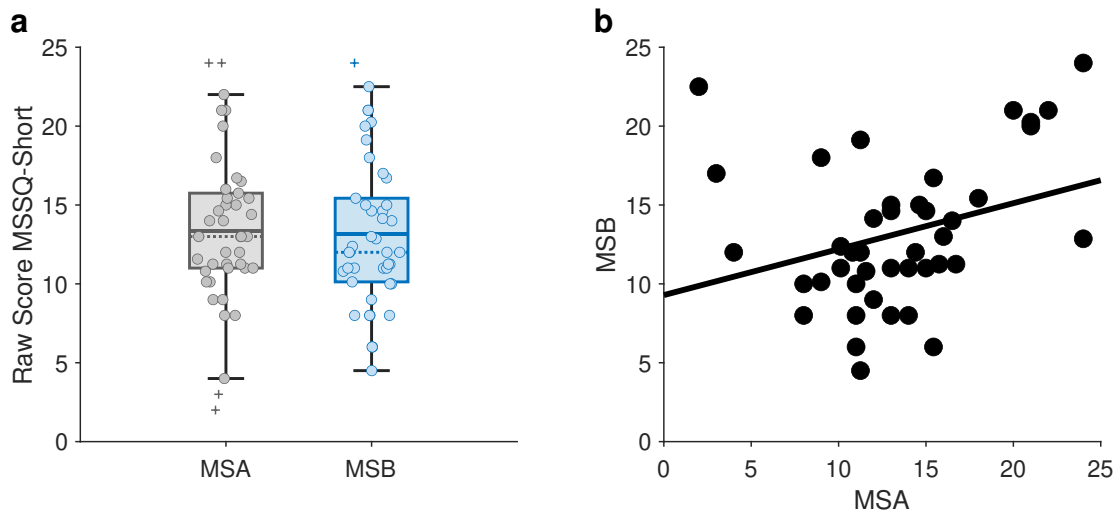


Figure 9: **(a)** Box plot showing MSSQ-Short raw scores of MSA and MSB for all participants. Solid lines indicate mean; dashed lines indicate median. **(b)** Spearman correlation between MSA and MSB where each data point represents a participant (Spearman $\rho = 0.35$). MSSQ, motion sickness susceptibility questionnaire; MSA, below 12 years of age MSSQ scores; MSB, over the last 10 years MSSQ scores. Reproduced from [Molefi, McLoughlin and Palaniappan \(2025\)](#).

SSQ total scores ($p = 0.9510$, unpaired-sample t -test), and SSQ nausea factor scores ($p = 0.7426$, unpaired-sample t -test).

To determine the acute neuromodulatory effects of taVNS administration on the cortical neuronal generators of EEG, I compared estimated source activity using eLORETA across three timepoints (“baseline”, “stimulation”, and “recovery”) with active taVNS and sham in different frequency bands. Note that all brain images hereinafter are presented in neurological convention; that is, the left side of the brain is shown on the left.

I found significant differences in the estimated source activity in the insula (BA 13, sub-lobar, $MNI_{x,y,z} = 35 -20 15$, $t = 5.96$) and middle frontal gyrus (BA 46, frontal lobe, $MNI_{x,y,z} = -45 35 20$, $t = 5.47$) between active taVNS and baseline in the delta band; with increased activation prominent during taVNS administration ([Figure 10](#)). There were no significant differences between taVNS and baseline in other frequency bands.

Table 13: Summary of motion sickness assessment questionnaire (MSAQ), and simulator sickness questionnaire (SSQ) total and subscale scores across participants, respectively; in participants receiving transcutaneous auricular vagus nerve stimulation (taVNS) compared with sham. Data are shown as mean \pm SEM. Reproduced from [Molefi, McLoughlin and Palaniappan \(2025\)](#).

Scores	sham		taVNS		F-value	p-value
	Pre	Post	Pre	Post		
MSAQ						
Total _{MSAQ}	0.17 \pm 0.03	0.36 \pm 0.04	0.14 \pm 0.03	0.34 \pm 0.04	0.09	0.761
Gastrointestinal _{MSAQ}	0.06 \pm 0.03	0.30 \pm 0.04	0.08 \pm 0.03	0.29 \pm 0.04	0.18	0.676
Central _{MSAQ}	0.11 \pm 0.04	0.35 \pm 0.05	0.06 \pm 0.03	0.32 \pm 0.04	0.06	0.814
Peripheral _{MSAQ}	0.14 \pm 0.04	0.20 \pm 0.04	0.09 \pm 0.03	0.16 \pm 0.04	0.10	0.753
Sopite _{MSAQ}	0.26 \pm 0.04	0.42 \pm 0.04	0.18 \pm 0.03	0.39 \pm 0.04	1.05	0.311
SSQ						
Total _{SSQ}	0.24 \pm 0.04	0.56 \pm 0.04	0.15 \pm 0.03	0.37 \pm 0.03	4.58	0.038*
Nausea _{SSQ}	0.21 \pm 0.04	0.50 \pm 0.04	0.13 \pm 0.03	0.29 \pm 0.03	5.78	0.021*
Oculomotor _{SSQ}	0.24 \pm 0.04	0.60 \pm 0.03	0.19 \pm 0.03	0.46 \pm 0.04	2.79	0.102
Disorientation _{SSQ}	0.15 \pm 0.04	0.38 \pm 0.04	0.08 \pm 0.03	0.37 \pm 0.04	1.20	0.279

* Indicates significant difference in pre and post behavioral changes in response to electrical stimulation ($p < 0.05$) using a two-way repeated-measures ANOVA with the within-subjects factors “time” (pre vs. post) and “stimulation” (taVNS vs. sham). The presented F and p values are for the interaction effects from a two-way repeated measures ANOVA.

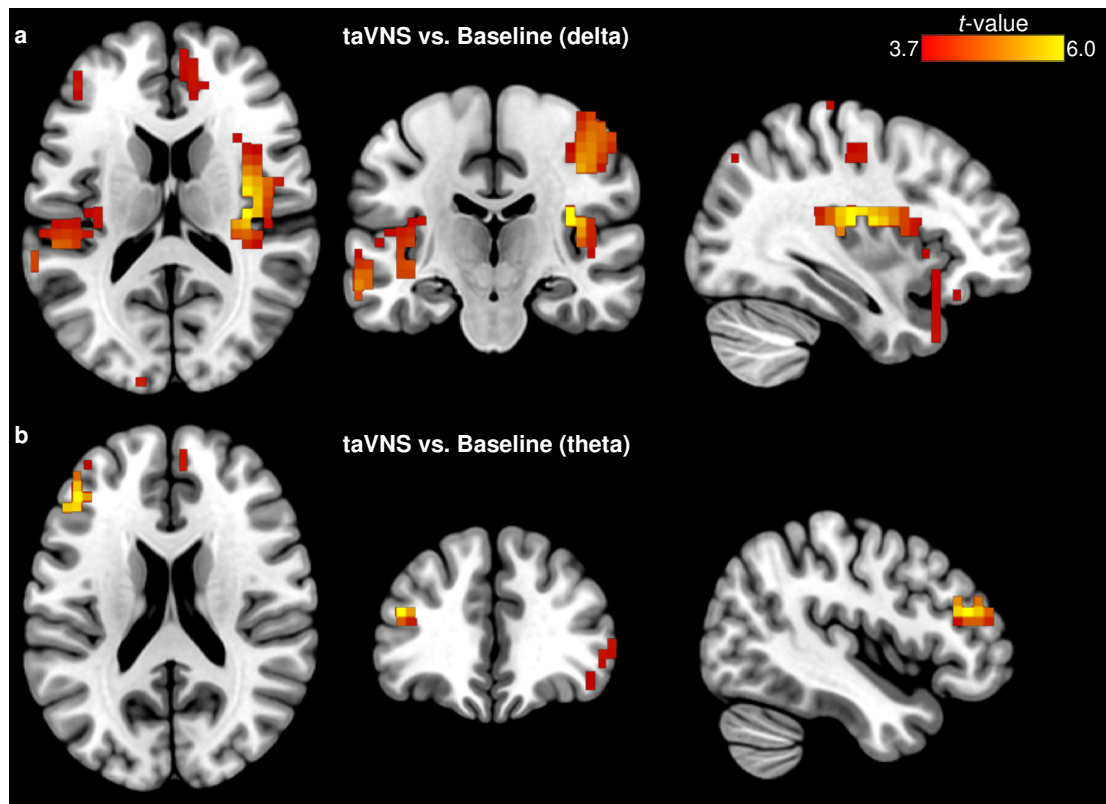


Figure 10: eLORETA of taVNS versus Baseline contrast. **(a)** Differential estimated source activity (delta) at the right insula (BA 13, peak $MNI_{x,y,z} = 35 -20 15$, $t = 5.96$). **(b)** Changes in source activity (theta) observed at the left middle frontal gyrus (BA 46, peak $MNI_{x,y,z} = -45 35 20$, $t = 5.47$). Slice views of source locations from left to right are axial, coronal, and sagittal images; viewed from top, back, and right. In all of the images, the left side of the brain is shown on the left. BA, Brodmann area. Reproduced from [Molefi, McLoughlin and Palaniappan \(2025\)](#).

taVNS caused profound brain activation across most of the frequency bands ([Figure 11](#)), with most prominent estimated source activity observed in the supramarginal gyrus (BA 40, parietal lobe, $MNI_{x,y,z} = -40 -50 35$, $t = 4.53$), middle frontal gyrus (BA 6, frontal lobe, $MNI_{x,y,z} = 40 0 45$, $t = 3.84$), parahippocampal gyrus (BA 35, limbic lobe, $MNI_{x,y,z} = 20 -25 -15$, $t = 4.62$), and precentral gyrus (BA 6, frontal lobe, $MNI_{x,y,z} = -55 -5 50$, $t = 3.98$), post taVNS than at baseline – in the delta, theta, alpha and gamma bands, respectively ([Figure 11](#)).

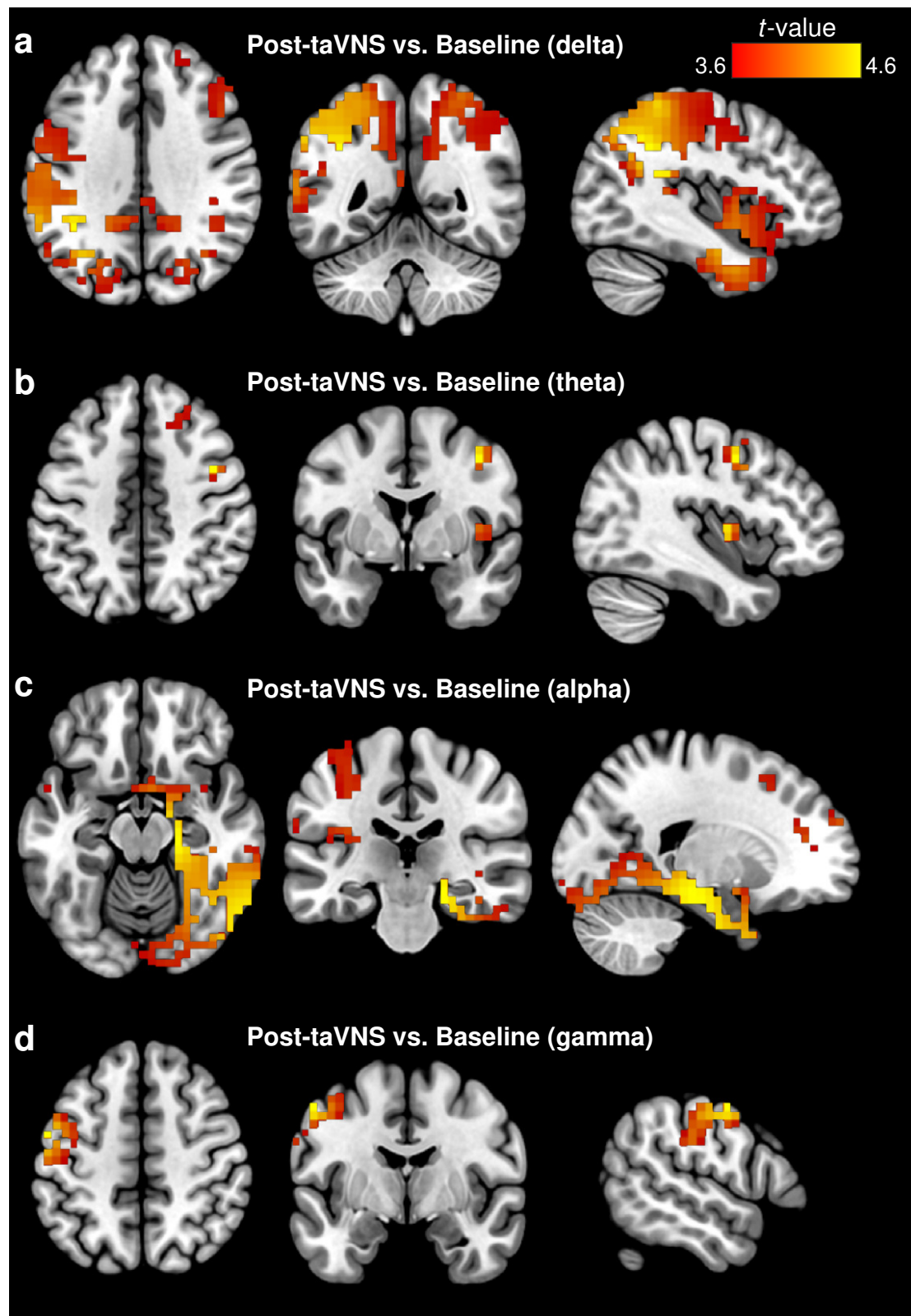


Figure 11: eLORETA of active Post-taVNS versus Baseline contrast. **(a)** Following taVNS, increased estimated source activity was observed at the supramarginal gyrus (BA 40, peak $MNI_{x,y,z} = -40 -50 35$, $t = 4.53$) for delta, **(b)** the middle frontal gyrus (BA 6, peak $MNI_{x,y,z} = 40 0 45$, $t = 3.84$) for theta, **(c)** the parahippocampal gyrus (BA 35, peak $MNI_{x,y,z} = 20 -25 -15$, $t = 4.62$) for alpha, **(d)** and the precentral gyrus (BA 6, peak $MNI_{x,y,z} = -55 -5 50$, $t = 3.98$) for gamma. Slice views of source locations from left to right are axial, coronal, and sagittal images; viewed from top, back, and right. In all of the images, the left side of the brain is shown on the left. taVNS, transcutaneous auricular vagus nerve stimulation; BA, Brodmann area. Reproduced from [Molefi, McLoughlin and Palaniappan \(2025\)](#).

I found that sham applied to the earlobe increased insula activation (BA 13, sub-lobar, $MNI_{x,y,z} = 35 -20 20$, $t = 7.83$) in the delta band, compared to baseline ([Figure 12a](#)). Activation was also noted in anterior cingulate (BA 24, limbic lobe, $MNI_{x,y,z} = 5 35 10$, $t = 3.34$; [Figure 13](#)) in the beta band; however this was not significant. Following sham stimulation, while I observed widespread brain activation, the middle frontal gyrus (BA 9, frontal lobe, $MNI_{x,y,z} = 45 30 40$, $t = 5.70$) demonstrated prominent activation compared to baseline in the EEG alpha band ([Figure 12b](#)).

Next, I asked if there were differential effects of active vs. sham taVNS on the estimated source activity both during and post electrical stimulation. I observed that the contrast $(\text{During-Pre})_{\text{taVNS}}$ vs. $(\text{During-Pre})_{\text{sham}}$ revealed markedly increased theta brain activity in the left middle occipital gyrus (BA 19, occipital lobe, $MNI_{x,y,z} = -50 -60 -10$, $t = 3.97$) ([Figure 14](#)). I then determined how taVNS-induced BA 19 theta neuronal activity related to participant subjective responses. A Pearson correlation revealed a significant positive correlation between BA 19 activation and MSA responses (Pearson $r = 0.43$, $p = 0.0041$; [Figure 15a](#)). Moreover, this observed taVNS-induced contribution of BA 19 theta neuronal response correlated with reductions in motion sickness symptoms as evaluated by SSQ total scores (Spearman $\rho = 0.35$, $p = 0.0229$; [Figure 15b](#)). These results also remained significant after adjusting for age and sex using partial correlations. For the $(\text{Post-Pre})_{\text{taVNS}}$ vs. $(\text{Post-Pre})_{\text{sham}}$ contrast, I found no significantly increased or decreased brain activation in the functional regions that were revealed.

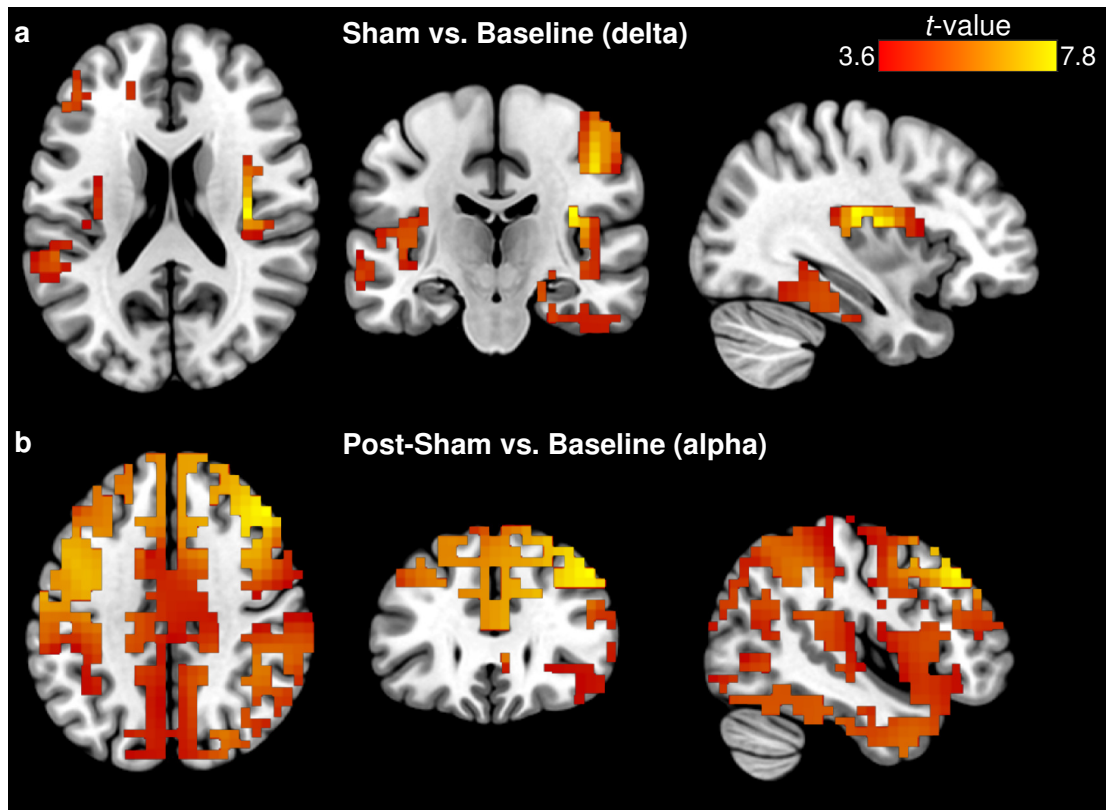


Figure 12: eLORETA of Sham versus Baseline, and Post-Sham versus Baseline contrasts. **(a)** Changes in estimated source activity (delta) between Sham (i.e., during stimulation period) and Baseline were identified in the right insula (BA 13, peak $MNI_{x,y,z} = 35 -20 20$, $t = 7.83$). **(b)** Estimated source activity (alpha) differences between Post-Sham and Baseline were identified at the right middle frontal gyrus (BA 9, peak $MNI_{x,y,z} = 45 30 40$, $t = 5.70$). Slice views of source locations from left to right are axial, coronal, and sagittal images; viewed from top, back, and right. In all of the images, the left side of the brain is shown on the left. BA, Brodmann area. Reproduced from [Molefi, McLoughlin and Palaniappan \(2025\)](#).

4.4 Discussion

I conducted crossover randomised controlled studies to examine the acute neural effects of non-invasive vagus nerve stimulation on healthy human participants before, during, and after concurrent electrical stimulation with either active taVNS or sham and nauseogenic stimulation. Using eLORETA, I observed taVNS-induced differential functional brain activation in comparison to sham. Moreover, taVNS demonstrated significant reduction in motion sickness symptom severity as measured by the SSQ

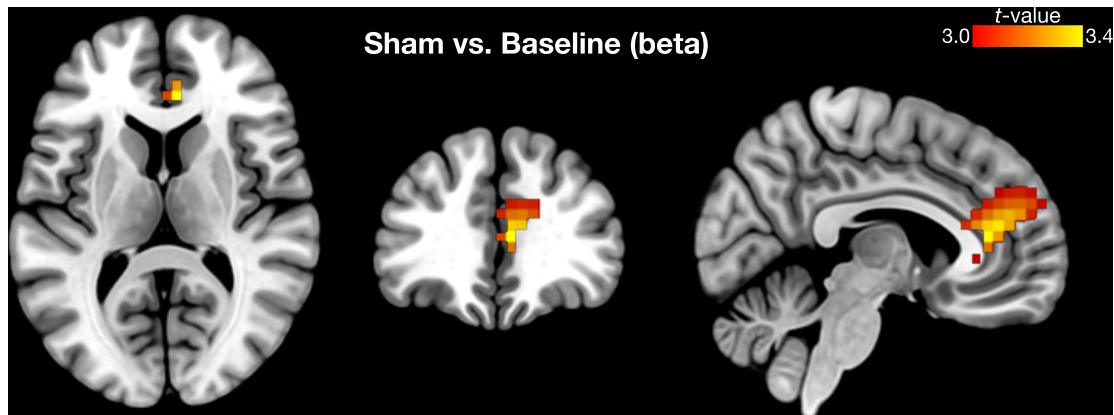


Figure 13: Exact low-resolution brain electromagnetic tomography (eLORETA) of active Sham versus Baseline contrast. Differential source activity of beta oscillation was observed at the anterior cingulate (BA 24, limbic lobe, $MNI_{x,y,z} = 5\ 35\ 10$, $t = 3.34$). Slice views of source locations from left to right are axial, coronal, and sagittal images; viewed from top, back, and right. BA, Brodmann area. Reproduced from [Molefi, McLoughlin and Palaniappan \(2025\)](#).

instrument. Specifically, the scores of the SSQ total, and SSQ nausea subscale were markedly lower when participants received taVNS compared with sham stimulation. These findings provide novel evidence that during motion-induced nausea, taVNS-driven neural dynamics are different compared to sham, and that taVNS evokes acute neural effects that relate to accompanying subjective effects, suggesting that taVNS has potent therapeutic potential for motion sickness-induced nausea.

In the pilot study herein ([Molefi, McLoughlin and Palaniappan, 2023b](#)), I showed that taVNS paired with nauseogenic stimulation induced lower levels of EEG theta spectral power in multiple cortical regions ([Figure 7](#)), which have previously been demonstrated to reveal motion sickness-associated perturbations ([Huang, Jung and Makeig, 2009](#); [Chen et al., 2010](#); [Nürnberg et al., 2021](#)). Furthermore, these taVNS brain effects – which were consistent with findings from both human ([Lewine et al., 2019](#)) and animal ([Castillo et al., 2022](#)) models – were associated with a differential reduction in malaise severity symptoms ([Table 11](#)). However, in that first study, while I demonstrated that the administration of taVNS may have therapeutic utility for motion sickness, I noted an important limitation that for the sham condition, null stimulation was performed. In a bid to address this, and other limitations that were acknowledged

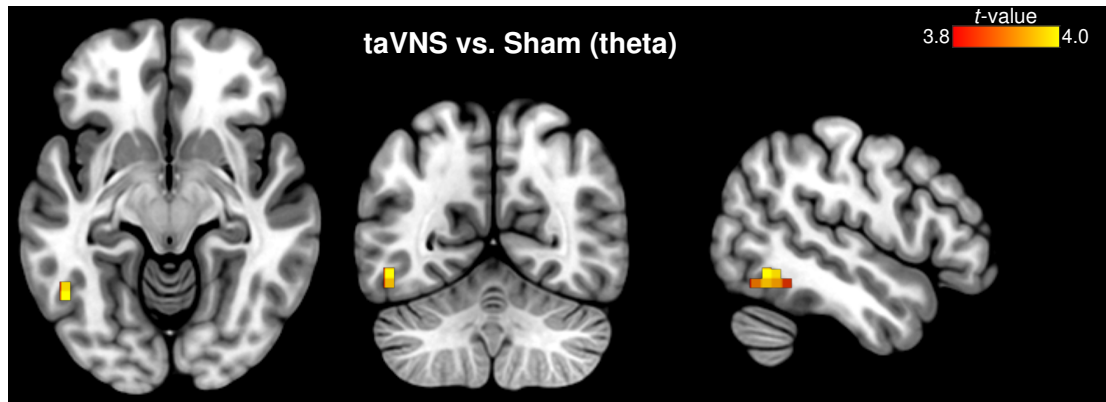


Figure 14: eLORETA of active taVNS versus Sham contrast. Differential source activity of theta oscillation was observed at the left middle occipital gyrus (BA 19, peak $MNI_{x,y,z} = -50 -60 -10$, $t = 3.97$). Slice views of source locations from left to right are axial, coronal, and sagittal images; viewed from top, back, and right. In all of the images, the left side of the brain is shown on the left. taVNS, transcutaneous auricular vagus nerve stimulation; BA, Brodmann area. Reproduced from [Molefi, McLoughlin and Palaniappan \(2025\)](#).

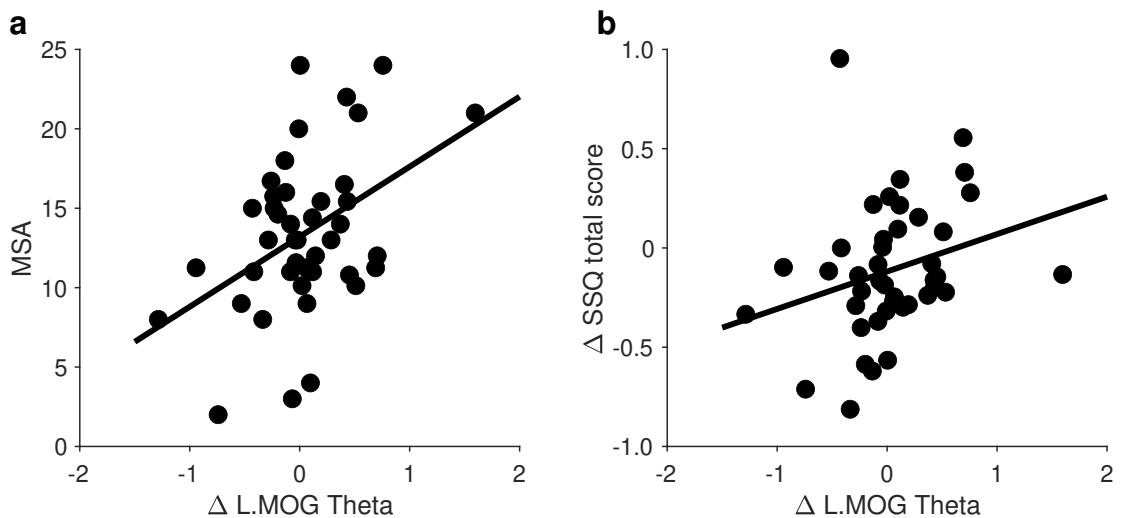


Figure 15: **(a)** Scatter plots show that the change in activation of the left middle occipital gyrus (L.MOG) between sham and taVNS stimulation was positively associated with MSA responses (Pearson $r = 0.43$), **(b)** and correlated with the change in SSQ total scores (Spearman $\rho = 0.35$). MSSQ, motion sickness susceptibility questionnaire; MSA, below 12 years of age MSSQ scores; SSQ, simulator sickness questionnaire. Reproduced from [Molefi, McLoughlin and Palaniappan \(2025\)](#).

therein, I performed a sequel study including a cohort of 42 healthy human participants for which much of the discussion here will be devoted to.

I found that taVNS administration leads to an increase in functional brain activation in the right insula (BA 13; [Figure 10a](#)). Previous fMRI studies have shown that tragus stimulation produces significantly increased activation in the insula ([Kraus et al., 2007, 2013](#)), indicating that afferent input targeting the auricular branch of the vagus nerve is projected to the brain via the brainstem. Thus, my findings support a modulatory role for taVNS in response to nasueogenic stimulation. It is interesting to note that I observed this insula activation using a different taVNS protocol compared to both of these aforementioned studies, suggesting that my taVNS parameters were sufficient for brainstem nuclei activation. I noted that this insula activation was a strong contributor for delta oscillations, suggesting that these oscillations may be serving as a response marker for taVNS-induced effects.

My data also demonstrated insula activation during sham stimulation ([Figure 12a](#)). This is unlikely to be an effect of vagal afferent input, but rather an activation driven by malaise; [Napadow et al. \(2013\)](#) observed that the insula was among brain regions activated by motion sickness-induced nausea. Moreover, a recent meta-analysis of neuroimaging studies demonstrated that, when compared to null stimulation (i.e., no stimulation), transcutaneous vagus nerve stimulation significantly augmented activity in the insula ([Rajiah et al., 2022](#)); suggesting that the brain dynamics I observed during taVNS were dissimilar to those noted during sham.

Furthermore, I additionally observed increased neuronal response at the left middle frontal gyrus (MFG; BA 46) during taVNS ([Figure 10b](#)), but not during sham stimulation; this MFG activation was shown as a strong generator of theta oscillations. Moreover, the MFG activation I noted here is consistent with work describing that tragus stimulation activates the cerebral afferents of the vagal pathway ([Badran et al., 2018](#)); further indicating that my taVNS protocol can bring about cortical effects that are similar to previous taVNS brain imaging studies. To interpret these taVNS-induced neural effects, I surmise taVNS may be enhancing interoceptive processes ([Paciorek and Skora, 2020](#)); thus, through this improved interoceptive awareness, participants are better able to cope with exposure to nauseogenic stimulation. This implies that participants become more resilient. Indeed, it is important to note that the MFG –

which forms part of the dorsolateral prefrontal cortex (dlPFC) – has previously been related to resolution of attentional-perceptual conflicts (Adelhöfer et al., 2019; Leroy and Cheron, 2020). Further, we have long known that the insula plays an important role in the integration of internal body state information (Damasio et al., 2000), and that it has also been implicated in higher-order brain systems – one of which is the salience network (SN) (Seeley et al., 2007; Menon and Uddin, 2010). I speculate that, it is through this activation of the SN – a neural system involved in the integration of internal and external sensory inputs that vie for our brain's attention, and neural resources – that participants adjust or self-regulate their body state and thus tolerate or buffer nauseogenic stimulation effects.

Because the MFG was not revealed during sham stimulation suggests that participants might have been experience a sense of agitation; indeed, Farmer et al. (2015) presented a nausea-inducing motion video to a cohort of healthy participants and noted perturbations in their level of autonomic arousal which suggested they responded to the stimulus as if it were a threat. Thus, an implication of this finding is that this may have the case in my study for the sham condition. Of note, I observed increased neuronal response in the anterior cingulate (Figure 13) during sham stimulation but not during taVNS administration; while this activation was not significant, disrupted anterior cingulate cortical response has been reported in motion-induced nausea (Napadow et al., 2013; Ruffle et al., 2019).

Of the most novel observations I made here was the prominent neuronal response localized to the middle occipital gyrus (MOG; BA 19) (Figure 14), when comparing taVNS to sham stimulation – that is, taVNS versus sham contrast. I observed that neuronal generation of theta oscillations was contributed by this BA 19 activation. Previously, increased brain activity at the left occipital lobe was reported in response to stimulation applied at the surface of the neck, that is, via tcVNS (Frangos and Komisaruk, 2017). By analysing high-resolution positron emission tomography (HR-PET) scans obtained during tcVNS paired with traumatic stress scripts, Wittbrodt et al. (2021) observed a differential increase in BA 19 brain activity. Consistent with these findings, my data indicate that stimulation of the tragus evokes similar regional brain activation. My

observation that BA 19 activation was related to subjective responses of motion sickness as indexed by the MSA scores; including the marked correlation with a differential reduction in SSQ total scores, suggests participants achieved better symptom relief. In other words, this indicates that participants with greater levels of BA 19 activity derived the most benefit from taVNS. For the marked relationship between MSA scores and BA 19 activation in particular, this suggests that MSA scores may be a useful predictor of taVNS response; meaning that herein, participants who exhibited higher MSA scores were more responsive to taVNS. A possible explanation for these results is that BA 19 may be portraying an essential role in representing effects that are a function of taVNS in tandem with nasueogenic with stimulation. It is tempting to speculate that this MOG activation may be solely responsible for the observed malaise symptom alleviation. Thus, I do not rule out the potential role of other cortical regions in eliciting these effects.

Because BA 19 resides in the extrastriate visual cortex – where the extrastriate body area (EBA) ([Downing et al., 2001](#)) can also be found – including early fMRI evidence for EBA response to self-produced body movements ([Astafiev et al., 2004](#)), I surmise here that taVNS signaling to higher-order brain structures normalises or stabilises the sensory conflict at the level of neural oscillations (via MOG neurons) generated by conjured up illusory body representations of participants during nauseogenic stimulation. Using tcVNS, [Wittbrodt et al. \(2020\)](#) described a mechanism by which participants presented with traumatic scripts showed activation at the left fusiform gyrus (BA 20) – found in the temporal lobe – and interpreted this neural response as an implication that participants reconstructed their body form and environment during the traumatic event. In the same vein, I postulate that this taVNS-induced left MOG cortical activity represents a differential therapeutic benefit.

In addition to functional brain response observed during stimulation, taVNS demonstrated profound peak neuronal activation at the supramarginal gyrus (SMG; BA 40), MFG (BA 6), parahippocampal gyrus (PHG; BA 35), and precentral gyrus (PCG; BA 6) ([Figure 11](#)). While ([Frangos and Komisaruk, 2017](#)) also observed SMG activation via non-invasive vagal stimulation, their finding was noted during the stimulation period;

additionally, they targeted the cervical branch of the vagus nerve. These differences in findings could be due to differences in protocol design; thus, implying that my taVNS-evoked SMG response may be relevant for malaise-reduction effects. I also note that this may suggest vagal nerve branch specificity, that is, auricular versus cervical; indeed, a recent study in a rodent model confirmed that taVNS can evoke responses comparable to cervical VNS at the neuronal level, however, achieving this via differential neuronal pathways (Owens et al., 2024).

The SMG has a long identified role in vestibular processing; together with the angular gyrus, it forms part of the inferior parietal lobule. Previous work of Klaus et al. (2020) showed a role for the left inferior parietal lobule in vestibular information processing; whereby the spatial processing of self-motion is linked with the spatial processing required to imagine self-motion. Because vestibular sensations are among some of the sensory information disrupted during motion sickness, by triggering the SMG, taVNS could be aiding maintain normal vestibular processing and function. It is important to note that I did not observe this differential effect with sham stimulation. In fact, neuronal activity following sham was much more widespread (Figure 12) while that following taVNS appeared more organised and localised (Figure 11). To interpret this ambiguous activation following sham, which was nonetheless revealed as a peak neural response at the MFG (BA 9) and serving as the generator of the alpha oscillations, I speculate participants may be feeling agitation even beyond nauseogenic stimulation; indeed, previous research has observed a differential increase in sympathetic activation after nauseogenic stimuli (LaCount et al., 2011; Sclocco et al., 2016). Moreover, this aforementioned dIPFC (MFG) activation has previously been implicated with increasing motion-induced nausea levels (Napadow et al., 2013); hence, I surmise here that these neural effects following sham may be indicative of response to motion-induced nausea – for instance, participants in recovery but still feeling nauseous – and not sham neural effects *per se*.

Here I also show an increase of PHG neuronal activation following taVNS (Figure 11c). In early fMRI studies, the PHG – a limbic brain region implicated in (among

other functions) emotion, and visuospatial processing – was found to decrease in response to transcutaneous vagus nerve stimulation (Kraus et al., 2007, 2013). While interestingly I noted an increase rather than a decrease; my observation may relate back to the notion of EBA, suggesting in this instance that participants become aware of their perceived body representation via visuospatial processing ability. A possible explanation for activation of these brain regions (i.e., SMG, MFG, PHG, PCG) may suggest a concerted multisensory integration to restore visuo-vestibular interaction profiles to a non-conflicting state. Furthermore, it implies oscillations contributed by these different regions may be working in concert to modulate neuronal activity across the frontal (MFG, PCG), parietal (SMG) and limbic (PHG) functional structures of the brain. These results further bolster the finding that taVNS elicits specific differential neuronal responses than do sham. Toschi et al. (2017) provided evidence for augmentation of functional connectivity between nausea-processing brain regions and those triggered by the nauseogenic visual stimulus; thus, for future research, it would be important to explore how connectivity analysis performed on a motion sickness model similar to that herein could aid deeper understanding of taVNS application to motion sickness. My observation of differential alpha and gamma oscillations following taVNS (Figure 11c, d), but not during stimulation period, suggests a possible indication of taVNS-induced delayed effects after cessation of both taVNS and nauseogenic stimulation. Corroborating these findings, Borgmann et al. (2021) demonstrated delayed effects of taVNS on brainstem neuronal responses of healthy participants through acute stimulation of the left cymba conchae.

Previous work showed that tragus stimulation evokes neuronal responses that persist after cessation of the stimulation (Frangos, Ellrich and Komisaruk, 2015); consistent with this, I observed differential taVNS effects on delta and theta oscillations during and following tragus stimulation (Figures 10 and 11), giving the impression that my taVNS protocol produced effects that appear to last over time. In another study (Dimitrov and Gatev, 2015), also in line with my findings, sustained delta and theta oscillations were demonstrated 20 min post stimulation period; of note, this was shown via stimulation applied to the right cymba conchae. Recent work from Ricci et al. (2020)

also showed delta oscillations following stimulation of the left external acoustic meatus. Altogether, these findings may have implications for the role of taVNS in altering neural activity of these slow oscillations of the brain (i.e., delta, theta), with potentially long-lived effects, and merit further study.

Surprisingly, however, my post-taVNS versus post-sham revealed no differences, suggesting that possibly in the context motion-induced nausea, real-time taVNS administration may provide differential neuromodulatory effects of therapeutic value. Moreover, it suggests these effects are profound when the device is active (i.e., during stimulation period). These results additionally endorse the viability of managing malaise in a manner whereby taVNS induces demand-based, modulatory effects – with important implications for adaptive taVNS. Current antiemetic drugs such as anticholinergics (e.g., scopolamine), amphetamines (e.g., dextroamphetamine) and serotonin (e.g., rizatriptan) show efficacy toward motion sickness symptom alleviation by influencing the cholinergic (Kohl and Homick, 1983), dopaminergic (Schmäl, 2013), and serotonergic (Furman, Marcus and Balaban, 2011) pathways, respectively. Because stimulation of the vagus nerve has been demonstrated to engage these aforementioned brain pathways, i.e., cholinergic (Hulsey et al., 2016), dopaminergic (Perez et al., 2014), and serotonergic (Hulsey et al., 2019) (albeit in animal models); it suggests that my neuronal activation findings herein may be stem from taVNS-induced alterations on neural processes of these neuromodulatory systems. Moreover, it reveals just how multifaceted the effects of electrically stimulating the vagus nerve may be – and hinting at how vagal stimulation seems to help with so many other ailments.

4.5 Conclusion

My results show that taVNS, a non-invasive form of brain stimulation, has differential therapeutic effects in healthy human participants exposed to nauseogenic stimulation. Using eLORETA analysis, I demonstrate that taVNS-induced functional brain activation reveals a marked correlation with the alleviation of motion sickness symptom severity. However and importantly, taVNS will depend on stimulation parameters, such as pulse

width, frequency, and location, among others. Future work to confirm the results presented here is important, as well addressing the search for optimal taVNS dosage for motion sickness management.

Chapter 5

Autonomic Effects of taVNS on Visually Evoked Motion Sickness in Humans

5.1 Introduction

Efferent preganglionic fibers of the vagus nerve provide sympathetic and parasympathetic innervation between the brain and heart – among other thoracoabdominal organs. Accordingly, an induced elevation or diminution on the level of autonomic arousal may be observed, depending on which vagal neural pathway is activated, and how stimulation to that pathway was performed. For instance, [Jansen et al. \(2011\)](#) demonstrated that left cervical vagus nerve stimulation (VNS) induced a differential increase in the low-frequency to high-frequency power ratio (LF/HF) of the heart rate variability (HRV) in individuals with refractory epilepsy – concluding that VNS evoked a shift in autonomic function toward sympathetic predominance. Whereas the findings of [Clancy et al. \(2014\)](#) showed that stimulating the branch of the vagus nerve that supplies the outer ear at the tragus, significantly reduced the LF/HF ratio, indicating a pronounced dominance of parasympathetic over sympathetic nerve outflow.

Because the vagus nerve is a major component of the parasympathetic nervous

system, it is possible that stimulation of this neural structure could increase parasympathetic tone. Indeed, on the most extreme end, it is well known that excessive stimulation of the vagus nerve can cause vasovagal syncope ([van Lieshout et al., 1991](#); [Jardine et al., 1998](#); [Carlson, 2021](#)) – a syndrome characterized by a reduction in heart rate and blood pressure. Importantly, by leveraging the role of the vagus nerve as a heart-brain conduit for parasympathetic neural transmission, modern research has revealed that non-invasive stimulation of branches of this neural structure – for example, at the neck (cervical branch) or ear (auricular branch) – may have therapeutic effects for conditions as diverse as tinnitus ([Ylikoski et al., 2017](#)), heart failure ([Tran et al., 2019](#); [Kumar et al., 2023](#)), and metabolic syndrome ([de Moraes et al., 2023](#)); wherein improved autonomic balance was observed.

Previous research in visually induced motion sickness has demonstrated decreased parasympathetic neural activity during nauseogenic stimulation (reviewed in [Farmer et al., 2014b](#)); thus, suggesting that prevention or reversal of this withdrawal in parasympathetic tone could represent a key therapeutic target for ameliorating motion sickness severity. Non-invasive electrical stimulation modalities such as transcutaneous electrical nerve stimulation (TENS) ([Chu et al., 2012, 2013](#)) and transcutaneous electrical acustimulation (TEA) ([Zhao et al., 2022](#)) have shown potential to normalise motion sickness-associated autonomic imbalances, however, no study has yet examined whether electrically stimulating the vagus nerve may have a similarly positive influence.

To address this research gap, I investigated transcutaneous auricular VNS (taVNS) – a novel neuromodulation tool for effective vagal afferent stimulation – for potential alleviation of motion sickness severity. I collected electrocardiogram (ECG) data to characterise taVNS-induced changes in HRV, and ECG morphology (shape) and variability in a human model of motion sickness. Additionally, I recorded the subjective responses of motion sickness symptom severity to test for behavioural effects as well as probe the relationship with taVNS administration-related physiological changes. Of note, parts of this chapter have been modified from research described in [Molefi, McLoughlin and Palaniappan \(2023a,c, 2024\)](#).

5.2 Methods

5.2.1 ECG Data Processing

ECG signal acquisition has been described in the “[Materials and Methods](#)” chapter. All ECG signals were processed and analysed in MATLAB R2022a, R2023a, and R2024a using custom scripts. For Dataset 1 (i.e., data from Study 1, see [Chapter 3](#) for more details), epoch selection was identical to that previously described ([Molefi, McLoughlin and Palaniappan, 2023a](#)), and based on a combination of percept- and condition-based analysis methods used in previous studies in the literature ([LaCount et al., 2011](#); [Sclocco et al., 2016](#); [Toschi et al., 2017](#)). Briefly, using the continuous ECG recordings, I extracted 5 min epochs from “Baseline” and “Nausea” intervals. The 5 min “Baseline” epochs were extracted prior to nauseogenic visual stimulation onset (see [Figure 4](#) on page 49). Epoch extraction for the “Nausea” interval was performed by applying the following logic: 5 min epochs were obtained prior to nauseogenic stimulus offset if the participant completed the full 20 min interval of nauseogenic visual stimulation without providing a nausea subjective rating of at least 2 (moderate nausea), or for scenarios where the participant triggered premature stoppage of the nauseogenic visual stimulation due to a subjective feeling of severe nausea; moreover, for participants reporting a nausea subjective rating of at least 2, the 5 min epochs were obtained prior to the maximum nausea rating reported. For Dataset 2 (data from my second study, see [Chapter 3](#) for additional details), epoch preparation was performed as previously described ([Molefi, McLoughlin and Palaniappan, 2024](#)); whereby 5 min epochs were obtained at “Baseline” (prior to nauseogenic stimulus onset), “Stimulation” (prior to nauseogenic stimulus offset), and “Recovery” (following nauseogenic stimulus offset) experimental intervals, respectively.

For R-peak detection, the raw ECG signals were first visually inspected for the presence of disturbances and distortions. Next, I used the Pan-Tompkins algorithm ([Pan and Tompkins, 1985](#)) for detection of the QRS complexes. Briefly, the Pan-Tompkins algorithm involves performing bandpass filtering between 5 and 15 Hz to attenuate

various unwanted spectral content (e.g., 50 Hz power-line noise, muscle noise, baseline wander, and *T* wave interference) from an ECG signal (Figure 16b), followed by a derivative filter to obtain QRS complex slope information (Figure 16c), a squaring function to amplify high frequency content (i.e., QRS complexes) (Figure 16d), and applying a moving-window integrator to provide waveform feature information including the slope of the *R* wave (Figure 16e). Finally, adaptive thresholding is applied to obtain the locations of the QRS complexes (Pan and Tompkins, 1985). In my implementation of this algorithm, to prevent phase distortion, I used the `filtfilt` MATLAB function to perform zero-phase filtering. Following QRS complex detection, and the ensuing R-peak detection, the RR time series (RR intervals) were generated. I performed visual inspection to ensure the quality of the RR time series retained.

Separate ECG signal processing was performed for analysis that did not necessitate R-peak detection. Here, the ECG signals were zero-phase highpass and lowpass filtered using 4th-order Butterworth filters with cutoff frequencies of 0.5 and 30 Hz, respectively. To remove electrical stimulation-evoked artifacts, I performed notch filtering at 20 Hz using a high-order Butterworth infinite impulse response (IIR) filter; this was implemented using the `designNotchPeakIIR` MATLAB function. Next, the ECG signals were normalised to lie within the range $[0, 1]$.

5.2.2 Heart Rate Variability (HRV)

I performed HRV analysis in accordance with recommended standards by the [Task Force of the European Society of Cardiology and the North American Society of Pacing and Electrophysiology \(1996\)](#). For HRV methods that were not fully addressed in this aforementioned standardisation document – in particular, nonlinear methods – I referred to [Sassi et al. \(2015\)](#). It is important to note that a wide range of parameters can be derived from the HRV signal; here, I focus on those that were reviewed in sections [Autonomic Effects of taVNS](#) and [Autonomic Effects of Motion Sickness](#). Plus, an additional heretofore unexplored measures which demonstrated potential to advance our understanding of taVNS-mediated physiological changes.

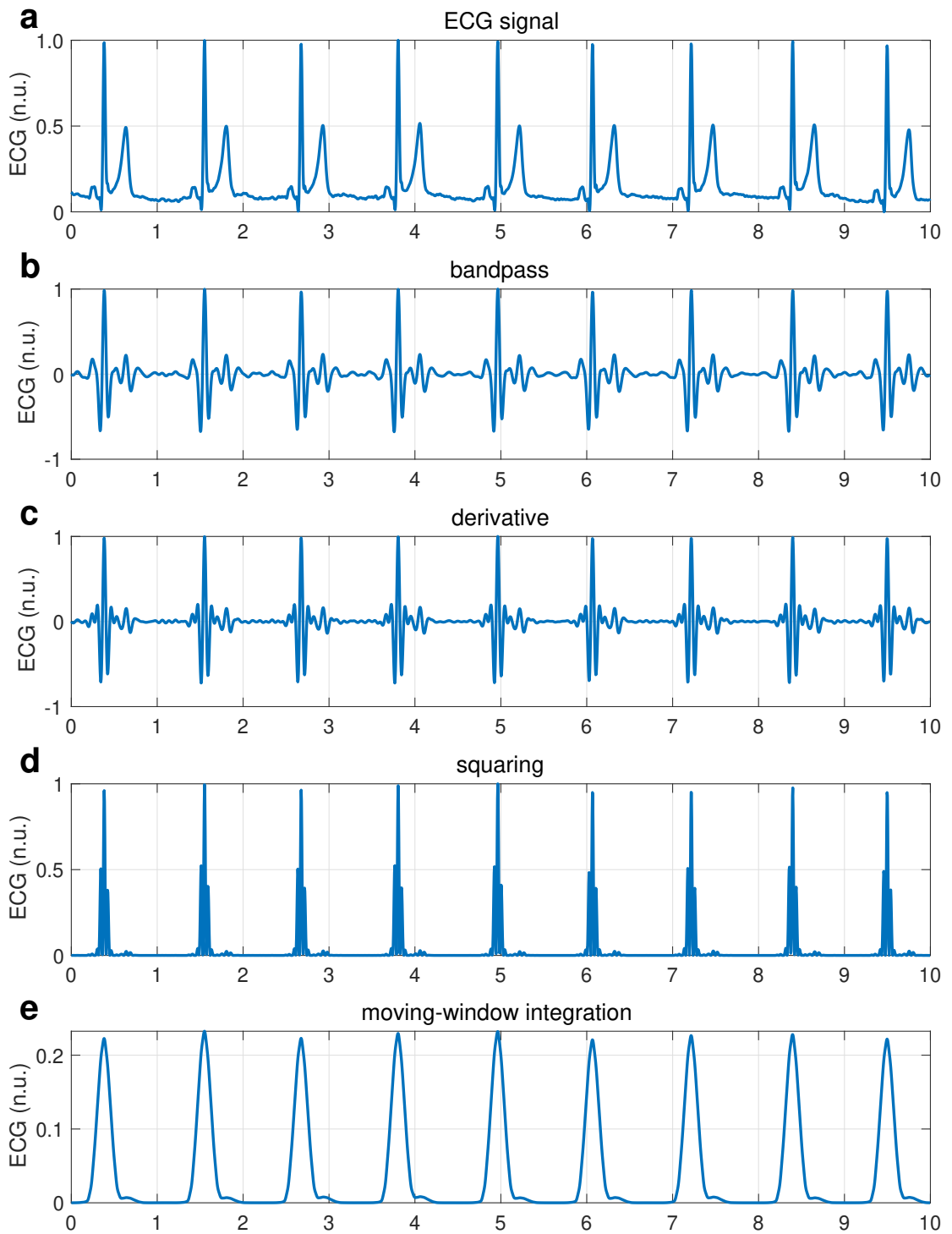


Figure 16: Pan–Tompkins QRS algorithm procedures. **(a)** A 10 s ECG signal for one example participant. **(b)** Output of bandpass filter. **(c)** Output of differentiator. **(d)** Output of squaring procedure. **(e)** Output from performing moving-window integration.

Time-Domain Analysis

All statistical HRV time-domain measures that were studied in this chapter are summarized in [Table 14](#). Of note, in addition to computing most of the well-established measures recommended by the [Task Force of the European Society of Cardiology and the North American Society of Pacing and Electrophysiology \(1996\)](#), I also calculated more recently proposed measures which have been demonstrated to be useful at distinguishing between physiological and pathological states – namely, the percentage of absolute differences in successive NN values > 20 ms ([Mietus et al., 2002](#)), and the ratio of standard deviation of NN intervals (SDNN) to root mean square of successive differences of NN intervals (RMSSD) ([Balocchi et al., 2006](#)). To calculate these measures ([Table 14](#)), for an RR series $RR = (RR_1, RR_2, \dots, RR_n)$, including N successive intervals, I obtained the mean RR interval using [Equation \(16\)](#), and corresponding mean heart rate via [Equation \(17\)](#), defined respectively here as:

$$\overline{RR} = \frac{1}{N} \sum_{n=1}^N RR_n \quad (16)$$

$$\overline{HR} = 60/\overline{RR} . \quad (17)$$

SDNN, a marker of overall HRV, and RMSSD, an indicator of parasympathetic neural activity, were calculated respectively in the standard way by:

$$SDNN = \sqrt{\frac{1}{N-1} \sum_{n=1}^N (RR_n - \overline{RR})^2} \quad (18)$$

$$RMSSD = \sqrt{\frac{1}{N-1} \sum_{n=1}^{N-1} (RR_{n+1} - RR_n)^2} \quad (19)$$

For the pNNx family of statistics, I calculated the widely used and standard pNN50 measure ([Ewing, Neilson and Travis, 1984](#); [Task Force of the European Society of Cardiology and the North American Society of Pacing and Electrophysiology, 1996](#)). Additionally, I calculated the pNN20 statistic, proposed by [Mietus et al. \(2002\)](#). These

Table 14: HRV time-domain measures.

Parameter	Description
\overline{NN}	Mean of NN intervals
\overline{HR}	Mean heart rate
SDNN	Standard deviation of NN intervals
RMSSD	Root mean square of successive differences of NN intervals
pNN20	Percentage of successive NN intervals that differ by > 20 ms
pNN50	Percentage of successive NN intervals that differ by > 50 ms
SDNN/RMSSD	Ratio of SDNN-to-RMSSD interbeat interval variability
SDSD	Standard deviation of successive NN intervals

measures were computed using Equation (20), where x is 20 and 50 ms for pNN20 and pNN50, respectively. Note that x can be a value between 5 and 100 ms.

$$pNNx = \frac{1}{N-1} \sum_{n=1}^{N-1} (|RR_{n+1} - RR_n| \geq x) \times 100. \quad (20)$$

The ratio between SDNN and RMSSD can be calculated from the measures given by Equations (18) and (19):

$$SDNN/RMSSD_{ratio} = \frac{SDNN}{RMSSD}. \quad (21)$$

Frequency-Domain Analysis

Because the HRV signal is inherently nonstationary, to perform RR series power spectral density (PSD) estimation, I used the Lomb-Scargle periodogram (Lomb, 1976; Scargle, 1982) method. This was achieved using the MATLAB `plomb` function. Note that unlike the commonly used nonparametric fast Fourier transformation (FFT) for spectral power decomposition of heart rate, the Lomb-Scargle periodogram method does not require a uniformly sampled RR series. Moreover, early work from Moody (1993) demonstrated that this method produces robust PSD estimates of heart rate. To illustrate the output of PSD estimation via these two approaches, I obtained the

Lomb-Scargle PSD estimate (Figure 17c), and the Welch PSD estimate (Figure 17d), for an example ECG signal (Figure 17a). It is important to point out that subtraction of the mean and cubic spline interpolation at 4 Hz preprocessing steps were performed prior to the computation of the Welch PSD estimate shown in Figure 17d; example MATLAB code of how this was achieved is presented in Code 5.1. While other resampling or interpolation methods are possible – for example, linear interpolation – cubic spline interpolation is often preferred because it augments LF, and HF power. HRV literature reports a range of resampling rates between 1 and 10 Hz. We choose 4 Hz in accordance with a relevant previous study in nausea perception (LaCount et al., 2011).

Code 5.1: Mean subtraction and cubic spline interpolation for HRV spectral power decomposition via FFT- or wavelet-based PSD estimates.

```

NN = diff(locs);
tNN = cumsum(NN);

NNnorm = NN - mean(NN);

fs4Hz = 4;
vq = tNN(1):1/fs4Hz:tNN(end);
NNinterp = interp1(tNN(:), NNnorm(:), vq(:), "spline");

% Welch's power spectral density estimate
[pxx, f] = pwelch(NNinterp, [], [], 2^nextpow2(length(NNinterp)), fs4Hz);

```

To accomplish HRV spectral feature extraction, I derived the spectral components presented in Table 15 following the Task Force of the European Society of Cardiology and the North American Society of Pacing and Electrophysiology (1996) guidelines. Here, I calculated power in the very low frequency (VLF; ≤ 0.04 Hz) range in order to compute low frequency (LF) and high frequency (HF) power components in normalized units (n.u.) using Equations (22) and (23) below. To normalize the LF/HF ratio measure, I took the natural logarithm (ln) of the calculated values as given by Equation (24).

$$LF_{norm} = \frac{LF \text{ power}}{Total \text{ power} - VLF \text{ power}} \times 100 \quad (22)$$

$$HF_{norm} = \frac{HF \text{ power}}{Total \text{ power} - VLF \text{ power}} \times 100 \quad (23)$$

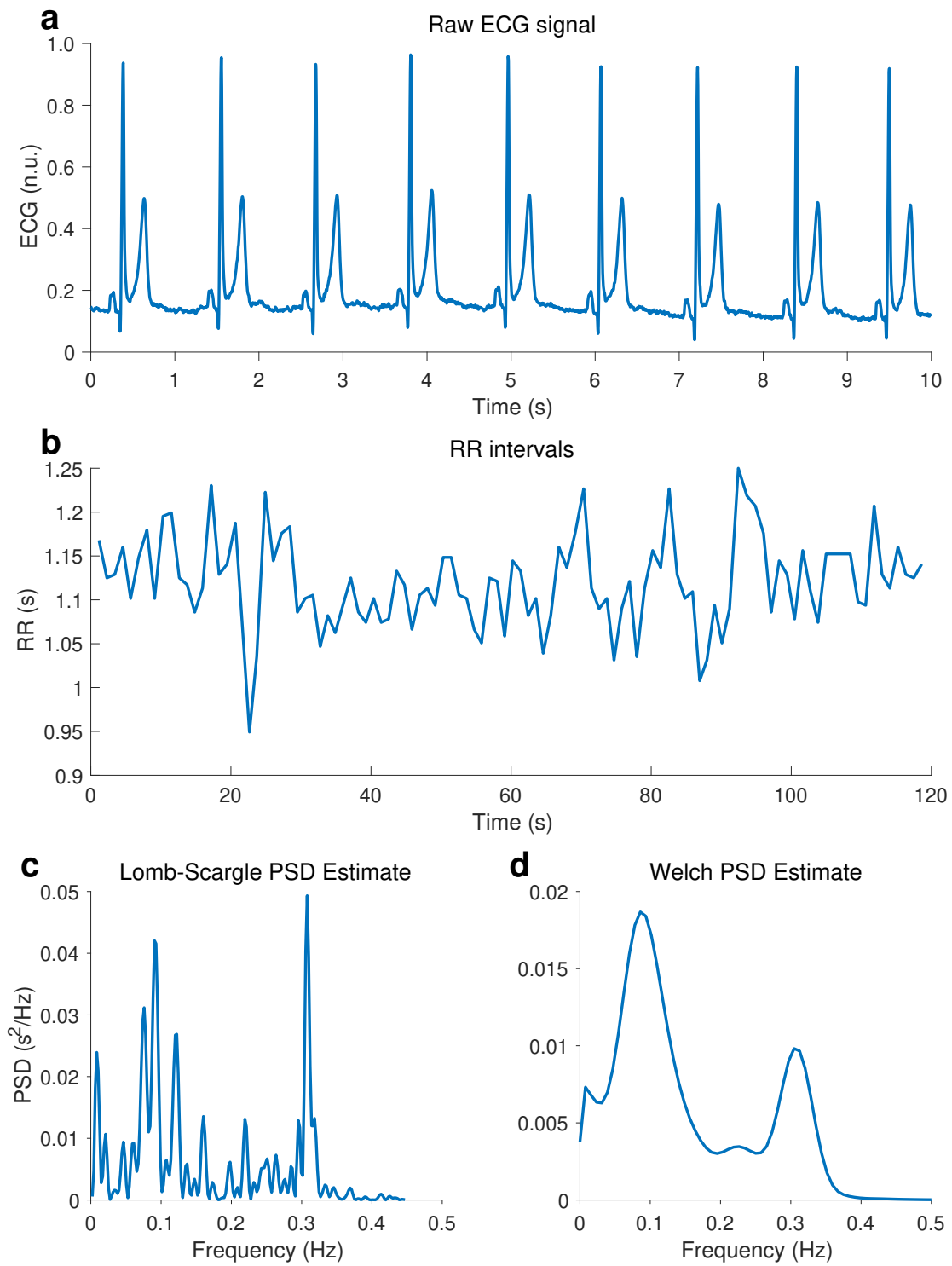


Figure 17: Using `p_lomb` to estimate and plot the PSD of the nonuniformly sampled signal. **(a)** A 10 s ECG signal for one example participant. **(b)** RR interval for a 120 s ECG segment. **(c)** Output of `p_lomb` function. **(d)** Output of `p_welch` function.

Table 15: HRV frequency-domain measures.

Parameter	Description	Frequency band
Total power	Variance of NN intervals	≤ 0.40 Hz
VLF	Power in very low frequency range	≤ 0.04 Hz
LF	Power in low frequency range	0.04–0.15 Hz
HF	Power in high frequency range	0.15–0.40 Hz
LF/HF	Ratio of LF-to-HF power	

$$\ln LF/HF_{ratio} = \log\left(\frac{LF \text{ power}}{HF \text{ power}}\right) \quad (24)$$

Nonlinear-Domain Analysis

While the clinical meaning and application of HRV nonlinear methods are yet to be widely recognised, it is indisputable that the genesis of HRV comprises nonlinear phenomena. Hence the long-held view that HRV assessment via these nonlinear parameters, represent good potential to provide additional physiological insights and interpretation on HRV beyond traditional methods – that is, time- and frequency-domain analyses. Accordingly, I investigated the set of parameters summarised in [Table 16](#). While these parameters were not originally addressed in the early [Task Force of the European Society of Cardiology and the North American Society of Pacing and Electrophysiology \(1996\)](#) standards, most of them were critically reviewed and summarised in [Sassi et al. \(2015\)](#).

Poincaré Plot. Poincaré plot analysis was performed by plotting NN_{n+1} as a function of NN_n (see [Figure 18](#) for illustration); enabling summarisation and assessment of HRV dynamics through a geometric, or phase space representation. For Poincaré plot quantitative analyses, I fitted ellipsoids to the resultant point cloud in this phase space representation, as depicted in [Figure 18](#); and subsequently derived the standard deviation of Poincaré plot of RR intervals perpendicular to the line-of-identity ($SD1$) –

Table 16: HRV nonlinear measures.

Parameter	Description
SD1	Standard deviation of Poincaré plot of RR intervals perpendicular to the line-of-identity
SD2	Standard deviation of Poincaré plot of RR intervals along the line-of-identity
CVI	Cardiac vagal index
CSI	Cardiac sympathetic index
SampEn	Regularity and complexity of a time series
FuzzyEn	Regularity and complexity of a time series
LLE	Chaos and complexity of a time series

see Equation (26) – and standard deviation of Poincaré plot of RR intervals along the line-of-identity ($SD2$) – see Equation (27) – from the fitted ellipsoids (Figure 18; Tulppo et al., 1996). As illustrated in Figure 18, $SD1$ and $SD2$ correspond to the length of the minor and major axes of the fitted ellipsoid, respectively. Physiologically, the $SD1$ measure corresponds to short-term HRV; whereas the $SD2$ measure captures short- and long-term HRV. To perform qualitative visual analyses of the Poincaré plots, I classified their geometric properties – which have been demonstrated to be indicative of perturbations in parasympathetic and sympathetic modulation – as follows: “comet shape” for balanced sympathetic-parasympathetic activity; “tight cluster” for complete autonomic blockade; and “cigar shape” for parasympathetic blockade (or unopposed sympathetic activity) (Brennan, Palaniswami and Kamen, 2002).

$$SDSD = \sqrt{\frac{1}{N} \sum_{n=1}^N [(RR_n - RR_{n+1}) - (\overline{RR} - RR_{n+1})]^2} \quad (25)$$

$$SD1 = \sqrt{\frac{1}{N-1} \sum_{n=1}^{N-1} \frac{(RR_n - RR_{n+1})^2}{2}} = \frac{\sqrt{2}}{2} SDSD \quad (26)$$

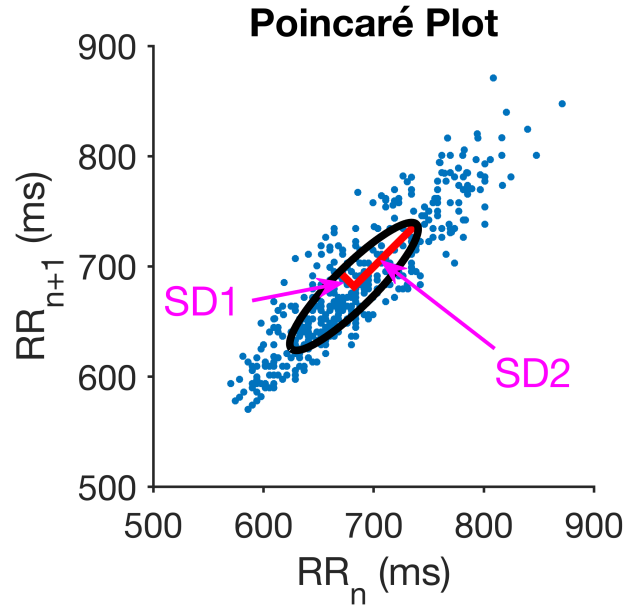


Figure 18: Poincaré plot for the normal-to-normal interval (NN_{n+1}) versus the subsequent interval (NN_n).

$$SD2 = \sqrt{\frac{1}{N-1} \sum_{n=1}^{N-1} \frac{(RR_n + RR_{n+1} - 2\overline{HR})^2}{2}} = \sqrt{2SDNN^2 - \frac{1}{2}SDSD^2} \quad (27)$$

Because the Poincaré plot quantitative metrics (i.e., SD1, SD2) have been demonstrated to characterise HRV dynamics similar to existing time-domain measures of the HRV (Brennan, Palaniswami and Kamen, 2001) – also shown in Equations (25) to (27) – and, including the fact that the RMSSD has been reported to be identical to the metric SD1 (Ciccone et al., 2017); I thus additionally examine the Poincaré/Lorenz plot according to Toichi et al. (1997); computing the parameters cardiac vagal index (CVI) and cardiac sympathetic index (CSI) as given by Equations (28) and (29), respectively, via the definitions of SD1 and SD2 from Equations (26) and (27), respectively. Importantly, Toichi et al. (1997) concluded that these measures – that is, CVI and CSI – are reliable markers of short-term cardiac parasympathetic (vagal) and sympathetic function, respectively.

$$CVI = \log_{10}(SD1 * SD2) \quad (28)$$

$$CSI = \frac{SD2}{SD1} \quad (29)$$

Sample Entropy (SampEn). To measure the regularity and complexity of the RR time series, I computed the sample entropy (SampEn) (Richman and Moorman, 2000). Of note, the SampEn family of statistics was developed to overcome the shortcomings of the early approximate entropy (ApEn) (Pincus, Gladstone and Ehrenkranz, 1991); which included computation of inconsistent results, a bias effect (due to inclusion of self-matches), and a dependency on time series data length; for this reason, in addition to the fact that values generated by both methods are interpreted and used alike, I consider its computation over ApEn. Elaborate details of computing SampEn have long been presented by Richman and Moorman (2000), and hence described here briefly. Given an N -point time series, embedding dimension m and radius of similarity r , the correlation integral is defined using $C_i^m(r) = \frac{N_i^m(r)}{N-m}$ and average regularity computed via Equation (30). In the same vein, $\Phi^{(m+1)}(r)$ can be defined by considering $m + 1$ points. The SampEn value can then be computed using Equation (31) (Richman and Moorman, 2000). I performed all calculations for SampEn and Fuzzy Entropy (FuzzyEn) using $m = 2$ and $r = 0.2$, based on previous research (Richman and Moorman, 2000; Solís-Montufar, Gálvez-Coyt and Muñoz-Diosdado, 2020).

$$\Phi^m(r) = \frac{\sum_{i=1}^{N-m} C_i^m(r)}{N-m}, \quad (30)$$

$$SampEn(m, r, N) = -\ln \frac{\Phi^{(m+1)}(r)}{\Phi^{(m)}(r)}. \quad (31)$$

Fuzzy Entropy (FuzzyEn). Chen et al. (2007) expatiated on the FuzzyEn mechanism. Methodologically, FuzzyEn is akin to SampEn with the important exception that, here, a fuzzy membership function $\mu(d_{ij}^m, r) = e^{-\ln(2)(d_{ij}^m/r)^2}$ is used to calculate the

similarity degree between two vectors; this puts emphasis on the vectors' shapes as opposed to their absolute coordinates – which is the case for both ApEn and SampEn. Following this import of a fuzzy function, [Equation \(30\)](#) gets applied and the FuzzyEn statistic estimated using [Equation \(32\)](#):

$$FuzzyEn(m, r, N) = -\ln \frac{\Phi^{(m+1)}(r)}{\Phi^{(m)}(r)}. \quad (32)$$

Largest Lyapunov Exponent (LLE). To estimate the level of chaos and complexity of HRV dynamics, I computed the largest Lyapunov exponent (λ_1) – well-documented by [Rosenstein, Collins and De Luca \(1993\)](#). Briefly, defining λ_1 as $d(t) = Ce^{\lambda_1 t}$ where $d(t)$ is the average divergence of trajectories at time t , and constant C normalizes their initial separation; [Rosenstein, Collins and De Luca \(1993\)](#) demonstrated that λ_1 can thus be computed precisely using a least-squares fit to the “average” line defined by

$$y(i) = \frac{1}{\Delta t} \langle \ln d_j(i) \rangle, \quad (33)$$

where $\langle \rangle$ indicates averaging over all values of j . Because of the time component in [Equation \(33\)](#), I performed cubic spline interpolation at 4 Hz prior to computing the LLE value; for cubic spline interpolation I used the same approach as illustrated in [Code 5.1](#).

Time-Frequency Analysis

To evaluate the dynamics of HRV, I computed the smoothed pseudo Wigner-Ville distribution (SPWVD) ([Cohen, 1995](#)) of the RR series data; knowing that this has the added advantage of revealing how the frequency components of a signal varies over time. Importantly, being able to observe the progression of symptoms as the participant suffers bouts of sickness may help elucidate how motion sickness evolves, in addition to how taVNS may be involved in the sickness evolution process. Prior to computing the SPWVD, I performed a 4 Hz cubic spline interpolation to obtain a uniformly sampled RR series (see [Code 5.1](#) for illustration of performing cubic spline interpolation).

We may recall from section [Frequency-Domain Analysis](#) that this preprocessing step is necessary for frequency/time-frequency decomposition when methods such as those based on Fourier transforms, or wavelet-based PSD estimates are applied (i.e., these approaches assume uniform sampling) ([Toschi et al., 2017](#); [Task Force of the European Society of Cardiology and the North American Society of Pacing and Electrophysiology, 1996](#)). Next, I computed the Hilbert transform to obtain the analytic signal association to the HRV signal. Finally, to compute a high-resolution time-frequency power representation of the HRV, I performed the SPWVD – a well-known method for its good time-frequency resolution and robustness towards cardiovascular signal analysis ([Orini et al., 2012](#)). In MATLAB, computing the SPWVD can be performed using the `wvd` function with the “smoothedPseudo” argument as illustrated in [Code 5.2](#). The SPWVD method has previously been utilised in obstructive sleep apnea (OSA) detection using the ECG (e.g., [Quiceno-Manrique et al., 2009](#)), in addition to the detection of drowsiness (e.g., [Vicente et al., 2016](#)). The SPWVD is a member of the Cohen’s class family of time-frequency distributions ([Cohen, 1995](#)), and can be defined as follows:

$$SPWVD_x^{g,H}(t, f) = \int_{-\infty}^{\infty} g(t) H(f) x\left(t + \frac{\tau}{2}\right) x^*\left(t - \frac{\tau}{2}\right) e^{-j2\pi f\tau} d\tau \quad (34)$$

where $*$ denotes complex conjugation. The term $g(t)$ represents performing a convolution (smoothing) in time. Whereas, the term $H(f)$ represents spectral smoothing of $g(t)$ using the FFT. Of utmost importance, by looking at the local features of the signal x in time t , SPWVD enables independent smoothing in time and in frequency ([Pola et al., 1996](#)); this is one of the notable advantages for why the SPWVD was performed herein. Further, because the SPWVD performs a smoothing in time and frequency, it thus attenuates interference terms – which can have negative values – that often complicate the interpretation of a distribution computed using the Wigner-Ville distribution (WVD) ([Cohen, 1995](#)). Moreover, it is important to remark that the SPWVD is superior at computing a high-resolution time-frequency representation of a signal compared to other methods such as the multitaper spectrogram (MTSP) ([Orini et al., 2012](#)), and short-time Fourier transform (STFT) (i.e., spectrogram) ([Ahmed, Djebbari and Benabdellah, 2018](#)).

Code 5.2: Computing the smoothed pseudo Wigner-Ville distribution (SPWVD).

```
% Compute the smoothed pseudo Wigner-Ville distribution
[d, f, t] = wvd(x, fs, "smoothedPseudo");
```

5.2.3 Symmetric Projection Attractor Reconstruction (SPAR)

To quantify and visualise ECG morphology and variability, I performed symmetric projection attractor reconstruction (SPAR) – a novel mathematical tool inspired by nonlinear dynamical systems, that transforms any approximately periodic signal into a two-dimensional (2D) representation (attractor) (Aston et al., 2014, 2018; Nandi, Venton and Aston, 2018; Nandi and Aston, 2020; Lyle and Aston, 2021). Importantly, in addition to using all of the available time series data, factoring out baseline variation, being robust to signal outliers, and computationally simplistic, the SPAR method has been shown to characterise dynamics of cardiovascular function different to standard methods, such as HRV (Aston et al., 2014). Moreover, this method has been demonstrated to work for ECG signals (Lyle et al., 2017).

Because SPAR transformation has been documented in detail previously (Aston et al., 2018; Lyle and Aston, 2021), it is described here in brief. Given an ECG time series $x(t)$ (Figure 19a), perform phase space reconstruction via Takens' delay coordinate embedding (Takens, 1981) with an embedding dimension of $N = 3$ to define (Aston et al., 2018)

$$y(t) = x(t - \tau), \quad z(t) = x(t - 2\tau), \quad (35)$$

where time delay $\tau > 0$ is defined as $1/N$ of the average cardiac cycle length (i.e., mean RR interval). To determine the average cardiac cycle length, we used the Pan-Tompkins algorithm (Pan and Tompkins, 1985) for QRS detection. Of note, while the average cycle length can be determined via QRS detection algorithms such as Pan-Tompkins for ECG signals; equally reliably, spectral decomposition using fft-based methods can be utilised, as shown in Code 5.3. Plotting the embedded points in phase

space results in a three-dimensional (3D) attractor (Figure 19b). Next, to remove baseline shift – for example, which may result from respiration and movement – the 3D reconstructed attractor is projected onto a plane (v, w) that is orthogonal to the vector $[1, 1, 1]$ via (Aston et al., 2018):

$$v = \frac{1}{\sqrt{6}}(x + y - 2z), \quad w = \frac{1}{\sqrt{2}}(x - y). \quad (36)$$

Plotting (v, w) generates a 2D attractor as depicted in Figure 19c. Masked in this 2D attractor, is information about the degree of overlap between trajectories of the embedded points; to reveal this information, we derived a density (i.e., heatmap) from the observed attractor as shown in Figure 19d. To interpret the 2D attractor with overlaid density (Figure 19d), the red colour indicates regions that are visited more frequently (high density), whereas the less frequently visited (low density) regions tend to a blue colour.

Code 5.3: MATLAB code to compute average cycle length (ACL) via the Fourier transform.

```
ecgnorm = ecg - mean(ecg);

[pxx, f] = periodogram(ecgnorm, [], [], fs);

[pk, maxFreq] = findpeaks(pxx, NPeaks=1, SortStr="descend");
acl = 1/f(maxFreq);

figure, hold on
plot(f, pxx)
plot(f(maxFreq), pk, "o")

xlim([0 10])
xlabel("Frequency"), ylabel("Magnitude")
```

Since the ECG is a complex waveform, hereinafter I perform SPAR via the generalised implementation presented in Lyle and Aston (2021). Using this advanced implementation, an ECG time series $x(t)$ with period T is embedded into $N \geq 3$ dimensions using the time delay $\tau = T/N$ by the coordinates $x_{N,j}(t) = x(t - j\tau)$, $j = 0, \dots, N - 1$; next Lyle and Aston (2021), define the $a_{N,k}(t)$ and $b_{N,k}(t)$ coordinates as

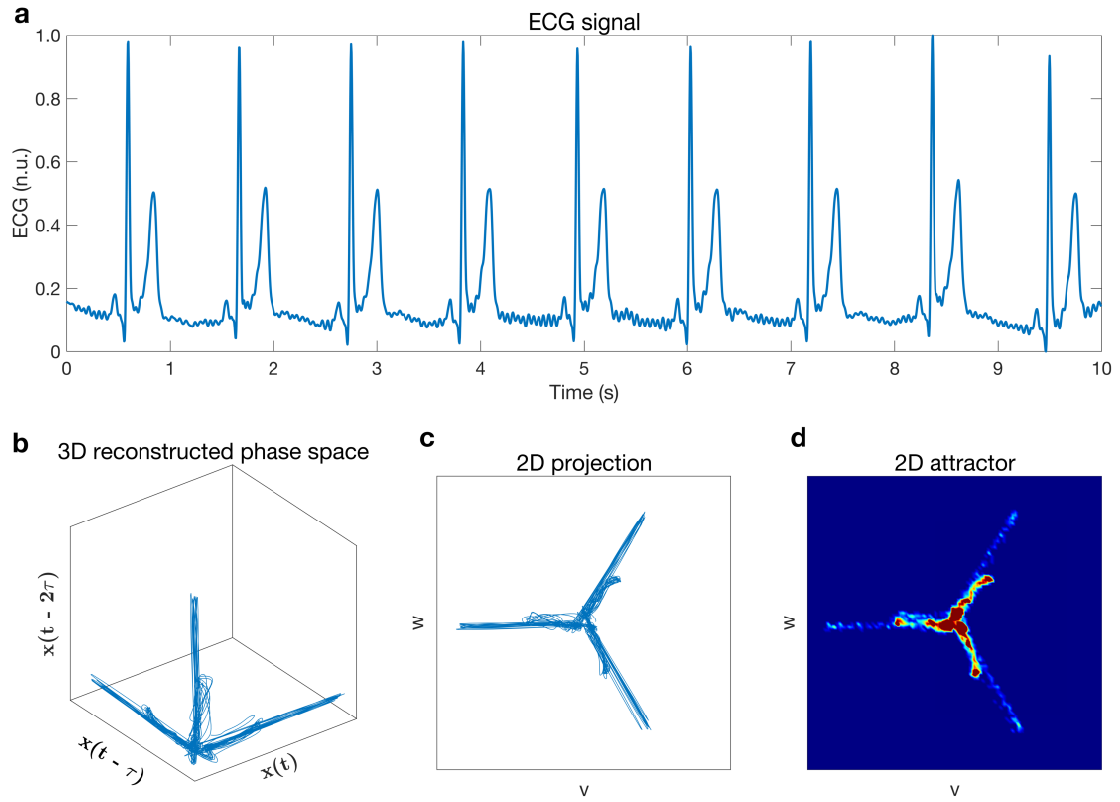


Figure 19: Generation of a two-dimensional (2D) attractor from an electrocardiogram (ECG) signal. (a) A 10 s ECG signal for one example participant. (b) A three-dimensional (3D) reconstructed attractor for $N = 3$ embedding using Takens' delay coordinates. (c) A 3D reconstructed attractor projected onto a plane (v, w) perpendicular to the vector $[1, 1, 1]$. (d) A 2D attractor overlaid with a density (i.e., heatmap). Reproduced from [Molefi, McLoughlin and Palaniappan \(2024\)](#).

$$\begin{aligned}
 a_{N,k}(t) &= \frac{1}{\sqrt{N}} \sum_{j=0}^{N-1} \cos(2\pi jk/N) x_{N,j}(t), \\
 b_{N,k}(t) &= -\frac{1}{\sqrt{N}} \sum_{j=0}^{N-1} \sin(2\pi jk/N) x_{N,j}(t)
 \end{aligned} \tag{37}$$

for $k = 1, \dots, \lfloor (N-1)/2 \rfloor$. Throughout this chapter and the next (i.e., [Using Supervised Learning to Predict Motion-Induced Nausea, and Effects of taVNS](#)), I use $k = 1$ for all embedding projections. [Figure 20](#) shows example attractors obtained via this higher embedding dimensional implementation. As a side note, the SPAR method

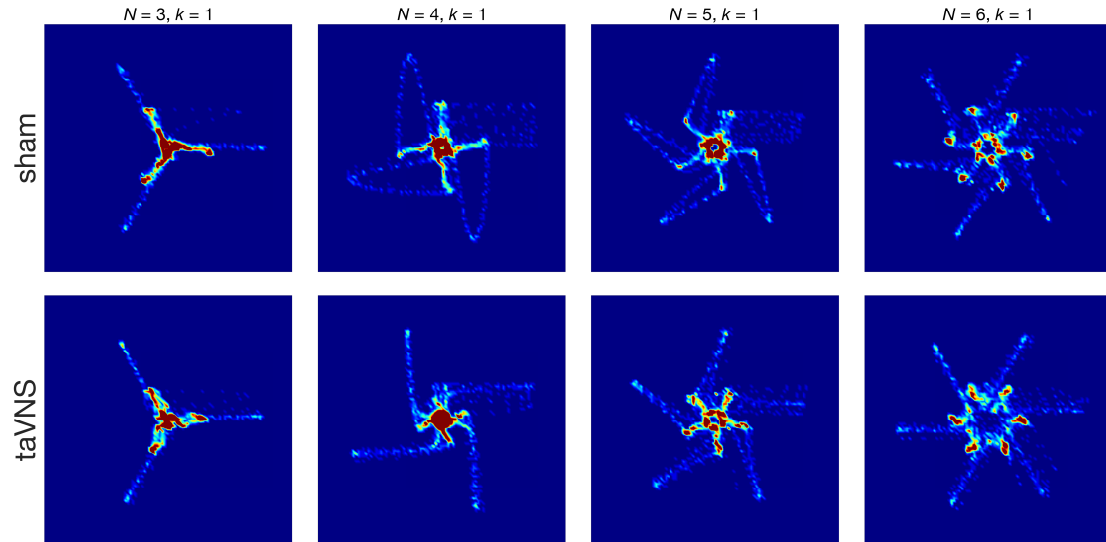


Figure 20: Electrocardiogram (ECG)-derived symmetric projection attractor reconstruction (SPAR) images in response to sham and taVNS. (**sham**) The (N, k) attractors generated from a 10 s ECG signal of one example participant for $N = 3, 4, 5, 6$ embeddings from sham condition, (**taVNS**) and taVNS condition. Reproduced from [Molefi, McLoughlin and Palaniappan \(2024\)](#).

in this extended implementation can also be interpreted from the perspective of applying the discrete Fourier transform (DFT) to the time delay coordinates; including from the context of the Koopman operator theory ([Rowley et al., 2009](#); [Arbabi and Mezic, 2017](#)). For SPAR quantitative analyses, I derived the radial density distribution (r density), θ density distribution (θ density), and attractor outline r from the obtained attractors (see [Figure 21](#)); herein, I work with the maximum values of these attractor measure set profiles, including the maximum density of the attractor (maximal density).

5.2.4 Statistical Analysis

All statistical analyses were performed using MATLAB (R2022b, R2023a, and R2024a). I report data as median and quartiles, or mean \pm standard error of the mean (SEM). Paired-sample tests were used for comparisons including HRV and SPAR parameters (Student's t -test) and for MSAQ and SSQ scores (Wilcoxon signed rank test). I

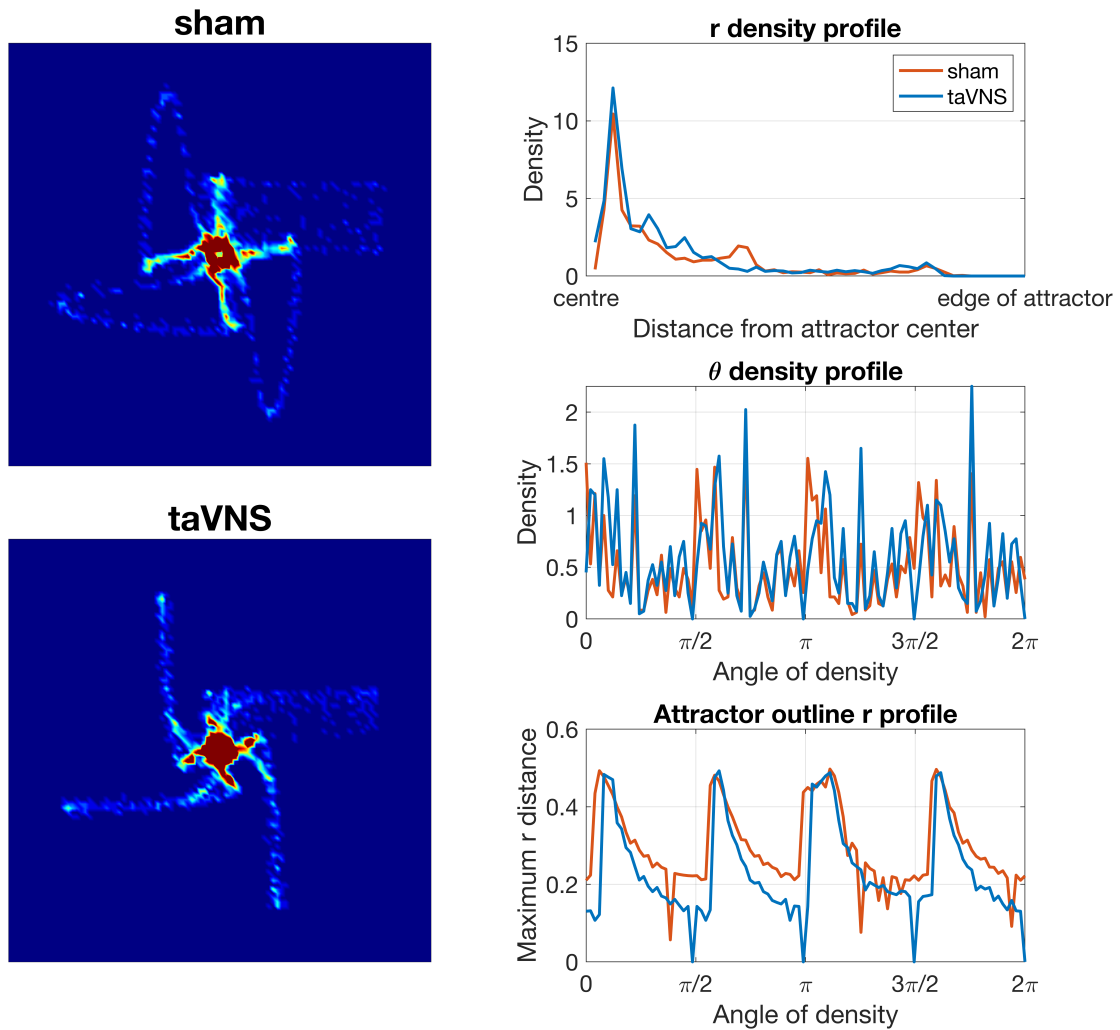


Figure 21: Example attractors for embedding dimensions $N = 4$, derived from electrocardiogram (ECG) signals of a participant at sham and taVNS conditions (**left**), and respective attractor measures including the radial density distribution (r density), θ density distribution (θ density), and attractor outline r from the obtained attractors (**right**).

computed Pearson's correlation coefficient (expressed as Pearson r) for normally distributed data; and Spearman's rank correlation coefficient (expressed as Spearman ρ) for non-normally distributed data. Time-frequency representations (TFR) of SPWVD were examined using non-parametric permutation-based statistics. I note that the idea of permutation-based statistics is heavily used in neuroscience; however, the methods are amenable to statistical analysis of time-frequency matrices. Early, neuroscience

focused research comprehensively detailed the theory and justifications of permutation statistics (Cohen, 2014; Nichols and Holmes, 2002). All permutation-based statistical tests were two-tailed. At the participant level, I examined TFR power using pixel-based permutation statistics (i.e., to correct for multiple comparisons). At each of the 1000 random permutations, I extracted the two most extreme values (i.e., minimum and maximum) from the TFR difference matrix to generate a null distribution. Then the threshold was determined by taking the 2.5th and 97.5th percentiles from the distribution, applying $p = 0.05$. Clusters found using this statistical method can be observed in (Figure 22c). To examine the differences in the time-frequency representations of SPWVD at the sample level, I used non-parametric cluster-based permutation tests (Maris and Oostenveld, 2007). From the basis of a significance threshold at ($p = 0.05$), I computed a z-value, which, in turn, was used to threshold the z-transformed time-frequency power difference between verum and sham condition. To generate a null distribution, I performed 1000 random permutations, where at each permutation extracting the maximum cluster mean of the z-values. Our pilot analysis is based on discussing the temporal clusters found as shown in (Figure 23b). However, it is worthy of caution that clusters identified using this method may represent effects detected though maybe not supported by the permutation test (Sassenhagen and Draschkow, 2019). A difference worthy of note between cluster and extreme-pixel correction is that, cluster correction tends to support bigger clusters. Whereas, pixel-based correction is more stringent though it can detect smaller clusters or single pixels. Hence, our rationale for using cluster correction at the sample level. Normality tests were performed using the Shapiro-Wilk test (Shapiro and Wilk, 1965). Aside from our pilot data, all statistical tests were two-tailed at ($p < 0.05$).

5.3 Results

5.3.1 HRV Responses to Motion-Induced Nausea

To establish the physiological effect of the nauseogenic stimulation on motion sickness induction, I evaluated HRV temporal and spectral parameters in a pilot study sample of

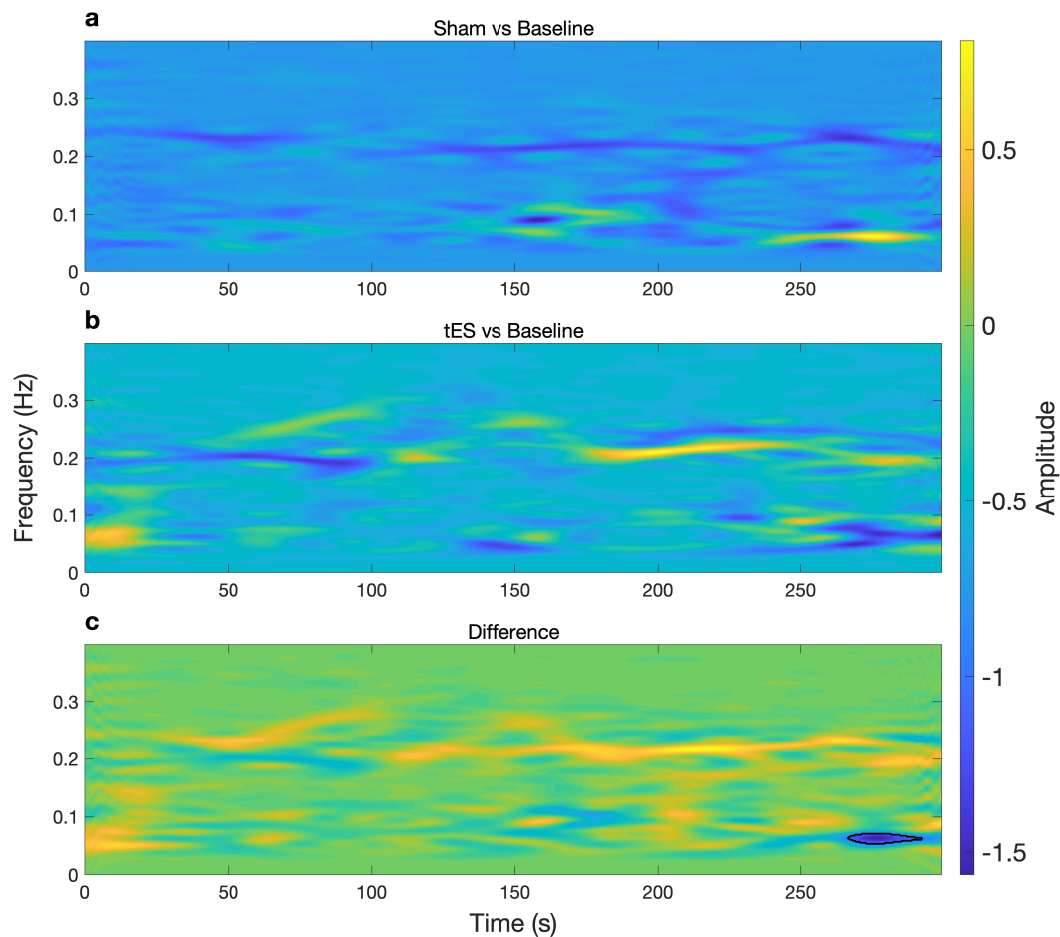


Figure 22: Time-varying power representations of heart rate variability (HRV) using the smoothed pseudo Wigner-Ville distribution (SPWVD) for an example participant. **(a)** Time-frequency power during sham (baseline subtracted) condition **(b)** and tES (baseline subtracted) condition. **(c)** Shows the time-frequency power difference between (Sham vs Baseline) and (tES vs Baseline). A statistical pixel-based permutation test using a pixel-level significance threshold of $p < 0.05$ revealed 1 cluster around 270-290 s (two-tailed non-parametric permutation tests). The significant cluster (region) is outlined by a black contour in **(c)**. Reproduced from [Molefi, McLoughlin and Palaniappan \(2023a\)](#).

14 participants; differences in these parameters were compared by contrasting nausea state against baseline. In line with previous reports ([Cowings et al., 1986](#); [Holmes and Griffin, 2001](#); [LaCount et al., 2009](#); [Kim et al., 2011](#)), I observed marked increases in HR during motion sickness-induced nausea as compared to baseline state ([Table 17](#)).

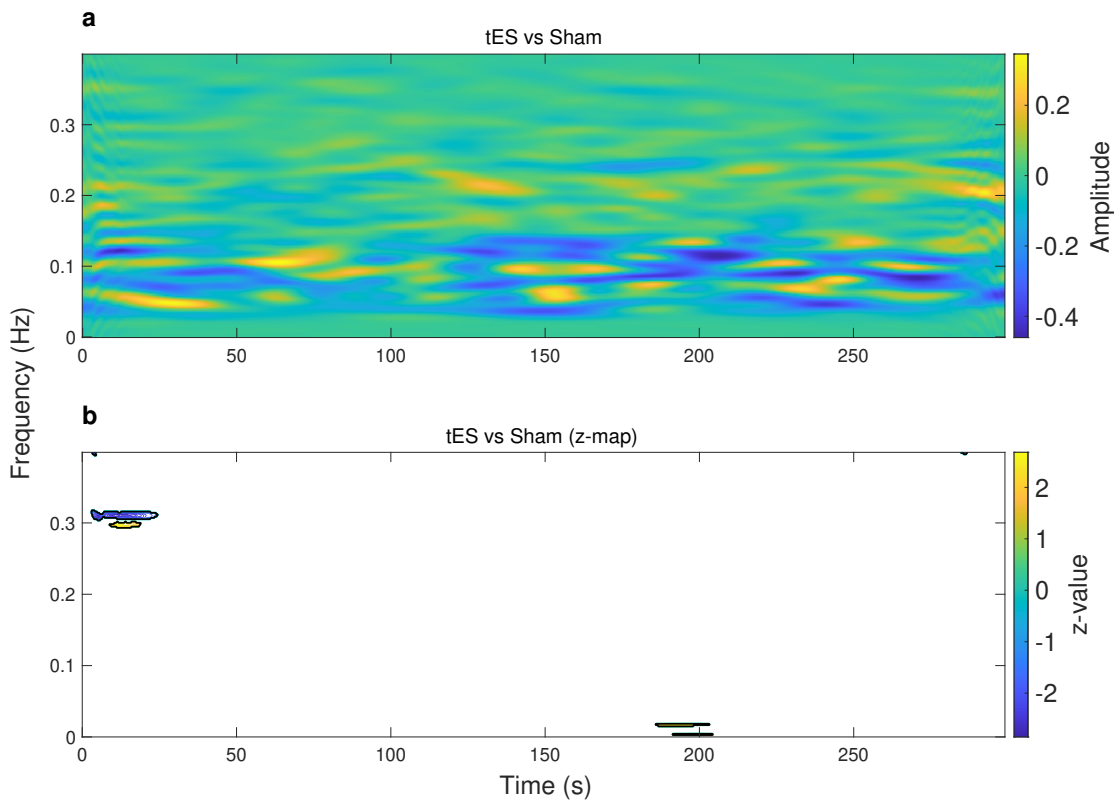


Figure 23: Time-varying power representations of heart rate variability (HRV) using the smoothed pseudo Wigner-Ville distribution (SPWVD) at the sample level. **(a)** Time-frequency power representation showing the power differences in tES and sham condition (after baseline subtraction within each condition). **(b)** Statistical z-map of the time-frequency power representation at the sample level, based on a cluster-level significance threshold $p < 0.05$ (two-tailed non-parametric permutation tests). Significant clusters (regions) are indicated by black contours on the statistical z-map. Reproduced from [Molefi, McLoughlin and Palaniappan \(2023a\)](#).

Moreover, I found that in the presence of nauseogenic stimulation, participants exhibited greater levels of overall HRV as measured by SDNN ([Table 17](#)); a similar observation was reported by [Park et al. \(2014\)](#), wherein motion sickness was induced via a 3D video. There was also a trend toward reduced parasympathetic neural activity in response to motion-induced nausea as quantified by the RMSSD; however, this was not significant ([Table 17](#)).

All HRV spectral parameters revealed marked differences during nausea compared to baseline; more specifically, I observed increases in normalised LF power and LF/HF ratio, and a reduction in normalised HF power ([Table 17](#)) – consistent with previous

Table 17: A summary of the results. Data are mean \pm SEM. Adapted from [Molefi, McLoughlin and Palaniappan \(2023c\)](#).

Autonomic parameters	Baseline	Nausea	p-value
HR (bpm)	70.06 \pm 2.91	72.57 \pm 2.73	0.0258
SDNN (ms)	62.07 \pm 6.94	73.14 \pm 8.09	0.0136
RMSSD (ms)	53.45 \pm 7.68	50.04 \pm 7.29	0.0962
LF (n.u.)	46.26 \pm 4.91	60.82 \pm 6.02	0.0021
HF (n.u.)	53.74 \pm 4.91	39.18 \pm 6.02	0.0021
LF/HF (ln)	-0.19 \pm 0.23	0.49 \pm 0.29	0.0026
SDNN/RMSSD	1.24 \pm 0.09	1.57 \pm 0.13	0.0006
CSI	2.25 \pm 0.19	2.97 \pm 0.27	0.0005
CVI	3.39 \pm 0.10	3.45 \pm 0.09	0.1082
SampEn	1.67 \pm 0.06	1.52 \pm 0.08	0.0275
FuzzyEn	1.27 \pm 0.05	1.14 \pm 0.06	0.0006
LLE	0.67 \pm 0.01	0.64 \pm 0.01	0.0004

studies ([Yokota et al., 2005](#); [Kim et al., 2011](#); [Lin et al., 2011](#); [LaCount et al., 2011](#)). These results suggest that nauseogenic stimulation reliably induces marked physiological arousal in healthy humans.

I then extended my analyses to use Poincaré maps to evaluate whether nonlinear HRV dynamics were characterised differently during motion-induced nausea compared to baseline. [Figure 24](#) shows the resulting topography of autonomic dynamics for two example participants; visually, nauseogenic stimulation produced ellipsoids with a longer and narrower area, portraying a “cigar shape” – which is indicative of increased sympathetic neural response. An average over all participants revealed a pronounced difference in CSI ([Table 17](#)) – a Poincaré quantitative marker of sympathetic activation. This is consistent with work demonstrating increased CSI response during motion sickness induced via a motion video ([Farmer et al., 2015](#)). I observed no significant differences between motion-induced nausea and baseline for CVI ([Table 17](#)).

Next, I investigated whether nauseogenic stimulation changed measures of physiologic complexity and chaos, as compared with baseline. I observed that during motion-induced nausea, participants exhibited a high degree of regularity; that is, lower values of SampEn and FuzzyEn, compared to baseline ([Table 17](#) and [Figure 25ab](#)). All values of the LLE were positive; a feature of physiologic chaos. Contrasting LLE responses at

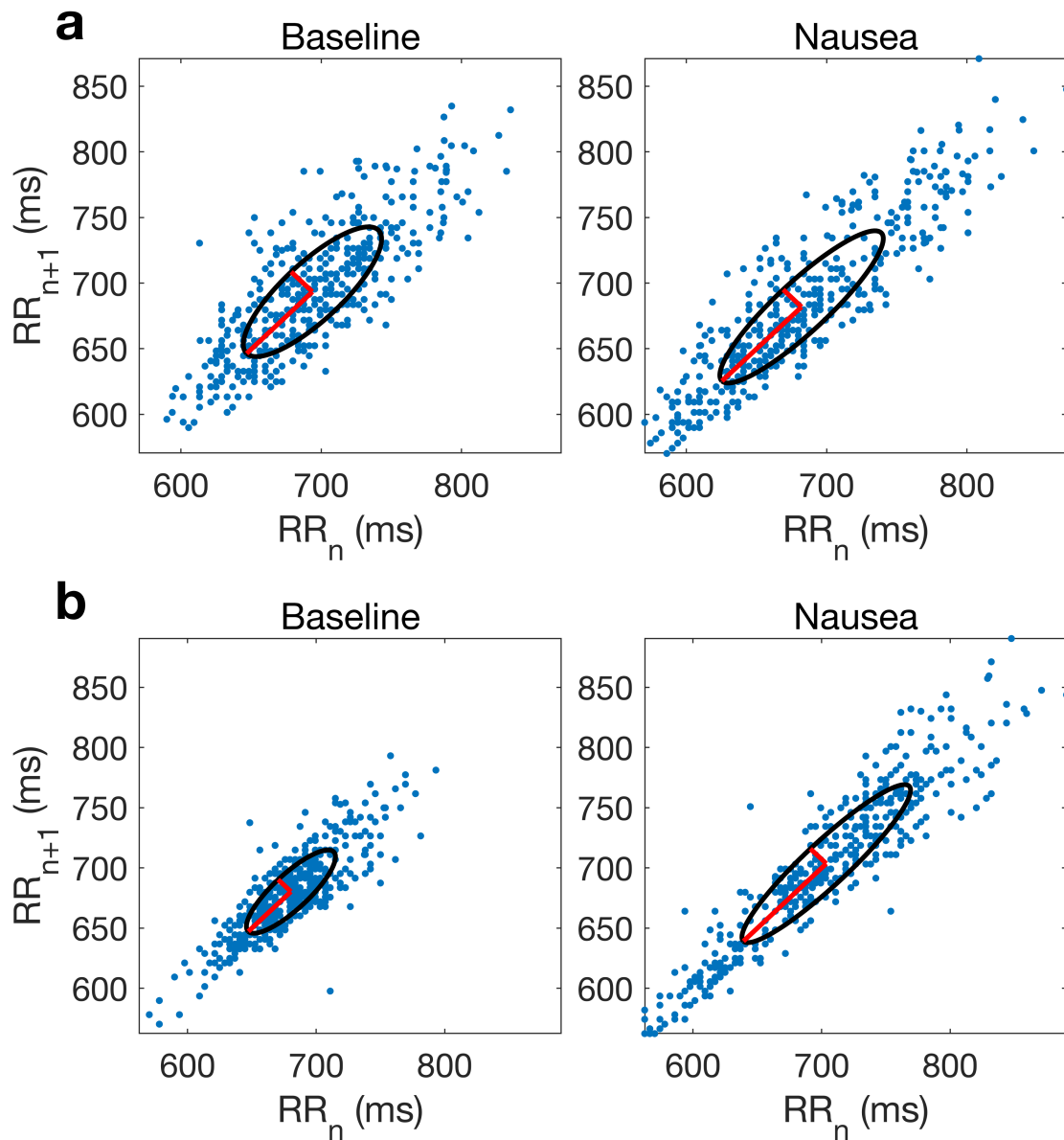


Figure 24: Poincaré plots illustrations for Baseline and Nausea states for two example participants. Reproduced and rearranged from [Molefi, McLoughlin and Palaniappan \(2023c\)](#).

baseline with those during nausea state showed significantly reduced chaos activity in the physiology of the participants ([Table 17](#) and [Figure 25c](#)).

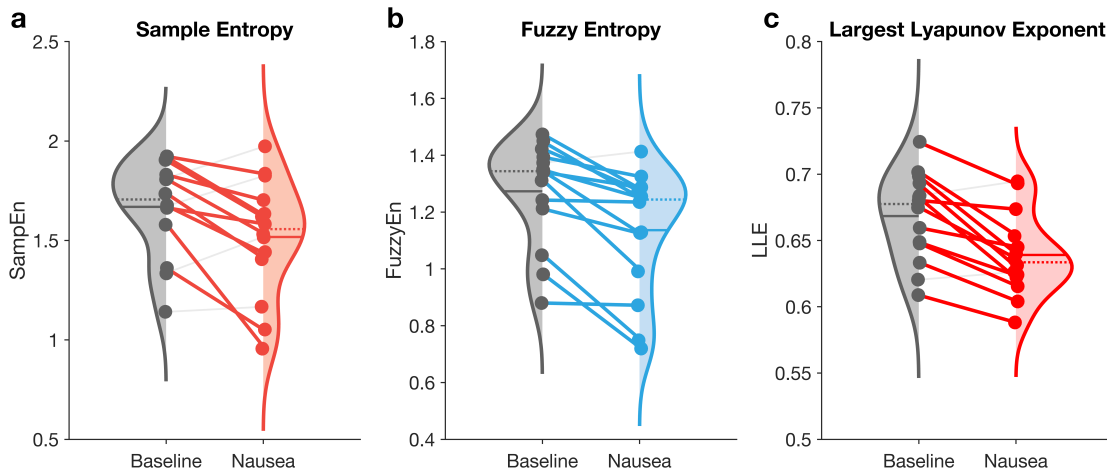


Figure 25: Nonlinear HRV comparisons for Baseline and Nausea states for all participants ($n = 14$) (a) Sample entropy (SampEn), (b) Fuzzy entropy (FuzzyEn), (c) Largest Lyapunov exponent (LLE). Adapted from a poster for Molefi, McLoughlin and Palaniappan (2023c).

5.3.2 Effects of taVNS on HRV for Motion-Induced Nausea

Compared to sham, taVNS demonstrated increased parasympathetic neural activity as assessed by RMSSD ($t = -2.09$, $p = 0.0451$), pNN20 ($z = -2.43$, $p = 0.0151$), and pNN50 ($z = -2.39$, $p = 0.0167$) (Figure 26). Furthermore, I observed a taVNS-induced differential increase in HF power ($z = -2.06$, $p = 0.0397$; Figure 26), in comparison to sham. Notably, these results suggest that stimulating the tragus of the left ear increases vagal tone.

In addition to the traditional time- and frequency-domain analysis, I compared HRV nonlinear measure changes of taVNS to sham; preliminary evidence of reduced physiologic complexity and chaos was reported by in a pilot study of healthy participants undergoing nauseogenic stimulation (HRV Responses to Motion-Induced Nausea; Molefi, McLoughlin and Palaniappan, 2023c). Both the SampEn and FuzzyEn – indicators of HRV regularity and complexity – did not show significant differences between the two conditions; this is unsurprising since these measures share methodological resemblance. However, I observed a taVNS-related marked increase in the values of the LLE, suggesting that taVNS may have a role in normalising the level of chaos in autonomic function.

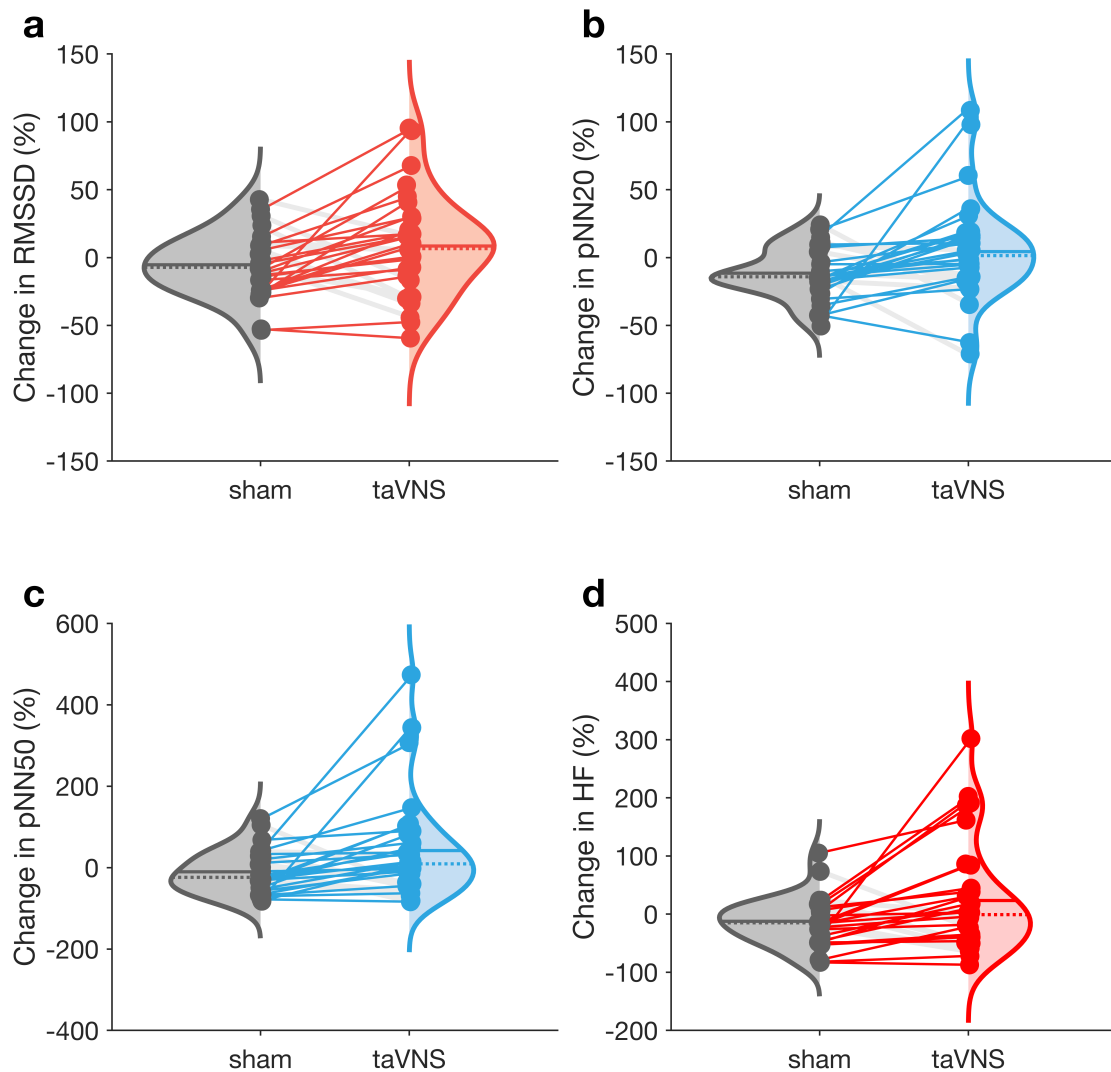


Figure 26: Time- and frequency-domain HRV comparisons for sham and taVNS conditions for all participants ($n = 32$) **(a)** Root mean square of successive differences of NN intervals (RMSSD), **(b)** Percentage of successive NN intervals that differ by > 20 ms (pNN20), **(c)** Percentage of successive NN intervals that differ by > 50 ms (pNN50), **(d)** high frequency HRV power (HF).

5.3.3 Differential Effects of taVNS for Motion Sickness on ECG SPAR Transforms

Further investigating taVNS-induced effects, I demonstrate that when comparing quantitative measures of ECG-derived attractor images (see [Figure 20](#)), including the radial

(r) density, theta (θ) density, attractor r outline, and maximal density across four attractor embedding dimensions (i.e., $N = 3, 4, 5, 6$), significant differences are revealed between taVNS and sham stimulation (Figure 27) ($n = 29$). I found significant differences between taVNS and sham in the attractor measures of $N = 3, 4, 5, 6$ embeddings during and following electrical stimulation. Specifically, marked reductions were observed for peak theta density ($t = 2.76$, $p = 0.0101$, $d = -0.83$; Figure 27b), and maximal density ($t = 2.42$, $p = 0.0223$, $d = -0.77$; Figure 27d) attractor measures but not for the peak radial density (Figure 27a) and peak attractor outline (Figure 27c) during taVNS versus sham.

Furthermore, attractor measures following taVNS and sham administration revealed taVNS-induced reductions in peak radial density ($t = 2.13$, $p = 0.0417$, $d = -0.41$; Figure 27e), peak theta density ($t = 2.91$, $p = 0.0069$, $d = -0.95$; Figure 27f), and maximal density ($t = 2.47$, $p = 0.0199$, $d = -0.66$; Figure 27h); but no difference was observed for peak attractor outline responses (Figure 27g).

For additional analyses, I computed correlations between changes in SSQ nausea scores and MSB scores, and changes in attractor measures that revealed marked significance. Maximal density during taVNS versus sham demonstrated a high positive correlation with MSB (Spearman $\rho = 0.52$, $p = 0.0040$); however, this significance was not observed for the post-stimulation interval. I also found a marked negative correlation between peak theta density for post-taVNS versus post-sham with SSQ nausea scores.

5.4 Discussion

Here I examined how HRV dynamics, and ECG morphology and variability of healthy human volunteers change during and following either active taVNS or sham administration concurrent with nauseogenic stimulation. My findings reveal that when taVNS is administered at the tragus of the left ear during motion-induced nausea, it induces a differential increase in markers of parasympathetic neural activity including RMSSD, pNN20, pNN50, and HF power, in comparison to sham stimulation at the left earlobe.

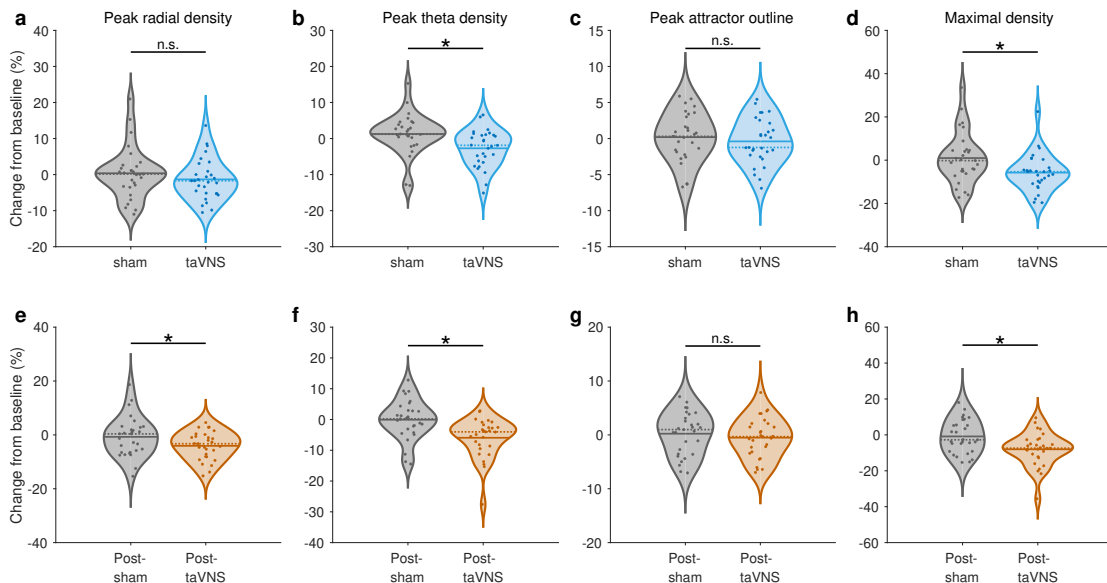


Figure 27: Attractor features show marked reductions by taVNS versus sham stimulation. (a-d) Violin plots showing attractor measures as percentage change from baseline across all participants for $N = 3, 4, 5, 6$ embeddings during sham and taVNS administration. (e-h) And following sham and taVNS administration. Solid lines indicate mean; dashed lines indicate median. n.s., not significant. Reproduced from [Molefi, McLoughlin and Palaniappan \(2024\)](#).

Furthermore, taVNS demonstrated a marked increase in the level of physiologic chaos, as measured by the LLE. Moreover, I demonstrate here for the first time that ECG-derived SPAR transforms can differentiate the effects of taVNS on ECG morphology and variability from sham stimulation, suggesting SPAR as a useful quantification and visualisation tool to assay taVNS effects on the ECG – both for motion-induced nausea and other conditions where taVNS is being applied.

I found that taVNS administration, when compared to sham stimulation, demonstrated an increase in all of the HRV measures that have long been suggested to be reflective of cardiac vagal tone ([Figure 26](#)). These differential effects are in line with previous results showing that HRV measures including RMSSD, pNN50, and HF power are significantly augmented by taVNS in healthy individuals ([Keute et al., 2021](#); [Geng et al., 2022](#); [Maestri et al., 2024](#)). Here I additionally show that pNN20 – a statistic of the pNNx family that has been demonstrated to show profound sensitivity in differentiating normal and pathological conditions ([Mietus et al., 2002](#)) – captures the effects of

taVNS in individuals provoked with a nauseogenic stimulus. We have long known that RMSSD and pNN50 are highly correlated; and that both these measures have a strong link with HF power (Kleiger, Stein and Bigger Jr, 2005). It is thus not surprising that all revealed a differential response to taVNS. Interestingly, that I observed a marked change in pNN20 in tandem, suggests consistency in my observed taVNS-induced effects, in addition to the implication that this measure may play an important role as a physiological readout for activation of the vagus nerve. Taken together, my findings suggest an increase in parasympathetic neural activity induced by acute taVNS during nauseogenic stimulation. Importantly, indicating that autonomic neural modulation via taVNS may maintain or restore autonomic balance to desirable levels; thus, pivotal in states of increasing levels of motion-induced nausea where perturbations in autonomic balance are observed.

In addition to showing that taVNS evokes elevated levels of parasympathetic tone during motion-induced malaise, I found that participants also exhibited greater levels of physiological chaos with taVNS versus sham. It has long been suggested that healthy heart rate dynamics are complex, and chaotic (Goldberger, Rigney and West, 1990). In other words, perturbed cardiac physiology reveals autonomic nervous system dynamics that are less complex – and susceptible to a decline in adaptive capacity. Indeed, early evidence implicated aging and disease with negative affect on physiologic complexity (Lipsitz and Goldberger, 1992). Contributing to this notion, this work previously demonstrated that participants exposed to a nauseogenic visual stimulus showed a marked reduction in physiological chaos (Molefi, McLoughlin and Palaniappan, 2023c). Suggesting that the aversive experience of motion-induced nausea denatures the intrinsic variability of autonomic control; thereby, reducing its coping mechanism. My observation that taVNS leads to increased physiological chaos during exposure to nauseogenic stimulation suggests that participants had improved capacity to offset motion sickness symptom severity.

One of the most novel findings in this work is the differential effects revealed by ECG-derived attractor measures during and following the administration of taVNS versus sham. taVNS (20 Hz) administration has been demonstrated previously to prolong

sinus cycle length in atrial fibrillation ([Stavrakis et al., 2015](#)); most importantly, suggesting that transcutaneous electrical stimulation of the auricular branch of the vagus nerve at the tragus leads to alterations in ECG morphology (shape) and variability. Herein, by using SPAR, I was able to show that taVNS differential effects on ECG shape may be indexed by ECG-derived attractor measures ([Figure 27](#)); in turn, providing initial insights for the hypothesis that this analytical tool may play an important role in facilitating evaluation of taVNS-induced effects on ANS function.

While I found significant alterations in peak radial density post-stimulation to suggest that taVNS attractors had lower density compared to sham, peak theta density appeared to be the most sensitive measure of taVNS response, showing large effect sizes (robust Cohen's $d > 0.8$) in taVNS-induced reductions in attractor density both during and following stimulation. Furthermore, I observed a marked relationship between the peak theta density metric and a significant reduction in motion sickness severity symptoms (as measured by SSQ nausea scores), suggesting that reduced attractor density may be a reliable physiological readout of taVNS for motion-induced nausea management. Previous work considered higher attractor densities to convey dynamics in ECG T wave morphology ([Lyle et al., 2017](#)); hence, I surmise here that taVNS may be inducing shifts in ECG T wave morphology and, in turn, ventricular repolarization, thus providing a mechanism by which participants experience less severe malaise with taVNS in contrast to sham.

My data additionally indicate that taVNS consistently reduced maximal density of the attractors both during and following stimulation ([Figure 27d, h](#)). Importantly, this finding is consistent with evidence showing significantly lower attractor maximal density during vasodilation ([Thanaj, Chipperfield and Clough, 2019](#)). Moreover, prior work demonstrated that undergoing a head-up tilt of 60 degrees increases maximal density ([Nandi and Aston, 2020](#)); although the sample size was small, the authors suggested that this increase was reflective of reduced waveform variability. From this finding, it can be inferred that taVNS may be promoting increased ECG variability, suggesting potential physiologic utility in taVNS for motion-induced nausea. Together, this also suggests a plausible explanation for the peak radial density observation discussed

above.

5.5 Conclusion

My studies provide initial evidence to suggest that taVNS could be a potent therapeutic for visually induced motion sickness. However, this will need to be confirmed in future at-scale studies. Considering that currently the most effective non-pharmacological intervention for motion sickness is habituation ([Keshavarz and Golding, 2022](#)); these findings further suggest a notable step forward in addressing the critical unmet need for novel therapeutic options toward motion sickness management. My results also demonstrate that SPAR can successfully be applied to evaluate differential effects of taVNS therapy. Moreover and importantly, my results raise the possibility that taVNS may be beneficial for other sources of nausea – for example, chemotherapy-induced nausea.

Chapter 6

Using Supervised Learning to Predict Motion-Induced Nausea, and Effects of taVNS

6.1 Introduction

The electrocardiogram (ECG) is an essential tool for assessing the electrical activity of the heart; importantly, it provides detailed insights into the morphological characteristics of heart function and dysfunction. However, the ECG is limited in scope since most researchers in the vagus nerve stimulation (VNS) literature – for both invasive and non-invasive VNS modalities – utilise it to derive the heart rate variability (HRV) signal and, consequently, examine vagally-mediated HRV measures for insights into effective vagal stimulation; except for studies investigating conditions that have established morphological properties in the ECG, such as sudden cardiac death ([Schomer et al., 2014](#); [Verrier et al., 2016](#); [Pukropski et al., 2024](#)) and atrial fibrillation ([Stavrakis et al., 2015, 2020](#); [Kulkarni et al., 2021](#)). This work takes a different perspective to ECG time series analysis in tandem with machine learning (ML), with the aim of gaining insights into ECG morphology and variability through the use of the waveform data in its entirety, and thus, utilise the ECG to its maximum potential.

To the author's knowledge, only two other recent studies have investigated target engagement of afferent vagal pathways via non-invasive vagal stimulation using ML methods. In recent work using transcutaneous cervical VNS (tcVNS) for traumatic stress triggers, [Gurel et al. \(2020\)](#) examined whether biomedical sensing modalities including the ECG, photoplethysmogram (PPG), seismocardiogram (SCG), and respiratory effort (RSP), and physiological features extracted therein could determine the stimulation type – that is, active tcVNS or sham. Their study demonstrated that ECG-derived heart rate, PPG-derived vasomotor activity, and ECG- and PPG-obtained pulse arrival time, yielded sufficient information to detect target engagement of tcVNS in comparison to sham with an area under the receiver operating characteristic curve (AUC) of 0.96. In the study by [Tarasenko et al. \(2022\)](#), which examined transcutaneous auricular VNS (taVNS) on stress processing, the authors showed that an ML model trained on RR series data extracted from the ECG, and time traces of HRV-derived measures including the low frequency (LF) and high frequency (HF) power components, and their ratio, LF/HF, in addition to the standard deviation of NN intervals and the root mean square of successive differences of NN intervals (RMSSD), classified taVNS versus null stimulation with an accuracy of 70%.

Here, in lieu of utilising the ECG as a proxy for HRV signal derivation, I considered ECG time series directly; whereby, I leveraged the morphological properties of the ECG via the symmetric projection attractor reconstruction (SPAR) method. SPAR has been proposed as a technique capable of quantifying and visualising subtle differences in the ECG which are highlighted by the attractor. To recall from [Chapter 5](#), SPAR – a nonlinear dynamical systems-inspired mathematical tool – was originally introduced in [Aston et al. \(2018\)](#), extended by [Lyle and Aston \(2021\)](#), and described briefly herein [see [Symmetric Projection Attractor Reconstruction \(SPAR\)](#)]. Previous work has suggested that SPAR can be useful in investigating cardioactive drug effects of dofetilide from ECG recordings, especially when embedding in higher dimensions, given the complexity of the ECG signal ([Lyle, Nandi and Aston, 2019](#)). In another study, SPAR was employed to explore the changes of the microcirculatory dynamics and classify two haemodynamic steady states via linear discriminant analysis from blood flow

signals (Thanaj, Chipperfield and Clough, 2019). I have previously demonstrated the utility of SPAR to differentiate taVNS-driven effects from sham stimulation (Chapter 5). In this chapter, my focus was to investigate whether features extracted from ECG-derived attractor images could facilitate detection of electrical stimulation type – that is, active taVNS versus sham – and thus inform on stimulation delivery.

Additionally, I performed a set of experiments that were based on *transfer learning* – a widely used technique in deep learning applications – to determine ECG-derived attractors that show differential response to motion-induced nausea. In transfer learning, a model previously trained on a larger dataset is fine-tuned to learn a new task using a smaller amount of data (Weiss, Khoshgoftaar and Wang, 2016). Transfer learning plays an important role in healthcare because of limited datasets due to various reasons that include, most importantly, limited participant cohorts. Of note, parts of this chapter have been adapted from research previously described in Molefi and Palaniappan (2024) and Molefi, McLoughlin and Palaniappan (2024).

6.2 Experiment 1: Transfer Learning of Motion-Induced Nausea ECG SPAR Transforms

6.2.1 Methods

Here, I considered the dataset described in Table 18; these data are attractor images generated from ECG recordings of 12 participants at rest (i.e., baseline) and during nausea via SPAR transformation; for elaborate details on SPAR see *Symmetric Projection Attractor Reconstruction (SPAR)* in Chapter 5. It is important to note here that SPAR allows for subtle differences in the raw ECG time series to be highlighted through attractor reconstruction. That is, SPAR provides a good feature space for which better classification of the two states – baseline versus nausea – may be observed. Figure 28 shows an illustration of how an attractor image is generated from an ECG time series. Briefly, for an ECG time series $x(t)$, phase space reconstruction is performed based on Takens' delay coordinate embedding (Takens, 1981); for an N -dimensional phase

Table 18: Dataset description for [Experiment 1: Transfer Learning of Motion-Induced Nausea ECG SPAR Transforms](#); these data are attractor images computed from 10 s ECG signals obtained from 12 participants during states of “baseline” and “nausea” (see [Figure 28](#) for how an attractor image is computed from an ECG time series).

Participant	Baseline	Nausea	Baseline + Nausea
PT 01	18	18	36
PT 02	18	18	36
⋮	⋮	⋮	⋮
PT 12	18	18	36
$n = 12$	216	216	432

space, this procedure facilitates generation of N time series via $x_i(t) = x(t - (i - 1)\tau)$ for $i = 1, \dots, N$, where time delay τ is computed as $1/N$ of the mean cardiac cycle length. By projecting the reconstructed attractor onto a plane (v, w) orthogonal to the vector $[1, 1, 1]$, a two-dimensional (2D) attractor is obtained which when a density (i.e., heatmap) is applied to, can provide visually informative and quantifiable changes in ECG morphology and variability ([Aston et al., 2018](#); [Lyle and Aston, 2021](#)). For attractor generation, I considered embedding dimensions $N = 3, 4, 5, 6$; enabling the computation of attractors as displayed in [Figure 29](#). Prior to SPAR transformation, ECG epochs ($n = 432$) of 10 s duration were detrended, smoothed with a Savitzky-Golay filter, and range normalized to the interval $[0, 1]$. For each participant, there were 36 attractor images with 18 images per each state, that is, “baseline” and “nausea” ([Table 18](#)) – for each embedding dimension. The computed attractors were persisted to storage in portable network graphics (PNG) format with a resolution of 1000×1000 pixels and in colour to respectively prevent compression artefacts and ensure compatibility with some classification approaches I explored below (e.g., CNNs).

To examine whether computational models can differentiate normal ECG-derived attractors from those showing signs of malaise ([Figure 29](#)), I explored a number of approaches that accept images as input; some of these approaches were a novel analysis of attractor image data while others – for example, CNNs – had been previously demonstrated to have potential for classification of attractor images. The four approaches I considered are summarised below:

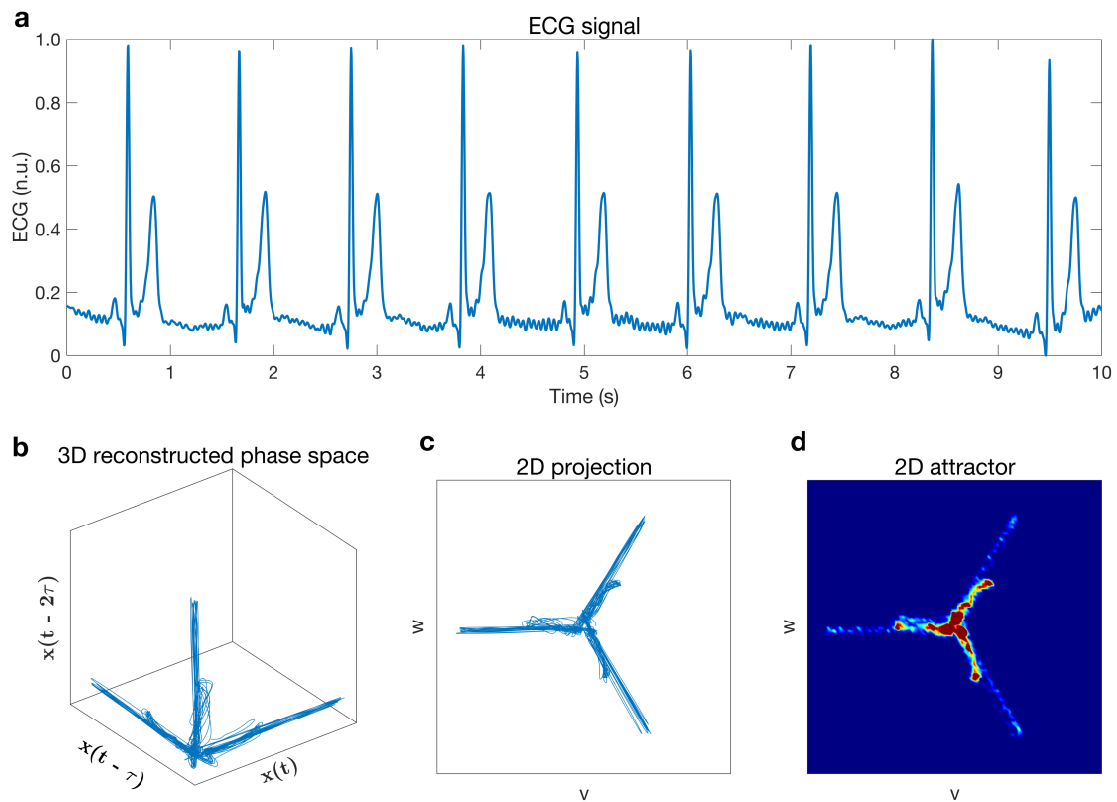


Figure 28: Generation of a two-dimensional (2D) attractor from an electrocardiogram (ECG) signal. (a) A 10 s ECG signal for one example participant. (b) A three-dimensional (3D) reconstructed attractor for $N = 3$ embedding using Takens' delay coordinates. (c) A 3D reconstructed attractor projected onto a plane (v, w) perpendicular to the vector $[1, 1, 1]$. (d) A 2D attractor overlaid with a density (i.e., heatmap). Reproduced from [Molefi, McLoughlin and Palaniappan \(2024\)](#).

Singular Value Decomposition (SVD)

The singular value decomposition (SVD) is a matrix factorisation that can be used to compute optimal, low-rank approximations ([Brunton and Kutz, 2019](#)). In addition, the SVD has an important role as a data reduction tool; in particular, as the underlying algorithm of principal component analysis (PCA). Previous work has demonstrated interesting properties of the SVD in the so-called eigenfaces example ([Turk and Pentland, 1991](#); [Swets and Weng, 1996](#); [Belhumeur, Hespanha and Kriegman, 1997](#); [Brunton and Kutz, 2019](#)); wherein the SVD is performed on a dataset of facial images to extract the most dominant correlations among the images of human faces. Akin to eigenfaces,

the aim here was to compute the SVD on the obtained attractor image data whereby, in this context, the SVD produces a low-rank embedding space that may enable differentiation of baseline versus nausea attractors. [Code 6.1](#) demonstrates example MATLAB code for computing such a low-rank embedding space or feature space for the SPAR transformed images using the MATLAB `svd` function. The data in the matrix U provide a coordinate system such that projecting an attractor image (from a baseline or nausea condition) onto the first r PCA modes – r here can be chosen by observing the singular values in the matrix S – enables a set of coordinates to be obtained. Importantly, projecting the attractor images from the conditions onto principal components that have captured the most useful features for telling the two conditions apart provides the basis for classification.

Code 6.1: Performing SVD on mean-subtracted attractor image data.

```
XData = [baselineAttractors nauseaAttractors];
X = XData - mean(XData(:));

% Perform singular value decomposition (SVD), such that X = U*S*V'
[U, S, V] = svd(X, "econ");
```

Bag of Features

Like the SVD, this was a novel approach to classification of SPAR transformed images between baseline and nausea. The notion here being to organise attractor images obtained at baseline and nausea conditions into baseline and nausea categories, respectively. Interpreting the attractor image data in this way allows for image category classification by creating a bag of features (or a bag of visual words) ([Csurka et al., 2004](#); [Nister and Stewenius, 2006](#)). This approach creates a vocabulary – or bag of features – via the speeded-up robust features (SURF) detector – as applied in this case – to extract features from the attractor images; and uses them to train an image category classifier. I implemented this by using the `bagOfFeatures` MATLAB function as shown in [Code 6.2](#).

Code 6.2: Attractor image category (baseline vs. nausea) classification using bag of features.

```
bag = bagOfFeatures(trainingData);  
categoryClassifier = trainImageCategoryClassifier(trainingData, bag);  
confusionMatrix = evaluate(categoryClassifier, testData);
```

Vision Transformer (ViT)

Here, I considered a pretrained vision transformer (ViT) neural network; which is a network model that encodes image inputs into feature vectors using the transformer architecture (Dosovitskiy, 2020). This network comprises two main components: the backbone performs feature extraction from the input images; and the classification head maps the extracted features to prediction scores. Fine-tuning of the model to perform classification on attractor image data was implemented using transfer learning; note that this technique is also used below when considering CNNs given the limited dataset. This was implemented by obtaining the ViT neural network using the `visionTransformer` MATLAB function, and fine-tuning only the attention layers and freezing the other learnable parameters (Touvron et al., 2022); training was performed using the `trainnet` function. Note that similar to the SVD and bag of features, the ViT approach was applied here to SPAR transformed images for the first time.

Convolutional Neural Networks (CNNs)

Deep convolutional neural networks (CNNs) have previously been demonstrated to have potential in attractor image classification (Aston et al., 2019; Venton et al., 2021). In particular, Aston et al. (2019) investigated the use of deep learning via transfer learning in classification of attractor images derived from ECG signals of wild-type and *Scn5a*^{+/-} mutant mice; their findings prompted me to investigate whether these methods could aid us gain insights into human data as well, especially given the complexity of motion-induced nausea. I considered a total of six pretrained deep neural networks from the MATLAB R2023b Deep Learning Toolbox™ (<https://github.com/matlab-deep-learning/MATLAB-Deep-Learning-Model-Hub>; The MathWorks, Inc., Natick, MA, USA); namely, the DenseNet-201 (Huang et al., 2017), ResNet-50 (He et al., 2016),

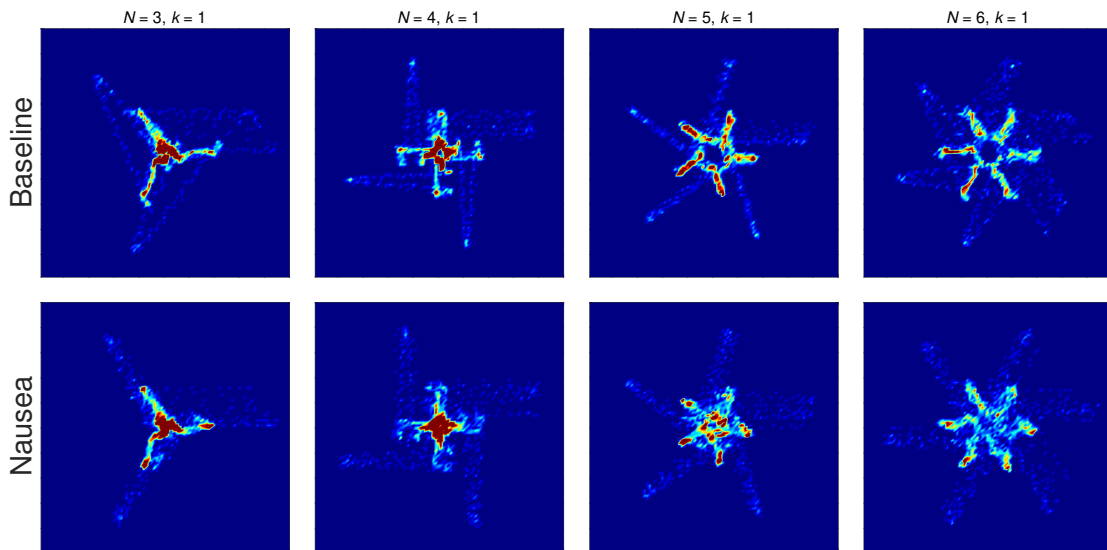


Figure 29: Example attractors for embedding dimensions $N = 3, 4, 5, 6$, generated from electrocardiogram (ECG) signals of a participant at baseline (i.e., rest) and during nausea states. Modified from [Molefi and Palaniappan \(2024\)](#).

ResNet-101 ([He et al., 2016](#)), Xception ([Chollet, 2017](#)), Inception-v3 ([Szegedy et al., 2016](#)), and Inception-ResNet-v2 ([Szegedy et al., 2017](#)) CNNs. Of all the approaches I investigated, this approach showed consistent results and thus, the ensuing methods, results, and discussion of this experiment will be based on analyses performed using this approach (i.e., using CNNs).

To perform transfer learning using the CNNs approach, I used augmented image datastores to automatically resize the attractor images to the input size of the of the respective network for compatibility (e.g., 224×224 for DenseNet-201); [Figure 30](#) illustrates the transfer learning workflow for this experiment. Because the last few layers (i.e., network head) of these network models are configured for 1000 classes, I fine-tuned these final layers for the new binary classification task (“baseline” and “nausea” classes); replacing the last layer with learnable weights with a new fully connected layer with an output size of 2 (setting the learning rate factor for weights and biases on this layer to 10; to learn faster). Additionally, I replaced the classification layer with a new one without class labels. For neural network training, I used the `trainNetwork` MATLAB (R2023b) function; of note, this function automatically sets the output classes of the classification layer during model training. It is also important to note that, at the

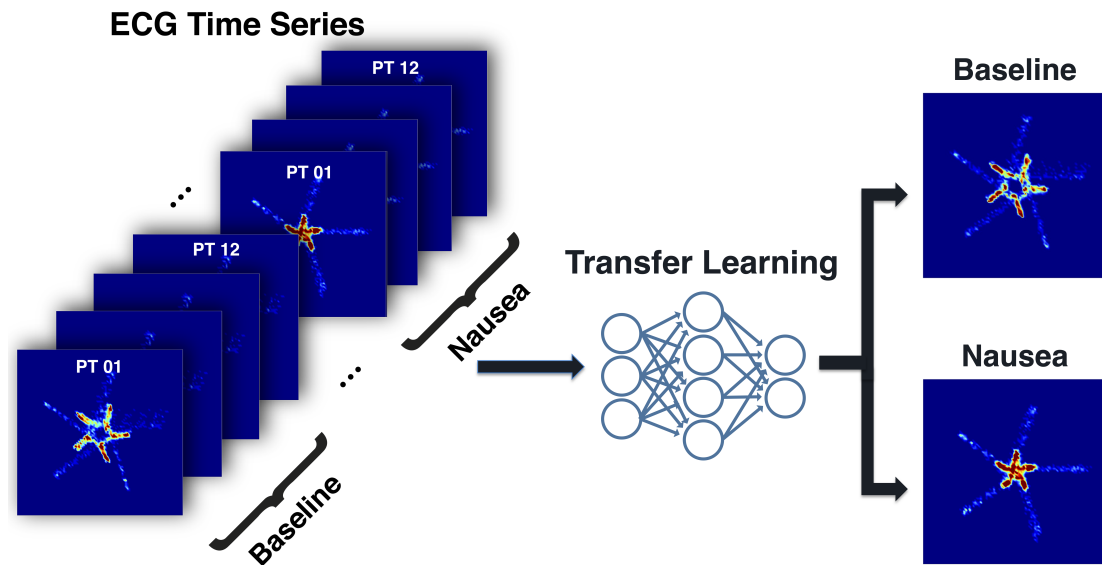


Figure 30: Deep transfer learning of ECG-derived attractor image data from ECG signals recorded at Baseline and Nausea states. Adapted from a poster for [Molefi and Palaniappan \(2024\)](#).

time of writing this, MATLAB no longer recommends using the `trainNetwork` function, and instead suggests using the updated function `trainnet` – which I used for the ViT neural network training above.

I utilized Bayesian optimization with 100 iterations to tune the hyperparameters (1) mini-batch size (`MiniBatchSize: [32 256]`); (2) initial learning rate (`InitialLearnRate: [1e-2 1]`); (3) contribution of previous parameter update step (`Momentum: [0.8 0.98]`); and factor for L_2 regularization (i.e., weight decay) (`L2Regularization: [1e-10 1e-2]`), using the stochastic gradient descent with momentum (SGDM) solver. These hyperparameters were tuned for each of the six pretrained deep neural networks mentioned above (i.e., ResNet-50, ResNet-101, DenseNet-201, Xception, Inception-v3, and Inception-ResNet-v2). To evaluate model performance and robustness, I implemented the leave-one-participant-out cross-validation (LOPOCV) procedure; whereby, I left out all images of one participant from the training images. This is of utmost importance to avoid biased classification performance. I iterated this procedure for each of the 12 participants in this experiment.

Experimental Setup. To conduct the experiments, I used the Hydra cluster – a server on the University of Kent School of Computing High Performance Computing facility – to execute MATLAB code scripts. To manage jobs within the cluster, I used the SLURM workload manager (<https://slurm.schedmd.com>); a Slurm script from one of my experiments to request the required GPU resources is presented in [Code 6.3](#). All transfer learning experiments were performed in MATLAB R2023b on a node consisting of a single 80GB NVIDIA A100 GPU.

Code 6.3: A Slurm script to request the required GPU resources.

```
#!/bin/bash

#SBATCH -p gpu
#SBATCH --gres=gpu:1
#SBATCH --mem=80G
#SBATCH --job-name=Seadragon
#SBATCH --output=Seadragon.txt
#SBATCH --mail-type=begin,end
#SBATCH --mail-user=em576@kent.ac.uk

matlab -nodisplay -batch em_seadragon
```

Statistical Analysis. All statistical analyses were performed using MATLAB (R2023b, and R2024a). Model performance optimization and evaluation were performed using Bayesian optimization and a LOPOCV procedure, respectively. I assessed the area under the receiver operating characteristic curve (AUC), which is a robust metric of classification performance; an AUC of 1 represents perfect classification and an AUC of 0.5 corresponds to random classification. The statistical property of the AUC is equivalent to the nonparametric Wilcoxon rank sum test; that is, representing the probability with which the model ranks a randomly chosen positive instance higher than a randomly chosen negative instance. Additional to ROC curve plots, I computed the accuracy performance metric; however, it should be noted that the AUC is a more useful measure of classification performance compared to accuracy. The accuracy performance metric in the standard way and also via a majority voting scheme whereby a condition (baseline or nausea) was correctly classified if the number of correctly classified

Table 19: Pretrained neural networks results for binary classifications at four attractor embedding dimensions, presented as accuracy % (top), majority vote % (bottom). Reproduced from [Molefi and Palaniappan \(2024\)](#).

Network	3	4	5	6
ResNet-50	67.13	69.21	68.52	68.98
	70.83	79.17	75.00	83.33
ResNet-101	69.21	70.37	65.51	67.59
	79.17	79.17	66.67	66.67
DenseNet-201	70.14	67.59	70.14	69.91
	75.00	70.83	79.17	79.17
Xception	65.05	66.44	62.50	65.28
	75.00	66.67	66.67	66.67
Inception-v3	67.82	67.13	62.04	66.20
	87.50	83.33	66.67	79.17
Inception-ResNet-v2	66.67	68.52	65.28	69.68
	70.83	83.33	66.67	70.83

attractor images was at least 19; recall that there are 18 attractor images per condition (see [Table 18](#)). Note that this approach of majority vote is based on previously described methods ([Aston et al., 2019](#); [Bonet-Luz et al., 2020](#); [Huang et al., 2022](#)).

6.2.2 Results

The binary image classification results of all the pretrained neural networks I studied for attractor image analysis are summarized in [Table 19](#); for each network, the top row presents scores using accuracy as a metric, whereas the bottom row shows accuracy scores using majority voting (see [Statistical Analysis](#) above for how this was implemented). [Figure 31](#) presents the ROC curves of all the networks for each of the four embedding dimensions. I observed that the DenseNet-201 network outperformed the other networks in detecting the response to motion-induced nausea as evaluated by accuracy for attractors generated using $N = 3, 5,$ and 6 points ([Table 19](#)). Using the AUC as a metric, I found that ResNet-50 and ResNet-101 both achieved AUC scores considered acceptable for 4-point attractors (AUC = 0.7091 and AUC = 0.7275, respectively; [Figure 31a, b](#)). Moreover, the DenseNet-201 model demonstrated acceptable AUCs for attractors computed using embedding dimensions

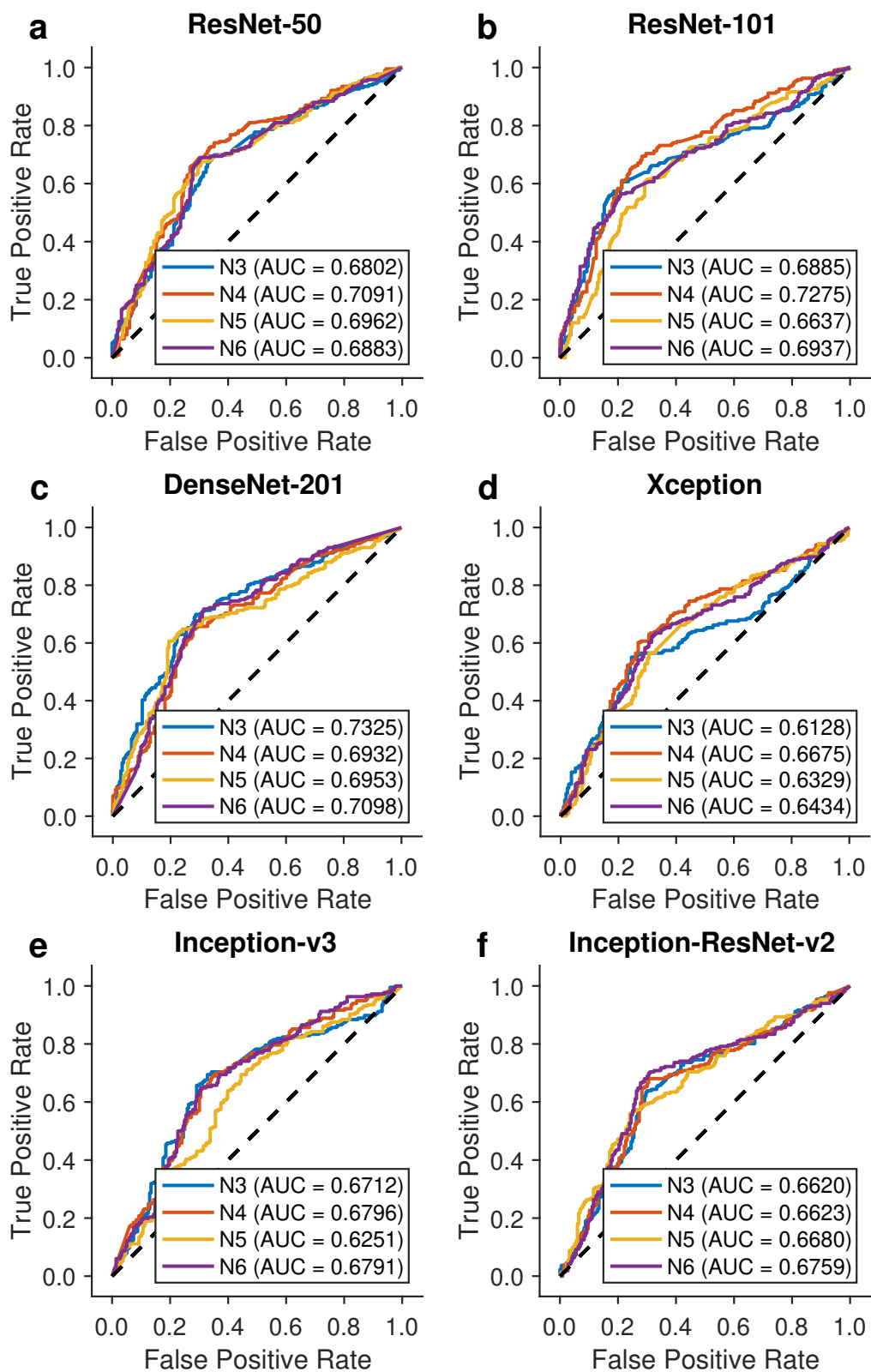


Figure 31: **(a-f)** ROC curves of all explored pretrained deep neural networks and embedding dimensions showing the true positive rate (TPR), or sensitivity, versus the false positive rate (FPR), or 1-specificity, for the “nausea” class. Reproduced from [Molefi and Palaniappan \(2024\)](#).

($N = 3$; AUC = 0.7325) and ($N = 6$; AUC = 0.7098) ([Figure 31c](#)). Xception, Inception-v3, and Inception-ResNet-v2 models showed the lowest AUC values across all embedding dimensions ([Figure 31d, e, f](#)), suggesting they were the least accurate at classifying malaise versus healthy.

In response to [Nauseogenic Stimulation](#), participants exhibited differential ECG morphology that could be distinctively discerned in the attractors. [Figure 29](#) summarises the attractor appearance – at four embedding dimensions, i.e., $N = 3, 4, 5, 6$ – of an example participant during states of rest (i.e., baseline; top row panels) and motion-induced nausea (bottom row panels). By performing visual examination of attractor appearance, I noted differential features of motion sickness-induced nausea ([Figure 29](#); Nausea panels) compared to rest ([Figure 29](#); Baseline panels). In particular, I observed that the arms of the (3,1) attractor at baseline are wider than those of the nausea (3,1) attractor ([Figure 29](#)). Moreover, the observation of a much greater visual distinction between baseline and nausea (5,1) attractors – portraying how baseline attractors are less dense near the center than their nausea counterparts ([Figure 29](#)) – may explain the respectable performance demonstrated by the DenseNet-201 network for $N = 5$ embedding, where it achieved 70.14% accuracy; whereas using majority vote as a metric, obtained 79.17% accuracy ([Table 19](#)).

6.3 Experiment 2: Detection of taVNS Response Using ECG SPAR-Based Features

6.3.1 Methods

[Table 20](#) displays a description of the dataset I considered for this experiment; these data are attractor images obtained from ECG recordings of 29 participants during a

Table 20: Dataset description for [Experiment 2: Detection of taVNS Response Using ECG SPAR-Based Features](#); these data are attractor images computed from 10 s ECG signals obtained from 29 participants during sham and taVNS conditions (see [Figure 28](#) for how an attractor image is computed from an ECG time series).

Participant	sham	taVNS	sham + taVNS
PT 01	30	30	60
PT 02	30	30	60
⋮	⋮	⋮	⋮
PT 29	30	30	60
$n = 29$	870	870	1740

sham and a taVNS condition. To generate these images, the raw ECG data were pre-processed by first applying a 4th-order Butterworth bandpass IIR filter between 0.5 and 30 Hz ([Dennison, Wisti and D’Zmura, 2016](#)) to eliminate baseline wander and muscle noise. Then, to remove electrical stimulation-evoked artifact, a Butterworth notch IIR filter was applied at 20 Hz. Zero-phase filtering was performed to avoid phase distortion. Finally, the artifact-free ECG time series were then used to extract 5 min epochs at “baseline” (prior to nauseogenic stimulus onset), and “stimulation” (prior to nauseogenic stimulus offset). Prior to performing SPAR, these de-noised ECG data were segmented into epochs of 10 s, and range normalized to the interval $[0, 1]$; then SPAR transformation was performed followed by generation of attractor profiles (for elaborate details, see the [Methods](#) section of [Chapter 5](#)). Following attractor profile generation, in addition to maximal density, I extracted the peak values of the radial density distribution, theta density distribution, and attractor outline in the θ direction, as attractor measures, according to previously described methods ([Lyle, Nandi and Aston, 2021](#)). Then I constructed attractor features for the classification task by deriving attractor measures obtained from the “stimulation” interval as percentage change from “baseline” attractor measures (for each participant at each condition, i.e., sham and taVNS). In other words, the attractor features were computed as $\Delta = 100((X - X_0)/X_0)$, where X denotes “stimulation” intervals, and X_0 denotes “baseline”.

For machine learning, I investigated a collection of classification-based models for detection of taVNS response using ECG SPAR-based features; a subset of these classification models were previously studied by [Gurel et al. \(2020\)](#) on their examination

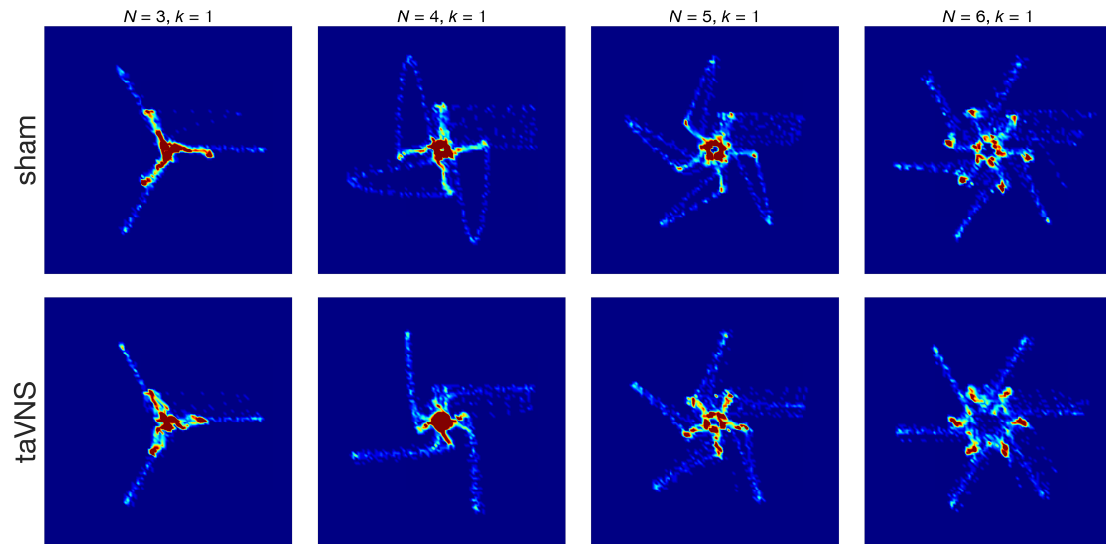


Figure 32: Electrocardiogram (ECG)-derived symmetric projection attractor reconstruction (SPAR) images in response to sham and taVNS. (**sham**) The (N, k) attractors generated from a 10 s ECG signal of one example participant for $N = 3, 4, 5, 6$ embeddings from sham condition, (**taVNS**) and taVNS condition. Reproduced from [Molefi, McLoughlin and Palaniappan \(2024\)](#).

of target engagement detection in tcVNS for traumatic stress triggers. While those based on an ensemble of learners for classification were included owing to their differential performance at classifying malaise versus healthy ([Keshavarz et al., 2022](#)). The explored classifiers were discriminant analysis, ensemble (with AdaBoostM1 and LogitBoost), logistic regression, naïve Bayes, neural network, and support vector machine (with Gaussian, linear, polynomial, and sigmoid kernels), as respectively implemented by the functions `fitcdiscr`, `fitcensemble`, `fitckernel`, `fitcnb`, `fitcnet`, and `fitcsvm`, in MATLAB 2023b. The response variable was a participant’s binary stimulation type (taVNS or sham). Provided as input were attractor features constructed by deriving attractor features obtained from above.

For model training, I used LOPOCV procedure (this was introduced in the previous experiment, see [Convolutional Neural Networks \(CNNs\) in Experiment 1: Transfer Learning of Motion-Induced Nausea ECG SPAR Transforms](#)); that is, all data for one participant were excluded from the training dataset and used for generalization. Of note, LOPOCV is well-known as leave-one-subject-out cross-validation (LOSO-CV), a

term utilized by [Gurel et al. \(2020\)](#); importantly, this procedure ensures that the training dataset would not contain data of the test participant. This procedure was iterated for each of the 29 participants. To find hyperparameters that minimize five-fold, ten-fold, and leave-one-participant-out cross-validation loss, I used Bayesian optimization with 100 iterations. [Table 21](#) shows the hyperparameters that were optimised for each of the classifiers. All experiments were performed on a node consisting of a single 80GB NVIDIA A100 GPU.

Statistical Analysis

All statistical analyses were performed using MATLAB (R2023b, and R2024a). Model performance optimization and evaluation were performed using Bayesian optimization and a LOPOCV procedure, respectively. Additionally, I computed the AUC metric similar to [Experiment 1: Transfer Learning of Motion-Induced Nausea ECG SPAR Transforms](#); recall that an AUC of 1 represents perfect classification and an AUC of 0.5 corresponds to random classification.

6.3.2 Results

I used machine learning to perform classification of stimulation type – active or sham taVNS – from a set of 20 features extracted from attractor image data derived from records of ECG data obtained during taVNS and sham conditions ([Table 20](#)); [Figure 32](#) presents sample attractors for one example participant. Of the trained classifiers, an ensemble of boosted classification trees using adaptive logistic regression (LogitBoost) classifier demonstrated great performance when minimizing five-fold (AUC = 0.72) and ten-fold (AUC = 0.81) cross-validation loss ([Table 22](#)). Importantly, the results suggest that the classification ensemble (AdaBoostM1 and LogitBoost) models show above

Table 21: All the hyperparameters examined for each of the classification models used for detection of taVNS response.

Model	Hyperparameters
Discriminant Analysis	'Delta': [1e-6 1e3]
	'Gamma': [0 1]
Ensemble (AdaBoostM1)	'DiscrimType': {'linear' 'quadratic' 'diagLinear' 'diagQuadratic' 'pseudoLinear' 'pseudoQuadratic'}
	'NumLearningCycles': [10 500]
	'LearnRate': [1e-3 0.3]
	'MinLeafSize': [1 28]
Ensemble (LogitBoost)	'MaxNumSplits': [1 28]
	'NumLearningCycles': [10 500]
	'LearnRate': [1e-3 0.3]
	'MinLeafSize': [1 28]
Logistic Regression	'MaxNumSplits': [1 28]
	'Lambda': [1.7857e-7 1.7857e3]
	'Regularization': {'ridge' 'lasso'}
Naïve Bayes	'DistributionNames': {'normal' 'kernel'}
	'Width': [1e-3 1e3]
	'Kernel': {'normal' 'box' 'epanechnikov' 'triangle'}
Neural Network	'Standardize': {'true' 'false'}
	'NumLayers': [1 5]
	'Activations': {'relu' 'tanh' 'sigmoid' 'none'}
	'Standardize': {'true' 'false'}
	'Lambda': [1.7857e-7 1.7857e3]
	'Layer_1_Size': [1 400]
	'Layer_2_Size': [1 400]
'Layer_3_Size': [1 400]	
SVM (Gaussian)	'Layer_4_Size': [1 400]
	'Layer_5_Size': [1 400]
	'BoxConstraint': [1e-3 1e3]
SVM (Linear)	'KernelScale': [1e-3 1e3]
	'Standardize': {'true' 'false'}
	'BoxConstraint': [1e-3 1e3]
SVM (Polynomial)	'KernelScale': [1e-3 1e3]
	'PolynomialOrder': [2 4]
	'Standardize': {'true' 'false'}
SVM (Sigmoid)	'BoxConstraint': [1e-3 1e3]
	'Standardize': {'true' 'false'}

Table 22: The AUC values of ten models for binary classification of taVNS therapy response derived using LOPOCV with nested 5-fold, 10-fold, and leave-one-participant-out cross-validation. AUC, area under the receiver operating characteristic (ROC) curve; taVNS, transcutaneous auricular vagus nerve stimulation; LOPOCV, leave-one-participant-out cross-validation; SVM, support vector machine. Reproduced from [Molefi, McLoughlin and Palaniappan \(2024\)](#).

Model	5-fold	10-fold	LOPOCV
Discriminant Analysis	0.72	0.69	0.72
Ensemble (AdaBoostM1)	0.71	0.79	0.72
Ensemble (LogitBoost)	0.72	0.81	0.67
Logistic Regression	0.69	0.69	0.69
Naïve Bayes	0.66	0.69	0.69
Neural Network	0.67	0.53	0.55
SVM (Gaussian)	0.69	0.69	0.66
SVM (Linear)	0.72	0.69	0.66
SVM (Polynomial)	0.62	0.62	0.59
SVM (Sigmoid)	0.66	0.66	0.45

chance levels to reveal which electrical stimulation – taVNS or sham – a given participant received; in particular, when using five-fold and ten-fold cross-validation ([Table 22](#)). Notably, I observed that the AdaBoostM1 classifier also achieved an acceptable AUC score with nested LOPOCV (AUC = 0.72). Furthermore, as presented in [Table 22](#), discriminant analysis, and SVM with linear kernel classifiers also obtained AUC values considered acceptable (AUCs > 0.7).

6.4 Discussion

I applied a SPAR transformation based on nonlinear dynamical systems to compute attractor images from ECG signals for detection of differential response to motion-induced nausea, and taVNS therapy response. By fine-tuning a set of pretrained

deep neural networks with transfer learning, wherein the networks examined ECG-derived attractor images obtained at rest (baseline) and during malaise, I have provided evidence showing that the expression of motion-induced nausea could be determined from information encapsulated in these attractors. Furthermore, I have demonstrated that machine learning models trained on features extracted from attractor images based on ECG responses during sham and taVNS conditions, reveal which electrical stimulation – taVNS or sham – a given participant received – with an acceptable classification performance as measured using the AUC.

Previous efforts using deep learning to detect motion sickness from physiological signals have generally attempted to do so through multimodal signal fusion (Islam et al., 2020; Hwang, Bang and Lee, 2022). In contrast, here I show for the first time that the confluence of deep learning and SPAR reveals the potential of objectively identifying individuals using the ECG – a simple, ubiquitous, and low-cost physiological modality. I found that the models generally showed higher accuracy of malaise detection when using a majority voting scheme – for example, Inception-v3 demonstrated a majority vote accuracy of 87.50% for embedding dimension $N = 3$ (Table 19); without using this scheme, the model showed random performance. However, when considering the ROC curves (Figure 31), only the DenseNet-201 and ResNet-variant models achieved acceptable AUC values, suggesting that this metric provided robust discriminatory power of model performance compared to accuracy-based metrics. Overall, I note that these models were not developed to specifically handle motion-induced malaise attractor images; however, these observations suggest a potential avenue for attractor-tailored deep learning algorithms to detect or predict motion sickness. Moreover, this motivates future work to harness ECG SPAR-based transforms for early detection of symptom onset – including potentially real-time malaise detection. Demonstrating this has important implications for timely pharmacological or non-pharmacological (for example, neuromodulation) therapeutic intervention.

Examining taVNS response with machine learning, I show that when trained on

a set of ECG-derived attractor features, machine learning models demonstrate differential performance in detecting the electrical stimulation type (taVNS or sham) administered to an individual participant. While the ensemble classifiers outperformed other models when minimizing ten-fold cross-validation loss (Table 22), the LogitBoost classifier showed higher discriminatory power – achieving an AUC value of 0.81. It is important to remark that although my model’s predictive performance is potentially interesting, especially for future taVNS protocols, a model from a tcVNS protocol (Gurel et al., 2020) performed better. This could be attributable to the methodological differences that exist between this previous study and the study herein; most notably, the notion that taVNS targets the auricular branch of the vagus nerve whereas tcVNS engages the cervical branch. Early evidence showed that tcVNS elicited regional brain activation comparable to that of taVNS (Frangos and Komisaruk, 2017); however, there is currently no study showing that there could be analogous physiological effects on autonomic function between the two modalities. Considering recent evidence for distinct neural pathways revealed by taVNS and invasive cervical VNS from a study using a rodent model (Owens et al., 2024), the implication may be that these modalities influence cardiovascular function differently. On the other hand, a more plausible explanation is the fact that Gurel et al. (2020) performed model training using multimodal inputs of ECG- and PPG-derived variables, which also enabled extraction of a significantly larger feature set (176 features in total) compared to that herein (20 features). Indeed, multimodal signal fusion has an important role in machine learning applications for improving model performance (Baltrušaitis, Ahuja and Morency, 2018); and I acknowledge that my model could have benefited from combining signals from other modalities.

In earlier ML applications using SPAR features based on ECG data, the constructed models were demonstrated to facilitate examination of dofetilide-induced antiarrhythmic effects (Lyle, Nandi and Aston, 2019), detection of a genetic mutation in a murine model of Brugada syndrome (Bonet-Luz et al., 2020), and differentiation between two biologically distinct groups (Lyle, Nandi and Aston, 2021) – including the detection of paroxysmal atrial fibrillation from normal sinus rhythm in equine athletes (Huang

et al., 2022). My findings add to this accumulating evidence and suggest that ECG SPAR-generated features have potential to detect response to taVNS. Importantly, my work implicates a model trained on these features for a role in adaptive taVNS; that is, the modification of taVNS dosage in real-time based on autonomic nervous function dynamics that co-vary with the severity of motion-induced malaise symptoms.

Although [Figure 31](#) and [Table 22](#) suggest that the models I considered here demonstrated above chance level to detect differential response to motion-induced nausea, and reveal which electrical stimulation (taVNS or sham) a given participant received, respectively; there is still significant room for improvement on several aspects. First, while my epoch length choice of 10 s is consistent with previous work ([Lyle, Nandi and Aston, 2019, 2021](#); [Lyle and Aston, 2021](#)), it may not have been optimal for my experiments; suggesting future investigations to optimise epoch length. Notably, the work of [Huang et al. \(2022\)](#) utilised an epoch length of 20 s for attractor generation. Secondly, model performance improvement might have also been possible through performing attractor embedding in higher dimensions compared to the maximum dimension ($N = 6$) considered herein – for example, [Lyle, Nandi and Aston \(2021\)](#) optimised attractor generation over $N = 3, 4, 5, \dots, 17$ and found that using attractors from $N = 3, 5, \dots, 13$ embeddings allowed for different features of the ECG to be amplified. Third, here I performed my analyses on images/features of individual embedding dimensions (see [Figure 31](#)); however, constructing a feature set from all embeddings coupled with appropriate feature selection methods implies further potential to improve classification performance. Finally, all my experiments utilised projection $k = 1$; however, an embedding dimension N may have different projections $k = 1, \dots, \lfloor (N - 1)/2 \rfloor$, suggesting that optimising over these projections may enhance model performance.

6.5 Conclusion

The findings from my experiments reveal that ECG-derived attractors show potential promise for detection of differential response to motion-induced nausea using deep neural networks. This suggests that utilising SPAR-generated attractor images could

lead to improved motion-induced nausea detection; further, it implies that manual feature extraction via SPAR transformation may potentially aid quantification and assessment of new therapeutics for motion sickness management. Moreover, my findings demonstrate that features extracted from ECG attractors could be helpful in determining taVNS therapy response; suggesting that exploiting these features – potentially complemented by standard measures, for example, vagally-mediated HRV measures – could support optimal and effective taVNS administration. Clearly, there is a need for a more comprehensive examination of the wider role of SPAR for understanding and predicting or detecting motion sickness effects on autonomic function; furthermore, I would argue that the SPAR tool is worth investigating for non-invasive vagal nerve stimulation therapies, especially for taVNS and tcVNS biomarker identification.

Chapter 7

General Discussion

7.1 Overview

This thesis presents analyses of brain, autonomic, and behavioural changes from two crossover randomised controlled studies – one characterised as a pilot study (Study 1) and one comprising a relatively larger cohort (Study 2) – wherein participants undergoing nauseogenic visual stimulation were administered taVNS (200 μ s, 20 Hz) over the left tragus. In Study 1, taVNS demonstrated a marked reduction in EEG theta spectral power in regions of the brain implicated in motion-induced nausea, namely frontal, parietal, and occipital cortices ([Chapter 4; Molefi, McLoughlin and Palaniappan, 2023b](#)); moreover, autonomic data from this study revealed that tragus stimulation led to improved HRV compared to sham ([Chapter 5; Molefi, McLoughlin and Palaniappan, 2023a](#)).

For Study 2, a functional brain imaging technique called eLORETA was used to perform EEG source localization. This technique helped identify electric neuronal generators underlying taVNS administration, and showed that, compared to sham, taVNS induced differential neuronal response in the middle occipital gyrus (MOG; BA 19) that generated theta oscillations ([Chapter 4; Molefi, McLoughlin and Palaniappan, 2025](#)). Furthermore, examination of ECG records obtained in this study with the SPAR approach resulted in the identification of attractor responses evoked by taVNS compared to sham ([Chapter 5; Molefi, McLoughlin and Palaniappan, 2024](#)). Additionally, I also

demonstrated the application of machine learning methods for taVNS therapy response detection using ECG-derived attractor features (Chapter 6; Molefi, McLoughlin and Palaniappan, 2024).

Here, I discuss some of the limitations in the above-summarised studies and their implications for the interpretation of the results as described therein and in Chapters 4 to 6. I suggest how these limitations may potentially account for the mixed evidence in the literature thus far. Crucially, given that this thesis provides the first insights into the effects of taVNS for motion-induced nausea, I highlight how future studies bear an important role in addressing the subsequently discussed limitations in efforts to confirm the findings herein.

7.2 Sham Condition in taVNS Studies

The pilot data in Chapters 4 and 5 (Molefi, McLoughlin and Palaniappan, 2023a,b) were limited in that null stimulation was applied as a sham condition; that is, the electrical stimulator was mounted to the earlobe but providing no active stimulation. While this approach has been utilised previously (e.g., Hein et al., 2013), participants' perception of verum and sham stimulation could potentially bias the results. To address this, new data were collected whereby actual stimulation of the earlobe was performed for the sham condition (Chapters 4 and 5; Molefi, McLoughlin and Palaniappan, 2024, 2025). Importantly, this latter method adheres to an international consensus (Farmer et al., 2021); moreover, the earlobe is a hitherto most commonly used sham stimulation site in taVNS literature; and we know from neuroimaging studies that earlobe stimulation does not affect brainstem structures thought to be involved in taVNS mechanism, such as the NTS and LC (Frangos, Ellrich and Komisaruk, 2015; Yakunina, Kim and Nam, 2017). While it should be noted that the earlobe (Butt et al., 2020) and, by extension, control paradigms in non-invasive vagus nerve stimulation studies (Rajiah et al., 2022), cannot be considered physiologically inert, early cadaveric evidence suggests that the earlobe is free from vagal innervation and is innervated solely by the greater auricular nerve (Peuker and Filler, 2002). However, because the debate of whether earlobe

stimulation may be recognised as the gold-standard for sham in taVNS studies remains unresolved (Butt et al., 2020; Cheng et al., 2025), further research will be required to corroborate the findings herein. In addition, future efforts should also consider stimulating the scapha – a plausible sham site previously utilised in Fang et al. (2016), for example – in lieu of the earlobe. Taken together, while pilot data herein should be interpreted with caution, data from Study 2 are based on a sound implementation of sham condition, and thus provide meaningful insights into taVNS neural and autonomic changes toward amelioration of motion sickness.

7.3 taVNS Dosage for Motion-Induced Nausea

For taVNS dosage, both Study 1 and 2 utilised current-controlled 200 μ s asymmetrical biphasic square pulses at a rate of 20 Hz for a maximum of 20 min. As described earlier (see [Electrical Stimulation](#) in the [Materials and Methods](#) chapter), the rationale behind the selection of these stimulation parameters – pulse width and frequency, in particular – was supported by previously described methods (e.g., Beh and Friedman, 2019; Tran et al., 2019; Cao et al., 2021). Early in research planning, a pulse width of 250 μ s had been proposed for this work, seeing as most of the reviewed studies adopted it (see [Tables 1](#) and [2](#) in the [Literature Review](#) chapter). However, initial testing of taVNS administration with this pulse width setting – prior to the pilot study herein – was described as painful. Programming the electrical stimulator to a lower pulse width of 200 μ s produced tolerable stimulation; notably, this is the second most used parameter setting for pulse width from the reviewed literature ([Tables 1](#) and [2](#) in [Literature Review](#)). A possible explanation for this differential sensitivity in tolerated stimulation may be due to the fact that all the reviewed studies herein that employed a pulse width setting of 250 μ s performed electrical stimulation using a Cerbomed Nemos[®] device (tVNS Technologies GmbH, Erlangen, Germany); whereas this thesis used the EM6300A TENS device (Med-Fit UK Ltd, Stockport, UK). In their recent systematic review and meta-analysis, Kim et al. (2022) found that device – and electrode – types used for taVNS

administration varied significantly; with a majority of 22 studies (27.5%) utilising a Cerbomed Nemos[®] device. This suggests to future studies to explore taVNS for motion sickness management using the Cerbomed Nemos[®] device, including the suggestion that stimulation sensitivity – or more importantly, tolerability – may be device-specific.

Rationale for electrical stimulation of 20 min (maximum) is supported by previously described methods (e.g., [LaCount et al., 2009](#); [Kim et al., 2011](#); [LaCount et al., 2011](#); [Napadow et al., 2013](#); [Sclocco et al., 2016](#); [Toschi et al., 2017](#); also see [Nauseogenic Stimulation](#) in the [Materials and Methods](#) chapter). Importantly, this stimulation duration setting conformed to the 10-20 min recommended dose for vagus nerve stimulation by the device manufacturer. While [Clancy et al. \(2014\)](#) delivered electrical stimulation at a high frequency (30 Hz) compared to that herein (20 Hz), the authors showed that 15 min of tragus stimulation induced enhanced and attenuated parasympathetic and sympathetic neural activity, respectively. Furthermore, it is worthy to note that taVNS effects have also been documented at a stimulation duration of 10 min ([De Couck et al., 2017](#)), albeit this was observed with right cymba conchae stimulation. Together, this suggests that the maximal stimulation duration for the protocol implemented here may have been sufficient to observe taVNS-induced effects.

Acknowledging the limitation that only one dosage of taVNS (200 μ s, 20 Hz) was examined in this research, it is possible that the findings herein may not necessarily generalise, including the potential that this electrical stimulation dosage may not have been optimal for alleviation of motion-induced nausea. Nevertheless, the fact that tailored stimulation current intensity was utilised in Study 2 for taVNS administration, provides support for the reliability and efficacy of the proposed taVNS protocol; most importantly, this sheds new light on neurostimulation for motion sickness via evaluation of taVNS-induced effects on neural and autonomic function, including at the level of behaviour. In sum, optimisation of the electrical stimulation parameters and intensity levels needs to be further explored to fully unlock taVNS therapeutic potential and enhance evidence for its application in mitigating motion sickness.

7.4 Interpreting Differential eLORETA

LORETA – which has now been superseded by sLORETA (Pascual-Marqui, 2002) – is a method used to estimate the 3D intracerebral current density distribution from EEG data (Pascual-Marqui, Michel and Lehmann, 1994). The most recent implementation of this family of inverse solutions – eLORETA – reconstructs cortical electrical activity with exact, zero error localization to test point sources (Pascual-Marqui, 2007; Pascual-Marqui et al., 2011). eLORETA has been demonstrated to outperform sLORETA (Pascual-Marqui et al., 2011), and a systematic comparison of source localization with sLORETA and eLORETA showed that eLORETA generates smoother and better neuroimages (Jatoi et al., 2014). Recent neuroscience studies are increasingly performing estimation of cortical activity with eLORETA (e.g., Canuet et al., 2011; Aoki et al., 2015; Kaboodvand, Karimi and Irvani, 2024; Lee and Tramontano, 2024; Orui et al., 2024). In the available literature to date, only one other study has investigated the effects of taVNS on neural function using a LORETA-based method (Dimitrov and Gatev, 2015); and the present work (Chapter 4; Molefi, McLoughlin and Palaniappan, 2025) is the first to examine taVNS brain effects using eLORETA – aiming to pave the way for functional localization of taVNS-evoked neuronal activity in the human brain from scalp-recorded EEG.

But what does eLORETA tell us – and not tell us – about neuronal activity? eLORETA does not detect neuronal activity *per se*, but rather estimates it from the observable EEG data. As described earlier in Chapter 2 (see [Electroencephalography](#) section), EEG signals provide direct measurement of neural activity; however, EEG does not reveal the source or location of brain areas generating this observed neuronal activity. Identifying neuronal generators implicated in this measured brain response requires solving an ill-posed inverse problem. eLORETA provides a solution to this problem by computing the 3D distribution of the electrically active neuronal generators in the brain as current density under the assumption of coherent firing of neighbouring cortical pyramidal neurons (Pascual-Marqui et al., 2011).

Although eLORETA intracerebral current density signals are indirect measures of

neural activity, it is important to note that they are still useful given that they have marked crossmodal validity and agreement with various neuroimaging modalities, such as positron emission tomography (PET) (Dierks et al., 2000; Pizzagalli et al., 2004; Zumsteg et al., 2005), structural MRI (Worrell et al., 2000), and fMRI (Vitacco et al., 2002; Mulert et al., 2004), including intracranial EEG (iEEG) (Zumsteg et al., 2006). Moreover, evidence from recent research further validates eLORETA as a reliable EEG source imaging tool (Smith, Cavanagh and Allen, 2018; Hauk, Stenroos and Treder, 2022; Popov et al., 2023; Allouch et al., 2023). In addition, previous research has shown that eLORETA has differential performance at controlling for false positives compared to other source localization methods (Halder et al., 2019). Importantly, these studies provide encouraging support for the reliability and value of findings presented in Chapter 4 (Molefi, McLoughlin and Palaniappan, 2025).

However, these findings should be interpreted with caution due to the spatial resolution limitations inherent in eLORETA. This should not be surprising, given eLORETA data are inferred from scalp recorded EEG signals which we know – despite having excellent temporal resolution – characterise by low spatial resolution. Although the 64-channel EEG recordings used herein are adequate for source reconstruction, higher densities such as 128- or 256-channel EEG have been shown to improve spatial resolution and localization accuracy of deep sources (Song et al., 2015). A possible alternative to address the limitation of spatial resolution would be to use fMRI; neuroimaging with 7 Tesla fMRI yields higher spatial resolution compared to 3 Tesla fMRI. Most importantly, with fMRI, it would be easy to detect brainstem nuclei implicated with differential taVNS response, such as the NTS, LC, and dorsal raphe nucleus (DRN). Overall, acknowledging the limited capacity that eLORETA has to delineate brainstem nuclei, the eLORETA findings here are consistent with previous fMRI evidence on the effects of taVNS (see the Discussion in Chapter 4), suggesting that eLORETA may have an important role to play in settings where fMRI is unavailable; however, more data are needed to establish eLORETA in assessing taVNS-related neural changes.

7.5 HRV as a Biomarker for taVNS

The vagus nerve is a major neural substrate of the parasympathetic nervous system, but whether HRV metrics of parasympathetic vagal modulation can serve as indicators of taVNS response remains a matter of debate. This is in part because studies investigating the relationship between taVNS and HRV measures have provided mixed evidence (see [Autonomic Effects of taVNS](#) in the [Literature Review](#) chapter); and in part due to the underappreciated mechanism that taVNS indirectly modulates heart rate dynamics via brainstem nuclei. That is, taVNS excites NTS neurons with projections to the dorsal vagal motor nucleus (DVN) and nucleus ambiguus (NA); and in turn, these vagal efferent neurons promote vagal input to the SA node ([Murray et al., 2016](#)).

Despite a taVNS-induced increase in HRV being anatomically plausible, a meta-analysis of 16 single-blind studies comparing taVNS versus sham in healthy participants concluded that taVNS does not affect vagally mediated HRV across a wide range of settings ([Wolf et al., 2021](#)); however, the authors also added that taVNS has potential to elicit positive neuromodulatory effects in limited cases – for example, via right-sided vagal stimulation or in participants presenting with differential cardiac vagal activity at baseline. Although the conclusion by [Wolf et al. \(2021\)](#) warrants caution in the interpretation of HRV findings in [Chapter 5](#), it is worth highlighting the results of recent studies showing that taVNS may improve HRV ([Geng et al., 2022](#); [Forte et al., 2022](#); [Shen et al., 2022](#); [Maestri et al., 2024](#)).

Of the many factors that could affect the role of HRV as a biomarker for taVNS, stimulation parameters have documented evidence. [Machetanz et al. \(2021\)](#) demonstrated that taVNS-evoked improvements in HRV are location- and charge-dependent. While the authors additionally provide specific parameters for the observed changes in HRV, it is likely that such parameters may be device-specific; suggesting that the parameters identified in the study may not translate to other taVNS devices – further making interpretation of HRV findings challenging.

While HRV is an important indicator of ANS response and its validation as a robust biomarker for taVNS is highly sought, it is a signal that is commonly derived from the

ECG. Therefore, as an alternative – but complementary – to this ECG-to-HRV methodology, [Chapter 5 \(Molefi, McLoughlin and Palaniappan, 2024\)](#) suggests the hypothesis that ECG-based SPAR may be a candidate biomarker for detecting effects of taVNS on autonomic function. If this hypothesis is validated in future larger studies, it provides a new avenue for examining taVNS response – which is crucial if we are to maximise taVNS potential in facilitating autonomic balance. Interestingly, this hypothesis may even hold for other biomedical signals, such as arterial blood pressure, baroreflex sensitivity, and PPG, given that SPAR can be performed on any approximately periodic signal. Collectively, while a pattern of improved HRV is observed with taVNS in a growing number of adequately designed studies, HRV results herein will require further study and replication in studies from other labs; and the same goes for the ECG-based SPAR findings.

7.6 Implications of Sex Differences

The datasets used herein were obtained mainly from female participants, which may skew the findings towards this demographic. There is both early and recent evidence from animal models showing that VNS effects are more pronounced in females; most probably due to estrogen influence on muscarinic acetylcholine in the CNS ([Du, Dart and Riemersma, 1994](#); [Yaghouby et al., 2020](#)). Given the role hormonal levels play in differential ANS function between males and females, it seems likely that these animal model findings should translate to human models ([Koenig and Thayer, 2016](#); [Koenig et al., 2017](#); [Farmer et al., 2021](#)). Indeed, [De Couck et al. \(2017\)](#) performed right-sided cymba conchae stimulation and found a consistent taVNS-induced SDNN increase in females compared to males. While it is plausible to suggest that this effect may have been driven by vagal lateralisation, given that the authors observed stronger effects with right ear versus left ear stimulation, the findings are paralleled by data from a more recent study suggesting that left cymba conchae stimulation elicits a more consistent ANS response in female participants ([Yokota et al., 2022](#)). This warrants future

studies to validate the findings herein in male participants, including in a more gender-balanced participant cohort. Nevertheless, these findings are important given that a within-subjects study design was used; and more importantly, previous studies have shown that motion sickness susceptibility is higher for females than males (Golding, 2006; Paillard et al., 2013; Mittelstaedt, 2020) – albeit evidence for this is based on self-reports rather than physiological assessments (Lackner, 2019). Overall, the data presented here reveal differential effects of taVNS at the level of behaviour, physiology, and underlying neural dynamics that fit well with previously described findings from studies with participant cohorts consisting of only female individuals (Kim et al., 2011; LaCount et al., 2011; Napadow et al., 2013), or only male individuals (Chu et al., 2012, 2013), as well as the wider literature. Furthermore, these beneficial taVNS therapeutic effects pivot gender imbalance in the study cohorts herein from being a limitation to a strength, given the notion that females have an increased susceptibility to motion-induced malaise.

7.7 Influence of Sample Size

We may recall from the studies surveyed in the [Literature Review](#) chapter that there was mixed evidence for taVNS-induced neural and autonomic effects. Of the multiple factors that may have contributed to this, small sample size is one plausible key factor; [Burger et al. \(2020\)](#) provide a detailed discussion on this challenge in their narrative review of potential biomarkers for tVNS. A study with a small sample size would limit the statistical power of analyses therein; and therefore, impede the replicability of the findings, including their potential generalisability. Moreover, for machine learning – particularly deep learning – models can overfit to small datasets, which, in turn, may lead to inadequate generalisation to unseen examples; hence, the use of transfer learning in [Chapter 6 \(Molefi and Palaniappan, 2024\)](#). Accordingly, while the findings of the pilot data presented here ([Chapters 4 and 5; Molefi, McLoughlin and Palaniappan, 2023a,b](#)) require replication in larger samples prior to their acceptance as generalisable, they do suggest potential therapeutic neural and autonomic changes attributable to taVNS in

motion-induced nausea; and could serve as a launchpad for further research seeking to add to the data pool for this line of research – including contributing information which could help inform the design (e.g., power sample calculation) of future randomised controlled trials. Also, these findings may have a role in future quantitative meta-analyses. Finally, it is important to remark that the new additional data presented in [Chapters 4 to 6](#) ([Molefi, McLoughlin and Palaniappan, 2024, 2025](#)) showcases notable sample size; thus, mitigates this concern. However, in the absence of previous studies, further studies are warranted to validate the therapeutic benefits of taVNS for motion sickness management at the level of neural and autonomic function.

Chapter 8

Conclusions and Future Directions

8.1 Conclusions

In this thesis I aimed to investigate the potential neuromodulatory effects of taVNS on brain and autonomic responses of neurotypical individuals undergoing nauseogenic stimulation. To this end, I developed a nauseogenic visual stimulus for nausea induction in tandem with taVNS (200 μ s, 20 Hz) administration during continuous EEG and ECG data acquisition. Using biomedical signal processing and computational techniques, including machine learning of ECG SPAR transforms, I provided novel evidence to suggest that taVNS – a non-invasive form of brain stimulation – may play an important role in motion sickness management.

For millennia, humans have suffered from motion sickness thought to stem from ambiguous sensory information – which not only continues to affect us today, but may even be increasing in importance thanks to technology advances such as portable or immersive displays and autonomous driving. While early discoveries have led to the development of effective antiemetic compounds for this polysymptomatic condition, these mainstay medications carry undesirable side effects, and some, provide inadequate efficacy. On the other hand, progress on developing non-pharmacological tools to alleviate motion-induced malaise has been glacial. With the most effective treatment for motion-induced nausea still being habituation ([Keshavarz and Golding, 2022](#)); an interventional tool that requires long-term compliance, the need for new, innovative

therapeutic tools to mitigate this elusive syndrome remains.

Because of recent findings suggesting that non-invasive vagus nerve stimulation may induce a parasympathetic response, including accumulating evidence for therapeutic benefits of this neurostimulation modality on migraine, I piloted and trialled my taVNS protocol – described in the [Materials and Methods](#) chapter – for motion sickness; given our understanding that this malady presents with parasympathetic withdrawal, and that it has links with migraine. My analyses on [Effects of taVNS on the Human Brain in Visually Induced Motion Sickness](#) revealed that participants receiving taVNS had differential functional brain activation in comparison with sham stimulation; and that through these taVNS-mediated neural effects, participants achieved better symptom relief.

My ensuing analyses on [Autonomic Effects of taVNS on Visually Evoked Motion Sickness in Humans](#) utilising HRV dynamics showed that my taVNS protocol evoked a parasympathetic response, suggesting that participants were experiencing less agitation with taVNS versus sham – indicative of differential autonomic therapeutic effects. Moreover, I quantified and visualised, for the first time, the effects of taVNS on ECG morphology and variability using SPAR – a mathematical tool inspired by nonlinear dynamical systems – and demonstrated that this tool may have utility parsing effects of taVNS; with implications for taVNS biomarker identification – especially considering the ongoing debate of whether HRV is indicative of taVNS response ([Wolf et al., 2021](#)). Thus, my findings here additionally mark an important step in the search for a robust biomarker for taVNS.

In [Using Supervised Learning to Predict Motion-Induced Nausea, and Effects of taVNS](#), I coalesced ECG-derived attractors and deep learning demonstrating that machine learning models can detect differential response to motion-induced nausea from image data of ECG morphology and variability. Furthermore, I showed the utility of SPAR-generated features in taVNS response detection; therefore, implicating machine learning models for a role in effective and optimal taVNS administration, including adaptive taVNS, which would be paramount for a closed-loop taVNS protocol. The concept being that, I envision a real-time application of taVNS for motion sickness management.

8.2 Future Directions

The novel findings herein may lead to new pathways in understanding taVNS-induced neural and autonomic effects for motion sickness management, including other nausea-related conditions; and it is exciting for this work to have developed a more potent taVNS protocol for optimal and effective non-invasive vagus nerve stimulation. To this end, future work should consider replicating these results and, more importantly, conducting a parametric study concurrent with nauseogenic stimulation to find optimal taVNS dosage. This would entail examining effects of stimulation on both the cervical and auricular branch of the vagus nerve with different pulse width, frequency, and duty cycle. Additionally, investigating the effects of laterality – that is, left versus right ear – including tragus versus cymba conchae (or both) may advance understanding on how best to ameliorate motion-induced malaise, and related nauseogenic ailments. This is a huge parameter space – possibly combinatorial – and thus may require tools such as Bayesian optimisation.

I also note that I employed continuous stimulation of the vagus nerve; it would be interesting to explore intermittent delivery of taVNS as well. Ideally, an adaptive taVNS protocol would be desirable to eschew vagus nerve overstimulation; put differently, despite taVNS being safe, there is limited data on the effects of chronic vagus nerve stimulation in humans. A direction along this path of adaptive taVNS may lead to development of a closed-loop neurostimulation protocol. Future studies could also leverage machine learning and artificial intelligence to maximise the value of neuroimaging and physiological data collected. That is, herein, machine learning was only applied to physiological data ([Chapter 6](#)); however, constructing features from both neural and autonomic data may help improve detection of motion-induced nausea, taVNS response and, importantly, may enable optimal machine learning design for closed-loop systems to personalise delivery of non-invasive vagal nerve stimulation (i.e., taVNS and tcVNS). Crucially, effective, robust alleviation of motion sickness via taVNS in real-time potentially requires an integration of an optimal stimulation protocol with individually tailored stimulation parameters for a more precise reduction of symptom severity.

Future studies may also explore the use of different resolutions for the eLORETA analyses to determine if findings herein still hold; for example, investigating with 4 s epochs in lieu of 8 s as described in [Chapter 4](#). Furthermore, previous work has described the use of singular value decomposition (SVD) and eLORETA to identify EEG networks and responses to transcranial photobiomodulation (tPBM) ([Wang et al., 2022](#)); therefore, it would be interesting to explore the confluence of these techniques for examination of the EEG data herein ([Chapter 4](#)) to deepen our understanding of the brain effects of taVNS.

While the work herein focused on application of taVNS to ameliorate motion-induced nausea, it is important to remark that these findings may also have important implications for addressing other sources of nausea – such as, chemotherapy-induced nausea, postoperative nausea, and migraine – plus for navigating conditions such as stress and anxiety. It is also important to highlight that the data here may help inform future design of neuromodulation systems for motion sickness management, and thus has implications for commercialisation; it is notable that neuromodulation tools that aim to treat for example, cluster headache, already exist ([Nesbitt et al., 2015](#)). Collectively, if replicated, the results herein support that taVNS has promise as an effective neurostimulation tool for motion sickness management; thus, future research should further investigate this hypothesis.

Bibliography

- Abe, K., Oda, N. and Hatta, H. (1984). Behavioural Genetics of Early Childhood: Fears, Restlessness, Motion Sickness and Enuresis. *Acta geneticae medicae et gemellologiae: twin research*, 33(2), pp. 303–306, <https://doi.org/10.1017/S0001566000007340>.
- Adelhöfer, N., Gohil, K., Passow, S., Beste, C. and Li, S.-C. (2019). Lateral prefrontal anodal transcranial direct current stimulation augments resolution of auditory perceptual-attentional conflicts. *NeuroImage*, 199, pp. 217–227, <https://doi.org/10.1016/j.neuroimage.2019.05.009>.
- Ahmed, I. H., Djebbari, A. and Benabdellah, M. (2018). High-resolution time-frequency energy features of HRV signals using the SPWVD and the STFT-spectrogram. In *2018 International Conference on Electronics, Control, Optimization and Computer Science (ICECOCS)*, IEEE, pp. 1–7, <https://doi.org/10.1109/ICECOCS.2018.8610511>.
- Allouch, S. et al. (2023). Effect of channel density, inverse solutions and connectivity measures on eeg resting-state networks reconstruction: A simulation study. *NeuroImage*, 271, p. 120006, <https://doi.org/10.1016/j.neuroimage.2023.120006>.
- Andrievskaia, P., Berti, S., Spaniol, J. and Keshavarz, B. (2023). Exploring neurophysiological correlates of visually induced motion sickness using electroencephalography (EEG). *Experimental Brain Research*, 241(10), pp. 2463–2473, <https://doi.org/10.1007/s00221-023-06690-x>.
- Angelaki, D. E. and Cullen, K. E. (2008). Vestibular System: The Many Facets of a

- Multimodal Sense. *Annual Review of Neuroscience*, 31(1), pp. 125–150, <https://doi.org/10.1146/annurev.neuro.31.060407.125555>.
- Antonino, D. et al. (2017). Non-invasive vagus nerve stimulation acutely improves spontaneous cardiac baroreflex sensitivity in healthy young men: A randomized placebo-controlled trial. *Brain Stimulation*, 10(5), pp. 875–881, <https://doi.org/10.1016/j.brs.2017.05.006>.
- Aoki, Y. et al. (2015). Detection of EEG-resting state independent networks by eLORETA-ICA method. *Frontiers in Human Neuroscience*, 9, p. 31, <https://doi.org/10.3389/fnhum.2015.00031>.
- Arbabi, H. and Mezic, I. (2017). Ergodic Theory, Dynamic Mode Decomposition, and Computation of Spectral Properties of the Koopman Operator. *SIAM Journal on Applied Dynamical Systems*, 16(4), pp. 2096–2126, <https://doi.org/10.1137/17M1125236>.
- Arshad, Q. et al. (2015). Electrocortical therapy for motion sickness. *Neurology*, 85(14), pp. 1257–1259, <https://doi.org/10.1212/WNL.0000000000001989>.
- Astafiev, S. V., Stanley, C. M., Shulman, G. L. and Corbetta, M. (2004). Extrastriate body area in human occipital cortex responds to the performance of motor actions. *Nature Neuroscience*, 7(5), pp. 542–548, <https://doi.org/10.1038/nn1241>.
- Aston, P. J., Nandi, M., Christie, M. I. and Huang, Y. H. (2014). Comparison of attractor reconstruction and HRV methods for analysing blood pressure data. In *Computing in Cardiology 2014*, IEEE, pp. 437–440, <https://www.cinc.org/archives/2014/pdf/0437.pdf>.
- Aston, P. J., Christie, M. I., Huang, Y. H. and Nandi, M. (2018). Beyond HRV: attractor reconstruction using the entire cardiovascular waveform data for novel feature extraction. *Physiological Measurement*, 39(2), p. 024001, <https://dx.doi.org/10.1088/1361-6579/aaa93d>.

- Aston, P. J. et al. (2019). Deep Learning Applied to Attractor Images Derived from ECG Signals for Detection of Genetic Mutation. In *2019 Computing in Cardiology (CinC)*, IEEE, pp. 1–4, <https://doi.org/10.22489/CinC.2019.097>.
- Babadi, B. and Brown, E. N. (2014). A Review of Multitaper Spectral Analysis. *IEEE Transactions on Biomedical Engineering*, 61(5), pp. 1555–1564, <https://doi.org/10.1109/TBME.2014.2311996>.
- Badran, B. W. et al. (2018). Neurophysiologic effects of transcutaneous auricular vagus nerve stimulation (taVNS) via electrical stimulation of the tragus: A concurrent taVNS/fMRI study and review. *Brain Stimulation*, 11(3), pp. 492–500, <https://doi.org/10.1016/j.brs.2017.12.009>.
- Balocchi, R. et al. (2006). Revisiting the potential of time-domain indexes in short-term HRV analysis. *Biomed Tech (Berl)*, 51(4), pp. 190–193, <https://doi.org/10.1515/BMT.2006.034>.
- Baltrušaitis, T., Ahuja, C. and Morency, L.-P. (2018). Multimodal Machine Learning: A Survey and Taxonomy. *IEEE Transactions on Pattern Analysis and Machine Intelligence*, 41(2), pp. 423–443, <https://doi.org/10.1109/TPAMI.2018.2798607>.
- Beck, A. (1890). Die Bestimmung der Gehirn-und Rücken-markfunktionen vermittelst der electrischen Erseimungen. *bl Physiol*, 4, pp. 473–476.
- Beh, S. C. and Friedman, D. I. (2019). Acute vestibular migraine treatment with noninvasive vagus nerve stimulation. *Neurology*, 93(18), pp. e1715–e1719, <https://doi.org/10.1212/WNL.0000000000008388>.
- Belhumeur, P. N., Hespanha, J. P. and Kriegman, D. J. (1997). Eigenfaces vs. Fisherfaces: recognition using class specific linear projection. *IEEE Transactions on Pattern Analysis and Machine Intelligence*, 19(7), pp. 711–720, <https://doi.org/10.1109/34.598228>.
- Berger, H. (1929). Über das Elektrenkephalogramm des Menschen. *Archiv für*

- Psychiatrie und Nervenkrankheiten*, 87(1), pp. 527–570, <https://doi.org/10.1007/BF01797193>.
- Bermejo, P. et al. (2017). Innervation of the Human Cavum Conchae and Auditory Canal: Anatomical Basis for Transcutaneous Auricular Nerve Stimulation. *BioMed Research International*, 2017(1), p. 7830919, <https://doi.org/10.1155/2017/7830919>.
- Biasiucci, A., Franceschiello, B. and Murray, M. M. (2019). Electroencephalography. *Current Biology*, 29(3), pp. R80–R85, <https://doi.org/10.1016/j.cub.2018.11.052>.
- Billman, G. E. (2011). Heart rate variability—a historical perspective. *Frontiers in Physiology*, 2, p. 16984, <https://doi.org/10.3389/fphys.2011.00086>.
- Bles, W., Bos, J. E., De Graaf, B., Groen, E. and Wertheim, A. H. (1998). Motion sickness: only one provocative conflict? *Brain Research Bulletin*, 47(5), pp. 481–487, [https://doi.org/10.1016/S0361-9230\(98\)00115-4](https://doi.org/10.1016/S0361-9230(98)00115-4).
- Bonet-Luz, E. et al. (2020). Symmetric Projection Attractor Reconstruction analysis of murine electrocardiograms: retrospective prediction of Scn5a+/-genetic mutation attributable to Brugada syndrome. *Heart Rhythm O2*, 1(5), pp. 368–375, <https://doi.org/10.1016/j.hroo.2020.08.007>.
- Borges, U., Laborde, S. and Raab, M. (2019). Influence of transcutaneous vagus nerve stimulation on cardiac vagal activity: Not different from sham stimulation and no effect of stimulation intensity. *PLoS ONE*, 14(10), p. e0223848, <https://doi.org/10.1371/journal.pone.0223848>.
- Borgmann, D. et al. (2021). Technical Note: Modulation of fMRI brainstem responses by transcutaneous vagus nerve stimulation. *NeuroImage*, 244, p. 118566, <https://doi.org/10.1016/j.neuroimage.2021.118566>.
- Bos, J., Damala, D., Lewis, C., Ganguly, A. and Turan, O. (2007). Susceptibility to seasickness. *Ergonomics*, 50(6), pp. 890–901, <https://doi.org/10.1080/00140130701245512>.

- Bos, J. E. and Bles, W. (2004). Motion sickness induced by optokinetic drums. *Aviation, Space, and Environmental Medicine*, 75(2), pp. 172–174, <https://www.ingentaconnect.com/content/asma/ asem/2004/00000075/00000002/art00013>.
- Bos, J. E., Bles, W. and Groen, E. L. (2008). A theory on visually induced motion sickness. *Displays*, 29(2), pp. 47–57, <https://doi.org/10.1016/j.displa.2007.09.002>.
- Brainard, D. H. (1997). The Psychophysics Toolbox. *Spatial Vision*, 10 4, pp. 433–6, <https://doi.org/10.1163/156856897X00357>.
- Brennan, M., Palaniswami, M. and Kamen, P. (2001). Do existing measures of Poincaré plot geometry reflect nonlinear features of heart rate variability? *IEEE Transactions on Biomedical Engineering*, 48(11), pp. 1342–1347, <https://doi.org/10.1109/10.959330>.
- Brennan, M., Palaniswami, M. and Kamen, P. (2002). Poincaré plot interpretation using a physiological model of HRV based on a network of oscillators. *American Journal of Physiology-Heart and Circulatory Physiology*, 283(5), pp. H1873–H1886, <https://doi.org/10.1152/ajpheart.00405.2000>.
- Bretherton, B. et al. (2019). Effects of transcutaneous vagus nerve stimulation in individuals aged 55 years or above: potential benefits of daily stimulation. *Aging (alban NY)*, 11(14), p. 4836, <https://doi.org/10.18632/aging.102074>.
- Brunton, S. L. and Kutz, J. N. (2019). *Data-Driven Science and Engineering: Machine Learning, Dynamical Systems, and Control*. Cambridge University Press, <https://doi.org/10.1017/9781108380690>.
- Burger, A. et al. (2019a). The effect of transcutaneous vagus nerve stimulation on fear generalization and subsequent fear extinction. *Neurobiology of Learning and Memory*, 161, pp. 192–201, <https://doi.org/10.1016/j.nlm.2019.04.006>.
- Burger, A. M., Van der Does, W., Thayer, J. F., Brosschot, J. F. and Verkuil, B. (2019b).

- Transcutaneous vagus nerve stimulation reduces spontaneous but not induced negative thought intrusions in high worriers. *Biological Psychology*, 142, pp. 80–89, <https://doi.org/10.1016/j.biopsycho.2019.01.014>.
- Burger, A. M., D'Agostini, M., Verkuil, B. and Van Diest, I. (2020). Moving beyond belief: A narrative review of potential biomarkers for transcutaneous vagus nerve stimulation. *Psychophysiology*, 57(6), p. e13571, <https://doi.org/10.1111/psyp.13571>.
- Butt, M. F., Albusoda, A., Farmer, A. D. and Aziz, Q. (2020). The anatomical basis for transcutaneous auricular vagus nerve stimulation. *Journal of Anatomy*, 236(4), pp. 588–611, <https://doi.org/10.1111/joa.13122>.
- Candès, E. J., Li, X., Ma, Y. and Wright, J. (2011). Robust principal component analysis? *Journal of the ACM (JACM)*, 58(3), pp. 1–37, <https://doi.org/10.1145/1970392.1970395>.
- Canuet, L. et al. (2011). Resting-State EEG Source Localization and Functional Connectivity in Schizophrenia-Like Psychosis of Epilepsy. *PLoS ONE*, 6(11), p. e27863, <https://doi.org/10.1371/journal.pone.0027863>.
- Cao, J. et al. (2021). Different modulation effects of 1 Hz and 20 Hz transcutaneous auricular vagus nerve stimulation on the functional connectivity of the periaqueductal gray in patients with migraine. *Journal of Translational Medicine*, 19, pp. 1–11, <https://doi.org/10.1186/s12967-021-03024-9>.
- Carlson, M. D. (2021). Syncope. *Emergency Neurology*, pp. 89–98, https://doi.org/10.1007/978-3-030-75778-6_4.
- Castillo, G. et al. (2022). Transcutaneous Cervical Vagus Nerve Stimulation Induces Changes in the Electroencephalogram and Heart Rate Variability of Healthy Dogs, a Pilot Study. *Frontiers in Veterinary Science*, 9, p. 878962, <https://doi.org/10.3389/fvets.2022.878962>.
- Caton, R. (1875). Electrical Currents of the Brain. *The Journal of Nervous and Mental Disease*, 2(4), p. 610.

- Cevette, M. J. et al. (2012). Oculo-Vestibular Recoupling Using Galvanic Vestibular Stimulation to Mitigate Simulator Sickness. *Aviation, Space, and Environmental Medicine*, 83(6), pp. 549–555, <https://doi.org/10.3357/asem.3239.2012>.
- Chen, J. D., Yin, J. and Wei, W. (2017). Electrical therapies for gastrointestinal motility disorders. *Expert Review of Gastroenterology & Hepatology*, 11(5), pp. 407–418, <https://doi.org/10.1080/17474124.2017.1298441>.
- Chen, W., Wang, Z., Xie, H. and Yu, W. (2007). Characterization of Surface EMG Signal Based on Fuzzy Entropy. *IEEE Transactions on Neural Systems and Rehabilitation Engineering*, 15(2), pp. 266–272, <https://doi.org/10.1109/TNSRE.2007.897025>.
- Chen, Y.-C. et al. (2009). Motion-Sickness Related Brain Areas and EEG Power Activates. In *Foundations of Augmented Cognition. Neuroergonomics and Operational Neuroscience: 5th International Conference, FAC 2009 Held as Part of HCI International 2009 San Diego, CA, USA, July 19-24, 2009 Proceedings 5*, Springer, pp. 348–354, https://doi.org/10.1007/978-3-642-02812-0_41.
- Chen, Y.-C. et al. (2010). Spatial and temporal EEG dynamics of motion sickness. *NeuroImage*, 49(3), pp. 2862–2870, <https://doi.org/10.1016/j.neuroimage.2009.10.005>.
- Cheng, C. et al. (2025). Can earlobe stimulation serve as a sham for transcutaneous auricular vagus stimulation? evidence from an alertness study following sleep deprivation. *Psychophysiology*, 62(1), p. e14744, <https://onlinelibrary.wiley.com/doi/pdf/10.1111/psyp.14744>.
- Cheung, B., Howard, I. and Money, K. (1991). Visually-induced sickness in normal and bilaterally labyrinthine-defective subjects. *Aviation, Space, and Environmental Medicine*, 62(6), pp. 527–531.
- Chollet, F. (2017). Xception: Deep Learning with Depthwise Separable Convolutions. In *2017 IEEE Conference on Computer Vision and Pattern Recognition (CVPR)*, pp. 1251–1258, <https://doi.org/10.1109/CVPR.2017.195>.

- Chu, H., Li, M.-H., Juan, S.-H. and Chiou, W.-Y. (2012). Effects of Transcutaneous Electrical Nerve Stimulation on Motion Sickness Induced by Rotary Chair: A Crossover Study. *The Journal of Alternative and Complementary Medicine*, 18(5), pp. 494–500, <https://doi.org/10.1089/acm.2011.0366>.
- Chu, H., Li, M.-H., Huang, Y.-C. and Lee, S.-Y. (2013). Simultaneous transcutaneous electrical nerve stimulation mitigates simulator sickness symptoms in healthy adults: a crossover study. *BMC Complementary and Alternative Medicine*, 13(1), p. 84, <https://doi.org/10.1186/1472-6882-13-84>.
- Chuang, S.-W., Chuang, C.-H., Yu, Y.-H., King, J.-T. and Lin, C.-T. (2016). EEG Alpha and Gamma Modulators Mediate Motion Sickness-Related Spectral Responses. *International Journal of Neural Systems*, 26(02), p. 1650007, <https://doi.org/10.1142/s0129065716500076>.
- Ciccone, A. B. et al. (2017). Reminder: RMSSD and SD1 are identical heart rate variability metrics. *Muscle & Nerve*, 56(4), pp. 674–678, <https://doi.org/10.1002/mus.25573>.
- Clancy, J. A. et al. (2014). Non-invasive Vagus Nerve Stimulation in Healthy Humans Reduces Sympathetic Nerve Activity. *Brain Stimulation*, 7(6), pp. 871–877, <https://doi.org/10.1016/j.brs.2014.07.031>.
- Classen, S. and Owens, A. (2010). Simulator sickness among returning combat veterans with mild traumatic brain injury and/or post-traumatic stress disorder. *Advances in Transportation Studies*.
- Coenen, A. and Zayachkivska, O. (2013). Adolf Beck: A pioneer in electroencephalography in between Richard Caton and Hans Berger. *Advances in Cognitive Psychology*, 9(4), p. 216, <https://doi.org/10.2478/v10053-008-0148-3>.
- Cohen, J. (2013). *Statistical Power Analysis for the Behavioral Sciences*. Routledge, <https://doi.org/10.4324/9780203771587>.

- Cohen, L. (1995). *Time-frequency analysis*, vol. 778. Prentice hall New Jersey, https://www.abarproject.ir/file_part/product_part/1394-10-29-20161191936423361601286963.pdf.
- Cohen, M. X. (2014). *Analyzing Neural Time Series Data: Theory and Practice*. The MIT Press, <https://doi.org/10.7551/mitpress/9609.001.0001>.
- Cohen, M. X. (2017). Where Does EEG Come From and What Does It Mean? *Trends in Neurosciences*, 40(4), pp. 208–218, <https://doi.org/10.1016/j.tins.2017.02.004>.
- Cowings, P. S., Suter, S., Toscano, W. B., Kamiya, J. and Naifeh, K. (1986). General autonomic components of motion sickness. *Psychophysiology*, 23(5), pp. 542–551, <https://doi.org/10.1111/j.1469-8986.1986.tb00671.x>.
- Csurka, G., Dance, C., Fan, L., Willamowski, J. and Bray, C. (2004). Visual Categorization with Bags of Keypoints. In *Workshop on Statistical Learning in Computer Vision, ECCV*, vol. 1, Prague, pp. 1–2.
- Cuomo-Granston, A. and Drummond, P. D. (2010). Migraine and motion sickness: what is the link? *Progress in Neurobiology*, 91(4), pp. 300–312, <https://doi.org/10.1016/j.pneurobio.2010.04.001>.
- da Silva, F. L. (2011). Computer-assisted EEG diagnosis: pattern recognition and brain mapping. In *Niedermeyer's Electroencephalography: Basic Principles, Clinical Applications and Related Fields*, Lippincott Williams & Wilkins, Philadelphia, pp. 1203–1226.
- da Silva, F. L. (2013). EEG and MEG: Relevance to Neuroscience. *Neuron*, 80(5), pp. 1112–1128, <https://doi.org/10.1016/j.neuron.2013.10.017>.
- Dai, M., Raphan, T. and Cohen, B. (2007). Labyrinthine lesions and motion sickness susceptibility. *Experimental Brain Research*, 178, pp. 477–487, <https://doi.org/10.1007/s00221-006-0759-1>.
- Damasio, A. R. et al. (2000). Subcortical and cortical brain activity during the feeling

- of self-generated emotions. *Nature Neuroscience*, 3(10), pp. 1049–1056, <https://doi.org/10.1038/79871>.
- De Couck, M. et al. (2017). Effects of short and prolonged transcutaneous vagus nerve stimulation on heart rate variability in healthy subjects. *Autonomic Neuroscience*, 203, pp. 88–96, <https://doi.org/10.1016/j.autneu.2016.11.003>.
- de Moraes, T. L. et al. (2023). Brief periods of transcutaneous auricular vagus nerve stimulation improve autonomic balance and alter circulating monocytes and endothelial cells in patients with metabolic syndrome: a pilot study. *Bioelectronic Medicine*, 9(1), p. 7, <https://doi.org/10.1186/s42234-023-00109-2>.
- Delorme, A. and Makeig, S. (2004). EEGLAB: an open source toolbox for analysis of single-trial EEG dynamics including independent component analysis. *Journal of Neuroscience Methods*, 134(1), pp. 9–21, <https://doi.org/10.1016/j.jneumeth.2003.10.009>.
- Dennison, M. S., Wisti, A. Z. and D’Zmura, M. (2016). Use of physiological signals to predict cybersickness. *Displays*, 44, pp. 42–52, <https://doi.org/10.1016/j.displa.2016.07.002>.
- Diels, C. and Bos, J. E. (2016). Self-driving carsickness. *Applied Ergonomics*, 53, pp. 374–382, <https://doi.org/10.1016/j.apergo.2015.09.009>.
- Dierks, T. et al. (2000). Spatial pattern of cerebral glucose metabolism (pet) correlates with localization of intracerebral eeg-generators in alzheimer’s disease. *Clinical Neurophysiology*, 111(10), pp. 1817–1824, [https://doi.org/10.1016/S1388-2457\(00\)00427-2](https://doi.org/10.1016/S1388-2457(00)00427-2).
- Dietrich, S. et al. (2008). A novel transcutaneous vagus nerve stimulation leads to brainstem and cerebral activations measured by functional MRI. *Biomedical Engineering*, <https://doi.org/10.1515/bmt.2008.022>.
- Dimitrov, B. and Gatev, P. (2015). Effects of Acute Transcutaneous Vagal Stimulation on the EEG Power Maps, EEG Sources Distribution and Steadiness of Quiet and

- Sensory-conflicted Stance. In *Posture, Balance and the Brain. International Workshop Proceedings. Biomedical Data Journal*, pp. 45–54, <http://dx.doi.org/10.11610/posture.07>.
- Dlugaiczek, J., Gensberger, K. D. and Straka, H. (2019). Galvanic vestibular stimulation: from basic concepts to clinical applications. *Journal of Neurophysiology*, 121(6), pp. 2237–2255, <https://doi.org/10.1152/jn.00035.2019>.
- Dosovitskiy, A. (2020). An Image is Worth 16x16 Words: Transformers for Image Recognition at Scale. *arXiv preprint arXiv:201011929*, <https://doi.org/10.48550/arXiv.2010.11929>.
- Downing, P. E., Jiang, Y., Shuman, M. and Kanwisher, N. (2001). A cortical area selective for visual processing of the human body. *Science*, 293(5539), pp. 2470–2473, <https://doi.org/10.1126/science.1063414>.
- Du, X.-J., Dart, A. and Riemersma, R. (1994). Sex differences in the parasympathetic nerve control of rat heart. *Clinical and Experimental Pharmacology and Physiology*, 21(6), pp. 485–493, <https://doi.org/10.1111/j.1440-1681.1994.tb02545.x>.
- Dużmańska, N., Strojny, P. and Strojny, A. (2018). Can simulator sickness be avoided? A review on temporal aspects of simulator sickness. *Frontiers in Psychology*, 9, p. 410742, <https://doi.org/10.3389/fpsyg.2018.02132>.
- Einthoven, W. (1901). Un nouveau galvanometre. *Arch Neerl Sc Ex Nat*, 6, pp. 625–633.
- Ellrich, J. (2019). Transcutaneous Auricular Vagus Nerve Stimulation. *Journal of Clinical Neurophysiology*, 36(6), pp. 437–442, <https://doi.org/10.1097/wnp.0000000000000576>.
- Ewing, D. J., Neilson, J. and Travis, P. (1984). New method for assessing cardiac parasympathetic activity using 24 hour electrocardiograms. *Heart*, 52(4), pp. 396–402, <https://doi.org/10.1136/hrt.52.4.396>.

- Fang, J. et al. (2016). Transcutaneous Vagus Nerve Stimulation Modulates Default Mode Network in Major Depressive Disorder. *Biological Psychiatry*, 79(4), pp. 266–273, <https://doi.org/10.1016/j.biopsych.2015.03.025>.
- Farmer, A. D. et al. (2014a). Normal values and reproducibility of the real-time index of vagal tone in healthy humans: a multi-center study. *Annals of Gastroenterology*, 27(4), p. 362, <https://pmc.ncbi.nlm.nih.gov/articles/PMC4188934>.
- Farmer, A. D., Al Omran, Y., Aziz, Q. and Andrews, P. L. (2014b). The role of the parasympathetic nervous system in visually induced motion sickness: systematic review and meta-analysis. *Experimental Brain Research*, 232, pp. 2665–2673, <https://doi.org/10.1007/s00221-014-3964-3>.
- Farmer, A. D. et al. (2015). Visually induced nausea causes characteristic changes in cerebral, autonomic and endocrine function in humans. *The Journal of Physiology*, 593(5), pp. 1183–1196, <https://doi.org/10.1113/jphysiol.2014.284240>.
- Farmer, A. D. et al. (2021). International Consensus Based Review and Recommendations for Minimum Reporting Standards in Research on Transcutaneous Vagus Nerve Stimulation (Version 2020). *Frontiers in Human Neuroscience*, 14, p. 568051, <https://doi.org/10.3389/fnhum.2020.568051>.
- Fiene, M. et al. (2020). Phase-specific manipulation of rhythmic brain activity by transcranial alternating current stimulation. *Brain Stimulation*, 13(5), pp. 1254–1262, <https://doi.org/10.1016/j.brs.2020.06.008>.
- Forte, G. et al. (2022). Ear your heart: transcutaneous auricular vagus nerve stimulation on heart rate variability in healthy young participants. *PeerJ*, 10, p. e14447, <https://doi.org/10.7717/peerj.14447>.
- Frangos, E., Ellrich, J. and Komisaruk, B. R. (2015). Non-invasive Access to the Vagus Nerve Central Projections via Electrical Stimulation of the External Ear: fMRI Evidence in Humans. *Brain Stimulation*, 8(3), pp. 624–636, <https://doi.org/10.1016/j.brs.2014.11.018>.

- Frangos, E. and Komisaruk, B. R. (2017). Access to Vagal Projections via Cutaneous Electrical Stimulation of the Neck: fMRI Evidence in Healthy Humans. *Brain Stimulation*, 10(1), pp. 19–27, <https://doi.org/10.1016/j.brs.2016.10.008>.
- Fuchs, M., Kastner, J., Wagner, M., Hawes, S. and Ebersole, J. S. (2002). A standardized boundary element method volume conductor model. *Clinical Neurophysiology*, 113(5), pp. 702–712, [https://doi.org/10.1016/s1388-2457\(02\)00030-5](https://doi.org/10.1016/s1388-2457(02)00030-5).
- Furman, J. M., Marcus, D. A. and Balaban, C. D. (2011). Rizatriptan reduces vestibular-induced motion sickness in migraineurs. *The Journal of Headache and Pain*, 12, pp. 81–88, <https://doi.org/10.1007/s10194-010-0250-z>.
- Gálvez-García, G., Hay, M. and Gabaude, C. (2015). Alleviating simulator sickness with galvanic cutaneous stimulation. *Human Factors*, 57(4), pp. 649–657, <https://doi.org/10.1177/0018720814554948>.
- Gálvez-García, G. et al. (2020). Decreasing motion sickness by mixing different techniques. *Applied Ergonomics*, 82, p. 102931, <https://doi.org/10.1016/j.apergo.2019.102931>.
- Gancheva, S. et al. (2018). Constant hepatic ATP concentrations during prolonged fasting and absence of effects of Cerbomed Nemos® on parasympathetic tone and hepatic energy metabolism. *Molecular Metabolism*, 7, pp. 71–79, <https://doi.org/10.1016/j.molmet.2017.10.002>.
- Geng, D., Liu, X., Wang, Y. and Wang, J. (2022). The effect of transcutaneous auricular vagus nerve stimulation on HRV in healthy young people. *PLoS ONE*, 17(2), p. e0263833, <https://doi.org/10.1371/journal.pone.0263833>.
- Gianaros, P. J., Muth, E. R., Mordkoff, J. T., Levine, M. E. and Stern, R. M. (2001). A questionnaire for the assessment of the multiple dimensions of motion sickness. *Aviation, Space, and Environmental Medicine*, 72(2), p. 115, <https://pubmed.ncbi.nlm.nih.gov/articles/PMC2910410>.

- Gianaros, P. J. et al. (2003). Relationship between temporal changes in cardiac parasympathetic activity and motion sickness severity. *Psychophysiology*, 40(1), pp. 39–44, <https://doi.org/10.1111/1469-8986.00005>.
- Goldberger, A. L., Rigney, D. R. and West, B. J. (1990). Chaos and fractals in human physiology. *Scientific American*, 262(2), pp. 42–49, <https://doi.org/10.1038/scientificamerican0290-42>.
- Golding, J. F. (1998). Motion sickness susceptibility questionnaire revised and its relationship to other forms of sickness. *Brain Research Bulletin*, 47(5), pp. 507–516, [https://doi.org/10.1016/s0361-9230\(98\)00091-4](https://doi.org/10.1016/s0361-9230(98)00091-4).
- Golding, J. F. (2006). Predicting individual differences in motion sickness susceptibility by questionnaire. *Personality and Individual Differences*, 41(2), pp. 237–248, <https://doi.org/10.1016/j.paid.2006.01.012>.
- Golding, J. F. and Gresty, M. A. (2015). Pathophysiology and treatment of motion sickness. *Current Opinion in Neurology*, 28(1), pp. 83–88, <https://doi.org/10.1097/wco.000000000000163>.
- Graybiel, A. (1970). *Susceptibility to acute motion sickness in blind persons*, vol. 1100. US Naval Aerospace Medical Institute, Naval Aerospace Medical Center.
- Graybiel, A. and Lackner, J. R. (1987). Treatment of severe motion sickness with antimotion sickness drug injections. *Aviation, Space, and Environmental Medicine*, 58(8), pp. 773–776.
- Gresty, M. A. and Golding, J. F. (2009). Impact of vertigo and spatial disorientation on concurrent cognitive tasks. *Annals of the New York Academy of Sciences*, 1164(1), pp. 263–267, <https://doi.org/10.1111/j.1749-6632.2008.03744.x>.
- Gresty, M. A., Golding, J. F., Le, H. and Nightingale, K. (2008). Cognitive impairment by spatial disorientation. *Aviation, Space, and Environmental Medicine*, 79(2), pp. 105–111, <https://doi.org/10.3357/asem.2143.2008>.

- Gurel, N. Z. et al. (2020). Automatic Detection of Target Engagement in Transcutaneous Cervical Vagal Nerve Stimulation for Traumatic Stress Triggers. *IEEE Journal of Biomedical and Health Informatics*, 24(7), pp. 1917–1925, <https://doi.org/10.1109/JBHI.2020.2981116>.
- Haas, L. F. (2003). Hans Berger (1873-1941), Richard Caton (1842-1926), and electroencephalography. *Journal of Neurology, Neurosurgery & Psychiatry*, 74(1), pp. 9–9, <https://doi.org/10.1136/jnnp.74.1.9>.
- Halder, T., Talwar, S., Jaiswal, A. K. and Banerjee, A. (2019). Quantitative Evaluation in Estimating Sources Underlying Brain Oscillations Using Current Source Density Methods and Beamformer Approaches. *eNeuro*, 6(4), <https://doi.org/10.1523/eneuro.0170-19.2019>.
- Hauk, O., Stenroos, M. and Treder, M. S. (2022). Towards an objective evaluation of EEG/MEG source estimation methods – The linear approach. *NeuroImage*, 255, p. 119177, <https://doi.org/10.1016/j.neuroimage.2022.119177>.
- He, K., Zhang, X., Ren, S. and Sun, J. (2016). Deep Residual Learning for Image Recognition. In *2016 IEEE Conference on Computer Vision and Pattern Recognition (CVPR)*, pp. 770–778, <https://doi.org/10.1109/CVPR.2016.90>.
- Hein, E. et al. (2013). Auricular transcutaneous electrical nerve stimulation in depressed patients: a randomized controlled pilot study. *Journal of Neural Transmission*, 120, pp. 821–827, <https://doi.org/10.1007/s00702-012-0908-6>.
- Henriques, I. F., Douglas de Oliveira, D. W., Oliveira-Ferreira, F. and Andrade, P. M. (2014). Motion sickness prevalence in school children. *European Journal of Pediatrics*, 173, pp. 1473–1482, <https://doi.org/10.1007/s00431-014-2351-1>.
- Himi, N. et al. (2004). Differences in autonomic responses between subjects with and without nausea while watching an irregularly oscillating video. *Autonomic Neuroscience*, 116(1-2), pp. 46–53, <https://doi.org/10.1016/j.autneu.2004.08.008>.

- Holmes, S. R. and Griffin, M. J. (2001). Correlation Between Heart Rate and the Severity of Motion Sickness Caused by Optokinetic Stimulation. *Journal of Psychophysiology*, 15(1), p. 35, <https://doi.org/10.1027//0269-8803.15.1.35>.
- Hromatka, B. S. et al. (2015). Genetic variants associated with motion sickness point to roles for inner ear development, neurological processes and glucose homeostasis. *Human Molecular Genetics*, 24(9), pp. 2700–2708, <https://doi.org/10.1093/hmg/ddv028>.
- Huang, G., Liu, Z., Van Der Maaten, L. and Weinberger, K. Q. (2017). Densely Connected Convolutional Networks. In *2017 IEEE Conference on Computer Vision and Pattern Recognition (CVPR)*, pp. 4700–4708, <https://doi.org/10.1109/CVPR.2017.243>.
- Huang, K.-C. et al. (2021). Comparing the Differences in Brain Activities and Neural Comodulations Associated With Motion Sickness Between Drivers and Passengers. *IEEE Transactions on Neural Systems and Rehabilitation Engineering*, 29, pp. 1259–1267, <https://doi.org/10.1109/TNSRE.2021.3092876>.
- Huang, R.-S., Jung, T.-P. and Makeig, S. (2009). Tonic Changes in EEG Power Spectra during Simulated Driving. In D. D. Schmorow, I. V. Estabrooke and M. Grootjen, eds., *Foundations of Augmented Cognition. Neuroergonomics and Operational Neuroscience*, Berlin, Heidelberg: Springer Berlin Heidelberg, pp. 394–403, https://doi.org/10.1007/978-3-642-02812-0_47.
- Huang, Y. H. et al. (2022). Detecting paroxysmal atrial fibrillation from normal sinus rhythm in equine athletes using Symmetric Projection Attractor Reconstruction and machine learning. *Cardiovascular Digital Health Journal*, 3(2), pp. 96–106, <https://doi.org/10.1016/j.cvdhj.2022.02.001>.
- Hulsey, D. R. et al. (2016). Reorganization of Motor Cortex by Vagus Nerve Stimulation Requires Cholinergic Innervation. *Brain Stimulation*, 9(2), pp. 174–181, <https://doi.org/10.1016/j.brs.2015.12.007>.

- Hulsey, D. R., Shedd, C. M., Sarker, S. F., Kilgard, M. P. and Hays, S. A. (2019). Norepinephrine and serotonin are required for vagus nerve stimulation directed cortical plasticity. *Experimental Neurology*, 320, p. 112975, <https://doi.org/10.1016/j.expneurol.2019.112975>.
- Hwang, J.-U., Bang, J.-S. and Lee, S.-W. (2022). Classification of Motion Sickness Levels using Multimodal Biosignals in Real Driving Conditions. In *2022 IEEE International Conference on Systems, Man, and Cybernetics (SMC)*, IEEE, pp. 1304–1309, <https://doi.org/10.1109/SMC53654.2022.9945559>.
- Irwin, J. (1881). THE PATHOLOGY OF SEA-SICKNESS. *The Lancet*, 118(3039), pp. 907–909, [https://doi.org/10.1016/S0140-6736\(02\)38129-7](https://doi.org/10.1016/S0140-6736(02)38129-7).
- Islam, R. et al. (2020). Automatic Detection and Prediction of Cybersickness Severity using Deep Neural Networks from user's Physiological Signals. In *2020 IEEE International Symposium on Mixed and Augmented Reality (ISMAR)*, IEEE, pp. 400–411, <https://doi.org/10.1109/ISMAR50242.2020.00066>.
- James, W. (1883). THE SENSE OF DIZZINESS IN DEAF-MUTES. *American Annals of the Deaf and Dumb*, 28(2), pp. 102–117, <https://www.jstor.org/stable/44460811>.
- Jansen, K. et al. (2011). Autonomic effects of refractory epilepsy on heart rate variability in children: influence of intermittent vagus nerve stimulation. *Developmental Medicine & Child Neurology*, 53(12), pp. 1143–1149, <https://doi.org/10.1111/j.1469-8749.2011.04103.x>.
- Jardine, D. L. et al. (1998). Autonomic control of vasovagal syncope. *American Journal of Physiology-Heart and Circulatory Physiology*, 274(6), pp. H2110–H2115, <https://doi.org/10.1152/ajpheart.1998.274.6.h2110>.
- Jatoi, M. A., Kamel, N., Malik, A. S. and Faye, I. (2014). EEG based brain source localization comparison of sLORETA and eLORETA. *Australasian Physical & Engineering Sciences in Medicine*, 37, pp. 713–721, <https://doi.org/10.1007/s13246-014-0308-3>.

- Johns Hopkins Medicine (2019). Anatomy and Function of the Heart's Electrical System. Available at: <https://www.hopkinsmedicine.org/health/conditions-and-diseases/anatomy-and-function-of-the-hearts-electrical-system>, [Accessed 6 Mar. 2024].
- Johnson, W. H., Sunahara, F. A. and Landolt, J. P. (1999). Importance of the vestibular system in visually induced nausea and self-vection. *Journal of Vestibular Research*, 9(2), pp. 83–87, <https://doi.org/10.3233/VES-1999-9202>.
- Kaboodvand, N., Karimi, H. and Iravani, B. (2024). Preparatory activity of anterior insula predicts conflict errors: integrating convolutional neural networks and neural mass models. *Scientific Reports*, 14(1), p. 16682, <https://doi.org/10.1038/s41598-024-67034-5>.
- Kaniusas, E. et al. (2019). Current Directions in the Auricular Vagus Nerve Stimulation I – A Physiological Perspective. *Frontiers in Neuroscience*, 13, p. 854, <https://doi.org/10.3389/fnins.2019.00854>.
- Kennedy, R. S., Drexler, J. and Kennedy, R. C. (2010). Research in visually induced motion sickness. *Applied Ergonomics*, 41(4), pp. 494–503, <https://doi.org/10.1016/j.apergo.2009.11.006>.
- Kennedy, R. S., Graybiel, A., McDonough, R. C. and Beckwith, D. (1968). Symptomatology under storm Conditions in the North Atlantic in Control Subjects and in Persons with Bilateral Labyrinthine Defects. *Acta Oto-Laryngologica*, 66(1-6), pp. 533–540, <https://doi.org/10.3109/00016486809126317>.
- Kennedy, R. S., Lane, N. E., Berbaum, K. S. and Lilienthal, M. G. (1993). Simulator Sickness Questionnaire: An Enhanced Method for Quantifying Simulator Sickness. *The International Journal of Aviation Psychology*, 3(3), pp. 203–220, https://doi.org/10.1207/s15327108ijap0303_3.
- Keshavarz, B. and Golding, J. F. (2022). Motion sickness: current concepts and management. *Current Opinion in Neurology*, 35(1), pp. 107–112, <https://doi.org/10.1097/wco.0000000000001018>.

- Keshavarz, B., Peck, K., Rezaei, S. and Taati, B. (2022). Detecting and predicting visually induced motion sickness with physiological measures in combination with machine learning techniques. *International Journal of Psychophysiology*, 176, pp. 14–26, <https://doi.org/10.1016/j.ijpsycho.2022.03.006>.
- Keute, M., Machetanz, K., Berelidze, L., Guggenberger, R. and Gharabaghi, A. (2021). Neuro-cardiac coupling predicts transcutaneous auricular vagus nerve stimulation effects. *Brain Stimulation*, 14(2), pp. 209–216, <https://doi.org/10.1016/j.brs.2021.01.001>.
- Kim, A. Y. et al. (2022). Safety of transcutaneous auricular vagus nerve stimulation (taVNS): a systematic review and meta-analysis. *Scientific Reports*, 12(1), p. 22055, <https://doi.org/10.1038/s41598-022-25864-1>.
- Kim, J., Napadow, V., Kuo, B. and Barbieri, R. (2011). A combined HRV-fMRI approach to assess cortical control of cardiovascular modulation by motion sickness. In *2011 Annual International Conference of the IEEE Engineering in Medicine and Biology Society*, IEEE, pp. 2825–2828, <https://doi.org/10.1109/IEMBS.2011.6090781>.
- Kim, J.-Y., Son, J.-B., Leem, H.-S. and Lee, S.-H. (2019). Psychophysiological Alteration After Virtual Reality Experiences Using Smartphone-Assisted Head Mount Displays: An EEG-Based Source Localization Study. *Applied Sciences*, 9(12), p. 2501, <https://doi.org/10.3390/app9122501>.
- Klaus, M. P. et al. (2020). Vestibular Stimulation Modulates Neural Correlates of Own-body Mental Imagery. *Journal of Cognitive Neuroscience*, 32(3), pp. 484–496, https://doi.org/10.1162/jocn_a.01496.
- Kleiger, R. E., Stein, P. K. and Bigger Jr, J. T. (2005). Heart rate variability: measurement and clinical utility. *Annals of Noninvasive Electrocardiology*, 10(1), pp. 88–101, <https://doi.org/10.1111/j.1542-474x.2005.10101.x>.
- Kleiner, M., Brainard, D. H. and Pelli, D. (2007). What's new in Psychtoolbox-3? *Perception*, 36, pp. 1–16, <https://doi.org/10.1177/03010066070360S101>.

- Klosterhalfen, S. et al. (2005). Effects of ethnicity and gender on motion sickness susceptibility. *Aviation, Space, and Environmental Medicine*, 76(11), pp. 1051–1057.
- Koch, K. (1999). Illusory self-motion and motion sickness: a model for brain-gut interactions and nausea. *Digestive Diseases and Sciences*, 44(8 Suppl), pp. 53S–57S.
- Koenig, J. and Thayer, J. F. (2016). Sex differences in healthy human heart rate variability: A meta-analysis. *Neuroscience & Biobehavioral Reviews*, 64, pp. 288–310, <https://doi.org/10.1016/j.neubiorev.2016.03.007>.
- Koenig, J., Rash, J. A., Campbell, T. S., Thayer, J. F. and Kaess, M. (2017). A Meta-Analysis on Sex Differences in Resting-State Vagal Activity in Children and Adolescents. *Frontiers in Physiology*, 8, p. 582, <https://doi.org/10.3389/fphys.2017.00582>.
- Kohl, R. L. and Homick, J. L. (1983). Motion sickness: a modulatory role for the central cholinergic nervous system. *Neuroscience & Biobehavioral Reviews*, 7(1), pp. 73–85, [https://doi.org/10.1016/0149-7634\(83\)90008-8](https://doi.org/10.1016/0149-7634(83)90008-8).
- Kovács, G., Raabe, M. and Greenlee, M. W. (2008). Neural correlates of visually induced self-motion illusion in depth. *Cerebral Cortex*, 18(8), pp. 1779–1787, <https://doi.org/10.1093/cercor/bhm203>.
- Kraus, T. et al. (2007). BOLD fMRI deactivation of limbic and temporal brain structures and mood enhancing effect by transcutaneous vagus nerve stimulation. *Journal of Neural Transmission*, 114, pp. 1485–1493, <https://doi.org/10.1007/s00702-007-0755-z>.
- Kraus, T. et al. (2013). CNS BOLD fMRI effects of sham-controlled transcutaneous electrical nerve stimulation in the left outer auditory canal – a pilot study. *Brain Stimulation*, 6(5), pp. 798–804, <https://doi.org/10.1016/j.brs.2013.01.011>.
- Kreisberg, E. et al. (2021). High-resolution computational modeling of the current flow in the outer ear during transcutaneous auricular Vagus Nerve Stimulation (taVNS). *Brain Stimulation*, 14(6), pp. 1419–1430, <https://doi.org/10.1016/j.brs.2021.09.001>.

- Kulkarni, K. et al. (2021). Low-Level Tragus Stimulation Modulates Atrial Alternans and Fibrillation Burden in Patients With Paroxysmal Atrial Fibrillation. *Journal of the American Heart Association*, 10(12), p. e020865, <https://doi.org/10.1161/jaha.120.020865>.
- Kumar, H. U. et al. (2023). Autonomic regulation therapy in chronic heart failure with preserved/mildly reduced ejection fraction: ANTHEM-HFpEF study results. *International Journal of Cardiology*, 381, pp. 37–44, <https://doi.org/10.1016/j.ijcard.2023.03.030>.
- Laborde, S., Mosley, E. and Thayer, J. F. (2017). Heart Rate Variability and Cardiac Vagal Tone in Psychophysiological Research – Recommendations for Experiment Planning, Data Analysis, and Data Reporting. *Frontiers in Psychology*, 8, p. 238557, <https://doi.org/10.3389/fpsyg.2017.00213>.
- Lackner, J. R. (2014). Motion sickness: more than nausea and vomiting. *Experimental Brain Research*, 232, pp. 2493–2510, <https://doi.org/10.1007/s00221-014-4008-8>.
- Lackner, J. R. (2019). Motion Sickness: Our Evolving Understanding and Problems. In *Reference Module in Neuroscience and Biobehavioral Psychology*, Elsevier, pp. 1–10, <https://doi.org/10.1016/B978-0-12-809324-5.21621-0>.
- LaCount, L. T. et al. (2009). Dynamic Cardiovagal Response to Motion Sickness: A Point-Process Heart Rate Variability Study. In *2009 36th Annual Computers in Cardiology Conference (CinC)*, IEEE, pp. 49–52, <https://pmc.ncbi.nlm.nih.gov/articles/PMC2863354>.
- LaCount, L. T. et al. (2011). Static and dynamic autonomic response with increasing nausea perception. *Aviation, Space, and Environmental Medicine*, 82(4), pp. 424–433, <https://doi.org/10.3357/asem.2932.2011>.
- Lamb, D. G., Porges, E. C., Lewis, G. F. and Williamson, J. B. (2017). Non-invasive Vagal Nerve Stimulation Effects on Hyperarousal and Autonomic State in Patients with Posttraumatic Stress Disorder and History of Mild Traumatic Brain Injury: Preliminary Evidence. *Frontiers in Medicine*, 4, p. 124, <https://doi.org/10.3389/fmed.2017.00124>.

- Lee, T.-W. and Tramontano, G. (2024). Neural consequences of 5-Hz transcranial alternating current stimulation over right hemisphere: an eLORETA EEG study. *Neuroscience Letters*, p. 137849, <https://doi.org/10.1016/j.neulet.2024.137849>.
- Leroy, A. and Cheron, G. (2020). EEG dynamics and neural generators of psychological flow during one tightrope performance. *Scientific Reports*, 10(1), p. 12449, <https://doi.org/10.1038/s41598-020-69448-3>.
- Levine, M. E., Stern, R. M. and Koch, K. L. (2014). Enhanced perceptions of control and predictability reduce motion-induced nausea and gastric dysrhythmia. *Experimental Brain Research*, 232(8), pp. 2675–2684, <https://doi.org/10.1007/s00221-014-3950-9>.
- Lewine, J. D., Paulson, K., Bangera, N. and Simon, B. J. (2019). Exploration of the Impact of Brief Noninvasive Vagal Nerve Stimulation on EEG and Event-Related Potentials. *Neuromodulation*, 22(5), pp. 564–572, <https://doi.org/10.1111/ner.12864>.
- Li, G. et al. (2020). Exploring the feasibility of mitigating VR-HMD-induced cybersickness using cathodal transcranial direct current stimulation. In *2020 IEEE International Conference on Artificial Intelligence and Virtual Reality (AIVR)*, pp. 123–129, <https://doi.org/10.1109/AIVR50618.2020.00030>.
- Lin, C.-L. et al. (2013). Self-adjustments may account for the contradictory correlations between HRV and motion-sickness severity. *International Journal of Psychophysiology*, 87(1), pp. 70–80, <https://doi.org/10.1016/j.ijpsycho.2012.11.003>.
- Lin, C.-T. et al. (2007). EEG Effects of Motion Sickness Induced in a Dynamic Virtual Reality Environment. In *2007 29th Annual International Conference of the IEEE Engineering in Medicine and Biology Society*, IEEE, pp. 3872–3875, <https://doi.org/10.1109/IEMBS.2007.4353178>.
- Lin, C.-T., Lin, C.-L., Chiu, T.-W., Duann, J.-R. and Jung, T.-P. (2011). Effect of respiratory modulation on relationship between heart rate variability and motion sickness. In *2011 Annual International Conference of the IEEE Engineering in Medicine and Biology Society*, IEEE, pp. 1921–1924, <https://doi.org/10.1109/IEMBS.2011.6090543>.

- Lipsitz, L. A. and Goldberger, A. L. (1992). Loss of 'complexity' and aging. Potential applications of fractals and chaos theory to senescence. *JAMA*, 267(13), pp. 1806–1809, <https://doi.org/10.1001/jama.1992.03480130122036>.
- Liu, R., Xu, M., Zhang, Y., Peli, E. and Hwang, A. D. (2020). A Pilot Study on EEG-Based Evaluation of Visually Induced Motion Sickness. *The Journal of Imaging Science and Technology*, 64(2), pp. 20501–1, <https://doi.org/10.2352/j.imagingsci.technol.2020.64.2.020501>.
- Lomb, N. R. (1976). Least-squares frequency analysis of unequally spaced data. *Astrophysics and Space Science*, 39, pp. 447–462, <https://doi.org/10.1007/BF00648343>.
- Lu, G., Yang, F., Taylor, J. A. and Stein, J. F. (2009). A comparison of photoplethysmography and ECG recording to analyse heart rate variability in healthy subjects. *Journal of Medical Engineering & Technology*, 33(8), pp. 634–641, <https://doi.org/10.3109/03091900903150998>.
- Lu, S. et al. (2008). Can photoplethysmography variability serve as an alternative approach to obtain heart rate variability information? *Journal of Clinical Monitoring and Computing*, 22, pp. 23–29, <https://doi.org/10.1007/s10877-007-9103-y>.
- Lyle, J. and Aston, P. (2021). Symmetric projection attractor reconstruction: Embedding in higher dimensions. *Chaos*, 31(11), <https://doi.org/10.1063/5.0064450>.
- Lyle, J. V., Nandi, M. and Aston, P. J. (2019). Investigating the Response to Dofetilide with Symmetric Projection Attractor Reconstruction of the Electrocardiogram. In *2019 Computing in Cardiology (CinC)*, IEEE, pp. Page–1, <https://doi.org/10.22489/CinC.2019.073>.
- Lyle, J. V., Nandi, M. and Aston, P. J. (2021). Symmetric Projection Attractor Reconstruction: Sex Differences in the ECG. *Frontiers in Cardiovascular Medicine*, 8, p. 709457, <https://doi.org/10.3389/fcvm.2021.709457>.

- Lyle, J. V. et al. (2017). Beyond HRV: Analysis of ECG signals using attractor reconstruction. In *2017 Computing in Cardiology (CinC)*, IEEE, pp. 1–4, <https://doi.org/10.22489/CinC.2017.091-096>.
- Machetanz, K., Berelidze, L., Guggenberger, R. and Gharabaghi, A. (2021). Transcutaneous auricular vagus nerve stimulation and heart rate variability: Analysis of parameters and targets. *Autonomic Neuroscience*, 236, p. 102894, <https://doi.org/10.1016/j.autneu.2021.102894>.
- Machuca-Márquez, P. et al. (2023). Vestibular CCK signaling drives motion sickness-like behavior in mice. *Proceedings of the National Academy of Sciences*, 120(44), p. e2304933120, <https://doi.org/10.1073/pnas.2304933120>.
- Maestri, R. et al. (2024). Impact of optimized transcutaneous auricular vagus nerve stimulation on cardiac autonomic profile in healthy subjects and heart failure patients. *Physiological Measurement*, 45(7), p. 075007, <https://doi.org/10.1088/1361-6579/ad5ef6>.
- Marcus, D. A., Furman, J. M. and Balaban, C. D. (2005). Motion sickness in migraine sufferers. *Expert Opinion on Pharmacotherapy*, 6(15), pp. 2691–2697, <https://doi.org/10.1517/14656566.6.15.2691>.
- Maris, E. and Oostenveld, R. (2007). Nonparametric statistical testing of EEG-and MEG-data. *Journal of Neuroscience Methods*, 164(1), pp. 177–190, <https://doi.org/10.1016/j.jneumeth.2007.03.024>.
- Maruta, J. (2024). On labyrinthine function loss, motion sickness immunity, and velocity storage. *Frontiers in Neurology*, 15, p. 1426213, <https://doi.org/10.3389/fneur.2024.1426213>.
- Matsangas, P. and McCauley, M. E. (2014). Yawning as a behavioral marker of mild motion sickness and sopite syndrome. *Aviation, Space, and Environmental Medicine*, 85(6), pp. 658–661, <https://doi.org/10.3357/asem.3897.2014>.

- Matsangas, P., McCauley, M. E. and Becker, W. (2014). The effect of mild motion sickness and sopite syndrome on multitasking cognitive performance. *Human Factors*, 56(6), pp. 1124–1135, <https://doi.org/10.1177/0018720814522484>.
- Mazziotta, J. et al. (2001). A probabilistic atlas and reference system for the human brain: International Consortium for Brain Mapping (ICBM). *Philosophical Transactions of the Royal Society of London Series B: Biological Sciences*, 356(1412), pp. 1293–1322, <https://doi.org/10.1098/rstb.2001.0915>.
- McKinley, P. S. et al. (2003). Deriving heart period variability from blood pressure waveforms. *Journal of Applied Physiology*, 95(4), pp. 1431–1438, <https://doi.org/10.1152/japplphysiol.01110.2002>.
- Meijs, H. et al. (2024). A posterior-alpha ageing network is differentially associated with antidepressant effects of venlafaxine and rTMS. *European Neuropsychopharmacology*, 79, pp. 7–16, <https://doi.org/10.1016/j.euroneuro.2023.11.002>.
- Menon, V. and Uddin, L. Q. (2010). Saliency, switching, attention and control: a network model of insula function. *Brain Structure and Function*, 214, pp. 655–667, <https://doi.org/10.1007/s00429-010-0262-0>.
- Mietus, J., Peng, C.-K., Henry, I., Goldsmith, R. and Goldberger, A. (2002). The pNNx files: re-examining a widely used heart rate variability measure. *Heart*, 88(4), pp. 378–380, <https://doi.org/10.1136/heart.88.4.378>.
- Mittelstaedt, J. M. (2020). Individual predictors of the susceptibility for motion-related sickness: A systematic review. *Journal of Vestibular Research*, 30(3), pp. 165–193, <https://doi.org/10.3233/VES-200702>.
- Molefi, E., McLoughlin, I. and Palaniappan, R. (2023a). On the potential of transauricular electrical stimulation to reduce visually induced motion sickness. *Scientific Reports*, 13(1), p. 3272, <https://doi.org/10.1038/s41598-023-29765-9>.
- Molefi, E., McLoughlin, I. and Palaniappan, R. (2023b). Transcutaneous Auricular Vagus Nerve Stimulation towards Visually Induced Motion Sickness Reduction: A Pilot

- Study. In *2023 45th Annual International Conference of the IEEE Engineering in Medicine & Biology Society (EMBC)*, pp. 1–4, <https://doi.org/10.1109/EMBC40787.2023.10340374>.
- Molefi, E., McLoughlin, I. and Palaniappan, R. (2023c). Heart Rate Variability Responses to Visually Induced Motion Sickness. In *2023 45th Annual International Conference of the IEEE Engineering in Medicine & Biology Society (EMBC)*, pp. 1–4, <https://doi.org/10.1109/EMBC40787.2023.10340636>.
- Molefi, E., McLoughlin, I. and Palaniappan, R. (2024). Symmetric projection attractor reconstruction: Transcutaneous auricular vagus nerve stimulation for visually induced motion sickness. *Autonomic Neuroscience*, Under Review.
- Molefi, E., McLoughlin, I. and Palaniappan, R. (2025). Transcutaneous Auricular Vagus Nerve Stimulation for Visually Induced Motion Sickness: An eLORETA Study. *Brain Topography*, 38(1), p. 11, <https://doi.org/10.1007/s10548-024-01088-6>.
- Molefi, E. and Palaniappan, R. (2024). Deep Transfer Learning for Visually Induced Motion Sickness Detection Using Symmetric Projection Attractor Reconstruction of the Electrocardiogram. In *2024 Computing in Cardiology (CinC)*, vol. 51, pp. 1–4, <https://doi.org/10.22489/CinC.2024.212>.
- Money, K. E. (1970). Motion sickness. *Physiological Reviews*, 50(1), pp. 1–39, <https://doi.org/10.1152/physrev.1970.50.1.1>.
- Money, K. E. (1990). *Motion sickness and evolution*. In: Crampton GH, editor. *Motion and space sickness*. Boca Raton: CRC Press.
- Money, K. E., Lackner, J. R. and Cheung, R. S. K. (1996). *The autonomic nervous system and motion sickness*. In: Yates BJ, Miller AD, editors. *Vestibular autonomic regulation*. Boca Raton: CRC Press.
- Moody, G. B. (1993). Spectral analysis of heart rate without resampling. In *Proceedings of Computers in Cardiology Conference*, pp. 715–718, <https://doi.org/10.1109/CIC.1993.378302>.

- Mulert, C. et al. (2004). Integration of fMRI and simultaneous EEG: towards a comprehensive understanding of localization and time-course of brain activity in target detection. *NeuroImage*, 22(1), pp. 83–94, <https://doi.org/10.1016/j.neuroimage.2003.10.051>.
- Murray, A. R., Atkinson, L., Mahadi, M. K., Deuchars, S. A. and Deuchars, J. (2016). The strange case of the ear and the heart: The auricular vagus nerve and its influence on cardiac control. *Autonomic Neuroscience*, 199, pp. 48–53, <https://doi.org/10.1016/j.autneu.2016.06.004>.
- Nandi, M. and Aston, P. J. (2020). Extracting new information from old waveforms: Symmetric projection attractor reconstruction: Where maths meets medicine. *Experimental Physiology*, 105(9), pp. 1444–1451, <https://doi.org/10.1113/ep087873>.
- Nandi, M., Venton, J. and Aston, P. J. (2018). A novel method to quantify arterial pulse waveform morphology: attractor reconstruction for physiologists and clinicians. *Physiological Measurement*, 39(10), p. 104008, <https://doi.org/10.1088/1361-6579/aae46a>.
- Napadow, V. et al. (2013). The brain circuitry underlying the temporal evolution of nausea in humans. *Cerebral Cortex*, 23(4), pp. 806–813, <https://doi.org/10.1093/cercor/bhs073>.
- Naqvi, S. A. A., Badruddin, N., Malik, A. S., Hazabbah, W. and Abdullah, B. (2013). Does 3D produce more symptoms of visually induced motion sickness? In *2013 35th Annual International Conference of the IEEE Engineering in Medicine and Biology Society (EMBC)*, IEEE, pp. 6405–6408, <https://doi.org/10.1109/embc.2013.6611020>.
- Naqvi, S. A. A. et al. (2015). EEG based time and frequency dynamics analysis of visually induced motion sickness (VIMS). *Australasian Physical & Engineering Sciences in Medicine*, 38, pp. 721–729, <https://doi.org/10.1007/s13246-015-0379-9>.
- Nesbitt, A. D., Marin, J. C., Tompkins, E., Rutledge, M. H. and Goadsby, P. J. (2015). Initial use of a novel noninvasive vagus nerve stimulator for cluster

- headache treatment. *Neurology*, 84(12), pp. 1249–1253, <https://doi.org/10.1212/wnl.0000000000001394>.
- Nichols, T. E. and Holmes, A. P. (2002). Nonparametric permutation tests for functional neuroimaging: A primer with examples. *Human Brain Mapping*, 15(1), pp. 1–25, <https://doi.org/10.1002/hbm.1058>.
- Nister, D. and Stewenius, H. (2006). Scalable Recognition with a Vocabulary Tree. In *2006 IEEE Computer Society Conference on Computer Vision and Pattern Recognition (CVPR'06)*, vol. 2, IEEE, pp. 2161–2168, <https://doi.org/10.1109/CVPR.2006.264>.
- Nitsche, M. A. et al. (2008). Transcranial direct current stimulation: State of the art 2008. *Brain Stimulation*, 1(3), pp. 206–223, <https://doi.org/10.1016/j.brs.2008.06.004>.
- Nürnbergger, M., Klingner, C., Witte, O. W. and Brodoehl, S. (2021). Mismatch of Visual-Vestibular Information in Virtual Reality: Is Motion Sickness Part of the Brains Attempt to Reduce the Prediction Error? *Frontiers in Human Neuroscience*, 15, p. 757735, <https://doi.org/10.3389/fnhum.2021.757735>.
- Oman, C. M. (1990). Motion sickness: a synthesis and evaluation of the sensory conflict theory. *Canadian Journal of Physiology and Pharmacology*, 68(2), pp. 294–303, <https://doi.org/10.1139/y90-044>.
- Oman, C. M. (1991). *Pictorial Communication in Virtual and Real Environments*, USA: Taylor & Francis New York, chap. Sensory conflict in motion sickness: an observer theory approach. pp. 362–376, <https://dl.acm.org/doi/10.5555/109350.109394>.
- Oman, C. M. and Cullen, K. E. (2014). Brainstem processing of vestibular sensory exafference: implications for motion sickness etiology. *Experimental Brain Research*, 232, pp. 2483–2492, <https://doi.org/10.1007/s00221-014-3973-2>.
- Orini, M., Bailon, R., Mainardi, L. T., Laguna, P. and Flandrin, P. (2012). Characterization of Dynamic Interactions Between Cardiovascular Signals by Time-Frequency

- Coherence. *IEEE Transactions on Biomedical Engineering*, 59(3), pp. 663–673, <https://doi.org/10.1109/TBME.2011.2171959>.
- Orui, J. et al. (2024). Psychophysiological and interpersonal effects of parallel group crafting: a multimodal study using EEG and ECG. *Scientific Reports*, 14(1), p. 17883, <https://doi.org/10.1038/s41598-024-68980-w>.
- Owens, M. M., Jacquemet, V., Napadow, V., Lewis, N. and Beaumont, E. (2024). Brain-stem neuronal responses to transcutaneous auricular and cervical vagus nerve stimulation in rats. *The Journal of Physiology*, <https://doi.org/10.1113/jp286680>.
- Paciorek, A. and Skora, L. (2020). Vagus Nerve Stimulation as a Gateway to Interoception. *Frontiers in Psychology*, 11, p. 1659, <https://doi.org/10.3389/fpsyg.2020.01659>.
- Paillard, A. C. et al. (2013). Motion sickness susceptibility in healthy subjects and vestibular patients: effects of gender, age and trait-anxiety. *Journal of Vestibular Research*, 23(4-5), pp. 203–209, <https://doi.org/10.3233/ves-130501>.
- Pan, J. and Tompkins, W. J. (1985). A Real-Time QRS Detection Algorithm. *IEEE Transactions on Biomedical Engineering*, BME-32(3), pp. 230–236, <https://doi.org/10.1109/TBME.1985.325532>.
- Park, S., Won, M., Mun, S., Lee, E. and Whang, M. (2014). Does visual fatigue from 3D displays affect autonomic regulation and heart rhythm? *International Journal of Psychophysiology*, 92(1), pp. 42–48, <https://doi.org/10.1016/j.ijpsycho.2014.02.003>.
- Pascual-Marqui, R. D. (2002). Standardized low-resolution brain electromagnetic tomography (sLORETA): technical details. *Methods Find Exp Clin Pharmacol*, 24(Suppl D), pp. 5–12, <https://www.institutpsychoneuro.com/wp-content/uploads/2015/10/sLORETA2002.pdf>.
- Pascual-Marqui, R. D. (2007). Discrete, 3D distributed, linear imaging methods of electric neuronal activity. Part 1: exact, zero error localization. *arXiv preprint arXiv:07103341*, <https://doi.org/10.48550/arXiv.0710.3341>.

- Pascual-Marqui, R. D., Michel, C. M. and Lehmann, D. (1994). Low resolution electromagnetic tomography: a new method for localizing electrical activity in the brain. *International Journal of Psychophysiology*, 18(1), pp. 49–65, [https://doi.org/10.1016/0167-8760\(84\)90014-X](https://doi.org/10.1016/0167-8760(84)90014-X).
- Pascual-Marqui, R. D. et al. (2011). Assessing interactions in the brain with exact low-resolution electromagnetic tomography. *Philosophical Transactions of the Royal Society A: Mathematical, Physical and Engineering Sciences*, 369(1952), pp. 3768–3784, <https://doi.org/10.1098/rsta.2011.0081>.
- Pelli, D. (1997). The VideoToolbox software for visual psychophysics: transforming numbers into movies. *Spatial Vision*, 10 4, pp. 437–42, <https://doi.org/10.1163/156856897X00366>.
- Perez, S. M., Carreno, F. R., Frazer, A. and Lodge, D. J. (2014). Vagal nerve stimulation reverses aberrant dopamine system function in the methylazoxymethanol acetate rodent model of schizophrenia. *Journal of Neuroscience*, 34(28), pp. 9261–9267, <https://doi.org/10.1523/jneurosci.0588-14.2014>.
- Perrin, F., Pernier, J., Bertrand, O. and Echallier, J. F. (1989). Spherical splines for scalp potential and current density mapping. *Electroencephalography and Clinical Neurophysiology*, 72(2), pp. 184–187, [https://doi.org/10.1016/0013-4694\(89\)90180-6](https://doi.org/10.1016/0013-4694(89)90180-6).
- Peuker, E. T. and Filler, T. J. (2002). The nerve supply of the human auricle. *Clinical Anatomy*, 15(1), pp. 35–37, <https://doi.org/10.1002/ca.1089>.
- Pietrzak, K., Grzybowski, A. and Kaczmarczyk, J. (2014). Adolf Beck (1863-1942)-a pioneer of electroencephalography. *European Neurology*, 71(1-2), pp. 32–34, <https://doi.org/10.1159/000354675>.
- Pincus, S. M., Gladstone, I. M. and Ehrenkranz, R. A. (1991). A regularity statistic for medical data analysis. *Journal of Clinical Monitoring*, 7, pp. 335–345, <https://doi.org/10.1007/bf01619355>.

- Pion-Tonachini, L., Kreutz-Delgado, K. and Makeig, S. (2019). ICLabel: An automated electroencephalographic independent component classifier, dataset, and website. *NeuroImage*, 198, pp. 181–197, <https://doi.org/10.1016/j.neuroimage.2019.05.026>.
- Pizzagalli, D. et al. (2004). Functional but not structural subgenual prefrontal cortex abnormalities in melancholia. *Molecular Psychiatry*, 9(4), pp. 393–405, <https://doi.org/10.1038/sj.mp.4001469>.
- Pola, S., Macerata, A., Emdin, M. and Marchesi, C. (1996). Estimation of the power spectral density in nonstationary cardiovascular time series: assessing the role of the time-frequency representations (TFR). *IEEE Transactions on Biomedical Engineering*, 43(1), pp. 46–, <https://doi.org/10.1109/10.477700>.
- Popov, T. et al. (2023). Test–retest reliability of resting-state EEG in young and older adults. *Psychophysiology*, 60(7), p. e14268, <https://doi.org/10.1111/psyp.14268>.
- Prescott, S. L. and Liberles, S. D. (2022). Internal senses of the vagus nerve. *Neuron*, 110(4), pp. 579–599, <https://doi.org/10.1016/j.neuron.2021.12.020>.
- Pukropski, J. et al. (2024). Short-term effects of transcutaneous auricular vagus nerve stimulation on T-wave alternans in people with focal epilepsy – An exploratory pilot study. *Epilepsy & Behavior Reports*, 26, p. 100657, <https://doi.org/10.1016/j.ebr.2024.100657>.
- Quiceno-Manrique, A. F., Alonso-Hernandez, J. B., Travieso-Gonzalez, C., Ferrer-Ballester, M. A. and Castellanos-Dominguez, G. (2009). Detection of obstructive sleep apnea in ECG recordings using time-frequency distributions and dynamic features. In *2009 Annual International Conference of the IEEE Engineering in Medicine and Biology Society*, pp. 5559–5562, <https://doi.org/10.1109/IEMBS.2009.5333736>.
- Rajiah, R., Takahashi, K., Aziz, Q. and Ruffle, J. K. (2022). Brain effect of transcutaneous vagal nerve stimulation: A meta-analysis of neuroimaging evidence. *Neurogastroenterology & Motility*, p. e14484, <https://doi.org/10.1111/nmo.14484>.

- Reason, J. T. (1969). Motion sickness—some theoretical considerations. *International Journal of Man-Machine Studies*, 1(1), pp. 21–38, [https://doi.org/10.1016/S0020-7373\(69\)80009-X](https://doi.org/10.1016/S0020-7373(69)80009-X).
- Reason, J. T. (1970). Motion sickness: a special case of sensory rearrangement. *Advancement of Science*, 26(130), pp. 386–393.
- Reason, J. T. (1978). Motion sickness adaptation: a neural mismatch model. *Journal of the Royal Society of Medicine*, 71(11), pp. 819–829, <https://doi.org/10.1177/014107687807101109>.
- Reason, J. T. and Brand, J. J. (1975). *Motion sickness*. Academic Press.
- Reavley, C. M., Golding, J. F., Cherkas, L. F., Spector, T. D. and MacGregor, A. J. (2006). Genetic influences on motion sickness susceptibility in adult women: a classical twin study. *Aviation, Space, and Environmental Medicine*, 77(11), pp. 1148–1152.
- Reed-Jones, R. J., Vallis, L. A., Reed-Jones, J. G. and Trick, L. M. (2008). The relationship between postural stability and virtual environment adaptation. *Neuroscience Letters*, 435(3), pp. 204–209, <https://doi.org/10.1016/j.neulet.2008.02.047>.
- Ricci, L. et al. (2020). Transcutaneous Vagus Nerve Stimulation Modulates EEG Microstates and Delta Activity in Healthy Subjects. *Brain Sciences*, 10(10), p. 668, <https://doi.org/10.3390/brainsci10100668>.
- Riccio, G. E. and Stoffregen, T. A. (1991). An ecological Theory of Motion Sickness and Postural Instability. *Ecological Psychology*, 3(3), pp. 195–240, https://doi.org/10.1207/s15326969eco0303_2.
- Richman, J. S. and Moorman, J. R. (2000). Physiological time-series analysis using approximate entropy and sample entropy. *Am J Physiol Heart Circ Physiol*, 278(6), pp. H2039–H2049, <https://doi.org/10.1152/ajpheart.2000.278.6.h2039>.

- Romano, J., Kromrey, J. D., Coraggio, J. and Skowronek, J. (2006). Appropriate Statistics for Ordinal Level Data: Should We Really Be Using t-test and Cohen's d for Evaluating Group Differences on the NSSE and other Surveys? In *Annu. Meet. Florida Assoc. Inst. Res.*, vol. 177, p. 34.
- Rorden, C. and Brett, M. (2000). Stereotaxic display of brain lesions. *Behavioural Neurology*, 12(4), pp. 191–200, <https://doi.org/10.1155/2000/421719>.
- Rosenstein, M. T., Collins, J. J. and De Luca, C. J. (1993). A practical method for calculating largest Lyapunov exponents from small data sets. *Physica D: Nonlinear Phenomena*, 65(1), pp. 117–134, [https://doi.org/10.1016/0167-2789\(93\)90009-P](https://doi.org/10.1016/0167-2789(93)90009-P).
- Rowley, C. W., Mezić, I., Bagheri, S., Schlatter, P. and Henningson, D. S. (2009). Spectral analysis of nonlinear flows. *Journal of Fluid Mechanics*, 641, pp. 115–127, <https://doi.org/10.1017/S0022112009992059>.
- Ruffle, J. K. et al. (2019). Functional brain networks and neuroanatomy underpinning nausea severity can predict nausea susceptibility using machine learning. *The Journal of Physiology*, 597(6), pp. 1517–1529, <https://doi.org/10.1113/jp277474>.
- Saredakis, D. et al. (2020). Factors Associated With Virtual Reality Sickness in Head-Mounted Displays: A Systematic Review and Meta-Analysis. *Frontiers in Human Neuroscience*, 14, p. 96, <https://doi.org/10.3389/fnhum.2020.00096>.
- Sassenhagen, J. and Draschkow, D. (2019). Cluster-based permutation tests of MEG/EEG data do not establish significance of effect latency or location. *Psychophysiology*, 56(6), p. e13335, <https://doi.org/10.1111/psyp.13335>.
- Sassi, R. et al. (2015). Advances in heart rate variability signal analysis: joint position statement by the e-Cardiology ESC Working Group and the European Heart Rhythm Association co-endorsed by the Asia Pacific Heart Rhythm Society. *Ep Europace*, 17(9), pp. 1341–1353, <https://doi.org/10.1093/europace/euv015>.
- Scargle, J. D. (1982). Studies in astronomical time series analysis. II-Statistical aspects of spectral analysis of unevenly spaced data. *Astrophysical Journal*, 263,

- pp. 835–853, https://ui.adsabs.harvard.edu/link_gateway/1982ApJ...263..835S/doi:10.1086/160554.
- Schmäl, F. (2013). Neuronal mechanisms and the treatment of motion sickness. *Pharmacology*, 91(3-4), pp. 229–241, <https://doi.org/10.1159/000350185>.
- Schomer, A. C., Nearing, B. D., Schachter, S. C. and Verrier, R. L. (2014). Vagus nerve stimulation reduces cardiac electrical instability assessed by quantitative T-wave alternans analysis in patients with drug-resistant focal epilepsy. *Epilepsia*, 55(12), pp. 1996–2002, <https://doi.org/10.1111/epi.12855>.
- Sclocco, R. et al. (2016). Brain Circuitry Supporting Multi-Organ Autonomic Outflow in Response to Nausea. *Cerebral Cortex*, 26(2), pp. 485–497, <https://doi.org/10.1093/cercor/bhu172>.
- Seeley, W. W. et al. (2007). Dissociable intrinsic connectivity networks for salience processing and executive control. *Journal of Neuroscience*, 27(9), pp. 2349–2356, <https://doi.org/10.1523/jneurosci.5587-06.2007>.
- Shapiro, S. S. and Wilk, M. B. (1965). An analysis of variance test for normality (complete samples). *Biometrika*, 52(3-4), pp. 591–611, <https://doi.org/10.1093/biomet/52.3-4.591>.
- Sharon, O., Fahoum, F. and Nir, Y. (2021). Transcutaneous Vagus Nerve Stimulation in Humans Induces Pupil Dilation and Attenuates Alpha Oscillations. *Journal of Neuroscience*, 41(2), pp. 320–330, <https://doi.org/10.1523/jneurosci.1361-20.2020>.
- Shen, L.-L. et al. (2022). Reassessment of the Effect of Transcutaneous Auricular Vagus Nerve Stimulation Using a Novel Burst Paradigm on Cardiac Autonomic Function in Healthy Young Adults. *Neuromodulation: Technology at the Neural Interface*, 25(3), pp. 433–442, <https://doi.org/10.1111/ner.13521>.
- Shupak, A. and Gordon, C. R. (2006). Motion sickness: advances in pathogenesis, prediction, prevention, and treatment. *Aviation, Space, and Environmental Medicine*, 77(12), pp. 1213–1223.

- Smith, E. E., Cavanagh, J. F. and Allen, J. J. (2018). Intracranial source activity (eLORETA) related to scalp-level asymmetry scores and depression status. *Psychophysiology*, 55(1), p. e13019, <https://doi.org/10.1111/psyp.13019>.
- Solís-Montufar, E. E., Gálvez-Coyt, G. and Muñoz-Diosdado, A. (2020). Entropy Analysis of RR-Time Series From Stress Tests. *Frontiers in Physiology*, 11, <https://doi.org/10.3389/fphys.2020.00981>.
- Song, J. et al. (2015). EEG source localization: Sensor density and head surface coverage. *Journal of Neuroscience Methods*, 256, pp. 9–21, <https://doi.org/10.1016/j.jneumeth.2015.08.015>.
- Spruston, N. (2008). Pyramidal neurons: dendritic structure and synaptic integration. *Nature Reviews Neuroscience*, 9(3), pp. 206–221, <https://doi.org/10.1038/nrn2286>.
- Sra, M., Jain, A. and Maes, P. (2019). Adding Proprioceptive Feedback to Virtual Reality Experiences Using Galvanic Vestibular Stimulation. In *Proceedings of the 2019 CHI Conference on Human Factors in Computing Systems*, pp. 1–14, <https://doi.org/10.1145/3290605.3300905>.
- Stavrakis, S. et al. (2015). Low-level transcutaneous electrical vagus nerve stimulation suppresses atrial fibrillation. *Journal of the American College of Cardiology*, 65(9), pp. 867–875, <https://doi.org/10.1016/j.jacc.2014.12.026>.
- Stavrakis, S. et al. (2020). TREAT AF (Transcutaneous Electrical Vagus Nerve Stimulation to Suppress Atrial Fibrillation): A Randomized Clinical Trial. *Clinical Electrophysiology*, 6(3), pp. 282–291, <https://doi.org/10.1016/j.jacep.2019.11.008>.
- Stern, R. et al. (1985). Tachygastria and motion sickness. *Aviation, Space, and Environmental Medicine*, 56(11), pp. 1074–1077.
- Swets, D. L. and Weng, J. J. (1996). Using discriminant eigenfeatures for image retrieval. *IEEE Transactions on Pattern Analysis and Machine Intelligence*, 18(8), pp. 831–836, <https://doi.org/10.1109/34.531802>.

- Szegedy, C., Vanhoucke, V., Ioffe, S., Shlens, J. and Wojna, Z. (2016). Rethinking the Inception Architecture for Computer Vision. In *2016 IEEE Conference on Computer Vision and Pattern Recognition (CVPR)*, pp. 2818–2826, <https://doi.org/10.1109/CVPR.2016.308>.
- Szegedy, C., Ioffe, S., Vanhoucke, V. and Alemi, A. (2017). Inception-v4, inception-ResNet and the impact of residual connections on learning. In *Proceedings of the Thirty-First AAAI Conference on Artificial Intelligence*, p. 4278–4284, <https://dl.acm.org/doi/10.5555/3298023.3298188>.
- Takens, F. (1981). Detecting strange attractors in turbulence. *Dynamical Systems and Turbulence, Warwick 1980, Lecture Notes in Mathematics*, 898, pp. 366–381, <https://doi.org/10.1007/BFb0091924>.
- Takeuchi, N., Mori, T., Suzukamo, Y. and Izumi, S.-I. (2018). Modulation of Excitability in the Temporoparietal Junction Relieves Virtual Reality Sickness. *Cyberpsychology, Behavior, and Social Networking*, 21(6), pp. 381–387, <https://doi.org/10.1089/cyber.2017.0499>.
- Tarasenko, A., Guazzotti, S., Minot, T., Oganesyanyan, M. and Vysokov, N. (2022). Determination of the Effects of Transcutaneous Auricular Vagus Nerve Stimulation on the Heart Rate Variability Using a Machine Learning Pipeline. *Bioelectricity*, 4(3), pp. 168–177, <https://doi.org/10.1089/bioe.2021.0033>.
- Task Force of the European Society of Cardiology and the North American Society of Pacing and Electrophysiology (1996). Heart Rate Variability: Standards of Measurement, Physiological Interpretation, and Clinical Use. *Circulation*, 93(5), pp. 1043–1065, <https://doi.org/10.1161/01.CIR.93.5.1043>.
- Tassorelli, C. et al. (2018). Noninvasive vagus nerve stimulation as acute therapy for migraine: The randomized PRESTO study. *Neurology*, 91(4), pp. e364–e373, <https://doi.org/10.1212/wnl.0000000000005857>.
- Thanaj, M., Chipperfield, A. J. and Clough, G. F. (2019). Attractor Reconstruction Analysis for Blood Flow Signals. In *2019 41st Annual International Conference of the*

- IEEE Engineering in Medicine and Biology Society (EMBC)*, IEEE, pp. 2281–2284, <https://doi.org/10.1109/EMBC.2019.8856856>.
- Toichi, M., Sugiura, T., Murai, T. and Sengoku, A. (1997). A new method of assessing cardiac autonomic function and its comparison with spectral analysis and coefficient of variation of R–R interval. *Journal of the Autonomic Nervous System*, 62(1-2), pp. 79–84, [https://doi.org/10.1016/s0165-1838\(96\)00112-9](https://doi.org/10.1016/s0165-1838(96)00112-9).
- Toschi, N. et al. (2017). Motion sickness increases functional connectivity between visual motion and nausea-associated brain regions. *Autonomic Neuroscience*, 202, pp. 108–113, <https://doi.org/10.1016/j.autneu.2016.10.003>.
- Touvron, H., Cord, M., El-Nouby, A., Verbeek, J. and Jégou, H. (2022). Three Things Everyone Should Know About Vision Transformers. In *European Conference on Computer Vision*, Springer, pp. 497–515, https://doi.org/10.1007/978-3-031-20053-3_29.
- Tran, N. et al. (2019). Autonomic Neuromodulation Acutely Ameliorates Left Ventricular Strain in Humans. *Journal of Cardiovascular Translational Research*, 12, pp. 221–230, <https://doi.org/10.1007/s12265-018-9853-6>.
- Treisman, M. (1977). Motion sickness: an evolutionary hypothesis. *Science*, 197(4302), pp. 493–495, <https://doi.org/10.1126/science.301659>.
- Tulppo, M. P., Makikallio, T. H., Takala, T., Seppanen, T. and Huikuri, H. V. (1996). Quantitative beat-to-beat analysis of heart rate dynamics during exercise. *American Journal of Physiology-Heart and Circulatory Physiology*, 271(1), pp. H244–H252, <https://doi.org/10.1152/ajpheart.1996.271.1.h244>.
- Turk, M. and Pentland, A. (1991). Eigenfaces for Recognition. *Journal of Cognitive Neuroscience*, 3(1), pp. 71–86, <https://doi.org/10.1162/jocn.1991.3.1.71>.
- van Lieshout, J. J., Wieling, W., Karemaker, J. M. and Eckberg, D. L. (1991). The vasovagal response. *Clinical Science (London)*, 81(5), pp. 575–586, <https://doi.org/10.1042/cs0810575>.

- Vance, C. G., Dailey, D. L., Rakel, B. A. and Sluka, K. A. (2014). Using TENS for pain control: the state of the evidence. *Pain Management*, 4(3), pp. 197–209, <https://doi.org/10.2217/pmt.14.13>.
- Venton, J., Harris, P. M., Sundar, A., Smith, N. A. and Aston, P. J. (2021). Robustness of convolutional neural networks to physiological electrocardiogram noise. *Philosophical Transactions of the Royal Society A*, 379(2212), p. 20200262, <https://doi.org/10.1098/rsta.2020.0262>.
- Verrier, R. L., Nearing, B. D., Olin, B., Boon, P. and Schachter, S. C. (2016). Baseline elevation and reduction in cardiac electrical instability assessed by quantitative T-wave alternans in patients with drug-resistant epilepsy treated with vagus nerve stimulation in the AspireSR E-36 trial. *Epilepsy & Behavior*, 62, pp. 85–89, <https://doi.org/10.1016/j.yebeh.2016.06.016>.
- Vicente, J., Laguna, P., Bartra, A. and Bailón, R. (2016). Drowsiness detection using heart rate variability. *Medical & Biological Engineering & Computing*, 54(6), pp. 927–937, <https://doi.org/10.1007/s11517-015-1448-7>.
- Vitacco, D., Brandeis, D., Pascual-Marqui, R. and Martin, E. (2002). Correspondence of event-related potential tomography and functional magnetic resonance imaging during language processing. *Human Brain Mapping*, 17(1), pp. 4–12, <https://doi.org/10.1002/hbm.10038>.
- Vosseler, A. et al. (2020). No modulation of postprandial metabolism by transcutaneous auricular vagus nerve stimulation: A cross-over study in 15 healthy men. *Scientific Reports*, 10(1), p. 20466, <https://doi.org/10.1038/s41598-020-77430-2>.
- Waller, A. D. (1887). A Demonstration on Man of Electromotive Changes accompanying the Heart's Beat. *The Journal of Physiology*, 8(5), p. 229, <https://doi.org/10.1113/jphysiol.1887.sp000257>.

- Wang, X., Wanniarachchi, H., Wu, A. and Liu, H. (2022). Combination of Group Singular Value Decomposition and eLORETA Identifies Human EEG Networks and Responses to Transcranial Photobiomodulation. *Frontiers in Human Neuroscience*, 16, p. 853909, <https://doi.org/10.3389/fnhum.2022.853909>.
- Weech, S., Wall, T. and Barnett-Cowan, M. (2020). Reduction of cybersickness during and immediately following noisy galvanic vestibular stimulation. *Experimental Brain Research*, 238(2), pp. 427–437, <https://doi.org/10.1007/s00221-019-05718-5>.
- Weiss, K., Khoshgoftaar, T. M. and Wang, D. (2016). A survey of transfer learning. *Journal of Big Data*, 3, pp. 1–40, <https://doi.org/10.1186/s40537-016-0043-6>.
- Wibirama, S., Nugroho, H. A. and Hamamoto, K. (2018). Depth gaze and ECG based frequency dynamics during motion sickness in stereoscopic 3D movie. *Entertainment Computing*, 26, pp. 117–127, <https://doi.org/10.1016/j.entcom.2018.02.003>.
- Wittbrodt, M. T. et al. (2020). Non-invasive vagal nerve stimulation decreases brain activity during trauma scripts. *Brain Stimulation*, 13(5), pp. 1333–1348, <https://doi.org/10.1016/j.brs.2020.07.002>.
- Wittbrodt, M. T. et al. (2021). Noninvasive Cervical Vagal Nerve Stimulation Alters Brain Activity During Traumatic Stress in Individuals With Posttraumatic Stress Disorder. *Psychosomatic Medicine*, 83(9), p. 969, <https://doi.org/10.1097/psy.0000000000000987>.
- Wolf, V., Kühnel, A., Teckentrup, V., Koenig, J. and Kroemer, N. B. (2021). Does transcutaneous auricular vagus nerve stimulation affect vagally mediated heart rate variability? A living and interactive Bayesian meta-analysis. *Psychophysiology*, 58(11), p. e13933, <https://doi.org/10.1111/psyp.13933>.
- Worrell, G. A. et al. (2000). Localization of the epileptic focus by low-resolution electromagnetic tomography in patients with a lesion demonstrated by MRI. *Brain Topography*, 12, pp. 273–282, <https://doi.org/10.1023/a:1023407521772>.

- Wright, J., Ganesh, A., Rao, S., Peng, Y. and Ma, Y. (2009). Robust Principal Component Analysis: Exact Recovery of Corrupted Low-Rank Matrices via Convex Optimization. *Advances in Neural Information Processing Systems*, 22, https://proceedings.neurips.cc/paper_files/paper/2009/file/c45147dee729311ef5b5c3003946c48f-Paper.pdf.
- Yaghouby, F., Jang, K., Hoang, U., Asgari, S. and Vasudevan, S. (2020). Sex Differences in Vagus Nerve Stimulation Effects on Rat Cardiovascular and Immune Systems. *Frontiers in Neuroscience*, 14, p. 560668, <https://doi.org/10.3389/fnins.2020.560668>.
- Yakunina, N., Kim, S. S. and Nam, E.-C. (2017). Optimization of Transcutaneous Vagus Nerve Stimulation Using Functional MRI. *Neuromodulation*, 20(3), pp. 290–300, <https://doi.org/10.1111/ner.12541>.
- Yates, B. J. and Miller, A. D. (2019). Vestibular respiratory regulation. In *Neural Control of the Respiratory Muscles*, CRC Press, pp. 271–284.
- Yates, B. J., Catanzaro, M. F., Miller, D. J. and McCall, A. A. (2014). Integration of vestibular and emetic gastrointestinal signals that produce nausea and vomiting: potential contributions to motion sickness. *Experimental Brain Research*, 232, pp. 2455–2469, <https://doi.org/10.1007/s00221-014-3937-6>.
- Yeo, S. S., Kwon, J. W. and Park, S. Y. (2022). EEG-based analysis of various sensory stimulation effects to reduce visually induced motion sickness in virtual reality. *Scientific Reports*, 12(1), p. 18043, <https://doi.org/10.1038/s41598-022-21307-z>.
- Ylikoski, J. et al. (2017). Non-invasive vagus nerve stimulation reduces sympathetic preponderance in patients with tinnitus. *Acta Oto-Laryngologica*, 137(4), pp. 426–431, <https://doi.org/10.1080/00016489.2016.1269197>.
- Yokota, H. et al. (2022). Effects of Stimulus Frequency, Intensity, and Sex on the Autonomic Response to Transcutaneous Vagus Nerve Stimulation. *Brain Sciences*, 12(8), p. 1038, <https://doi.org/10.3390/brainsci12081038>.

- Yokota, Y., Aoki, M., Mizuta, K., Ito, Y. and Isu, N. (2005). Motion sickness susceptibility associated with visually induced postural instability and cardiac autonomic responses in healthy subjects. *Acta Oto-Laryngologica*, 125(3), pp. 280–285, <https://doi.org/10.1080/00016480510003192>.
- Yuan, H. and Silberstein, S. D. (2016a). Vagus Nerve and Vagus Nerve Stimulation, a Comprehensive Review: Part I. *Headache*, 56(1), pp. 71–78, <https://doi.org/10.1111/head.12647>.
- Yuan, H. and Silberstein, S. D. (2016b). Vagus Nerve and Vagus Nerve Stimulation, a Comprehensive Review: Part II. *Headache*, 56(2), pp. 259–266, <https://doi.org/10.1111/head.12650>.
- Yuan, H. and Silberstein, S. D. (2016c). Vagus Nerve and Vagus Nerve Stimulation, a Comprehensive Review: Part III. *Headache*, 56(3), pp. 479–490, <https://doi.org/10.1111/head.12649>.
- Zabara, J. (1985). Time course of seizure control to brief, repetitive stimuli. *Epilepsia*, 26, p. 518.
- Zabara, J. (1992). Inhibition of Experimental Seizures in Canines by Repetitive Vagal Stimulation. *Epilepsia*, 33(6), pp. 1005–1012, <https://doi.org/10.1111/j.1528-1157.1992.tb01751.x>.
- Zhang, C., Li, S., Li, Y., Li, S. E. and Nie, B. (2020). Analysis of Motion Sickness Associated Brain Activity Using fNIRS: A Driving Simulator Study. *IEEE Access*, 8, pp. 207415–207425, <https://doi.org/10.1109/ACCESS.2020.3038039>.
- Zhao, Q. et al. (2022). Transcutaneous Electrical Acustimulation Ameliorates Motion Sickness Induced by Rotary Chair in Healthy Subjects: A Prospective Randomized Crossover Study. *Neuromodulation*, 25(8), pp. 1421–1430, <https://doi.org/10.1016/j.neurom.2021.09.004>.
- Zumsteg, D., Wennberg, R. A., Treyer, V., Buck, A. and Wieser, H. G. (2005). H215O or

¹³NH₃ PET and electromagnetic tomography (LORETA) during partial status epilepticus. *Neurology*, 65(10), pp. 1657–1660, <https://www.neurology.org/doi/pdf/10.1212/01.wnl.0000184516.32369.1a>.

Zumsteg, D., Friedman, A., Wieser, H. G. and Wennberg, R. A. (2006). Propagation of interictal discharges in temporal lobe epilepsy: Correlation of spatiotemporal mapping with intracranial foramen ovale electrode recordings. *Clinical Neurophysiology*, 117(12), pp. 2615–2626, <https://doi.org/10.1016/j.clinph.2006.07.319>.

Zużewicz, K., Saulewicz, A., Konarska, M. and Kaczorowski, Z. (2011). Heart rate variability and motion sickness during forklift simulator driving. *International Journal of Occupational Safety and Ergonomics*, 17(4), pp. 403–410, <https://doi.org/10.1080/10803548.2011.11076903>.

Appendix A

Ethics Approvals



Central Research Ethics Advisory Group
 Room 120, Rutherford Annexe
 University of Kent
 Canterbury
 Kent CT2 7NZ

Email: centralresearchethics@kent.ac.uk

18 January 2022

To: Emmanuel Molefi
 Email address: em576@kent.ac.uk
By email alone

Dear Emmanuel

Research ethics application: Non-pharmacological management of Motion Sickness Using Auricular Vagus nerve Stimulation (Ref: CREAG015-12-2021)

Thank you for your email of 18 January 2022.

I can confirm the Central Research Ethics Advisory Group (CREAG) has received the amended documents listed below and that these now comply with the conditions detailed in our letter dated 11 January 2022.

As a **positive consideration** of your research proposal was concluded by the Group, in our letter dated 11 January 2022 you may now commence with your project.

Documents received and approved

The documents received and approved were as follows:

<i>Document</i>	<i>Version</i>	<i>Date</i>
Checklist	V1	1 December 2021
Full Application Form	V2	1 December 2021
Research Proposal	V1	Undated
Participation Information Sheet	V1	Undated

Consent Form	V2	Undated
Motion Sickness Assessment Questionnaire	V1	Undated
Simulator Sickness Questionnaire	V1	Undated
Recruiting Participants Poster	V1	Undated

After ethical review

You are obliged to seek consideration of any changes which might affect the ethics of the project.

We wish you best wishes for the success of this project

Yours sincerely

Wendy

Wendy Atkins
Research Ethics Coordinator
 Research and Innovation Services

Enc. Documents listed above



Central Research Ethics Advisory Group
Room 120, Rutherford Annexe
University of Kent
Canterbury
Kent CT2 7NZ

Email: centralresearchethics@kent.ac.uk

14 September 2022

To: Emmanuel Molefi
Email address: em576@kent.ac.uk
Cc: Palaniappan Ramaswamy
By email alone

Dear Emmanuel

Amendment to CREAG015-12-21: Non-pharmacological management of Motion Sickness Using Auricular Vagus nerve Stimulation

Thank you for submitting your amended application to the Central Research Ethics Advisory Group (CREAG).

We are pleased to let you know that the CREAG has reviewed the documents at Appendix A and has given a **favourable ethical opinion** of the minor amendments. If you want to make any further changes to research activity that might affect the ethics of the project, please follow the guidelines attached before you begin that activity.

On completion of your research, the CREAG would appreciate confirmation of the actual end date and a high-level synopsis of the findings and any publication.

We wish you continued success.

A handwritten signature in black ink that reads "Kiershen MacKenzie".

Kiershen MacKenzie
Research Ethics Coordinator
Research and Innovation Services

<i>Document</i>	<i>Version</i>	<i>Date</i>
Amendment Cover Letter	n/a	14 September 2022
Research Proposal	V2	2 August 2022
Participation Information Sheet	V2	14 September 2022
Questionnaire	V1	14 September 2022

Appendix B

Nauseogenic Visual Stimulus

Code B.1: Nauseogenic visual stimulus.

```
%-----%
%   The taVNS Experiment Program
%   Experimental paradigm for study 1 and 2 randomized cross-over
%   trials.
%
%   2021-2024 Emmanuel Molefi (em576@kent.ac.uk)
%   School of Computing, University of Kent.
%-----%
close all; clear all; clc;
sca;
commandwindow;
%-----%
participantName = "Alice";
%-----%
triggerflag = 1;
lifecycleflag = 1;

logFilenameP1 = getLogFilename();
diary(logFilenameP1)
%-----%
try
    PsychDefaultSetup(2);

    Screen('Preference', 'SyncTestSettings', 0.001, 50, 0.1, 5);
    Screen('Preference', 'VisualDebugLevel', 3);
    Screen('Preference', 'SuppressAllWarnings', 1);

    KbName('UnifyKeyNames');
```

```

AssertOpenGL;

screens = Screen('Screens');
screenId = max(screens);

black = BlackIndex(screenId);
white = WhiteIndex(screenId);
gray = round((white+black)/2);

if gray == white, gray = white / 2; end

inc = (white - gray);

[window, windowRect] = PsychImaging('OpenWindow', screenId, gray)
;
[screenXpixels, screenYpixels] = Screen('WindowSize', window);

HideCursor;

arguments.window = window;
arguments.windowRect = windowRect;
arguments.black = black;
arguments.trigger = triggerflag;
arguments.lifecycle = lifecycleflag;
arguments.device = configureTriggerDevice(arguments);
arguments.participantName = participantName;

%-----%
RunExperimentWelcome(arguments);
%-----%

%-----%
fprintf('%%%%%%%%%%%% VNS Begin %%%%%%%%%%%%%\n')
fprintf('Participant ID: %s \n', participantName)
arguments.state = "Baseline";
fprintf('START Baseline: %s \n', getNowTimeString())
RunFixationCross(arguments);
fprintf('END Baseline: %s \n', getNowTimeString())
%-----%

%-----%
fprintf('START Motion Sickness Section: %s \n', getNowTimeString
())
movieDurationSecs = 60*20;
if ~arguments.lifecycle, movieDurationSecs = 20; end

gratingsize = 1920;

```

```
f = 0.005;

cyclespersecond = 62.5;

angle = 180; % grating angle (degrees)

texsize = gratingsize / 2;

p = ceil( 1/f ); % pixels per cycle
fr = f * 2 * pi; % radians
grating_thickness = 50;

visiblesize = 2 * texsize + 1;

x = meshgrid(-texsize:texsize + p, 1);

% compute grating
grating = gray + inc*square(fr * x, grating_thickness);

% Store 1-D single row grating in texture:
gratingtex = Screen('MakeTexture', window, grating);

% Query maximum useable priorityLevel on this system:
priorityLevel = MaxPriority(window);

% get more accurate timing if machine fast enough :)
Priority(priorityLevel);

% Definition of the drawn rectangle on the screen
dstRect = [0 0 visiblesize visiblesize];
dstRect = CenterRect(dstRect, windowRect);

% Query duration of one monitor refresh interval:
ifi = Screen('GetFlipInterval', window);

waitframes = 1; % 1 means: Redraw every monitor refresh

% frames into seconds
waitduration = waitframes * ifi;

% Recompute p (pixels/cycle)
p = 1/f;

shiftperframe = cyclespersecond * p * waitduration;

% configuration for keyboard input
KbQueueCreate;
KbQueueStart;
```

```

exitflag = false;

timeOutCounter = 0;
timeOutArray = {};
timeout = 0;
tStart = nan;
firstTouch = 0;
waitTime = 4;

% an initial VBL-Timestamp as timing baseline for our redraw loop
:
vbl = Screen('Flip', window);

vblendtime = vbl + movieDurationSecs;
frameCounter = 0;

tic;
while vbl < vblendtime
    if frameCounter == 0
        % send trigger
        arguments.state = "Nausea";
        arguments = sendTrigger(arguments);
        %-----%
        % new nausea rating triggers
        rtBool = false;
        rtCount = 0;
        rtStart = NaN;
        %-----%
    end

    % Shift the grating by "shiftperframe" pixels per frame
    xoffset = mod(frameCounter * shiftperframe, p);
    frameCounter = frameCounter + 1;

    % Define shifted srcRect that cuts out the properly shifted
    rectangular area from the texture
    srcRect = [xoffset 0 xoffset + visiblesize visiblesize];

    % Draw grating texture, rotated by "angle":
    Screen('DrawTexture', window, gratingtex, srcRect, dstRect,
angle);

    % Flip 'waitframes' monitor refresh intervals after last
    redraw
    vbl = Screen('Flip', window, vbl + (waitframes - 0.5) * ifi);

    [pressed, firstPress, firstRelease, lastPress, lastRelease] =
    KbQueueCheck;

```

```

    if pressed
        pressedKeys = find(firstPress);
        for k = 1:size(pressedKeys, 2)
            key = KbName(pressedKeys(k));

            if ~any(strcmp(key, 'NumLock')) % guard against
NumLock

                if strcmp(key, 'ESCAPE')
                    ShowCursor;
                    sca;
                    return;
                elseif strcmpi(key, 'N') % severe sickness so
continue to recovery
                    % or we are in debug and we just want to
continue to
                        % next task
                        exitflag = true;
                    elseif any(strcmp(key, 'Return')) || any(strcmp(
key, '-')) % This is for Nausea rating
                        % long-press version 2
                        tStart = tic;

                        timeOutCounter = timeOutCounter + 1;
                        timeOutArray(timeOutCounter, :) = {
timeOutCounter, key, firstPress( find(firstPress) )};

                        % sickness rating; so send triggers
                        arguments.state = "Rating";
                        arguments = sendTrigger(arguments);
                        %-----%
                        % new rating triggers
                        rtBool = true;
                        if isnan(rtStart), rtStart = tic; end
                        rtCount = rtCount + 1;
                        %-----%
                    end

                end % NumLock
            end

            if exitflag, break; end
        end % end of pressed
    %-----%
    % new nausea rating triggers
    if ~isnan(rtStart) && toc(rtStart) >= 3 % seconds
        % now send nausea rating trigger
        nauseaRatingTrigger = num2str(rtCount);
    end

```

```

arguments.state = "RatingNew";
arguments.nauseaRatingTrigger = nauseaRatingTrigger;
arguments = sendTrigger(arguments);
%
rtBool = false;
rtCount = 0;
rtStart = NaN;
end
if ~isnan(rtStart) && abs(vbl-vblendtime) < 3 % seconds
% now send any pending nausea rating trigger
nauseaRatingTrigger = num2str(rtCount);
arguments.state = "RatingNew";
arguments.nauseaRatingTrigger = nauseaRatingTrigger;
arguments = sendTrigger(arguments);
%
rtBool = false;
rtCount = 0;
rtStart = NaN;
end
%-----%
[keyIsDown, secs, keyCode] = KbCheck;

if ~any(keyCode(KbName('NumLock')) % guard against NumLock
    if keyIsDown && (any(keyCode(KbName('Return')) || any(
keyCode(KbName('-')))) && ~isnan(tStart)
        tEnd = toc(tStart);
        if tEnd >= 4 % e.g. 4 seconds
            exitflag = true; % participant opted to abort MS
section
                fprintf(2, 'The participant has opted out at %s
!!!\n', datetime('now'))
                % Send an "X" as a rating trigger code
arguments.state = "RatingNew";
arguments.nauseaRatingTrigger = 'X';
arguments = sendTrigger(arguments);
            end
        else
            tStart = tic;
        end
    end % NumLock
    if exitflag, break; end
    %%%
    if length(timeOutArray) > 4 && ~timeout
        tmpArr = flip(timeOutArray);
        tme = tmpArr{1,3} - tmpArr{4,3};
        if tme > 0 && tme < 1 % within 4 seconds
            % user opted out

```

```

        fprintf(2, 'The participant has opted out at %s !!!\n
', datetime('now'))
        timeout = 1;
    end
end
end
toc;
KbQueueRelease;
fprintf('END Motion Sickness Section: %s \n', getNowTimeString())
%-----%

%-----%
arguments.state = "Recovery";
fprintf('START Recovery: %s \n', getNowTimeString())
RunFixationCross(arguments);
fprintf('END Recovery: %s \n', getNowTimeString())
fprintf('%%%%%%%%%%%% VNS End %%%%%%%%%%%%%\n')
%-----%

%-----%
RunExperimentThankYou(arguments);
%-----%

Priority(0);
sca;
catch
    ShowCursor;
    sca;
    psychrethrow(psychlasterror);
end

diary off
if exist(logFilenameP1, "file")
    movefile(logFilenameP1, ...
        replace(logFilenameP1, 'log.txt', getLogFilename()) );
    fprintf('File rename successful! \n')
else
    fprintf(2, 'Expected file %s but was not found!!! \n',
logFilenameP1)
end

%% HELPER FUNCTIONS
%-----%
function RunFixationCross(arguments)
%-----%
window = arguments.window;
windowRect = arguments.windowRect;

```

```

black = arguments.black;
lifecycle = arguments.lifecycle;

fixationDurationSecs = 60*10;
if ~lifecycle, fixationDurationSecs = 4; end
ifi = Screen('GetFlipInterval', window);
Screen('BlendFunction', window, 'GL_SRC_ALPHA', '
    GL_ONE_MINUS_SRC_ALPHA');
Screen('TextFont', window, 'Ariel');
Screen('TextSize', window, 48);
[xCenter, yCenter] = RectCenter(windowRect);
fixCrossDimPix = 50;
xCoords = [-fixCrossDimPix fixCrossDimPix 0 0];
yCoords = [0 0 -fixCrossDimPix fixCrossDimPix];
allCoords = [xCoords; yCoords];
lineWidthPix = 12;

KbQueueCreate;
KbQueueStart;
exitflag = false;
tic;
startTime = GetSecs;
elapsedTime = 0;
while elapsedTime < fixationDurationSecs
    if elapsedTime == 0
        Screen('DrawLines', window, allCoords, lineWidthPix, black, [
xCenter yCenter], 2); % good quality antialiasing
        Screen('Flip', window);

        arguments = sendTrigger(arguments);
    end
    elapsedTime = GetSecs - startTime;
    [pressed, firstPress] = KbQueueCheck;
    if pressed
        pressedKeys = find(firstPress);
        for k = 1:size(pressedKeys, 2)
            key = KbName(pressedKeys(k));
            if ~any(strcmp(key, 'NumLock')) % guard against NumLock
                if strcmp(key, 'ESCAPE')
                    ShowCursor;
                    sca;
                    return;
                elseif strcmpi(key, 'N') % avoid using 'Return'
                    exitflag = true;
                elseif all(strcmp(key, 'Return')) || all(strcmp(key,
'-'')) % This is for Nausea rating
                    % sickness rating; so send triggers
                    arguments.state = "Rating";
            end
        end
    end
end

```

```

        arguments = sendTrigger(arguments);
    end
    end % NumLock
end
    if exitflag, break; end
end
end
toc;
KbQueueRelease;

if strcmp(arguments.state, 'Rating')
    arguments.state = "Recovery";
end
if strcmp(arguments.state, 'Recovery')
    arguments.state = "End";
    arguments = sendTrigger(arguments);
end
%-----%
end % [EOF]

%-----%
function RunExperimentWelcome(arguments)
%-----%
window = arguments.window;
windowRect = arguments.windowRect;
participantName = arguments.participantName;

xpixels = windowRect(3);
ypixels = windowRect(4);

Screen('FillRect', window);
Screen('TextFont', window, 'Century Gothic');
Screen('TextStyle', window, 1);
timeTxt = char(getNowTimeString2);

Screen('TextSize', window, 30);
Screen('TextStyle', window, 1+2);
DrawFormattedText(window, timeTxt, xpixels*.81);

Screen('TextSize', window, 50);
Screen('TextStyle', window, 1);
txt_msg1 = ['Hello ' char(participantName) ', and welcome to the
    taVNS experiment!'];
if (participantName == "")
    txt_msg1 = 'Hello, and welcome to the taVNS experiment!';
end

```

```

instructions = "During and after the stimulus, \nplease use the
  following scale for nausea rating: ..." + ...
  "\n\n0 = no nausea \n1 = mild \n2 = moderate \n3 = strong \npress
  and hold = severe nausea";

instructions = 'During and after the stimulus, \nplease press the
  Minus ( - ) key \nthe following number of times for nausea rating
  : ...';

DrawFormattedText(window, txt_msg1, 'center', ypixels*.20, [0 0 255])
  ;

xint = .25;
DrawFormattedText(window, instructions, xpixels*xint, ypixels*.39, [0
  0 255]);

nauseaRatingScale = '\nMild           = 1 \nModerate   = 2 \nStrong
  = 3 \nSevere           = press and hold';
DrawFormattedText(window, nauseaRatingScale, xpixels*xint, ypixels
  *.54, [0 0 255]);

fprintf('Requested font: %s, got: %s\n', 'Century Gothic', Screen('
  TextFont', window));

Screen('TextFont', window, 'Times');
Screen('TextSize', window, 30);
txt_msg_continue = 'Hit return key to begin experiment.';
DrawFormattedText(window, txt_msg_continue, 'center', ypixels*.95,
  [255, 0, 0, 255]);

Screen('Flip', window);

KbQueueCreate;
KbQueueStart;
exitflag = false;
while ~exitflag
  [pressed, firstPress] = KbQueueCheck;
  if pressed
    pressedKeys = find(firstPress);
    for k = 1:size(pressedKeys, 2)
      key = KbName(pressedKeys(k));
      if strcmp(key, 'ESCAPE')
        ShowCursor;
        sca;
        return;
      elseif strcmpi(key, 'S')
        exitflag = true;

```



```
%-----%
function em_fprintf(triggerCode)
%-----%
fprintf(2, '##### trigger code : %s [%s]\n', triggerCode,
        getNowTimeString())
%-----%
end % [EOF]

%-----%
function arguments = sendTrigger(arguments)
%-----%
trigger = arguments.trigger;
state = arguments.state;
device = arguments.device;

if strcmp(class(device), 'internal.Serialport') && sum(strcmp(
    serialportlist('available'), 'COM4')) == 1
    disp('Reconnecting to serialport!!')
    clear device;
    device = serialport("COM4", 115200);
    arguments.device = device;
    disp('Reconnecting to serialport successful.')
end

if trigger && arguments.lifecycle % 29.11.22
    triggerCode = extract(state, 1);
    if strcmpi(state, 'Baseline')
        write(device, triggerCode, "string")
        em_fprintf(triggerCode)
    elseif strcmpi(state, 'Nausea')
        write(device, triggerCode, "string")
        em_fprintf(triggerCode)
    elseif strcmpi(state, 'Rating')
        triggerCode = 'S'; % 'S' for subjective
        write(device, triggerCode, "string")
        em_fprintf(triggerCode)
    elseif strcmpi(state, 'RatingNew')
        triggerCode = arguments.nauseaRatingTrigger;
        write(device, triggerCode, "string")
        em_fprintf(triggerCode)
    elseif strcmpi(state, 'Recovery')
        write(device, triggerCode, "string")
        em_fprintf(triggerCode)
    elseif strcmpi(state, 'End')
        write(device, triggerCode, "string")
        em_fprintf(triggerCode)
    elseif strcmpi(state, 'TestBeforeExperiment')
```

```

write(device, triggerCode, "string")
    em_fprintf(triggerCode)
    end
end
%-----%
end % [EOF]

%-----%
function timeStringFormat = getNowTimeString()
%-----%
timeStringFormat = string( datetime("now") );
%-----%
end % [EOF]

%-----%
function timeStringFormat = getNowTimeString2
%-----%
timeStringFormat = string( datetime("now", "Format", "eeee, MMMM d, y
    ") );
%-----%
end % [EOF]

%-----%
function logFilename = getLogFilename()
%-----%
logFilename = replace(getNowTimeString(), " ", "--").replace(":",
    "-").append("_log.txt");
%-----%
end % [EOF]

%-----%
% http://psychtoolbox.org/download.html
% Installation
% [1] PsychtoolboxVersion
%
% http://psychtoolbox.org/docs/GStreamer
%
% Stable version (tested by EM):
% '3.0.19 - Flavor: beta - Corresponds to SVN Revision 13508
% For more info visit:
% https://github.com/Psychtoolbox-3/Psychtoolbox-3'
%-----%

```